THE STRENGTH AND FATIGUE PERFORMANCE OF 319 ALUMINUM ALLOY CASTINGS

by

GLENN EDWIN BYCZYNSKI

A thesis submitted to the Faculty of Engineering
of The University of Birmingham
for the degree of

DOCTOR OF PHILOSOPHY

School of Metallurgy and Materials
Faculty of Engineering
University of Birmingham
Birmingham
B15 2TT
United Kingdom
June 2002

ABSTRACT

Analysis of fatigue samples sectioned from commercial 319 (Al-Si-Cu-Mg) alloy cylinder block castings showed that shrinkage pore networks and oxide films played an important role in fatigue failure.

A reduced pressure technique was employed to study the relationship between porosity and oxide films. Links between oxide films and porosity were made and mechanisms for the inflation of films into porosity networks were established.

Tensile tests performed on samples cast with and without filters showed that the ultimate tensile strengths of the filtered group had a Weibull modulus 2.4 times that of the unfiltered. Samples with abnormally low strengths were found to contain oxide film defects. These films had an approximately 5 times greater damaging effect on strength than that predicted by reduction in cross sectional area. The fracture strengths of these flawed samples were found to obey a linear elastic fracture mechanics model (LEFM).

A LEFM crack growth model was particularly successful in predicting the life of fatigue samples that initiated at oxide films. Having crack-like geometry, and a minute crack tip radius, oxide films effectively acted as preformed cracks. Consequently there was an absence of crack nucleation time, explaining the correlation of predicted propagation life to fatigue life.

To my sons, Gabriel and Benjamin, for bringing so much joy into my life.

ACKNOWLEDGEMENTS

I would like to thank Professor John Campbell for his guidance both on the academic and professional levels during my time at the University of Birmingham. It was an honour and a pleasure to number among his students. His knowledge and integrity inspire others to strive to attain their personal bests.

I would like to acknowledge Ford Motor Company, for the Ford Technical Fellowship that funded my research program. In particular I would like to recognize the management of Windsor Aluminum Plant, who had the foresight and the confidence in my abilities to recommend and sponsor me for this work.

I would like to thank Messrs. A. Caden and J. Pfeiffer for their technical assistance in the experimental portion of my work and to the other members of the IRC casting group for their helpful discussions, kindness and friendship.

Most of all I would like to express my deepest gratitude to my wife and best friend Natalie, for her love and support during this work and always.

CONTENTS

LIST OF SYMBOLS

Symbol	Meaning	Symbol	Meaning
a	crack length	R	stress ratio
a_C	critical crack length	S_r	ratio of LEFM predicted stress to collapse stress
a_f	final crack length	U	ratio of effective stress intensity range to nominal stress intensity range
a_i	initial crack length	U_r	value of U at a given stress ratio
C	constant	W	width of plate
da/dN	crack growth rate	w	width of fold of oxide film
E	Young's modulus	x	random variable
G	strain energy release rate	x_0	minimum value of x
G_C	critical strain energy release rate	Y	compliance factor
K	stress intensity factor	$Y(a_i)$	crack size dependent Y
ΔK	alternating stress intensity factor range	μ	sample mean
K_{app}	applied fracture toughness	ν	Poisson's ratio
$K_{I,II,III\,C}$	fracture toughness, for crack opening modes I, II or III	γ	surface energy
K_{eff}	effective stress intensity factor	σ	standard deviation, uniform stress
K_{max}	maximum value of stress intensity factor	$\Delta\sigma$	alternating stress range
K_{min}	minimum value of stress intensity factor	$\sigma_{0.2Y}$	0.2% yield stress
K_{op}	value of stress intensity at which crack faces separate	σ_a	applied stress, alternating stress (fatigue)
K_r	ratio of applied value of fracture toughness to the ideal value of fracture toughness	σ_F	fracture stress
K_{th}	threshold stress intensity factor	σ_k	predicted stress (LEFM)
L_r	ratio of applied stress to yield stress	σ_m	mean stress
m	Weibull modulus or shape factor, Paris equation exponent	σ_{max}	maximum stress in the fatigue cycle
N	number of cycles	σ_{min}	minimum stress in the fatigue cycle
N_f	total fatigue life	σ_n	net section stress
N_i	fatigue initiation life	σ_r	range of stress (fatigue)
N_p	fatigue propagation life	σ_U	uniaxial stress
$P(x)$	cumulative frequency distribution of x	σ_{UTS}	ultimate tensile stress
Q	defect shape factor	σ_Y	yield stress
r	radial distance from crack tip	θ	the Weibull scale parameter or characteristic value

Chapter 1

INTRODUCTION

Today aluminum castings are the materials of choice for automotive cylinder block and cylinder heads. They have proven themselves to be a lightweight alternative to the much heavier iron based versions of the past. The resultant reduction in vehicle weight remains as one of the largest single improvements to overall vehicle fuel economy. Despite having firmly established themselves in this niche, aluminum castings are poised for yet future growth. Industry analysts (Lessiter 2000) predict an increase in aluminum castings in motor vehicles over the next ten years. Projections in the order of 60% and 96% increases in the use of aluminum based cylinder blocks and heads respectively. Ford Motor Company has also recently announced that aluminum alloys are to migrate further into what have been (up until now) exclusively ferrous based casting applications, e.g. truck engines that include eight and ten cylinder designs. The result of this expansion of the role of aluminum castings is a need for improved casting properties. The fatigue performance of the cylinder block casting in particular is a concern. In terms of casting properties, high cycle fatigue life appears to be the most appropriate measure for determining the robustness of these castings in service. Factors that influence this robustness include casting design, casting quality, alloy composition, and heat treatment process. For low volume applications the use of costly high purity alloys, 100% inspection or high safety factors are capable of overcoming most fatigue issues. However for high volume automotive applications cost is of great importance. Recently it has been shown (Nyahumwa 1998a) that aluminum castings may only be achieving 1% of their potential fatigue performance due to defects present in the casting. If the liquid metal is handled correctly and the mould design optimized it should be possible to capitalize on significantly more of this fatigue potential, regardless of the type of alloy used.

In this work failed fatigue samples taken from production castings were analyzed and found to contain oxide films and porosity. This led to the exploration of the relationship between oxides and porosity using the remelt reduced pressure test, a purpose built instrument under development at the University of Birmingham. In order to study the effects of oxide films on casting properties further, test castings were produced using the commercial alloy used by Ford. Cast with and without filters, these were designed to produce castings with different levels of oxide films. Tensile and fatigue tests were conducted to determine the effects of oxide films on the static strength and fatigue life of these castings.

Chapter 2

LITERATURE REVIEW

2.1 FORD MOTOR COMPANY - COSWORTH PRECISION SAND PROCESS

In the late 1980's Ford Motor Company set out to find a casting process for its new generation of lightweight cylinder head and block applications. A specific task force was assembled to perform a worldwide search for this optimum casting process, on which Ford would build the future of its lightweight casting business. The Cosworth casting process had established its quality and consistency in the realm of high performance racing, but at this time had yet to be proven to meet the demands of a high volume production environment. A unique prototype plant was constructed to validate the Cosworth casting process. Designed to use full-scale production equipment for moulding and casting, Ford's Cast Aluminum Research and Development (CARD) plant was built in 1988. After successfully proving the capability of the process, Ford Motor Company purchased an exclusive worldwide license to use the Cosworth casting process for high volume production of castings. In 1992 construction of the Ford Windsor Aluminum Plant (WAP) was completed. Currently the plant has a capacity of approximately one million castings per year (Kanicki 1994).

There are several distinctive aspects of the Cosworth casting process (Campbell 1981). The three fundamental ideas are discussed below.

2.1.1 Minimization of Liquid Metal Damage

Minimization of liquid metal damage is definitively the most important aspect of the Cosworth casting process. The entire liquid metal handling is designed as not to entrain surface oxides. This starts with the treatment of the metal, whether melted 'in house' or received in the liquid form. The liquid metal is transferred by a simple launder system to the casting furnaces. The launder system is designed to be of the same elevation at all points along the delivery system so that the metal does not 'run' down hill or experience any turbulence during transfer. The size of the casting furnaces that receive the metal are sufficiently large for the metal to remain resident for upwards of ten hours under full production rates. These holding times allow for impurities to settle to the bottom of the furnace or rise to top of the melt depending on their density (Figure 2.1). The metal used for casting is pumped from the cleanest middle layer of the melt. This is performed using an electromagnetic pump that is partially submerged in the liquid metal bath. The metal is pumped in a controlled manner into a bottom-gated mould, once again in order to minimize metal surface turbulence (Figure 2.2). A feedback sensor/control system compares the actual level of the aluminum versus a preprogrammed value. The pump voltage (which varies directly with metal flow rate) is then adjusted, to ensure that the mould is filled at the correct rate by the liquid metal (Figure 2.3).

2.1.2 Mould Rollover

The use of a bottom-gated mould, while advantageous from a filling point of view has one major drawback. The hottest metal (or last metal into the mould) is located lower than the rest of the metal in the mould cavity. This is undesirable for two reasons: first, proper feeding will not take place, as the temperature gradient is unfavourable. Second, convection may occur, as the hot metal is inclined to exchange positions with the colder more dense metal. Both of these conditions can lead to a plethora of casting defects. To counter this situation, pump pressure is maintained after the mould has been completely filled and the mould is rotated 180° about the mould/pump interface point. This now allows for the correct temperature gradient and gives the added benefit of being able to separate the mould from the metal supply. This allows for the now full mould to be indexed away and the next casting cycle to begin. Production rates of 72 castings per hour for one casting machine are typical. Figure 2.4 shows a section of a V8 casting and the position of the feeder before roll over.

2.1.3 Precision Zircon Sand Mould and Cores

The Cosworth process is often accurately referred to as the Cosworth Precision Sand Process. One of the main features that makes this process high precision is that it employs zircon sand as a mould material. Unlike silica sand, zircon sand remains dimensionally stable, having a low and linear thermal expansion throughout the temperature range of molten aluminum. An additional benefit is that cores made with zircon sand and phenolic urethane binders have a very similar density to that of molten aluminum. This eliminates any buoyant force that cores of less density experience. These forces can lead to core distortion or even floatation resulting in poor dimensional repeatability of the final casting. Other features include the fact that cores are made at room temperature from dimensionally stable core boxes, and that zircon sand is chemically neutral to most binder systems and to liquid aluminum.

2.2 METALLURGY OF HYPOEUTECTIC ALUMINUM-SILICON ALLOYS

2.2.1 Microstructural Phases Present

2.2.1.1 Matrix Material

The matrix of the cast alloy is composed of aluminum dendrites with eutectic silicon, eutectic copper and iron intermetallics. The amount of each depends strongly on the alloy composition and solidification conditions. The composition limits for the 319 aluminum alloy are shown in Table 2.1. Composition limits for the alloy of interest to this study are found in Table 2.2. Note the tighter ranges used in the production of commercial castings.

Table 2.1 Composition Limits for Aluminum Association Alloy 319

Element	Si	Cu	Mg	Fe	Mn	Ti	Sr	Zn	Al
wt%	5.5-6.5	3.0-4.0	0.10	1.0 max	0.50	0.25 max	-	1.0	remainder

Table 2.2 Composition Limits for Ford Motor Company WAP Alloy 319

Element	Si	Cu	Mg	Fe	Mn	Ti	Sr	Zn	Al
wt%	7.0-7.8	3.3-3.7	0.25-0.35	0.40 max	0.20-0.30	0.10-1.15	residual	0.25	remainder

2.2.1.2 Eutectic Silicon

The addition of silicon in this family of alloys improves metal castability and reduces metal shrinkage during solidification. The natural morphology for the eutectic silicon is acicular or plate-like. Modification of this morphology to a less harmful geometry is normally performed by chemical additions (discussed in section 2.2.2) or by solution treatment. Chemical additions transform the growth mode of this eutectic phase so that a fine fibrous morphology results (Lu

1987; Shamsuzzoha 1993). The heat treatment mechanism is a solid state diffusion driven process where the eutectic silicon is fragmented and spherodized.

2.2.1.3 Copper Rich Phases

Copper is added as a hardener-strengthener. While the as-cast hardness of these alloys is usually acceptable, precipitation heat treatment fully develops the hardness and strength. Depending on the service conditions however, the peak-aged condition may not be optimum. Often castings are over-aged to provide a compromise between strength and dimensional stability in service. Copper-rich eutectic phases may take several forms depending on the on the alloy composition, solidification conditions and heat treatment. Common phases found in 319 are described in Table 2.3.

Table 2.3 Common Copper Bearing Phases found in 319

Phase description	Composition	References
Eutectic copper, blocky in shape	Al_2Cu	(Bäckerud 1990; Caceres 1999)
Fine eutectic	$Al_5Mg_8Cu_2Si_6$	(Bäckerud 1990; Samuel 1996)

2.2.1.4 Iron Rich Intermetallics

Secondary alloys (those produced from recycled material) have impurity levels that are generally higher than those commonly found in primary alloys. Depending on the level of iron, and elements known to form phases with iron, a large number of different types of iron rich intermetallics can be formed. The formation of these phases is also largely dependent on the local solidification rates (Crepeau 1995a) and melt holding temperature (Lakshmanan 1995). The two most common phases found in alloy 319 are listed in Table 2.4.

Table 2.4 Common Iron Bearing Intermetallics found in 319

Phase Description	Composition	Comments
α-phase or "Chinese script", multi-armed or semi-symmetrical in shape	$Al_{15}(FeMn)_3Si_2$	Preferred form, seen as less harmful to ductility, stable during heat treatment.
β-phase, thin plates	Al_5FeSi	Undesirable because of morphology. These are known to reduce casting ductility and increase shrinkage porosity by blocking feed paths (Narayanan 1994; Crepeau 1995a; Roy 1996b; Otte 1999). However, this phase may be fragmented and dissolved during heat treatment (Narayanan 1995).

2.2.2 Modification

Modification of the eutectic silicon is known to improve ductility in some alloys. By far the most common method of modification is by chemical additions. Pacz (1921) is credited with discovering the modifying effects of sodium on eutectic silicon. Since then a number of the group 1 and group 2 elements that are heavier than sodium have been discovered to have this effect. However, due to such issues as cost, health and safety, and process efficiency, sodium and strontium have become the two elements that have found the most use in industry. Sodium while the more potent of the two, has a tendency for its modifying effects to fade too quickly for many casting processes. Thus strontium has become the favoured addition for a vast number of metal casters. In principle the concept of the benefits of modification seems sound. However there are secondary negative effects that strontium additions seem to have on the soundness of castings. Strontium has been observed to increase the amount and size of the defect structure of the casting, particularly in the form of porosity and oxide inclusions. A notable study concerning this is (Tynelius 1993), where the causes of microporosity in A356 alloy castings were statistically analyzed. The authors found that while hydrogen was the strongest determinant for all aspects of microporosity studied, strontium was found to be the strongest alloy parameter in predicting percentage porosity, largest pore size and maximum pore area. Other authors have reported similar effects (Gruzleski 1984; Roy 1996a). An important fact to emphasize is that pore volume fraction increases with strontium modification, even when hydrogen levels and solidification rate appear to be held constant. Furthermore this increase in pore volume fraction is exaggerated at lower solidification rates. This is particularly important to metal casters using sand moulds.

The most popular theories linking strontium and porosity include the effects of strontium additions on: the depression of eutectic temperature (Argo 1988; Fang 1989), interfacial energy or surface tension (Fang 1989; Emadi 1993), hydrogen solubility (Denton 1985; Dimaguga 1988; Bian 2000) and oxide formation (Gruzleski 1984; Garat 1992). Unfortunately much evidence exists that both support and contradict many of these theories. Most of the proposed mechanisms may act independently of one another and perhaps it is the case that all are operative to some degree depending on the precise casting conditions.

Whatever the active mechanisms are, it is agreed that when using strontium as a modifier one is balancing opposite driving forces that influence casting quality. A modified eutectic silicon structure is desirable for material properties but this may be often offset (or overwhelmed in some cases) by the increase in amount of defect structure present. How well a modifier performs has been shown to be a function of melt holding time, local solidification rate, hydrogen level, alloy composition and the amount of trace elements, to list only the well-known effects. Consequently individual casting modification requirements vary greatly and recommended universal additions do not exist. This is clear when one considers the various levels of strontium commonly used in the industry today.

2.2.3 Grain Refinement

Grain refinement is another practice that is widely used in the aluminum casting industry. There are several methods to achieve fine grains in castings, and they may be categorized as follows: mechanical methods, thermal methods, constitutional supercooling, and chemical additions. Mechanical methods are those that agitate the solidifying melt e.g. ultrasonic vibration, and mechanically or electromagnetically induced stirring. The growing dendrite stalks are fragmented en mass and become mobilized to form a multitude of sites from which grains grow.

Thermal methods include reducing local solidification rates by the reduction of section size (not usually an option) or by the addition of chills and chill fins (as in sand casting) or placement of cooling lines and application of thermally conductive coatings (as in the various forms of die casting). Constitutional supercooling is achieved by adding elements of limited solubility to the alloy, thus increasing the dendrite growth restriction factor, slowing grain growth and allowing additional time for grains to nucleate resulting in an overall finer grain size. All of the above described methods require significant changes to the design of the casting and/or process, making the addition of chemical refiners by far the favoured option (although the chemical additions are not completely free of disadvantages, e.g. many exhibit fading characteristics).

Once again while many are familiar with the effects of grain refiner additions on the casting structure, there exists some uncertainty as to what the operative mechanisms are. Much research has been focused on the mechanisms of grain refinement. The theories will not be discussed in detail here. However those that have been found most favourable over the years include: change in nucleation entropy (Youdelis 1979; Youdelis 1980), constitutional undercooling (Sigworth 1996), the particle or boride theory (Cibula 1951), the duplex particle theory (Johnsson 1993; Mohanty 1995), hypernucleation (Jones 1985; Jones 1987), phase diagram based theories (Crossley 1951), and the peritectic "hulk" theory (Vader 1989; Bäckerud 1991). For a more detailed review of the mechanisms the reader is referred elsewhere (Mohanty 1995). It is important to note that all of these theories may not work completely independent of one another.

While it is true in general that finer grained castings are more desirable, grain size considered on its own has not been fundamentally linked with improved mechanical properties in conventional aluminum casting alloys. In these alloys improvements from grain refiners are usually related to casting soundness i.e. improved mass feeding, improved fluidity that result in less porosity and reduced pore sizes. It is most probably via these second order effects that mechanical and fatigue properties are improved rather than via the classical Hall-Petch benefits

.

2.2.4 Porosity

2.2.4.1 Hydrogen Porosity and Shrinkage Porosity

The causes of porosity in aluminum alloy castings are thought to be well known and fall into two basic categories. The first category is gas related porosity where dissolved hydrogen is rejected from the solidifying alloy because of its lower solubility in the solid state. The hydrogen concentration builds up ahead of the solidifying front and bubbles form from the supersaturated solution when the surface energy conditions are favourable. The resulting pore shape in the solidified casting is somewhat spherical in nature. The second type is shrinkage porosity, which is a result of the inability of the casting to feed the required amount of metal during the contraction from liquid to solid. The resulting pore morphology is complex and irregular and tends to follow the dendritic profile of the local structure. While these mechanisms are quite distinct, in practice it is only in rare cases where one mechanism will operate independently of the other. The more common case is where one assists the other and the resulting pore (and pore morphology) is a product of the combined mechanisms (Whittenberger 1952; Campbell 1991). This interaction results in a whole population of types of defects that range from “ideal” gas porosity at one extreme, to “ideal” shrinkage porosity at the other. Recently Anson and Gruzleski (Anson 1999a; Anson 1999b) have proposed a promising technique to discern between the two basic forms of porosity. They used a statistical approach based on the distance of a “nearest neighbour pore” on metallurgical cross sections (in combination with conventional pore shape analysis). The new idea here being that shrinkage pores manifest themselves as concise networks on 2-dimensional cross sections (Figure 2.5). This contrasts with the distinctly isolated nature of gas pores.

2.2.4.2 Nucleation of Porosity on Oxide Films

It has become a well-known fact that classic nucleation theory does not well describe the nucleation of pores in liquid metals. This has been shown by several authors (Fisher 1948; Campbell 1968; Shahani 1985; Gupta 1992). It is essentially a problem of the enormous theoretical stresses needed to “fracture” the liquid. The modern idea behind why porosity forms at much lower critical stresses is that porosity nucleates heterogeneously on favourable discontinuities in the (semi)liquid metal. Traditionally the belief was that these low energy nucleation sites may include roots of dendrite arms, intermetallic phase boundaries or non-metallic inclusions (Brondyke 1964; Taylor 1995). However the type of site with the highest propensity for nucleation of porosity must be entrained oxide films (Campbell 1996). The nature (discussed in the section 2.2.5) and sheer number of oxide films make them the most preferred candidate for porosity nucleation. The results from several investigations support this theory (Gruzleski 1990; Crepeau 1995b; Stucky 1998; Fox 2000). In all of these works oxides are discovered to act as nucleation sites for porosity.

2.2.4.3 Effects of Porosity on Casting Properties

The effects of porosity on casting properties are quite well known. Its adverse effects on ultimate tensile strength and elongation have been established in Al-Si castings by several authors (Herrera 1977; Eady 1986; Surappa 1986; Caceres 1995; Caceres 1996; Boileau 2001). Porosity is known to be even more damaging to fatigue performance of castings, and this is discussed under the fatigue section 2.5.3.2 of this work.

Of course the effects of porosity are not contained to the mechanical test laboratory. In the daily production of castings, porosity plays a leading role in issues such as casting soundness, pressure tightness, sealing surface imperfections and casting appearance.

2.2.5 Oxide Films

2.2.5.1 Formation of Oxide Films

Aluminum in the solid state will readily form a protective oxide layer when exposed to oxygen, preventing further oxidation of the parent metal. Unfortunately the oxidation process with the metal in the liquid state is far from helpful. Once again a stable oxide is formed, however it is not soluble in the liquid metal. There are actually a series of transformations that take place in the liquid aluminium oxidation process. Since these steps are chemical reactions they are sensitive to conditions such as temperature, pressure, and the purity and activity of the reactants. The oxidation sequence of pure liquid aluminum and that of liquid aluminum containing magnesium will now be discussed, as these two cases are relevant to the casting conditions in this work.

In its pure state, standard pressure and at typical molten aluminum casting temperatures (933 to 1073K) aluminum will immediately form an amorphous alumina film (Sleppy 1961; Dignam 1962). The next stage is believed to be the nucleation and growth of a crystalline transition alumina. Early papers dealing with the nature of these transition aluminas identified η-alumina as the preferred form (Sleppy 1961). This is in contrast to the current beliefs that γ-alumina is the dominant transitional form (Impey 1988; Agema 1989; Impey 1991). The next transformation is well agreed to be the formation of α-alumina. This transformation is believed to occur at the oxide-melt interface. This transformation results in a 24% reduction in oxide volume (Impey 1988), and is thought to cause film rupture further exposing the liquid metal. The metal then passes into and through these new channels and instantly reacts with the oxygen available at the surface. If left undisturbed it has been reported that a 1μm thick oxide layer is formed within an hour and after that the rate of oxidation is minimal (Mal'tsev 1956) cited by (Agema 1989). This is the situation in a static melt where no movement of the liquid metal occurs. This well describes the metal-oxide behaviour in a holding furnace or other such reservoir where stagnant conditions are present. More relevant to casting operations such as ladling, pumping and mould filling however, would be the situation of the first stage amorphous film forming and immediately fragmenting and being carried off into the bulk of the flowing metal. Since the vast majority of these films are surface entrained they constitute folded films in the melt. Liquid metal surface entrainment is easily achieved in these processes if care is not taken to consciously avoid it. Entrained films have one surface in good contact with the liquid metal (wet side) and the other surface trapping a small amount of atmosphere in between (dry side) (Figure 2.6). These films if allowed (sufficient time at sufficient temperature) will continue the transformations described above, utilizing the trapped air for the oxidation reactions, until the stable α-alumina phase is formed.

When magnesium is present in an aluminum alloy the reaction sequences are different than those in the pure metal. From a thermodynamic standpoint magnesium will preferentially oxidize compared with aluminum. Thus MgO will be the first oxide formed (Haginoya 1983). If the magnesium content of the alloy is significant (greater than 0.3 wt%) only magnesium will be oxidized (Wightman 1983). Once again an intermediate amorphous phase (in this case magnesia) is the early form of the oxide (Silva 1989). This amorphous MgO then transforms into crystalline MgO. The next reaction to occur is conversion of the MgO to $MgAl_2O_4$ (spinel) by reaction with aluminum. In lower magnesium containing alloys (less than 0.3 wt%) there will likely be concurrent oxidation reactions forming the initial phases of alumina and magnesia according to the local elemental activities. Table 2.5 summarizes the oxide reaction sequences in pure aluminum and aluminum-magnesium alloys

Table 2.5 Summary of Phases Present in the Oxidation of Al and Al-Mg Alloys

Reference	Alloy	Early phase	Transitional phase(s)	Stable phase
(Sleppy 1961; Dignam 1962; Simensen 1980)	Pure Al	amorphous alumina	γ- Al_2O_3or η- Al_2O_3	α- Al_2O_3
(Wightman 1983; Agema 1989)	Al-Mg (< 0.3 wt%)	amorphous alumina + MgO	γ- Al_2O_3 or η- Al_2O_3 + MgAlO (metastable prespinel)	α- Al_2O_3 $MgAl_2O_4$ (spinel)
(Cochran 1977; Haginoya 1983; Agema 1989; Silva 1989)	Al-Mg (> 0.3 wt%)	amorphous magnesia	MgO or MgAlO (metastable prespinel)	$MgAl_2O_4$ (spinel)

Other elements have been known to have influences both on the oxidation reaction rates and on the strengths of the oxide films themselves. Selected elements and their influences are summarized in Table 2.6

Table 2.6 Effects of Selected Elements on Oxidation rate and Strength of Oxide Film

Reference	Element(s)	Effects
(Thiele 1962) (Cochran 1977) (Balicki 1959) cited in (Agema 1989) (Kordes 1935) cited in (Plummer 1958)	Si, Fe, Cu, Zn, Mn Mg, Na, Se, Ca, Li Be	No effects Increases rate of oxidation Decreases rate of oxidation
(Kahl 1985) cited in (Agema 1989)	Mg, Na, Ca, Li,	Increases strength of film
(Kahl 1984)	Be, Si, Sb, Sr	Decreases the strength of film

2.2.5.2 Oxide Film Morphology

Due to the nature of oxide films, being very thin and extremely fragile, it is only because they are so numerous that we are able to detect them on standard microstructural cross sections. Unless the oxide content is extremely high, light optical microscopy is insufficient as a technique for their location and analysis. Even when the films are successfully located their apparent size is a gross under-representation since they appear as one-dimensional lines or scribbles. They are more frequently seen on tensile fracture or fatigue surfaces, but again only if the conditions are favourable i.e. the fracture crack path passed through or initiated at the oxide. This setting effectively offers clues to their true morphology (complex folded entanglements). The folded films in these cases have been prised apart and often a corresponding film is seen on the opposite side of the fracture.

Thickness measurements in the literature have taken two forms. The first method employs scanning electron microscopy to image the film. By estimating the width of the smallest wrinkle or crease, *w*, the thickness of the film can be approximated to be *w/2*. This method may be accurate only for sharp folds that contain little or no trapped metal. Alternatively in the rare case of the film positioned favourably, an edge-on view will reveal the thickness of the film directly. The second method deals with a very specific case where the oxide thickness is calculated by scraping away the oxide layer on a molten Al-Si alloy and noting the interference colours that formed over time. Using the corresponding wavelengths of light and correcting for reflected radiation the oxide thickness can be calculated (Agema 1989).

Table 2.7 Characteristics of Oxide Films

	Reference	Film age	Type of Phase (see Table 2.5)	Thickness (µm)	Description
YOUNG FILMS	(Agema 1989)	< 0.01 s	early	0.056 to 0.127	observed only as change in apparent colour of melt surface
	(Divandari 2000)	0.01 – 1s	early	0.050 to 0.500	delicate, transparent, thin film, with sharp creases or wrinkles
	(Campbell 1991)*	10s – 60s	early	10	flexible, extensive films
OLD FILMS	(Campbell 1991)*	10 min to 1 hr	transitional	100	thicker films less flexible
	(Campbell 1991)*	10 hrs to 10 days	stable	1000	rigid lumps and plates

*estimates

Young films are characterized by their minute thickness and wrinkled morphology. The wrinkled nature of young films is related to the dynamics of the liquid metal immediately after their formation. As the liquid metal flows into a mould a new oxide is continually formed as the one encasing the metal front fractures and becomes pinned against the mould wall. However with even the smallest amount of turbulence or liquid metal front perturbations present, the result will be the folding over of the film, entrainment, or fragmentation of these new very thin oxide films.

Given time and the correct conditions young oxide films will mature into old oxide films (see Table 2.7). The necessary conditions being access to further reactants i.e. oxygen, aluminum or magnesium and sufficient temperature. These conditions are easily met in a holding furnace or perhaps a casting with a long solidification time. These types of films may also be inherited in the metal supply. Old films are extremely stable and if care is not taken to remove them they can be carried through the entire life of the metal, until discovered in the end product.

2.2.5.3 Folded Films acting as Cracks

As mentioned in the previous section when oxide films fold over or are entrained a small amount of atmosphere is trapped between. There can be little if any bonding force between the two dry sides, and essentially the films act as a crack in the liquid metal. After solidification the cracks remain and in a best case scenario they would remain as small cracks throughout the casting. The detrimental effect of oxide films on the strength and reliability of castings has been established conclusively by Green and Campbell (Green 1995). Worst case scenarios could include becoming nucleation sites for gas pores, shrinkage pores and hot tears. Recent work by Nyahumwa (Nyahumwa 1998b; Nyahumwa 1998a; Nyahumwa 2001) has suggested that young films are particularly good at nucleating pores while old films remain rather inert in this respect. The concept is that in old films the trapped gas layer has reacted further than that of a young film resulting in some degree of bonding between the two dry sides. These bonds result in the old oxide becoming less favourable a nucleation site for porosity as it resists being unfurled or prised open. On the other hand new films with practically no bonding between the dry sides are easily opened and consequently act as the preferred nucleation sites. Recently, commonly known phenomena in aluminum castings have been proposed to influence the inflation of such films (Campbell 2001). Such effects as hydrogen gas precipitation (positive internal pressure - increasing film inflation force), metal shrinkage (negative external pressure – increasing film inflation force) and precipitation of intermetallics (straightening force) can be significant in the expansion of these oxides. The effect of this of course is to increase the size of the defect subsequently harming casting properties particularly those sensitive to defect size such as fatigue. The proviso to these processes is however, that solidification time must be sufficient to allow for the unfurling process to occur. This may be part of the reason that solidification rate seems to govern the properties of castings.

Oxides films have also been shown to reduce dramatically the fatigue life of Al-Si-Mg castings (Nyahumwa 1998b), because of their ability to act as crack initiators and nucleation sites for porosity Figure 2.7). While old films have been demonstrated to be less harmful than young films, they still may pose several concerns to the metal caster. Old oxides have been known to act as nucleation sites for fatigue cracks (Nyahumwa 1998b; Zhang 1999) Large oxide inclusions have also been known to act as hard spots (Fuoco 1999) and adversely effect tool life (Jorstad 1986).

2.2.5.4 Remelt Reduced Pressure Test

While fractography seems to be the most useful traditional technique for studying oxide films, clearly, if more rigorous studies are required, superior techniques had to be developed. Testing solidifying metals under reduced pressure has been a familiar technique for some time now in order to qualitatively measure the amount of dissolved gas present in a liquid melt (Jorstad 1993). As the sample solidifies dissolved gas is rejected from solution. The reduced pressure increases the volume of the evolving gas to form large bubbles that are frozen into the structure. Estimates of the gas content of the liquid metal are obtained by examination of the size and distribution of these bubbles, or by measurement of the density of the sample. It has been shown, that this test in fact measures the combined effects of gas content and inclusion levels (Rooy 1993; Sigworth 1993).

This technique has recently been built upon to study oxide films (Fox 2000). Solid samples e.g. coupons sampled from castings, are machined to size, placed into a crucible (or dry sand mould) and remelted. Immediately upon complete melting the sample is placed in a vacuum chamber with a clear lid and the vacuum pump is started. The clear lid enables the experimenter to note any observations such as bubbles breaking the surface of the sample. The enlightening results however, are realized when radiography of the solidified sample is performed. The radiographs yield information about the oxide film content of the sample. Figure 2.8 shows two samples tested with this apparatus (a) is solidified near atmospheric pressure at 100,000 Pa (1 bar) (b) is solidified at 1000 Pa (0.01 bar). One can clearly see that by reducing the pressure the trapped air between the entrained oxides is expanded, resulting in planar cracks in the reduced pressure specimen. The ability to visualize the oxide films is related to (at least) three factors: the hydrogen content of the metal, the amount of oxide films present, and the test pressure. Therefore it is necessary to have the capability of varying the amount of reduced pressure to account for the different melt conditions. Table 2.8 summarizes the effects of the level of test factors and test outcome.

Table 2.8 Effect of Remelt Reduced Pressure Test Factors on Test Outcome

Factor	Hydrogen level	Amount of Oxide films	Test Pressure
Too high	Large bubbles form and escape to surface of casting	Results difficult to interpret	Pressure too high to allow gas bubbles to inflate films
Too low	Not enough pressure to inflate films	Not frequent enough to observe	Large bubbles form and escape to surface of casting

Although still under development the remelt reduced pressure test shows tremendous promise, as it is the first test to attempt to study oxide film characteristics in solidified castings.

2.3 STATISTICAL ANALYSIS OF FRACTURE AND FATIGUE

When interpreting the properties of brittle materials such as glass, ceramics and (unfortunately in many cases) aluminum castings, a statistical approach must be used. After performing multiple mechanical tests on identical samples, the test results when complied will form a statistical distribution. If the measured property was independent of any defect effects, the distribution will tend towards a Normal or Gaussian pattern. Generally this is true for properties such as hardness or yield strength that are rather insensitive to defects. However defect sensitive properties such as ultimate tensile strength, tensile elongation and fatigue life will follow a different distribution. The distribution that these properties follow is based on the weakest-link concept. In this concept the material's flaws are arranged in series like the links of a chain, the strength of which is of course related to its weakest link. The most commonly used distribution that characterizes this behaviour is the Weibull distribution (Weibull 1939b; Weibull 1939a; Weibull 1951). Without lessening the importance of Weibull's contribution it is worthy to point out that his model was not developed from a theoretical basis. Distributions that were developed on the weakest link theory include those developed earlier (Fisher 1928) and during later periods (Freudenthal 1946; Freudenthal 1953; Freudenthal 1954). These models are known as extreme value distributions and have been applied (in addition to fatigue of metals) to predicting phenomena such as floods and droughts. The Gumbel distribution (also known as the LogWeibull or Fisher-Tippet distribution) is essentially the complementary distribution to the Weibull distribution. Due to the familiarity of the Weibull version it will be detailed here. The three-parameter form of the Weibull equation is as follows:

$$P(x) = 1 - \exp\left[-\left(\frac{x - x_0}{\theta - x_0}\right)^m\right] \tag{1}$$

Where *P(x)* is the cumulative frequency distribution of random variable x

m is the shape parameter, also known as the Weibull modulus

θ is the scale parameter, also known as the characteristic value

x_0 is the minimum allowable value of x

Depending on what property the Weibull distribution is describing, it may the case that x_0 will equal zero. In which case the two-parameter version is used:

$$P(x) = 1 - \exp\left[-\left(\frac{x}{\theta}\right)^m\right] \tag{2}$$

This form is commonly used for fracture strength distributions (Green 1993) or in fatigue life where there is no minimum life i.e. no endurance limit, as is commonly thought to be the case in aluminum alloys.

The Weibull distribution is easily transformed to a linear plot by taking logarithms twice and transforming equation 2 resulting in the following expression:

$$\ln\left(\ln\left(\frac{1}{1 - P(x)}\right)\right) = m\ln(x - x_0) - m\ln\theta \tag{3}$$

The slope of the linear plot is *m*, the Weibull modulus. The greater the slope the smaller the scatter in the random variable *x*. The most commonly applied method of computing the probability *P(x)*, is by ordering the values of *x* from least to greatest with each assigned a ranking of *j*:

$$P(x) = \frac{j - 0.5}{n} \tag{4}$$

where *n* is the number of data points.

The other common distribution particularly for fatigue life estimation is the lognormal distribution. It is as follows:

$$P(x) = \frac{1}{\sigma \cdot x\sqrt{2\pi}} \exp\left(-\frac{1}{2}\left(\frac{\log(x) - \mu}{\sigma} \right)^2 \right) \tag{5}$$

where *P(x)* is the cumulative frequency distribution of random variable *x*

σ is the standard deviation of the sample

μ is the sample mean (or location parameter)

Once again there is no obvious underlying relationship between the lognormal distribution to the theories of fatigue. Regardless of this fact it has been applied with success on a number of occasions. One of the earliest examples dealt with steel specimens at a single stress level (Muller-Stock 1938). In many light metal casting fatigue studies the lognormal distribution appears to yield an equally good fit (or better in some cases) as the Weibull distribution (Wakefield 1992; Schijve 1993; Davidson 2002). Despite the apparent universality of the Weibull distribution two commonly used engineering reference handbooks specifically state that "The lognormal distribution is the best choice for some material characteristics, for crack growth rate and for non-linear accelerating system deterioration." (Abernethy Robert 1993) and "that cycles to failure distributions at constant stress are lognormal…" (Shigley 1986) from (Weaver_Engineering 2002). It has also been noted that unless large numbers of tests are performed the two distributions are indistinguishable and that Weibull distributions with high moduli are often more conveniently treated by the lognormal distribution (Knott 1998a). In the general case however, the Weibull distribution does have the advantage of a third parameter which allows the data to be fitted more closely, where it is rational to do so. Weibull himself pointed out that the assumption of normality implies a finite probability of fracture at zero load and this he believes “is to exaggerate your pessimism”(Weibull 1949) from (Armitage 1961). Clearly until further links between the mechanisms of fatigue and statistical models are made it is wise to test multiple distributions to determine the best fit of the data.

2.4 FRACTURE MECHANICS

2.4.1 Introduction

One of the earliest experiments known that deals with fracture mechanics is the series of strength of materials investigations conducted by Leonardo Da Vinci. Da Vinci performed experiments where incremental loads (sand flowing into a bucket) were placed on different lengths of wire. The interesting results were that shorter wire lengths could support higher loads. His findings from this series of experiments could not readily be explained. Early translations put these confusing results down to mistakes in Da Vinci’s notes. A recent paper on the subject (Lund 2000) disagrees with a translation of Da Vinci’s work that suggests errors in terminology, but rather offers a fracture mechanics explanation. Based on the assumption that renaissance period wire was of rather inconsistent quality there existed a higher probability of longer wires having defects whose size would reduce the wire’s fracture strength. Unfortunately for modern engineering this result was overlooked and the dawn of the study of fracture mechanics suffered considerable delay.

2.4.2 Energy Criterion

Griffith (1920) is chiefly responsible for the theories behind modern fracture mechanics. He put forth the idea that in order for the crack to grow from the applied stress the <u>decrease</u> in potential energy of the system (the displacement of the outer boundaries and the change in the stored elastic energy) must equal the <u>increase</u> in surface crack energy due to crack growth. The energy criterion assumes linear elastic behaviour and relates the fracture stress σ_F to the length of a crack $2a$ Figure 2.9) by the following expression:

$$\sigma_F = \left(\frac{2E\gamma}{\pi(1-\nu^2)a} \right)^{\frac{1}{2}} \tag{6}$$

where *E* is Young's Modulus, *v* is Poisson's Ratio and γ is the surface energy.

The Griffith criterion was later modified by Irwin (1948) to include the energy dissipation by localized plastic flow. Also it was primarily Irwin (1956) that developed the most useful and what has become the present version of this method. This approach assumed that the energy required for creating new surfaces during crack growth comes from the strain energy loss from the entire elastic solid. This strain energy release rate was defined as *G* (in honour of Griffith). Irwin then demonstrated that *G* could be determined from the fields of stress and displacement in the localized region of the crack tip. Irwin stated that this single parameter *G*, or the crack extension force, measures the intensity of the crack tip stress field, as long as plastic deformation is limited to a small zone near the crack tip.

$$G = \left(\frac{\pi\sigma^2 a}{E} \right) \tag{7}$$

At the moment of fracture $G = G_C$, the critical energy release rate (which is a measure of fracture toughness) may be related as shown:

$$G_C = \left(\frac{\pi\sigma_F^2 a_C}{E} \right) \tag{8}$$

where a_C is the critical crack size.

2.4.3 Stress Intensity

Consider the element shown in Figure 2.10 to represent the state of stress near the crack tip shown in Figure 2.9. Irwin (1957) used Westergaard's complex stress functions to show that the in-plane stresses of this element are as follows:

$$\sigma_{xx} = \frac{K_I}{\sqrt{2\pi r}} \cos\left(\frac{\theta}{2}\right)\left[1 - \sin\left(\frac{\theta}{2}\right)\sin\left(\frac{3\theta}{2}\right)\right] \tag{9}$$

$$\sigma_{yy} = \frac{K_I}{\sqrt{2\pi r}} \cos\left(\frac{\theta}{2}\right)\left[1 + \sin\left(\frac{\theta}{2}\right)\sin\left(\frac{3\theta}{2}\right)\right] \tag{10}$$

$$\tau_{xy} = \frac{K_I}{\sqrt{2\pi r}} \cos\left(\frac{\theta}{2}\right)\sin\left(\frac{\theta}{2}\right)\cos\left(\frac{3\theta}{2}\right) \tag{11}$$

where r is the radial distance from the crack tip to the element and K_I is a constant known as the stress intensity factor**.**

The stress for an element extremely close to the crack tip in Figure 2.10 becomes:

$$\sigma = \frac{K_I}{\sqrt{2\pi r}} \tag{12}$$

and the stress intensity factor K_I for a central crack of length *2a* may be rewritten as:

$$K_I = \sigma\sqrt{\pi a} \tag{13}$$

Also K_I and G may be related (for plane stress conditions) by combining equations 2 and 8 resulting in:

$$G = \frac{K_I^2}{E} \tag{14}$$

The relationship is identical with the critical value of G (G_C) and the materials fracture toughness K_{IC}.

The subscript of K represents the opening mode (tensile = I, plane shear = II and antiplane shear = III) see Figure 2.11.

Equation 13 is only valid for the conditions described above. For finite bodies, and different crack geometries equation 13 needs to be modified by appropriate dimensionless geometrical factors. Knott and Withey (Knott 1998b) give K_I values for several common loading conditions:

Table 2.9 Stress Intensity K, Factors for Common Loading Conditions (from (Knott 1998b))

Type of Crack	Stress Intensity
Centre-crack, length 2a, infinite plate	$K_I = \sigma\sqrt{\pi a}$ (15)
Centre-crack length 2a plate of width W	$K_I = \sigma\sqrt{W\tan\left(\frac{\pi a}{W}\right)}$ (16)
Central, penny shaped crack, radius a, in infinite body	$K_I = 2\sigma\sqrt{\frac{a}{\pi}}$ (17)
Edge crack, length a, in semi-infinite plate	$K_I = 1.12\sigma\sqrt{\pi a}$ (18)
Two symmetrical edge cracks, each length a, in plate of total width W	$K_I = \sigma\sqrt{W}\left(\sqrt{\tan\left(\frac{\pi a}{W}\right) + 0.1\sin\left(\frac{2\pi a}{W}\right)}\right)$ (19)

Thus if the material parameter K_{IC} is known then one can relate the critical stress to a critical flaw size by simply applying the correct equation for the geometry of interest. However in many instances the component loading conditions may be complex and the compliance function not known. As a result of stress analysis on an edge cracked plate, a shape factor Q is introduced to account for the geometry of the flaw. The resulting equations for an embedded and surface flaw are as follows:

Embedded flaw:

$$\left(\frac{a}{Q}\right)_{cr} = \frac{K_{IC}^2}{\pi\sigma^2} \tag{20}$$

Surface flaw:

$$\left(\frac{a}{Q}\right)_{cr} = \frac{K_{IC}^2}{1.21\pi\sigma^2} \tag{21}$$

The value of Q is found from the *a/2c* vs. Q curves shown in Figure 2.12.

Fracture toughness values for aluminum casting alloys are difficult to locate in the literature. In particular K_{IC} values for the Ford version of 319 were not located at all. However one investigation on crack growth in this alloy was found (Caton 2001). Table 2.10. shows the critical values of K and K_{eff} for different solidification rates (indicated by dendrite arm spacing) and heat treatments (K_{eff} is explained in section 2.5.5). These values seemed to be lower but in the same range as measured K_{IC} values found for 357 alloys (18.7 to 19.8 MPa $m^{0.5}$ (Ozelton 1991) and 21 to 25 MPa $m^{0.5}$ (Tan 1995)).

Table 2.10 Critical Values of K_C and K_{eff} in MPa $m^{0.5}$ from (Caton 2001)

Heat treatment	Dendrite arm spacing of sample			
	23μm		100μm	
	K_C	$K_{C\,eff}$	K_C	$K_{C\,eff}$
T6	15.2	10.3	15.2	11.7
T7	16.7	13.9	13.2	11.4

2.4.4 Post Yield Fracture Mechanics

Linear elastic fracture mechanics (LEFM) does have limitations however. For example in cases where significant yielding occurs in cracked structures (usually when considering ductile materials) the assumptions made for LEFM analyses are no longer valid. Elastic-plastic fracture mechanics (EPFM) and general yielding fracture mechanics (GYFM) are likely extensions of LEFM and can be used individually or in conjunction with a LEFM approach depending on the conditions. For example a center-cracked body loaded in tension is shown in Figure 2.13. A stress near the crack tip is give as ${}_{l}\sigma$, the uniaxial stress given by σ_U, the net section stress by σ_n and the remote uniform stress by simply σ, Figure 2.13 (a) through (d) from (Turner 1984).

Case (a) ${}_{l}\sigma > \sigma_U > \sigma_n > \sigma$

Yielding is limited to the immediate vicinity of the crack, in the case of failure it occurs by unstable rapid propagation of the crack (LEFM regime)

Case (b) ${}_{l}\sigma > \sigma_U \geq \sigma_n > \sigma$

Yielding is extensive but does not extend to a lateral boundary of the structure and is thus contained, in the case of failure it occurs by unstable rapid propagation of the crack (EPFM regime, but LEFM with plastic zone correction may still give reasonable predictions)

Case (c) ${}_{l}\sigma > \sigma_n \geq \sigma_U > \sigma$

Yielding is very extensive and spreads to the lateral boundary ahead of the crack and is not contained (gross yield, yielding fracture mechanics must be applied), tough materials may fail by plastic collapse of the net section while less tough materials a crack may spread by stable or unstable growth)

Case (d) ${}_{l}\sigma > \sigma_n > \sigma > \sigma_U$

Since σ is greater than σ_U, extensive plasticity develops along the components as well as across the section, implying work hardening of the net section (general yield and GYFM are applied), failure by plastic collapse and limit analysis - however tearing or in some materials crack propagation may still be the failure mode.

Case (b) in particular is an important condition to the casting designer. Design methods that address situations such as this have been developed. These include crack tip opening displacement (CTOD), the J contour integral, and those approaches that employ failure assessment diagrams such as the strip yield model, PD6493 and the R6 method (for summaries of these methods see (Anderson 1995)). Failure assessment diagrams of this type are based on a two-model approach and provide the user with a plot that shows boundaries of safe and unsafe design. Although semi-empirical and/or finite element based, these diagrams have been verified by large amounts of experimental data where specimens have significant fractions of yield (Latzko 1984). Figure 2.14 shows an R6 plot with values of aluminum alloy 7010 (Wiltshire 1981). The abscissa S_r is the ratio of LEFM predicted stress σ_k, to collapse stress σ_F and the ordinate K_r is the ratio of the applied value of fracture toughness K_{app} to the “ideal” value of fracture toughness K_{IC}. Additionally the R6 method has been modified to incorporate materials that have a high initial rate of strain hardening Figure 2.15 (Knott 1998b). In this case the abscissa L_r represents ratio of applied stress σ_a to the yield stress σ_Y and includes values of L_r greater than unity. This version of R6 curve is defined by equation 22 (Edwards 1989):

$$K_r = \left(1 - 0.14L_r^2\right)\left(0.3 + 0.7\exp\left(-0.65L_r^6\right)\right) \tag{22}$$

2.5 FATIGUE

2.5.1 Introduction

2.5.1.1 General Aspects of Fatigue

Fatigue in metals generally falls into three main categories, low cycle fatigue (LCF) high cycle fatigue (HCF) and a transitional range that falls between the two (see Table 2.11). The distinction LCF and HCF goes beyond simply how many cycles a specimen undergoes during a test. In LCF tests samples experience relatively high values of stress and undergo plastic deformation. Controlling and interpreting the stress levels are difficult under these conditions and consequently tests are conducted with controlled cycles of elastic plus plastic strain instead of controlled load or stress. In HCF the deformation is elastic and occurs at lower applied stresses resulting in significantly longer lives.

Table 2.11 Fatigue Life Regimes

Fatigue Regime	Low Cycle Fatigue	Transition	High Cycle Fatigue
Number of cycles	10^1 to 10^4	10^4-10^5	10^5 and above

Fatigue test schematics are shown in Figure 2.16. Equations 23 through 26 define the stress parameters shown (Dieter 1986). It is important to note the distinctions between the different stress terms. In the literature parameters such as the stress range, mean stress and alternating stress amplitude are all used to describe stress levels in fatigue tests.

The range of stress σ_r is the algebraic difference between the maximum and minimum stress in a cycle:

$$\sigma_r = \sigma_{\max} - \sigma_{\min} \tag{23}$$

The alternating stress (or stress amplitude) σ_a is as follows:

$$\sigma_a = \frac{\sigma_r}{2} = \frac{\sigma_{\max} - \sigma_{\min}}{2} \tag{24}$$

The mean stress is the algebraic mean of the maximum and minimum stress in the cycle:

$$\sigma_m = \frac{\sigma_{\max} + \sigma_{\min}}{2} \tag{25}$$

And the stress ratio R is given by:

$$R = \frac{\sigma_{\min}}{\sigma_{\max}} \tag{26}$$

2.5.1.2 In Service Fatigue of Cylinder Block Castings

In an internal combustion engine the cylinder block contains the components that convert the energy of fuel combustion to rotational energy. The linear powerstroke of the pistons is transferred through the connecting rods to the crankshaft that drives the transmission and ultimately the drive wheels of the automobile. The crankshaft bearing caps are bolted to the main bearing saddle portion of the cylinder block, transferring significant cyclical loads to this area, Figure 2.17. In terms of static and dynamic loading the engineering safety factor is lowest in this region. This is in part due to fact that the properties of the casting are lowest in this region. A large section thickness and close proximity to the feeder during solidification result in a relatively coarse casting microstructure compared with the rest of the casting (recall Figure 2.4). As a consequence tensile and yield strength are significantly lower in this region and the size and amount of porosity are generally higher (Byczynski 2002). In addition geometrical factors such as notch effects from threaded boltholes, crankcase ventilation windows and cored oil feed lines further reduce the safety factor. During engine service cyclical tension-tension stress is experienced with a relatively high mean stress and small stress amplitudes (DeJack 2000). These elements combine to give cause for concern for high cycle fatigue failure.

2.5.2 Fatigue Testing

2.5.2.1 S-N curve

The stress-cycles to failure or S-N curve is a method of characterizing the fatigue properties of a metal. Fatigue tests are carried out at a number of different stresses (ordinate) and the mean cycles to failure for each stress level are plotted on a logarithmic abscissa (Figure 2.18). The testing usually starts at high stresses and continues to decrease until runouts (no failures) occur. In ferrous metals the highest stress at which a runout occurs is taken as the *fatigue limit* of the metal (Figure 2.18). Metals such as aluminum, magnesium and copper alloys do not exhibit this feature in the S-N curve and thus do not have fatigue limits (as defined here). The S-N curve continues to slope downwards at increasing cycles. Because of this property these alloys are frequently assigned a *fatigue strength* at an arbitrary life e.g. 10^7 or 10^8 cycles. One disadvantage of this technique is that mean life values are not representative of the distribution of lives at a given stress level. Figure 2.19 demonstrates “Normal” probability curves for S-N tests. The designer must take this into account when using S-N curve information for design of a component. Another disadvantage is that a large number of specimens required to generate a complete S-N curve (especially when generating a probabilistic one) and fatigue tests are time consuming and expensive to perform. Often a designer will want information on how process changes such as addition of alloying elements or changes in heat treatment affect the fatigue performance of an alloy. S-N testing is not ideal for these situations.

2.5.2.2 Staircase testing

The staircase or "up and down" method of fatigue testing is a method of assessing the mean fatigue life of an alloy (Dixon 1948). In brief the technique involves identifying a life cycle goal and testing samples sequentially at a stress level higher or lower (by a predetermined increment) than the previous test depending on whether the previous test specimen reached the life cycle goal or failed short of the goal. The fatigue strength estimate is calculated by taking the mean stress of either the failed or passed samples (which ever is lower in number). The logic behind choosing the outcome with the fewest results to calculate the mean is to minimize the effect of a poor estimate of the starting stress. A poor estimate of starting stress would lead to several tests of the same outcome before the incurring the opposite result. Figure 2.20 shows the results of two staircase tests performed by the author for different metal treatments on production castings (Byczynski 2002). The merits of this technique over standard probit analysis have been summarized elsewhere (Brownlee 1953). The main advantages are that it uses fewer samples than traditional methods and analysis of the data is straightforward. Disadvantages are that the tests need to be sequential and a reasonable amount of insight is needed to determine the initial stress and increment levels. Provided the estimates are reasonable and the samples are homogeneous, convergence on the mean fatigue strength is rather quickly achieved. The staircase testing is based on the life having a "Normal" distribution, a later version (Zhang 1998) of the technique is capable of estimating the fatigue strength if the distributions are not "Normal". Other accelerated testing methods are based on extrapolation from shorter fatigue lives, these include the ray-projected and parallel-projected methods (Wirsching 1983) from (Lin 2001). Lin et al. (2001) tested all the aforementioned methods and concluded that for populations with low variation of fatigue limits the parallel-projected method was superior and that the original Dixon and Mood approach was recommended for populations with high variation of fatigue limits.

2.5.3 Stages of Fatigue

In general fatigue life can be divided into four main categories (Dieter 1986):

1. Crack initiation
2. Slip-band crack growth (stage I crack growth)
3. Crack growth on planes of high tensile stress (stage II crack growth)
4. Ultimate ductile failure

Stages 1 through 3 will be reviewed in the following sections in the context of the fatigue of aluminum castings supported by data drawn from relevant literature.

2.5.3.1 Crack Initiation and Slip-band Crack Growth (category 1 and 2)

The first category generally refers to crack initiation from local stress concentrations. Invariably these are located at the free surface of the component or specimen. In the cases that initiation is internal, the site is normally an interface between the parent metal and second phase particles, in aluminum castings examples these sites include inclusions, intermetallics and precipitates. It is at these local stress concentrations that slip-bands build up, persistent slip-bands form and slip-band intrusions and extrusions may occur. These are known to act as initiation sites for fatigue cracks. These micro cracks initially grow along the persistent slip-bands, the rate of growth being extremely low.

In the practical case of fatigue of industrial castings, nucleation by persistent slip bands is relatively rare. Several studies on aluminum castings have noted that the initiation process is practically non-existent as cracks almost always nucleate on either porosity or oxide films (Couper 1990; Wakefield 1992; Skallerud 1993; Ting 1993; Stanzl-Tschegg 1995; Nyahumwa 1998a; Jiang 1999; Zhang 1999; Knott 2000; Wang 2001b). That is not to say the metallurgically sound principal of nucleation by persistent slip-bands does not occur at all in these alloys. In the case where many of the nucleation sites are eliminated by extremely close control of the solidification process or more commonly by employing hot isostatic pressing (HIP) techniques the persistent slip-band mechanism becomes enabled (Nyahumwa 2001; Wang 2001b) and seems to be commonplace.

2.5.3.2 Crack Growth on Planes of High Tensile Stress (category 3)

This is the portion of fatigue life that is chiefly associated with the relatively rapid stable crack growth. A single dominant crack (possibly formed from joining of multiple cracks) propagates in a plane perpendicular to the maximum tensile stress. Propagating cracks will often produce striations of the fracture surface. These appear as parallel crests and valley features that are perpendicular to the direction of crack propagation. One accepted mechanism for these features is that of crack tip blunting (Laird 1979). According to this model the spacing between striations is equal to the crack growth per cycle or *da/dN*. Overall propagation rates will depend heavily on the R-ratio and crack tip closure (discussed in section 2.5.5)

In the realm of aluminum casting alloys there appears to be little documented metallurgical or process factors that affect the rate of this stage of crack growth. Intuitively, processes that increase the toughness of the matrix would seem likely candidates for slowing this stage of crack growth. However studies on the effects of heat treatment (Couper 1990; Davidson 2002) have concluded no that difference in fatigue lives exists. Similarly HIPing, while effective at increasing the amount of fatigue life associated with initiation, has been shown to have no effect on crack propagation rates (Couper 1990; Mocarski 1991; Rading 1995; Davidson 2002). Evidently the presence of internal porosity does not affect the rate of crack growth.

One frequently sought-after method of improving the casting properties is reduced solidification time. This is an area of conflicting accounts. An early investigation (Bailey 1965) showed the positive effect of lower solidification times on fatigue life in 356 alloy. However another source (McLellan 1996) where fatigue test characteristics of 27 different groups of Al-Si-Mg alloy castings were summarized concluded that solidification rate had no influence on fatigue performance. Conversely there are other more recent studies (Wickberg 1985; Boileau 1998) that state that fatigue life improves with decreasing solidification time. Studies on the effect of grain size again show some conflicting views. Studies performed on a HIPed Al-Cu based alloy, B201 (Ozelton 1991) showed no apparent effect on crack growth rate or fracture toughness. This is contradicted by an earlier study (Chien 1973) that showed slower crack growth rates in coarse grained material (A201). Clearly there are discrepancies between the above mentioned studies. The problem is likely due to that solidification time itself is not a first order effect. That is to say solidification time as an entity cannot be separated from all the secondary factors it influences, which in turn affect the fatigue properties. These secondary factors include: pore size, pore distribution, potential to inflate oxide films (see section 2.2.5.3), size of intermetallics, and grain size. Thus one can see the difficulty in broadly stating the effects of solidification time on fatigue.

Notable attempts at separating these effects include those completed by Wang et al. (Wang 2001b; Wang 2001a). These investigations employed the use of HIPing in order to study various effects in the absence of porosity. Their key findings as well as others from the literature are summarized in table 2.12.

Table 2.12 Effects of Selected Factors on Fatigue Life in Aluminum Castings

Reference	Factor / Process	Fatigue Life	Comments
(Couper 1990; Davidson 2002)	Solution treatment	No effect	Solution treatment did not change the crack initiation or propagation life
(Wang 2001a)	Under aging	-	Underaged samples had lower fatigue lives compared with T6
(Wang 2001a)	Modification	+	Modification improved fatigue lives by 2 to 4 times (however interaction with solidification time)
(Wang 2001a)	↑ Mg level	-	Increases eutectic particle size and cracking
(Wang 2001a)	↑ Fe level	-	Increasing from 0.08 to 0.14 decreased fatigue life of large DAS specimens
(Nyahumwa 1998b; Zhang 1999; Wang 2001b)	Oxide films	-	Act as crack initiators
(Lee 1995a; Lee 1995b; Lee 1996; Gall 1999)	Silicon morphology	-	Unmodified silicon can result in particle cracking
		+	Modified silicon results in decohesion of silicon with the matrix (slower crack growth rate than unmodified)
(Wang 2001b)	↓ Solidification time (↓DAS)	+	Low solidification times (low DAS) increase fatigue life by increased dispersion hardening
(Couper 1990; Mocarski 1991; Rading 1995; Davidson 2002)	HIP	+	Eliminates initiation sites and lengthens crack initiation life, however does not affect crack propagation life
(Couper 1990; Wakefield 1992; Skallerud 1993; Ting 1993; Stanzl-Tschegg 1995; Nyahumwa 1998a; Jiang 1999; Zhang 1999; Knott 2000; Wang 2001b)	Porosity	-	Acts as a crack initiator, does not appear to affect crack propagation

+ positive effect, - negative effect

2.5.4 Fatigue Crack Growth Analysis

Paris and Erdogan (Paris 1963) are credited with originating the relationship between fatgiue crack propagation da/dN and stress intensity factor range ΔK:

$$\frac{da}{dN} = C(\Delta K)^m \tag{27}$$

where a is the crack length, N is the number of cycles and C and m are material constants, ΔK is defined as the range of the stress intensity factor or:

$$\Delta K = K_{\max} - K_{\min} \tag{28}$$

The Paris-Erdogan relationship has become well known in fracture mechanics and its applicability has been demonstrated on a number of occasions. Orginally Paris and Erdogan proposed an exponent of four but since that time values between two and ten have been fit depending on the type of material. It is important to note that the Paris-Erdogan power law (equation 27) is only valid for the central linear portion of the log-log plot of da/dN vs. ΔK described as "regime B" in Figure 2.21. The shape of the full curve is sigmoidal. At high values of log ΔK and da/dN ("regime C") it is bounded by K_C, the fracture toughness of the material.
In this region equation 27 underestimates the rapid crack growth as the maximum stress intensity factor approaches K_C. At low values of log ΔK and da/dN ("regime A") it is bounded by ΔK_{th} (the threshold parameter). Here equation 27 results in conservative estimates of the crack growth. It has been shown in different materials that there exists a threshold stress intensity factor range ΔK_{th} below which fatigue cracks do not propagate or perhaps grow at rates that are too small to detect experimentally (Ritchie 1979). In regimes A and C, mean stress (R-ratio effects) strongly influences the crack growth rates.

2.5.5 Crack Closure

Experiments performed by Elber (1970) gave insight into the fatigue threshold and R ratio effects. A difference was noted in the compliance from cracked specimens at different loads (Figure 2.22). At low loads the compliance was that of an uncracked specimen. Elber surmised that this was due to contact of the crack surfaces at low loads. This of course could be extended to fatigue crack growth rate, where at low values of ΔK crack closure could occur. Elber's concept was that crack closure decreased the crack growth rate by reducing the effective stress intensity range. Consider Figure 2.23, where a specimen is cyclically loaded between K_{max} and K_{min} over time. The crack faces are in contact below K_{op}, the stress intensity at which the crack faces become separated. Thus the portion of the curve below K_{op} does not contribute to the propagation of the crack. So an effective stress intensity range ΔK_{eff} is:

$$\Delta K_{eff} = K_{\max} - K_{op} \tag{29}$$

A ratio that defines the fraction of the effective stress intensity range to its nominal value is given by U_R, where:

$$U_R = \frac{\Delta K_{eff}}{\Delta K} \tag{30}$$

Finally the Paris-Erdogan equation can be modified to account for crack closure as follows (from equations 27 and 29):

$$\frac{da}{dN} = C(\Delta K_{eff})^m \tag{31}$$

Fatigue crack propagation with crack closure at different R-ratios has been well predicted with equation 31. The effects of R-ratio on crack closure however, are far from straightforward and much research has been performed in this area (Knott 1984; Borrego 2001; Kujawski 2001).

Several mechanisms of crack closure have been identified (Suresh 1984), these include crack closure induced by: plasticity, roughness, oxidation, viscous fluid and metallurgical transformations. The relevance of these mechanisms to a particular situation is dependent on the nature of material, its microstructure and yield strength, and environment.

Tables 2.13 and 2.14 summarize relevant literature and give the casting details and fatigue test parameters and results.

Table 2.13 Casting Details from Relevant Literature Sources

Reference	Alloy	Si	Cu	Mg	Fe	Ti	Sr	Heat Treatment	Casting Description
(Couper 1990)	CP601	7.00	-	0.43	0.13	0.032	0.025	T6	cut from billet material
(Skallerud 1993)	AlSi7Mg(0.4)	7.10	-	0.33	0.12	0.121	0.026	T4, T6	cut from commercial casting (wheel rims)
(Caton 1999)	319 (Ford)	7.43	3.33	0.22	0.38	0.120	0.030	T7 (all HIP)	end chill permanent wedge mould
(Wigant 1987)	A356	7.25	0.01	0.36	0.01	0.020	-	T6	CT specimen shaped, permanent mould
(Wang 2001b)	A356	7.13	<0.01	0.40	0.08	0.156	<0.018	T6 (some HIP)	end chill sand cast
(Ting 1993)	AA319	5.5-6.5	3.0-4.0	0.1	1.0	.25	-	-	provided by General Motors

Table 2.14 Details of Fatigue Tests from Relevant Literature Sources

Ref.	fatigue tests	Cond.	Mechanical Properties			Fatigue Test Parameters and Fatigue Properties							
			σ_{UTS} (MPa)	$\sigma_{0.2YS}$ (MPa)	El. (%)	σ_{max} (MPa)	σ_a (MPa)	σ_{mean} (MPa)	R CT,(Axial)	Freq. (Hz)	C (m/cycle)	m	$\Delta K_{eff,\ th}$ (MPa $m^{1/2}$)
Couper	axial	as cast	250	120	13	-	100 to 250	-50 to 50	n/a,(-1)	10-60	$6.3 * 10^{-11}$	4.00	1.3
		T6	310	220	8	-	100 to 250	-50 to 50	n/a,(-1)	10-60	$6.3 * 10^{-11}$	4.00	1.5
Skallerud	CT, axial	T4	260	130	-		80 to 180	-	0.1,(-1)	20	$2.7 * 10^{-10}$	1.99	1.4
		T6	290	220	-		80 to 180	-	0.1,(-1)	20	$9.2 * 10^{-11}$	3.07	1.4
Caton	CT, axial	HIP + T7 100µm DAS	185	154	0.6	100,140	-	-	0.1,(-1)	30	-	-	4.0
		HIP + T7 23µm DAS	312	202	5.9	100,140	-	-	0.1, (-1)	30	-	-	2.7
Wigant	CT	T6	266	224	-	-	-	-	0.1, 0.5,(n/a)	30-40	$1.5 * 10^{-20}$ to $1.2 * 10^{-12}$	5.0 to 11.2	1.3 to 4.2
Wang	axial	T6 (some HIP)	-	-	-	-	70,100	-	n/a,(0.1,0.2,-1)	55	$3.4 * 10^{-11}$ (R=0.1) $1.0 * 10^{-10}$ (R=-1)	~4	-
Ting	CT, axial	not specified	206	190	0.7	55 to 120			-1,(-1)	10-25			1.4 (estimate)

2.5.6 Fatigue Life Predictions Based on Initial Defect Size

The number of cycles required to propagate a long crack from an initial size a_i to a_f the size at fracture can be calculated by combining equations 30 and 31 to give:

$$\frac{da}{dN} = C(U_R \cdot \Delta K)^m \tag{32}$$

And by substituting equation 13 with the addition of the parameter $Y(a_i)$ a compliance factor to account for the geometry of the initially cracked body we arrive at:

$$\frac{da}{dN} = C(U_R \cdot Y(a_i)\Delta\sigma\sqrt{\pi a})^m \tag{33}$$

It has been shown that U is a function of stress ratio R and crack size a. But for a constant R, U_R and $Y(a_i)$ may be considered as constants (U and Y) without introducing significant error. We can now separate variables and integrate the resulting expression from a_i to a_f (initial and final crack sizes) and from N_i to N_f (initiation life and total life):

$$\int_{a_i}^{a_f}\left(\frac{da}{U^m \cdot Y^m \cdot (\pi a)^{\frac{m}{2}}}\right) = C(\Delta\sigma)^m \int_{N_i}^{N_f} dN \tag{34}$$

If we take the propagation life N_p to be equal to the total life minus the initiation life $(N_f - N_i)$, integration and rearranging gives:

$$a_i^{\frac{(2-m)}{2}} - a_f^{\frac{(2-m)}{2}} = \frac{2-m}{2} C \cdot U^m \cdot Y^m \cdot \pi^{\frac{m}{2}} \cdot (\Delta\sigma)^m \cdot N_p \tag{35}$$

For samples with small defects ($a_i << a_f$) the $a_f^{(2-m)/2}$ term can be considered negligible, and assuming the exponents of a_i and N_p are equal we can solve for Np as follows:

$$N_p = \frac{2}{a_i\left[(m-2)C \cdot U^m \cdot Y^m \cdot \pi^{\frac{m}{2}} \cdot \Delta\sigma^m\right]} \tag{36}$$

2.6 SUMMARY

Sources in the literature have almost exclusively dealt with Al-Si-Mg castings with varying quality and cast in variety of methods. The current study will address the Ford sand cast Al-Si-Cu-Mg alloy and process. First by focusing on samples machined from failed production castings tested using the staircase fatigue test and secondly by conducting casting experiments to investigate the effects of turbulently and quiescently cast samples on the statistical nature of tensile and fatigue properties. It will also determine the applicability of the fatigue and fracture mechanics models presented here, and to investigate and quantify the nature of the defect structure that appears to dominate the fatigue properties of these castings.

Chapter 3

EXPERIMENTAL PROCEDURE

3.1 STAIRCASE FATIGUE TESTS

3.1.1 Sample Preparation

Fourteen production 3.0L V6 cylinder block castings were used to provide samples for this test. These castings were produced under normal operating conditions at the Ford Motor Company's Windsor Aluminum Plant in Windsor, Ontario, Canada. Fatigue sample preparation and testing was performed at Climax Research Services, Farmington Hills, MI, USA. Fatigue samples were machined from the main bearing saddle region of the castings. The sample blanks were heat treated at a temperature of 394 K (121°C) for 400 hours in a recirculating air furnace, to simulate cylinder block service conditions. The samples were machined into fatigue bars according to ASTM E466-96. The dimensions of the test bars are shown in Figure 3.1.

3.1.2 Fatigue Test Parameters

Test samples were heated to 394 K for a minimum of 20 minutes prior to testing. The samples were maintained at this temperature for the duration of the fatigue test.

The fatigue tests were performed using *MTS* servo-hydraulic test machines. The samples were tested in accordance with ASTM E466-966. They were tested in fully reversed (R = -1) sinusoidal axial fatigue at a frequency of 75 Hz. The staircase parameters were as follows: initial staircase level was 55.2 MPa (max. stress), staircase step size was 3.4 MPa.

3.2 REMELT REDUCED PRESSURE TEST (RRPT)

These tests were performed at the University of Birmingham IRC Castings Laboratory by the author (trained by Dr. S. Fox). The RRPT instrument is shown in Figure 3.2, its main components are a vacuum chamber with a transparent lid for observations and a system for controlling the magnitude of the reduced pressure (from atmospheric pressure down to 1000 Pa

(0.010 bar)). Samples were sectioned from 319 ingot material and failed staircase fatigue bar ends. In each case the sample preparation is identical. The sample was sectioned using a hacksaw and ground using 240, 400 and 600 grit silicon carbide abrasive paper. A series of preliminary remelt reduced pressure tests (RRPT) were conducted on the ingot material to determine the optimum test conditions. This involved subjecting the molten sample to different reduced pressures to achieve the optimum level of film inflation and bubble size. High pressures do not encourage film inflation and very low pressures create bubbles large enough to become mobile in the liquid sample. Bubbles such as these move upwards to the top surface of the sample and either break through the air-melt oxide layer and burst or become trapped against this barrier. For the hydrogen level and oxide content present in the ingot material an absolute test pressure of 5000 Pa (0.050 bar) was used. An example of a prepared sampled is shown in Figure 3.3. The sample test configuration is shown in Figure 3.4. After the test the sample was sectioned, ground and photographed. The sample was placed in a small thin walled crucible surrounded by clean dry unbonded 60 AFS silica sand. The sample was placed in a 973K (700°C) resistance furnace until melted. A thermocoupled control sample was used to determine complete melting. Immediately after fully melted the sample was transferred to the vacuum chamber of the RRPT and the test was started. The pressure was rapidly reduced until an absolute pressure of 5000 Pa (0.050 bar) was reached. The sample was then observed through the transparent vacuum chamber lid and allowed to completely solidify before test completion.

3.3 PRODUCTION OF TEST BAR CASTINGS

The following experiments were performed at the University of Birmingham IRC Castings Laboratory by the author (with the assistance of Mr. A. Caden and Mr. J. Pfeiffer).

3.3.1 Mould Preparation

A pattern yielding ten bottom filled test bars was used (Figure 3.5) to form the mould used in the production of test bars. Dimensions of the pattern are given in Figure 3.6. Resin bonded sand moulds were prepared using was using 60 AFS silica sand and 0.6% (by weight), of *Ashland Chemical* 5112 (50%) and 5230 (50%) precatalyzed *Pepset*™ resin.

Two 2-mm thick aluminum inserts were placed in the pattern during moulding, and removed prior to mould assembly, so as to produce a chill fin along the tops of the test bars (seen in Figure 3.5). For the unfiltered castings the filterprints were left empty (Figure 3.7(a)). For the filtered castings two 20ppi FOSECO ceramic foam filters were placed in the mould as shown in Figure 3.7(b).

3.3.2 Casting

Approximately 220 kg of aluminum alloy 319 ingot, taken from production stock from *Ford Motor Company* was melted in a *Ramsell Naber* resistance heated tilting furnace.

The holding temperature was 1073K (800°C) in the furnace in order to allow for temperature loss in handling. This resulted in a pouring temperature of approximately 1033K (760°C).

The melt was degassed with pure argon using a *Hepworth* rotary degasser.

The hydrogen level was measured using the Severn Science Hyscan apparatus throughout casting. The level of hydrogen after degassing was consistently between 0.04 and 0.07 ml H/100g Al throughout the tests. The relative humidity during the tests was 38%.
The mould was fixed in a rotating fixture that allowed it to be rolled over after casting (Figure 3.8)

The metal from the large furnace was tilted into a small pouring crucible, which was then used for filling the mould. After the mould was filled a stopper was placed into the downsprue and the mould was turned 180° in order to allow for improved feeding of the test bar castings.
The order of casting was randomized to avoid any effects of test order on the measured properties.

3.3.3 Heat Treatment

The parameters chosen for this work were based on a commercial casting production process. The temperature and duration of the solution treatment and of the natural and artificial aging sequences were designed to replicate as close as possible the conditions of the cylinder block castings produced at Ford Windsor Aluminum Plant.

Samples were randomly arranged into two batches, each containing approximately 70 test samples from unfiltered and filtered castings. Each batch had the following identical heat treatments. Samples were solution treated at 773K (500°C) for 4 hours and 30 minutes in a *Carbolite* HRF 7/22 recirculating air electrical resistance heated furnace. A Eurotherm 2416CC temperature controller was used to control the furnace temperature and a Eurotherm 2132 was used as the over-temperature alarm. A thermocouple was placed in the center of a control sample and monitored to ensure the temperature was within +/- 1°C during the constant temperature portion of the cycle. The samples were water quenched into 20°C water to room temperature, and then held at room temperature for 19 hours. Samples were then artificially aged at 533K (260°C) for 4 hours as above and were allowed to cool in air for 5 minutes before water quenching to room temperature.

3.4 TENSILE TESTING

Tensile samples were machined using a CNC *Boxford* lathe.

Tensile sample dimensions are shown in Figure 3.9 and conform to ASTM E 8-00. The diameters were measured using a digital Mitutoyo micrometer with an accuracy of 0.001 mm.

The tensile machine used was the *Zwick* 1484. The *Instron* wedge action grips used were self-aligning. Test order was random and performed blind (i.e. sample casting conditions hidden). Samples were loaded in the same orientation for each test. The accuracy of the load cell is 0.1 N. The crosshead speed was 0.5mm / minute. Data from the load cell and extensometer was digitally recorded at 1 data point every 0.005 mm. The extensometer gauge length used was 30 mm.

3.5 FATIGUE TESTING

Samples were machined to a program generated by the author (with assistance from Mr. W. Hewitt) using a CNC *Boxford* lathe. Fatigue sample dimensions are shown in Figure 3.10 and conform to ASTM E466-96.

Samples were ground using a longitudinal polishing machine using the following abrasive particle sizes: 60µm, 40µm, 30µm, 15µm, and 9µm. The abrasive was *Imperial Microfinishing Film*™, an aluminum oxide, film backed abrasive roll manufactured by *3M*. Final polish was performed on a lathe with 6µm then 1µm-diamond paste to achieve a mirror like finish. Each sample was then examined under 20X-magnification stereomicroscope to determine if any non-longitudinal polishing marks or scratches existed. If found, the samples were re-polished until only longitudinal polishing marks remained.

The machine used for fatigue testing was the *Amsler* Type 2 HFP 421 high frequency Vibrophore axial fatigue testing machine. One machine was used for all fatigue tests. Samples were loaded in the same orientation for each test. Fatigue tests were performed at room temperature. The stress ratio (R) was 0.1, the stress regime was sinusoidal with a maximum stress of 150 MPa, mean stress 82.5 MPa and minimum stress 15 MPa. The test frequency was sample dependent but ranged from 107 to 110 Hz. Testing order was random and was performed blind.

3.6 FRACTOGRAPHY

The fracture surfaces of each sample were sectioned with a hacksaw and were carefully preserved in polyethylene sample bags. Scanning electron microscopy was performed using a *JEOL* 6300 SEM, fitted with a *Pioneer* detector located in the School of Metallurgy and Materials at the University of Birmingham. Energy dispersive spectroscopy was performed using a *Noran Vantage* microanalysis system in conjunction with the above instrument.

Chapter 4

RESULTS

4.1 STAIRCASE FATIGUE TESTS

4.1.1 Staircase Fatigue Life Analysis

Staircase fatigue tests were performed on samples machined out of production cylinder blocks. A graphical representation of the staircase test conducted is shown in Figure 4.1. The mean fatigue limit of 60.8 MPa was determined by taking the average of test stress of the failed samples. The test results were resorted according to fatigue life and test stress, and are shown in Table 4.1.

Table 4.1 Staircase Fatigue Testing Results from Production V6 Cylinder Blocks (Sorted by Cycles to Failure and Stress)

Sample	Test Stress (MPa)	Cycles to failure	Sample	Test Stress (MPa)	Cycles to failure
1	58.6	601,329	19	51.7	10,000,000
2	55.2	1,079,425	20	51.7	10,000,000
3	65.5	1,221,611	21	55.2	10,000,000
4	62.1	1,446,344	22	55.2	10,000,000
5	65.5	1,528,578	23	55.2	10,000,000
6	58.6	1,544,123	24	55.2	10,000,000
7	68.9	1,544,545	25	58.6	10,000,000
8	65.5	1,596,839	26	58.6	10,000,000
9	51.7	1,624,415	27	58.6	10,000,000
10	68.9	1,842,084	28	58.6	10,000,000
11	62.1	2,386,222	29	58.6	10,000,000
12	62.1	2,777,713	30	62.1	10,000,000
13	55.2	2,835,303	31	62.1	10,000,000
14	58.6	3,386,766	32	62.1	10,000,000
15	51.7	6,884,206	33	62.1	10,000,000
16	62.1	9,649,661	34	65.5	10,000,000
17	48.3	10,000,000	35	65.5	10,000,000
18	48.3	10,000,000			

4.1.2 Staircase Fatigue Sample Fractography

Several of the failed samples were studied using the SEM. In order to investigate the reasons for the large range in fatigue lives, samples at each end of the life cycle spectrum were selected.

The staircase fatigue sample 1 tested at 58.6 MPa lasting 601,329 cycles is shown in Figure 4.2. From this micrograph a large (~1mm) interconnected shrinkage pore network is shown. This pore acted as the initiation site for fatigue failure.

Figures 4.3 (a) and (b) are higher magnification (X95) SEM micrographs near the initiation site. These are identical areas imaged using secondary electron imagining (SEI) and back scattered electron imagining (BEI) respectively. Oxide films are seen in close proximity to the initiation site. In (a) oxide films are seen as nearly white phases surrounded by dark patches, compared with (b) where the films appear dark gray. Other prominent phases include the copper rich eutectic phases, which appear white in the BEI image. The brightness of the films in SEI mode is thought to occur because of the non-electrical conducting nature of the film and is a result of excessive charging of the phase.

Figure 4.4 (a) and (b) are higher magnification SEM micrographs (X750) of one of the oxide films present on the sample shown in the previous figures. Figure 4.4 (a) is SEI and (b) is BEI.

Figure 4.5 (a) and (b) is another example from this sample at, this time at X550, once again (a) is SEI and (b) is BEI.

Positive identification of the oxygen content in this phase is performed by energy dispersive x-ray analysis. Figure 4.6 is an x-ray map of the image in Figure 4.4, showing the following elements: oxygen, iron, copper, aluminum and silicon. Note the significant oxygen signal corresponding to the location of the film.

The staircase fatigue sample 2 tested at 55.2 MPa lasting 1,079,425 cycles is shown in Figure 4.7 (a) and (b). A X350 micrograph of the shrinkage pore network that initiated the fatigue crack is shown. Note the presence of an oxide film linking the pore network to the sample surface.

Figure 4.8 (a) shows a BEI image (X600) of an oxide film found on the fracture surface of staircase sample 16, tested at 51.7MPa lasting 9,649,661 cycles. The associated x-ray maps are shown in Figure 4.8 (b). Note the elements shown are aluminum, oxygen, silicon, copper magnesium, iron, and manganese. Also note the significant oxygen and lack of magnesium signal present in the area associated with the oxide film.

4.2 REMELT REDUCED PRESSURE TESTS

The post-test sectioned sample is shown in Figure 4.9. Note the presence of two types of pores present, large bubble like pores, with diameters in the 3 to 10mm range and smaller irregularly shaped pores in the 1 mm range. The frames indicate areas of interest. Figures 4.10 through 4.16 are SEM micrographs of the ingot and fatigue samples tested.

4.3 CASTING OF FILTERED AND UNFILTERED TEST BARS

The results of chemical analysis are shown in Table 4.2. Presented is the overall average composition of three chemical disks taken over the span of the casting experiments.

Table 4.2 Average Chemical Composition of Alloy Used

Element	Si	Cu	Fe	Mg	Mn	Zn	Ti	Sr
wt%	7.38	3.29	0.35	0.22	0.24	0.11	0.10	0.0006
Element	Ni	Sn	Pb	Na	Ca	Cr	Pb	Li
wt%	0.014	0.002	0.006	0.000	0.000	0.060	0.000	0.000
Element	B	Sb	Be	Bi	Cd	V	Zr	Al
wt%	0.002	0.001	0.000	0.000	0.000	0.011	0.006	Balance

4.4 TENSILE TESTS

The tensile test results for the filtered and unfiltered test bars are shown in Table 4.3.

Table 4.3 Tensile Properties of Unfiltered and Filtered Test Bars

Sample	**Unfiltered** UTS (MPa)	0.2%YS (MPa)	Elongation (%)	**Filtered** UTS	0.2%YS (MPa)	Elongation (%)
1	204.0	194.0	0.27	242.7	179.5	0.91
2	213.8	195.1	0.34	254.7	195.5	1.01
3	244.8	186.0	0.92	255.9	192.4	1.08
4	245.1	186.2	0.95	257.8	186.7	1.22
5	250.6	184.4	1.05	261.1	-	-
6	259.5	187.9	1.24	261.9	178.4	1.47
7	259.8	197.3	1.12	265.0	179.4	1.51
8	262.6	184.4	1.43	266.1	188.1	1.42
9	262.9	189.6	1.26	267.9	192.7	1.39
10	264.4	198.1	1.30	268.0	185.2	1.57
11	265.6	192.5	1.33	268.7	181.6	1.71
12	265.7	184.8	1.49	269.7	177.8	1.76
13	265.8	180.9	1.56	270.1	185.5	1.63
14	266.3	181.7	1.55	270.2	181.1	1.67
15	267.2	194.7	1.53	271.5	182.6	1.81
16	267.8	193.6	1.44	271.7	191.0	1.56
17	268.5	175.7	1.76	272.2	188.5	1.57
18	270.9	180.6	1.91	272.2	180.6	1.94
19	271.9	189.0	1.75	272.8	180.8	1.83
20	272.8	182.2	1.88	275.0	192.7	1.80
21	273.7	182.6	1.85	275.7	193.8	1.81
22	273.7	186.6	1.78	276.4	182.8	1.96
23	273.9	201.1	1.59	277.0	189.8	1.92
24	276.2	185.4	2.08	277.9	181.2	2.25
25	276.5	-	-	279.4	188.1	1.98
26	278.1	193.7	1.93	279.4	195.8	2.03

On two occasions the extensometer malfunctioned preventing elongation and 0.2% yield strength measurements.

4.4.1 Ultimate Tensile Strength

Histograms of ultimate tensile strength (UTS) for the two data sets are shown in Figure 4.17. While both data sets show a similar distribution, both data sets are clearly skewed. The unfiltered values in particular showed a longer “tail” in the lower UTS region. In order to compare the two data sets statistically the nature of the two distributions must be determined. The Ryan-Joiner test for normality (using an α of 0.05) was performed on both data sets to determine if normal statistics could be used to compare the two distributions. Averages and standard deviations were also computed and are shown in Table 4.4.

Table 4.4 Ryan-Joiner Normality Test Results (α of 0.05) for UTS

	Unfiltered UTS	Filtered UTS
Average	261.6	268.5
Standard Deviation	17.8	8.7
R	0.85	0.96
P value	< 0.0100	0.0396
Result	reject H_0; i.e. not normal	Reject H_0; i.e. not normal

The filtered data set with a P value of 0.04 was much closer to the critical value of α than the unfiltered, however both data sets failed the test for normality at the α of 0.05. Therefore “normal” statistical tests such as the commonly used t-test are not applicable. To determine if the distributions are significantly different, non-parametric statistic tools that are not dependent on the probability distribution of the data sets must be used. The Mann-Whitney test compares the equality of the medians of the two data sets (Table 4.5).

Table 4.5 Mann-Whitney Test Results for UTS (α of 0.05)

	Unfiltered UTS	Filtered UTS
Median	266.1	270.2
P value	0.1382 (adjusted for ties)	
Result	Cannot reject H_0; i.e. samples have equivalent medians	

The results of the Mann-Whitney test indicate that the medians of the two samples are not significantly different.

Several probability distribution models were investigated to determine the best fit for each of the individual data sets. In addition because of the results of the above Mann-Whitney test, models for the combined data sets were also explored. The results of models with the highest correlation coefficients are presented in Table 4.6.

Table 4.6 Correlation Coefficient (R) for Lognormal and Weibull Fitted Models for UTS

Model	Unfiltered (n=26)	Filtered (n=26)	Combined data set (n=52)
Normal	0.85	0.96	0.89
Lognormal	0.83	0.95	0.87
Weibull	0.84	**0.98**	**0.95**

In the unfiltered data set, all had correlation coefficients that were less than 0.86 indicating a marginal fit. The Weibull model appeared to be the best fit for filtered data set and for the combined data set. A Weibull plot comparing unfiltered and filtered UTS values is shown in Figure 4.18. Note the different Weibull moduli (the slope of the line of best fit) are 15.6 and 37.6 for the unfiltered and filtered values respectively.

A cumulative probability plot for the combined data sets is shown in Figure 4.19. The majority of the data fits a straight line and where the data departs from the straight line (the lowest twelve UTS specimens) is of interest. These twelve lowest UTS samples (seven unfiltered, five filtered) were found to have large defects on the fracture surface details of these results are found in section 4.4.4 Tensile Sample Fractography.

4.4.2 Yield Strength

Yield strength was measured at the 0.2% elongation point (0.2%YS). Once again statistical methods were used to determine its probability distribution for the unfiltered and filtered cases.
The Ryan-Joiner test for normality was performed and the results are shown in Table 4.7.

Table 4.7 Ryan-Joiner Normality Test Results for 0.2%YS (α of 0.05)

	Unfiltered 0.2%YS	Filtered 0.2%YS
Average	188.3	186.1
Standard Deviation	6.4	5.7
R	0.99	0.97
P value	> 0.1000	> 0.1000
Result	Cannot reject H_0; i.e. normally distributed	cannot reject H_0; i.e. normally distributed

Thus both 0.2%YS data sets follow the normal probability distribution and have similar averages and standard deviations. In order to statistically compare the two distributions it is necessary to perform a hypothesis test. The two sample t–test was performed to determine if the means are significantly different. The results of this test are shown in Table 4.8.

Table 4.8 Two Sample T-Test for 0.2%YS (α of 0.05)

	Unfiltered 0.2%YS	Filtered 0.2%YS
Mean	188.3	186.1
SE Mean	1.3	1.1
P value	0.195	
Result	Cannot reject H_0; i.e. samples have equivalent means	

The above test shows that the means are not significantly different at this level of α.

4.4.3 Elongation

Elongation to fracture was also measured and analyzed. The Ryan-Joiner test for normality was performed and the results are shown in Table 4.9.

Table 4.9 Ryan-Joiner Normality Test Results for %EL (α of 0.05)

	Unfiltered %EL	Filtered %EL
Average	1.4	1.6
Standard Deviation	0.5	0.3
R	0.96	0.98
P value	0.0698	> 0.1000
Result	Cannot reject H_0; i.e. normally distributed	Cannot reject H_0; i.e. normally distributed

The above results indicate that both are normally distributed. However, because the UTS values fit the Weibull distribution, it was tested for the elongation to fracture values as well.

Table 4.10 Correlation Coefficient (R) for Fitted Models for %EL

Model	Unfiltered (n=25)	Filtered (n=25)	Combined data set (n=50)
Normal	**0.96**	0.98	**0.97**
Weibull	0.93	**0.99**	0.93

It can be seen from Table 4.10 that while the normality test indicated that the values were normally distributed (Table 4.9), the Weibull model also yields reasonably high correlation coefficients (in fact higher than that of normal distribution in the filtered case). For the purpose of comparison with UTS Weibull plots, the Weibull plots of elongation to fracture are shown in Figure 4.20

Once again the two sample t-test was performed to determine if the means are significantly different. The results of this test are shown in Table 4.11.

Table 4.11 Two Sample T-Test for %EL (α of 0.05)

	Unfiltered %EL	Filtered % EL
Mean	1.41	1.63
SE Mean	0.09	0.07
P value	0.058	
Result	Cannot reject H_0; i.e. samples have equivalent means	

The above results indicate that the samples have equivalent means. However the resulting P value of 0.058 is only marginally larger than the chosen α of 0.05, indicating a lower confidence in this result compared with the previous results.

The tensile statistics are summarized in Table 4.12

Table 4.12 Summary of Tensile Property Statistics (U is unfiltered condition, F is filtered)

Property	Best Fit Model	Weibull Modulus		Mean		Standard Deviation		Significantly different?
		U	F	U	F	U	F	
UTS	Weibull	15.6	37.6	261.6	268.5	17.8	8.7	No
0.2% YS	Normal	-	-	188.3	186.1	6.4	5.7	No
% EL	Normal/Weibull	2.4	5.5	1.4	1.6	0.5	0.3	No

4.4.4 Tensile Sample Fractography

The twelve lowest UTS samples were found to have large defects on the fracture surface. Eleven samples of this subgroup contained large oxide films (the remaining one revealed a shrinkage pore defect). All eleven showed a corresponding defect (nearly identical in size and shape) on the opposite side of the fracture surface. Representative SEM micrographs of these samples are shown in Figures 4.21 to 4.40 and details of the samples can be found in Table 4.13.

Table 4.13 Details of Samples Containing Oxide Film Defects

Sample	ID	Condition	UTS (MPa)	Area of Sample (mm^2)	Defect location	Area of Defect (mm^2)
1	F2	U	204.0	36.49	edge	1.52
2	I9	U	213.8	36.57	edge	1.12
3	P0	F	242.7	37.29	edge	1.09
4	H6	U	244.8	36.96	edge	0.83
5	G9	U	245.1	36.53	edge	0.52
6	G4	U	250.6	37.44	edge	0.87
7	O2	F	254.7	36.47	edge	1.18
8	D0	F	255.9	37.39	embedded	0.68
9	B9	F	257.8	37.22	edge	0.23
10	G7	U	259.5	36.85	edge	0.30
11	O9	F	261.1	36.63	edge	0.73

4.5 FATIGUE TESTS

4.5.1 Fatigue Test Results

The results of the fatigue tests for the filtered samples and unfiltered samples are shown in Table 4.14. All but two of the samples failed. The term “runout” indicates that the fatigue sample did not fail after reaching 10^7 cycles and that the test was stopped at some arbitrary point after 10^7 cycles.

Table 4.14 Results of Fatigue Tests for Filtered and Unfiltered Samples

Sample	Filtered Cycles to Failure	Unfiltered Cycles to Failure
1	89,500	61,300
2	112,000	182,400
3	123,100	202,500
4	135,200	213,100
5	159,900	249,300
6	163,300	288,900
7	170,000	309,000
8	206,400	363,900
9	237,200	364,800
10	274,600	379,800
11	286,800	385,800
12	331,500	402,100
13	347,600	458,500
14	350,400	528,200
15	419,500	546,900
16	424,000	553,700
17	433,500	641,000
18	484,400	705,400
19	487,500	708,800
20	523,700	722,000
21	524,700	744,800
22	532,600	808,200
23	534,800	833,500
24	620,300	1,055,500
25	862,400	1,444,000
26	1,148,400	4,557,700
27	1,168,000	47,000,000*
28	1,493,400	-
29	1,515,500	-
30	2,120,600	-
31	19,358,130*	-

*runout

Histograms of the unfiltered and filtered data are shown in Figure 4.41 (a) and (b) respectively. Statistical analysis was performed on the failed samples to determine the probability distribution functions for the two data sets. The correlation coefficients for the three best models are shown in Table 4.15.

Table 4.15 Correlation Coefficient (R) for Normal, Lognormal and Weibull Fitted Models for Cycles to Failure

Model	Unfiltered (n=26)	Filtered (n=30)	Combined data set (n=50)
Normal	0.88	0.70	0.77
Lognormal	**0.96**	**0.99**	**0.99**
Weibull	0.95	0.96	0.97

Both the Weibull model and lognormal models sufficiently fit the data, however the highest correlation coefficients were that of the lognormal. In the lognormal model only one data point lay outside the 95% confidence bands compared with the Weibull model where several of the points near the tails fell outside the confidence bands (see Figures 4.42 and 4.43). Since the data sets were found to be lognormally distributed, standard normal statistic tests can be applied provided the logarithm (or natural logarithm) of the data is taken first.

Table 4.16 Two Sample T-Test for Natural Logarithm of Cycles to Failure (α of 0.05)

	Unfiltered Ln(N)	Filtered Ln(N)
Mean	13.080	12.875
SE Mean	0.16	0.15
P value	0.351	
Result	Cannot reject H_0; i.e. samples have equivalent means	

The two sample t-test indicates that there is no significant difference in the means of the two populations. In addition the standard deviations of the natural logarithm of cycles to failure were comparable at 0.800 and 0.821 for the unfiltered and filtered populations respectively.

The cumulative probability of failure plot is shown in Figure 4.44. In these plots the “runouts” are plotted at 10^7 (though the test were stopped at 1.9×10^7 and 4.7×10^7, and would probably have continued if allowed). It is not normally appropriate to plot these points on a failure plot such as this, however they are included in the sample ranking and are plotted for reference purposes only.

4.5.2 Fatigue Crack Initiation Sites

The failed samples from

Table 4.14 all showed classic fatigue failure on the fracture surface. Fatigue cracks in all cases were found to initiate from distinct initiation sites. The initiation sites were divided into five main categories (Table 4.17).

Table 4.17 Type, Frequency and Description of Initiation Sites Found in Fatigue Samples

Category	Frequency (%)	Initiation Site Description
Shrinkage pore	20	one distinct shrinkage pore revealed on fracture surface acting as initiation site
Shrinkage network	35	a grouping of shrinkage pores that appear to be interconnected acting as initiation site
Oxide film	18	folded oxide film acting as initiation site
Shrinkage + oxide	20	a shrinkage pore or network acting as the initiation site, however oxide films were present near the site
Other	7	those not fitting into the above four categories, examples include: persistent slip bands, eutectic silicon particles, and foreign particles

A pie chart showing the frequency of the different types of defects and the split between filtered and unfiltered samples is shown in Figure 4.45

The initiation site types and associated defect areas for the filtered and unfiltered failed samples are shown in Table 4.18 and Table 4.19 respectively.

Table 4.18 Fatigue Lifetimes, Initiation Site Type and Area for Filtered Samples

Sample	Cycles to Failure	Initiation Site	Area of Site (mm^2)
1	89,500	shrinkage network with oxide film	0.2974
2	112,000	shrinkage network	0.4051
3	123,100	oxide film	0.1100
4	135,200	shrinkage network	0.0454
5	159,900	shrinkage network	0.2400
6	163,300	shrinkage network	0.0740
7	170,000	shrinkage network	0.1600
8	206,400	shrinkage network	0.0893
9	237,200	shrinkage network with contaminants	0.0800
10	274,600	shrinkage network	0.0226
11	286,800	oxide film	0.0303
12	331,500	shrinkage network with oxide film	0.0785
13	347,600	shrinkage network with oxide film	0.0241
14	350,400	shrinkage network with oxide film	0.0334
15	419,500	shrinkage and old oxide	0.0227
16	424,000	shrinkage network	0.1156
17	433,500	shrinkage network with oxide film	0.0867
18	484,400	shrinkage pore	0.0147
19	487,500	shrinkage network	0.0175
20	523,700	shrinkage network	0.0894
21	524,700	oxide film	0.0136
22	532,600	shrinkage pore	0.0017
23	534,800	shrinkage network	0.0861
24	620,300	shrinkage network	0.0175
25	862,400	slip bands and shrinkage pore	0.0013
26	1,148,400	old oxide	0.0042
27	1,168,000	shrinkage pore	0.0069
28	1,493,400	oxide film	0.0003
29	1,515,500	shrinkage pore	0.0020
30	2,120,600	shrinkage pore	0.0100
31	19,358,130	runout	-

Table 4.19 Fatigue Lifetimes, Initiation Site Type and Area for Unfiltered Samples

Sample	Cycles to Failure	Initiation Site	Area of Site (mm^2)
1	61,300	shrinkage network	0.5600
2	182,400	shrinkage network	0.1647
3	202,500	shrinkage pore	0.0617
4	213,100	shrinkage network	0.0900
5	249,300	shrinkage network	0.0320
6	288,900	oxide film	0.0220
7	309,000	silicon particle	0.0057
8	363,900	shrinkage network with oxide surface sink	0.0547
9	364,800	shrinkage network	0.1300
10	379,800	oxides	0.0160
11	385,800	shrinkage and old oxide	0.1307
12	402,100	oxide film	0.0105
13	458,500	shrinkage pore	0.0110
14	528,200	shrinkage and old oxide	0.0160
15	546,900	shrinkage and old oxide	0.0199
16	553,700	shrinkage network with oxide surface sink	0.0242
17	641,000	oxide	0.0096
18	705,400	shrinkage pore	0.0098
19	708,800	shrinkage pore	0.0602
20	722,000	shrinkage network	0.0685
21	744,800	shrinkage pore	0.0108
22	808,200	oxide film surface sink	0.0069
23	833,500	shrinkage network	0.0185
24	1,055,500	foreign particle	-
25	1,444,000	shrinkage pore	0.0034
26	4,557,700	shrinkage network	0.0040
27	47,000,000	runout	-

The square root of the initiation site area is a measure of the defect size with units of length. This characteristic is often used in fracture mechanics as an estimate of initial crack length. The cumulative probability of defect size acting as initiation sites for the two casting conditions is shown in Figure 4.46

4.5.3 Fatigue Sample Fractography

Figures 4.47 through 4.61 show selected examples of fatigue sample fracture surfaces displaying the type and structure of the fatigue crack initiation site.

Plots of fatigue life against initiation site size are shown for all the defect types and for oxide films only in Figures 4.62 (a) and (b) respectively.

The cycles to failure probability plots (Weibull and lognormal) for shrinkage and oxide defects are shown in Figures 4.63 (a) and (b) respectively. Either distribution may be applied to satisfactorily describe the oxide initiated fatigue failure lives as the correlation coefficients are of 0.98 (Weibull) and 0.99 (lognormal) with all points in the 95% confidence interval. However for the shrinkage related failures the lognormal yields a superior fit, as the R is higher (0.99 compared to 0.96) and all points save one fall in the confidence bands (4 points lay outside the Weibull confidence bands).

Chapter 5

DISCUSSION

5.1 STAIRCASE FATIGUE TESTS

5.1.1 Fatigue Life Analysis

When examining the staircase data in Table 4.1 one can immediately see the variation in fatigue performance of the samples. Despite being machined from “identical” production castings the performance of the samples was notably inconsistent. There appears to be almost no correlation between applied stress and fatigue life. For example, runouts (10^7 cycles) were experienced by samples that underwent relatively high stresses regimes (6 samples in the >60 MPa range). Further adding to the disarray, several samples tested at relatively low stress regimes (there are 7 samples in the <60MPa range) failed relatively early in the test. In addition, for any given stress level (with exception of the extremes 48.3 and 68.9MPa) there were mixed test outcomes (i.e. failed tests and runouts). This is expected somewhat in staircase testing, however not to such a degree. The varying results for a given stress level can also be seen in the plot of the test results Figure 4.1. The peaks and valleys created by the points during the first 20 tests are a result of this inconsistency. The string of passed samples from test 15 through 19 usually occurs at the onset of a test as a result of a poor estimate at what stress to start the staircase series. The later portion of the test series (above test 20) shows a more typical staircase test pattern with the magnitudes of the peaks and valleys diminishing as they converge on what is later calculated as the mean fatigue limit.

Clearly investigation into the causes for fatigue failure in these samples was warranted. Fractographic investigations using the scanning electron microscope were performed.

5.1.2 Staircase Fatigue Sample Fractography

5.1.2.1 Introduction

Upon investigation into the fracture surfaces of the failed tests, the reasons for the variation in fatigue performance became apparent. Surface shrinkage pores acted as the fatigue crack initiation sites in all cases examined. This in itself is not surprising to the investigator. From the literature sources it is known that surface shrinkage pores are the most common fatigue crack initiation sites in aluminum castings. In addition, as mentioned earlier in this work, the staircase fatigue samples were machined from the main bearing saddle portion of cylinder block castings that is known to have marginal liquid feeding and relatively slow solidification rates. What was interesting however is that in every case examined oxide films were found to be present on the fracture surface. In samples with low fatigue lives there existed an abundance of these films often closely associated with the shrinkage pore that initiated the fatigue crack. Conversely, in the sample with the highest (failed) fatigue life, few oxide films were seen and these were seemingly randomly distributed on the fracture surface.

5.1.2.2 Selected Examples

Figure 4.2 is an SEM micrograph of staircase sample #1 from Table 4.1 tested at 58.6 MPa and failing after 601,329 cycles. The fatigue crack initiation site was a large interconnected shrinkage network. This network spans a length of approximately 1 mm. High magnification micrographs (X95) are shown in Figure 4.3 (a) and (b). These figures reveal the oxide films located near the shrinkage pore

Another staircase fatigue sample with a low fatigue life is sample #2 (Table 4.1). SEM micrographs of the initiating shrinkage pore can be seen in Figure 4.7. In this case an oxide film can be seen linking the pore to the fracture surface.

In the sample with the highest cycles to failure, sample #16 lasting 9,649,661 cycles, no films were seen near the initiation site but were found to be randomly distributed on the fracture surface. Figure 4.8(a) shows a BEI SEM micrograph of one example. An x-ray map analyzing all the main alloying elements again revealed a strong oxygen signal (Figure 4.8(b)). What further defines the nature of the film is that there appears to be no magnesium present in the phase. This indicates that it is the alumina variety of oxide film.

It can be seen in all of the aforementioned figures that the oxide phase is in close contact with the aluminum matrix. In fact the phase seems to follow the contour of the local microstructure. At high magnifications the film structure demonstrates a coarse, granular appearance. All of this evidence suggests that these films are the later forms of the alumina oxide film, i.e. the stable α-Al_2O_3 or old oxide (Table 2.7). As described in Chapter 2, it is in these films that the air gap between the dry sides has reacted and some degree of bonding exists. Such films have been allowed to fully react with the oxygen present and consequently the thin folded nature of the young oxide has been replaced by coarse inflexible old oxide.

The lack of the presence of young oxide films (Table 2.7) is not surprising when considering the loading conditions of the staircase fatigue tests. Due to the fully reversed stress regime (tensile/compressive) young films, typified by their thin, folded and fragile nature would likely be damaged or destroyed by the repetitive crashing of the opposite sides of the crack front.

In all of the cases studied the oxide film appears intact on a distinct plane of fracture, often not that of the surrounding material. The likely reason for this is that the crack progresses via normal mechanisms through the matrix, until it comes to the site of an oxide film where the crack front instantly diverts to pass through this weak plane. The resulting structure from this mechanism is the intact oxide film displayed on a distinct fracture plane. A similar mechanism may occur during the fast fracture portion of the fatigue failure. When these events take place the film itself must either fracture or come away from the matrix. The bond on the wetted side is in good contact with the matrix and is relatively strong and not likely to separate. However the weak bond between the dry sides is the likely area of fracture. If this were the case an accompanying film would be left on the opposite side of the fracture surface on a complimentary angled plane. Figure 5.1 shows SEM micrographs from opposite fracture surfaces from the failed staircase sample #1. The film shown is the same one shown in Figure 4.4. Here it can clearly be seen that the film exists on both sides of the fracture surface in a complimentary fashion. It is interesting to note too the presence of nearby iron rich intermetallics (light script phases). It seems the case that rather than debonding or pulling out from the matrix, they have fractured on an axis of symmetry leaving (nearly) mirror phases on the opposite fracture face.

As a result of the above mechanisms it can be seen that oxide films act as micro planes of weakness. These local weaknesses, of course, diminish the fatigue strength of the sample, as they accelerate fatigue crack growth. Minute amounts of these films would have little effect on fatigue life, however significant amounts would drastically increase the average crack propagation rate, cutting fatigue lives considerably.

Furthermore, it is more than coincidental that films tend to be located nearby shrinkage pores that acted as fatigue crack initiation sites. The shrinkage cavities themselves are likely to have nucleated on oxide films.

The above facts give credence to the hypothesis that it is the oxide films that are responsible for the inconsistent fatigue performance in these samples.

5.2 REMELT REDUCED PRESSURE TESTS

5.2.1 General Observations

A sample of the commercial ingot used for the casting experiments was sectioned and prepared as shown in Figure 3.3. The presence of fine inclusion related porosity seen on the ground surface is not unusual for ingot castings. The hydrogen and inclusion content are normally relatively high compared with the post-processed metal that is used in casting. After testing, the sample in the RRPT and sectioning the effects of solidifying under reduced pressure are clear, Figure 4.9. The top of the sample has risen to give a “bread loaf” shape to the sample. This is the effect of the enlarged gas bubbles moving up through the sample and pushing against the top surface (which is itself an oxide). During the test the top surface was observed to "puff up" and then deflate. These actions were repeated several times until the sample had sufficiently solidified preventing further movement of the top surface. This is undoubtedly the effect of the bubbles building up and then bursting or breaching the top surface and resulting in the bubbles deflating and causing the downward movement of the top surface. Samples from failed staircase fatigue bars were also subjected to this test and showed similar results as those from the ingot material.

5.2.2 Nature of Pores Present

There are two main types of pores present in the cross section. These can be classified in terms of pore diameter, but as they appear to be formed by different mechanisms they possess other dissimilar characteristics. The first type consists of large pores in the 3 to 10 mm diameter range. They are spherical in nature and display either a smooth featureless interior or a distinctly dendrite encrusted one Figure 4.10. The second class includes pores with diameters in the 0.1 to 1 mm range. These pores have a characteristic irregular shape, apparently corresponding to the dendritic shape of the surrounding aluminum matrix. Dendrites were seen on many of the interior surfaces of these also, but a only a few showed a wrinkled interior.

The mechanism for the formation of the large pores is expansion due to the reduced pressure. As solidification progresses, dissolved hydrogen precipitates at favourable sites, such as folded oxide films (Figure 5.2). The pore inflates and the original oxide film cannot accommodate the strain and it fractures. A new film then immediately replaces it, as the liquid metal reacts with the trapped air that was enclosed in the original double film. This new film is very thin (described in Table 2.7) and will continue to strain and fracture according to the degree of expansion of the pore. The next step in the formative stages of this class of pore can take two paths. First, if the pore continues to expand, its buoyant force may overcome the viscous and/or mechanical restraining forces (the latter becomes significant as the liquid metal solidifies) of the metal and it begins to move to the free surface as described above. The bubble may then escape through the free surface or become trapped remaining intact or later collapsing if a leak path is present. An example of the latter case and the accompanying oxide film are shown in Figures 4.11 and 4.12. In this unusual micrograph it is possible to estimate the thickness of the thin young film.

Measurement of the width of the sharpest fold yielded a value of approximately 100 nm. Therefore the single film can have a maximum thickness of 50 nm (less if there is a minute gap) This is in good agreement with estimates from the literature, see Table 2.7.

The second option is that the bubble remains stationary in the solidifying metal. In this case the liquid metal will solidify around the bubble and eventually it will experience the contracting force of the liquid metal. The internal gas pressure of the pore opposes this compressive solidification force, Figure 5.2. On a micro scale these counteractive forces are characterized by the aluminum dendrites coming into contact with the film that forms the interior (and exterior) of the bubble. What occurs next depends on the magnitude of local solidification pressures and on the strength of the film - which in turn is dependent on the “age” of film. If the film is old and relatively strong the pore interior will not be breached and a smooth featureless interior remains. If the film that makes up the interior surface is young or a combination of fractured old film and young films, the likely outcome is that dendrites will impinge and break through the film. This would result in a spherical pore with an interior covered in aluminum dendrites in a variety of orientations. Unlike the old films, young films are somewhat flexible. If the impinging strain imposed by the dendrite tips is not beyond that of the fracture strain of the young film, it will stretch and wrinkle to accommodate the dendritic intrusion. The resulting microstructures for these two cases (dendrite film break through and film compliance) will resemble those shown in Figure 4.14 and 4.15

In the second class of smaller pores the large expansion described above did not occur. It is thought that most of these smaller pores are interconnected and the gases contained within them passed into favourable pores that expanded into bubbles. Consequently these pores were inflated very little. In some cases this however, isolated pores were observed. These were not connected to other pores and their expansion was not great enough to fracture the original entrained film. This is due to the relatively small pressures generated from the minute amounts of air trapped in the folded oxide film. As a result, these films increase in volume only until encountering resistance from the solidifying dendrites, thus forming their characteristic irregular shape. In terms of the previous mechanism the films would not progress beyond the stage shown in 5.2 (b). The intact film can be seen on the interior surface of the pore seen in Figure 4.16.

5.3 TENSILE TESTS

5.3.1 Tensile Properties

Statistical analysis was performed and presented in Chapter 4. The results showed that the UTS values followed the Weibull distribution and that unfiltered samples had more scatter on the low end of the distribution compared with the filtered samples. This is illustrated in the UTS histograms shown in Figures 4.17 The statistical tests performed also showed that the two distributions did not have significantly different means. Despite this observation, it is clear that the performance of the two sample sets was not equivalent. From the Weibull plots (Figure 4.18), a Weibull modulus of 37.6 for the filtered samples compared with 15.7 for the unfiltered samples, indicates a much higher degree of repeatability in UTS values. It is the outlying lower UTS unfiltered values that result in the lower Weibull modulus. This is an example of the dangers of using common criteria such as population mean as a distinguishing factor. Used alone it would indicate that cast parts produced without filters are equivalent to filtered castings. In addition, it is worthy to note that this number of tests (approximately 30 per condition) should be considered the minimum necessary to depict the behaviour of the material with accuracy. It is the relatively rare cases of alarmingly low UTS values that limit how well a casting will perform in service.

What can be inferred from analysis of the data and statistical tests is that the two sets may be combined and analyzed as a larger group, as most of the samples in unfiltered condition have equivalent strengths as those of the filtered set. As noted in section 4.4.1, a plot of the cumulative probability of failure for the combined group showed 12 samples that departed from the distribution as a whole (Figure 4.19). These were analyzed using the SEM and found to contain significant defects on the fracture surface that undoubtedly contributed to the lower UTS values. The fractography of these samples is discussed in the next section.

Statistical tests on the yield strength indicated that the two distributions were normal and not significantly different. This is expected, as yield strength is known to be relatively insensitive to defects contained in the casting.

The distribution of elongation values showed a remarkably similar trend as that of the UTS values. Once again this is not surprising once it is understood that defects present in the samples appear to dominate the premature fracture of the test bars. The Weibull plots for elongation to fracture are shown in Figure 4.20, note the similarity to the trends discussed in the UTS Weibull plots (Figure 4.18.). The above arguments put forth for UTS results may also be applied when considering elongation performance of these samples.

5.3.2 Tensile Sample Fractography

The tensile sample fractography focused primarily on the samples with the lowest UTS. Samples with high UTS and several randomly selected samples were also examined. These samples showed no significant defects on the fracture surface.

The fractography and spectroscopy of selected low UTS samples are presented in Figures 4.21 through 4.40.

In most of the cases the oxide film can clearly be distinguished from the general fracture structure of the test bar. The general fracture appearance of the matrix follows that of ductile fracture, with some characteristics of brittle failure in the areas where eutectic silicon is present. The oxide film structure contains folds or wrinkles and on fracture surfaces is usually seen as a planar, homogeneous phase. The reason it appears as planar rather than its true three-dimensional complex shape is related to how it responds to the stresses imposed during the tensile test. These newly formed films have negligible strength compared with the surrounding structure. If the tensile sample contains many films with random orientations, the film that will pull apart will be the one with the largest area perpendicular to the applied stress. This film pulls apart and portions of the film will be left on both of the fracture surfaces. The phenomenon was found to exist in every sample that had an oxide film on its fracture surface. One exception to this planar morphology is shown in Figure 4.33. This is a oxide film fragment that rose upwards from the planar surface film (Figure 4.31). It appears to be an entangled film that has wrapped itself up resulting in a spherical shape. X-ray maps established the presence of aluminum, magnesium and oxygen, confirming its identity as an oxide film.

The films present in Figures 4.21 to 4.40 are all young films (Table 2.7). This was concluded from their folded appearance and thickness. However some are much thinner than others, indicating that they were very recently formed. The time scale for the formation of these very thin films is in the order of seconds or less, indicating that these were formed during the filling of the mould. The oxide films are a result of metal turbulence in the downsprue, filterprints, or even as late as the runner bar. The fact that oxide films were present in filtered castings as well as the unfiltered indicates that the filters were ineffective at preventing these types of defects. In fact it is possible to envision some cases in poorly designed filling systems where the filters could increase such a defect. For example if the downsprue is not completely filled during pouring it is possible for air to be remain in the filter during casting. If this occurs the filter acts as type of aerator that atomizes the liquid aluminum, combining it with the oxygen present. The result is conversion of the once beneficial filter into an efficient oxide film producing device.

At high magnifications the thin films are often found covering the thicker young films as in Figures 4.28, 4.31 and 4.34. Young films such as these are transparent and only become evident if folded.

In some rare case such as Figure 4.36(a) for example, it is possible to see where the film has torn or ruptured and a single thickness of the film has been imaged. X-ray spectra were analyzed and the film was discovered to contain aluminum, magnesium and oxygen (silicon and copper signals are from the background as these elements main alloying elements in the alloy Table 4.2). Another example of a torn film is shown in Figure 4.39.

The film seen in Figure 4.35 through 4.36 is unique in that it appears as planar on the fracture surface yet is connected to a pore. Closer examination of this pore showed that its interior walls were consisted of folded films and that it continued beyond the field of view twisting and turning down into the sample. This morphology suggests that this film/pore combination is what remains of an air bubble passing up the length of the sample during casting. A bubble moving through the melt leaves behind an oxide tube known as a bubble trail as it continually breaks and reforms the oxide that encases the bubble (Divandari 1999; 2001).

The one sample of the twelve lowest UTS samples that did not show any oxide films on the surface is shown in Figure 4.40. This sample exhibited a large shrinkage pore network located near the surface of the sample.

5.3.3 Tensile Stress Models

5.3.3.1 Load Limit Model

From the micrographs the area of oxide film defects can be measured. These defects effectively reduce the load bearing area (Table 5.1). In a simple strength vs. area model the percent reduction in strength is directly proportional to percent reduction in area. The reduction in strength is calculated as a percentage difference from the maximum UTS taken from all the tests (279.4 MPa).

Table 5.1 Load Limit Model Data for UTS Samples with Oxide Film Defects

Sample	ID	Condition	UTS (MPa)	Area of Sample (mm^2)	Area of Defect (mm^2)	**% Reduction of Area**	**% Less than Max. UTS**
1	F2	U	204.0	36.49	1.52	**4.2**	**27.0**
2	I9	U	213.8	36.57	1.12	**3.1**	**23.5**
3	P0	F	242.7	37.29	1.09	**2.9**	**13.1**
4	H6	U	244.8	36.96	0.83	**2.2**	**12.4**
5	G9	U	245.1	36.53	0.52	**1.4**	**12.3**
6	G4	U	250.6	37.44	0.87	**2.3**	**10.3**
7	O2	F	254.7	36.47	1.18	**3.2**	**8.8**
8	D0	F	255.9	37.39	0.68	**1.8**	**8.4**
9	B9	F	257.8	37.22	0.23	**0.6**	**7.7**
10	G7	U	259.5	36.85	0.30	**0.8**	**7.1**
11	O9	F	261.1	36.63	0.73	**2.0**	**6.5**

The relationship between these two parameters for the samples of interest is shown in Figure 5.3. A line of best fit has been applied. The overall trend is correct, however the correlation coefficient (R^2) of 0.51 indicates a relatively poor fit. Furthermore the relationship should take the form of a 1:1 ratio (reduction in strength : reduction in area) rather than the 5:1 slope shown in this Figure. Clearly the UTS is more sensitive to the size of the oxide defects than this model explains.

5.3.3.2 Fracture Mechanics Model

If the tensile bar containing the oxide film is considered a cracked body (Figure 5.4), we can apply fracture mechanics based models to predict the fracture stress. By measuring the dimensions of the revealed flaw (a and $2c$), applying the shape factor Q (Figure 2.12), and using the fracture toughness of the material K_{IC} we are able to predict the fracture stress from the LEFM equations 20 and 21 for the embedded and surface defects respectively. However the stresses that these samples failed at are above the yield stress. Therefore the LEFM model alone does not apply. A hybrid model that accounts for plasticity effects such as the R6 failure assessment diagram must be employed. Figure 5.5 shows the eleven tensile samples that contained oxide film defect plotted on the R6 (revision 3) diagram. The LEFM calculated points fall in the failed region and indicate a plastic collapse at L_r=1.05. This corresponds to a K_r of 0.50 (from equation 22). Thus the appropriate stress intensity factor for the LEFM equations in this situation is exactly half of K_{IC}. Using the best estimate of K_{IC} from the literature for the conditions used in this study (see Table 2.10) yields a K_{IC} estimate of 16.7 MPa m$^{0.5}$. The data used for this model and its predictions are given in Table 5.2.

Table 5.2 Data Used for Plotting on R6 Plot and Prediction of Failure Stress

ID	defect type	*a* (mm)	*2c* (mm)	*a/2c*	*Q*	YS (MPa)	**UTS (MPa)**	LEFM *K*	L_r	K_r	Cutoff *K* (0.5K_{IC})	**Predicted Failure Stress (MPa)**
F2	edge	0.88	2.02	0.44	1.95	194.0	**204.0**	8.56	1.05	0.51	8.35	**201.6**
I9	edge	0.44	2.48	0.18	1.07	195.1	**213.8**	8.74	1.10	0.52	8.35	**211.2**
P0	edge	0.66	1.55	0.43	1.94	179.5	**242.7**	8.87	1.35	0.53	8.35	**232.2**
H6	edge	0.60	1.52	0.39	1.75	186.0	**244.8**	8.78	1.32	0.53	8.35	**232.3**
G9	edge	0.45	1.21	0.37	1.67	186.2	**245.1**	8.01	1.32	0.48	8.35	**260.9**
G4	edge	1.04	1.56	0.67	3.10	184.4	**250.6**	8.95	1.36	0.54	8.35	**233.8**
O2	edge	0.56	1.30	0.43	1.94	195.5	**254.7**	8.53	1.30	0.51	8.35	**252.1**
D0	embed.	0.38	1.73	0.22	1.17	192.4	**255.9**	9.21	1.33	0.55	8.35	**263.1**
B9	edge	0.24	0.53	0.45	2.01	186.7	**257.8**	5.65	1.38	0.34	8.35	**391.9**
G7	edge	0.38	1.11	0.34	1.55	187.9	**259.5**	8.03	1.38	0.48	8.35	**273.5**
O9	edge	0.55	1.17	0.47	2.09	-	**261.1**	8.44	-	0.51	8.35	**264.0**

The plot of predicted versus actual failure stress along with the 1:1 reference line are shown in Figure 5.6 (a). All of the data save one point fall close to the 1:1 line. On considering this point to be anomalous and excluding it from the correlation study the plot may be re-scaled and is shown in Figure 5.6 (b). The model appears to be in general on the conservative side, however the average error in strength prediction is less than 3.6%. In addition the correlation coefficient R^2 was calculated for the fit of the data to the 1:1 line, this resulted in a value of 0.80.

The primary reason the model is successful is that the oxide films act as ideal cracks. Their planar morphology and negligible bonding are essentially the definition of the classic fracture mechanics crack (Figure 5.4). Specific equations are employed for centrally located films (embedded cracks, equation 20) or those at the sample surface (edge cracks, equation 21). The utilization of defect shape correction factors (Figure 2.12) further refines the model. These factors take into account the shape of oxide on the fracture surface.

It is particularly sobering to consider the value of the corrected fracture toughness. The already rather low (for metals) estimate of 16.7 MPa $m^{0.5}$ is effectively reduced by 50% in the conditions described, resulting in a value approaching that of ceramic materials. Thus, the impact of oxide films goes further than only increasing scatter in properties but can be seen to undermine the intrinsic toughness of the metal. From the point of view of the casting designer, the seriously deleterious effect of oxide films on properties raises serious concerns.

5.4 FATIGUE TESTS

Unlike the staircase method of testing, the stress level in this series of fatigue tests was held constant and designed for all the samples to fail, hence the use of an unusually high maximum stress of 150 MPa (for this alloy and T7 temper). Failed samples were the desired outcome as no information about the fatigue failure can be gleaned from runout samples. In order to identify fatigue crack initiation sites it was necessary to examine the fracture surfaces of the failed samples. To perform these tasks in a reasonable amount of time, the fatigue test was designed for all the samples to fail before 10^7 cycles. The stress ratio (see section 2.5.1.1) was chosen as 0.1, this also differs from the staircase tests, which were performed at –1. The positive stress ratio (tension-tension) test not only corresponds to the production casting service conditions (see section 2.5.1.2) but also protects the fracture surface from damage, as the opposite faces should come into a minimal amount contact during the test.

5.4.1 Fatigue Test Results

The statistical analysis of the unfiltered and filtered sample fatigue lives showed no difference in the means of the two populations. The individual populations followed the lognormal distribution. Subtle differences in the fatigue lives however, can be seen from the cumulative probability plot shown in Figure 4.44. One somewhat surprising observation is that for the bulk of the probability range (i.e. between the 0.05 and 0.78 marks) the unfiltered fatigue samples have higher lives than the filtered group. The difference in fatigue lives while not great, is convincingly consistent in this range.

To understand the reason for this phenomenon it is important to recognize the nature of the defects that initiated the failure of these samples. One method to explore this relationship is to plot the cumulative probability of the occurrence the size of defect (square root of the area of the defect) for each distribution (Figure 4.46). Upon examination of this graph the reason for the shorter fatigue lives in the filtered samples becomes clear. In general, the size of the defect acting as the initiation site was larger in the filtered samples. Since 75% of the initiation sites were found to contain some form of shrinkage porosity, these defects were examined in detail.

When considering cracks initiated from shrinkage pore related defects the defect area is on average 10% higher in the filtered samples than the unfiltered. This would explain the shorter filtered fatigue lives and the trend shown in Figure 4.44 (the filtered samples had an average life 31% lower than that of the unfiltered case. It is not surprising that despite having inverted the mould immediately after pouring (to aid feeding to the maximum extent for this geometry), shrinkage porosity exists in the castings. The alloy in use is known to be prone to shrinkage porosity primarily because of its long freezing range. Evidence linking the larger shrinkage pores with the counter productive effect of the filter can be discovered by examination of the solidified gating and running system. In the unfiltered castings the (empty) filterprint showed a significant decrease in volume after solidification, in the order of 20-30% (Figure 5.7 (a) and (b)). This indicates that significant feeding of the rest of the casting occurred. In the filtered samples the filter (and its print) was apparently full of metal after solidification. This fact suggests that presence of the filter reduced the amount of available feed metal. This reduction may have occurred for two reasons. First, the rigidity of the filter prevented the collapse of the volume of metal in the print, resulting in less feed metal available to the casting. The second possibility is the filter restricted the flow of feed metal. This may have happened as a result of the covering of the face of the filter with oxide films and other inclusions, which the filter is designed to obstruct.

Comparing these results with those of Nyahumwa (1997), which were performed under the same test stress regime but with a different alloy, significant differences in the results can be observed (Figure 5.8). The Nyahumwa data shows a clear separation between unfiltered and filtered populations. This contrasts what was found in the current work where the two distributions were quite close and crossed over one another. This indicates that the alloy used in the current study is not nearly as responsive to the beneficial effects of in-mould filters (at the stress level tested). Rather it is evidently more sensitive to the deleterious effects of reduced feed metal, as fatigue life is highly dependent on the size of the defects present.

When plotted on the same graph the two data sets from the current work fall between the unfiltered and filtered Nyahumwa data. An interesting observation is that the unfiltered fatigue data overlays much of the Nyahumwa filtered data below the 0.60 probability mark. Referring back to the original Nyahumwa diagram Figure 2.8, it is at this transition point where the type of initiation sites changed from defect related to slip band related initiation sites. The current study shows no such change in slope, and correspondingly no deviation in the nature of initiation site, as virtually all failures were found to be related to defects.

Interestingly, the small subgroup of high life cycle samples is also seen in the current work. Although fewer in number (three compared to seven), these points indicate that the potential for long fatigue life exists in this alloy also. In specific terms the lives of samples in this group are an order of magnitude greater than 90% of the fatigue samples tested. It is worth noting that two of these samples did not fail, their lives extending well beyond 10^7 cycles.

5.4.2 Fatigue Crack Initiation Sites

As described in Chapter 4 the fatigue crack initiation sites fell into four basic groups: shrinkage porosity, oxide films, combination of shrinkage and oxide, and the “others” group (Figure 4.45 and Table 4.18). There appears to be little difference in the breakdowns of defect type between the unfiltered and filtered conditions. In every category there appeared to be a roughly 50/50 split between unfiltered and filtered, indicating that the presence of filters in the running system did not have any affect on the fatigue failure mode of the cast samples.

5.4.3 Fatigue Sample Fractography

Selected examples of the various types of initiation sites are shown in Figures 4.47 through 4.61.

The oxide films found to have initiated fatigue cracks were all young oxide films. This is apparent from their folded nature and thickness. These young films were also found to contain magnesium (Figure 4.56). When comparing the morphology of the young oxide films found on the tensile fracture surfaces a higher degree of fragmentation of the oxide film initiation sites is noted. The finer structural aspects of the films, e.g. sharp folds, thin transparent and characteristic delicate wispy flowing structures were not present on the fatigue fracture surfaces. This is due to the action of the cyclic stress regime imposed during the fatigue test. Despite being of the tension-tension stress ratio (R = 0.1), some degree of structural damage is expected due to the fragility of the film. In the tensile tests the oxide film was slowly pulled apart unidirectionally, avoiding any damage to the structure of the film.

Old oxides similar in structure to those found in the staircase fatigue samples were also observed. Like those found in the staircase samples they were often associated with the shrinkage pores that initiated fatigue cracks. Conversely to the young films discovered, these old films seem to be composed of only aluminum and oxygen (Figure 4.58) and were never found to act as initiation sites. This is verification of the work performed by Nyahumwa (1998a, 1998b, 2001) where old oxides were found not to be as favourable an initiation site as their younger counterparts.

Almost all fatigue crack initiation sites were located at the sample surface. In the few cases that were not obviously connected to the surface, the initiation site was within 10μm of the free surface (e.g. Figure 4.61).

5.4.4 Fatigue Life Prediction Model

The relationship between fatigue life (log scale) and the size of the different types of defects is shown in Figure 4.62. There appears to be an inverse relationship between fatigue life and defect size. In general, samples with long lives had small initiation sites, and samples that failed relatively early in the test were found to have initiated from large defects. There appears to be a large degree of scatter in the data, particularly when points associated with shrinkage porosity are included in the plot. When these are removed (Figure 4.62(b)) and only oxide films are plotted a more defined relationship is seen. The reason for higher degree of scatter when considering the shrinkage pores is because of the inability to measure the true size of these defects accurately. Estimating the true size of shrinkage pore from sample cross sections and fracture surfaces is a well known problem in the metallography of castings (Figure 2.5). The disconnected pore network often displayed on the fracture surface is what remains of a complex shaped three-dimensional pore that initiated the fatigue crack. Despite best efforts of quantifying defect size, both conservative and excessive estimates of actual pore size are conceivable.

Lines of best fit were not applied in Figures 4.62(a) and (b) as a model exists to for fatigue crack propagation life estimation based on initial defect size. As presented in section 2.5.6 the required information for application of equation 36 is as follows:

Initial defect size, a_i
This was measured from the fracture surface as the square root of the area of the initiation site.

Stress range, $\Delta\sigma$

This is an experimental parameter and was held constant for all tests at 135MPa.

Closure factor, U_R (equation 30)

The closure factor value depends largely on the test stress ratio R, and also to some extent on ΔK. Due to material differences and the number of crack closure modes there is no agreed universal relationship between U_R, R, and ΔK. From the literature (Couper 1990) it has been noted that U_R is dependent on heat treatment in aluminum casting alloys. Couper also noted that for R = -1 an appropriate value of U_R is 0.5, indicating crack closure during half the time in the tension-compression cycle. Wang (2001b) assumes a value of unity is used for a stress ratio of R = 0.1 indicating no crack closure in a T6 A356 alloy for the testing conditions used. This seems too an overestimate for the current test conditions. Some degree of crack closure is expected at this relatively low positive stress ratio of 0.1 (Knott 1984, Borrego, 2001 and Kujawski 2001). A value between 0.7-0.8 is a more appropriate estimate.

Compliance factor, $Y(a_i)$

The compliance factor for a plane part through crack in a cylinder has been estimated between 0.69 and 0.72 (Couper 1990) in this study a value of 0.7 is used.

Paris constants C and m

These values need to be experimentally measured from fatigue crack growth rate tests. A literature search provided Figure 5.9 (Caton, 1999). By estimating the slope of regime B, of the long crack data for the castings with fine microstructure (nearly identical conditions to that of the current experiment) values of $C = 1.27 \times 10^{-10}$ and $m = 3.9$ were determined.

The results of calculating the propagation life based on initial defect size and the above parameters are shown in Table 5.3 and Figures 5.10 (a) and (b).

Table 5.3 Summary of Initiation Site Size, Measured Fatigue Life and Predicted Propagation Life (Equation 36) (sorted by descending defect size)

Sample	Size of defect (mm)	Actual Fatigue Life	Predicted Propagation Life	Sample	Size of defect (mm)	Actual Fatigue Life	Predicted Propagation Life
1	0.748	61,300	72,113	29	0.150	419,500	358,570
2	0.636	112,000	84,789	30	0.150	274,600	358,823
3	0.545	89,500	98,963	31	0.148	288,900	363,721
4	0.490	159,900	110,154	32	0.141	546,900	382,102
5	0.406	182,400	132,976	33	0.136	833,500	396,883
6	0.400	170,000	134,911	34	0.132	487,500	407,793
7	0.362	385,800	149,278	35	0.132	620,300	408,271
8	0.361	364,800	149,667	36	0.127	379,800	426,174
9	0.340	424,000	158,714	37	0.126	528,200	426,893
10	0.332	123,100	162,709	38	0.121	484,400	444,457
11	0.300	213,100	179,881	39	0.117	524,700	462,877
12	0.299	206,400	180,532	40	0.105	458,500	513,621
13	0.299	523,700	180,618	41	0.104	744,800	518,673
14	0.294	433,500	183,252	42	0.102	402,100	527,746
15	0.293	534,800	183,915	43	0.100	2,120,600	539,644
16	0.283	237,200	190,793	44	0.099	705,400	546,407
17	0.280	331,500	192,642	45	0.098	641,000	550,916
18	0.272	163,300	198,423	46	0.083	1,168,000	649,655
19	0.262	722,000	206,186	47	0.083	808,200	650,457
20	0.248	202,500	217,297	48	0.075	309,000	715,278
21	0.245	708,800	219,970	49	0.065	1,148,400	835,879
22	0.234	363,900	230,748	50	0.063	4,557,700	857,226
23	0.213	135,200	253,309	51	0.058	1,444,000	926,436
24	0.183	350,400	295,068	52	0.045	1,515,500	1,206,681
25	0.179	249,300	301,680	53	0.041	532,600	1,324,505
26	0.174	286,800	309,793	54	0.036	862,400	1,481,957
27	0.156	553,700	346,932	55	0.016	1,493,400	3,302,569
28	0.155	347,600	347,738				

The LEFM crack growth model predicts crack propagation life. Actual fatigue life is made of up the time required to nucleate the cracks and the time required for crack propagation until the applied load cannot be supported by the reduced area and fast fracture occurs. If the cracks initiate from porosity and oxide films, this nucleation time should be minimal. This can be seen from these plots as the points tend to group around the 1:1 reference line. Unlike the bulk of the points in (a) the oxide film initiated samples in (b), conform very well to the 1:1 line. The reason the model performs better in predicting the fatigue lives associated with oxide film defects is two-fold.

The first reason for this could be the effect of error in area measurement. For the oxide film initiation sites it is very clear where the film/matrix boundaries are, and the defect remaining on the fracture surface is likely a good representation of the size of the original defect. Therefore reasonably accurate measurements are possible for this type of defect. This is not the case for the shrinkage porosity related initiation sites as discussed earlier in this section. If this model is reasonably correct then it appears from Figure 5.10 (a) that in general the size of shrinkage porosity defects were underestimated as most points fall to the right of the 1:1 line.

The second reason for this may be the crack like nature of the oxide films. The folded film defect is very thin and therefore defines a crack with a thickness in the sub-micron range. The small crack radius will make it an excellent initiator, equivalent to the effect of an existing fatigue crack. This explains the absence of initiation time and the oxide data points falling close to the predictions made by the model. Conversely, when considering the geometry of a shrinkage pore with rounded cavities extending among dendrites, the radius of the existing crack is now roughly half of the residual interdendritic spacing, (in this case in the range of 15-20μm). While still a favourable site for crack initiation, some amount of time for crack nucleation is required. Once again this theory is supported by the fact that most of the shrinkage porosity related points fall to the right of the 1:1 line.

The experimental results now plotted with the above model (solid line) are shown in Figure 5.11 (a) and (b). Once again (a) displaying all initiation site types and (b) showing only oxide film defects.

Chapter 6

CONCLUSIONS

1. Staircase fatigue samples taken from production castings failed from fatigue cracks nucleated from shrinkage pore networks. Samples with the shortest lives were found to have old oxides associated with the initiation site pore networks. Young oxides were not observed in these samples, as the damaging action of fully reversed stress regime (R = -1) most probably rendered these films unobservable.

2. In-mould filters do not completely prevent oxide films in the final casting. Surface turbulence of the liquid metal after the filters and movement of trapped air (bubble trails) both contribute to film production.

3. The use of in-mould filters increases the reliability of ultimate strength by reducing the probability of a sample containing large oxide films. Samples exhibiting the lowest strengths revealed oxide film defects on the fracture surface. The filtered samples had a Weibull modulus 2.4 times that of the unfiltered data samples.

4. The load limit model does not sufficiently describe the negative effects of oxide films on strength. Oxide films have approximately 5 times greater effect on strength than that predicted by reduction in cross sectional area.

5. Oxide films act as cracks and reduce the fracture strength of cast aluminum samples. A model based on linear elastic fracture mechanics (LEFM) is capable of predicting the fracture strength of castings containing these defects.

6. The proposed LEFM crack growth model is successful in calculating fatigue crack propagation lives. The model was particularly accurate in predicting the fatigue life of samples where cracks initiated at oxide films. The main reason for this is because oxide films act as ideal cracks. Possessing a very small crack tip radius and crack-like geometry, they are

essentially preformed fatigue cracks. As a result there is an absence of fatigue crack nucleation time, explaining the correlation of predicted propagation life to actual fatigue life.

7. Fatigue life was adversely affected by the presence of the filters. In the current mould design, the filters restricted the feeding of the test bars. This resulted in an average of 10% larger shrinkage pores compared with the unfiltered samples. Consequently with respect to the shrinkage initiated samples, the filtered samples had an average of 31% shorter fatigue lives.

8. The small group of samples with high fatigue lives indicates the potential fatigue performance of the alloy. The lives in this group are an order of magnitude greater than 90% of the fatigue samples tested. The fact that the studied production alloy contains significant levels of impurities did not detract from its fatigue performance. There were no cases of fatigue initiating from iron rich intermetallics and only one case where fatigue initiated from a eutectic silicon particle. This indicates that there is a hierarchy of favourable fatigue initiation sites that ranks porosity and oxide film defects foremost in importance.

Chapter 7

RECOMMENDATIONS FOR FUTURE WORK

1. The potential of the remelt reduced pressure test for investigating oxide films has been demonstrated. Further investigations into defining the optimum parameters for given casting conditions would assist in making the test even more useful. The technique could be developed into an industrial instrument to quantify oxide films in commercial castings or for use in quantifying the quality of incoming ingot.

2. For the casting producer it is clear that almost any size oxide defect has the potential to be dangerous from a fatigue crack initiation aspect. Even with careful metal handling and mould filling some amount oxide films will be generated. Conventional fluxing treatments and filtration methods are not sufficient at eliminating these films. New approaches to remove oxide films, perhaps based nontraditional methods would be a boon to the metal caster.

3. From this work the damaging effects of oxide films on fracture strength and fatigue life of Al-Si-Cu-Mg castings was shown. It would be beneficial to extend this work to other aluminum alloy systems. In particular alloys having a range of magnesium levels enabling the study of the effects of different types of oxide films. Suggested candidates include the Al-Mg, Al-Zn-Mg and the high strength Al-Cu classes of alloys.

REFERENCES

Abernethy Robert, B. (1993). The new Weibull handbook. North Palm Beach, Fla., Robert B. Abernethy 1993**:** 1-5.

Agema, K. and D. Fray (1989). Preliminary investigations on the deformation behaviour of an oxide scale on molten aluminium. Cambridge, U.K., Department of Materials Science and Metallurgy, University of Cambridge.

Anderson, T. L. (1995). Fracture mechanics : fundamentals and applications. Boca Raton ; London, CRC Press c1995.

Anson, J. P. and J. E. Gruzleski (1999a). "Effect of Hydrogen Content on Relative Shrinkage and Gas Microporosity in Al-7% Si Casting (99-26)." AFS Transactions(107): 135-142.

Anson, J. P. and J. E. Gruzleski (1999b). "The Quantitative Discrimination between Shrinkage and Gas Microporosity in Cast Aluminum Alloys Using Spatial Data Analysis - Metallographic observations." Materials Characterization **43**(5): 319-335.

Argo, D. and J. E. Gruzleski (1988). "Porosity in modified aluminum alloy castings." AFS Transactions **96**: 65-74.

Armitage, P. H. (1961). "Statistical aspects of fatigue." Metallurgical Reviews **6(**No.23): 353-385.

Bäckerud, L., G. Chai, et al. (1990). Solidification Characteristics of Aluminum Alloys, Foundry Alloys, AFS/Skanaluminium.

Bäckerud, L., P. Gustafson, et al. (1991). Aluminium **67**: 910.

Bailey, W. A. (1965). "How solidification affects fatigue of 356 aluminum alloy." Foundry.

Balicki, S. and J. Leitl (1959). Prace Instytutow Hutniczych **11**(2): 71-74.

Bian, X., Z. Zhang, et al. (2000). "Effect of Strontium Modification on Hydrogen Content and Porosity Shape of Al-Si Alloys." Materials Science Forum **331/337**(1): 361-366.

Boileau, J., J. Allison, et al. (1998). The Effect of Solidification Time and Heat Treatment on the Tensile and Fatigue Properties of a Cast 319 Aluminum Alloy. American Foundrymen's Society; Molten aluminum processing, Orlando, FL, AFS.

Boileau, J., S. J. Weber, et al. (2001). "The effect of porosity size on the tensile properties of cast 319-T7 aluminum alloy." AFS Transactions **109**: 187-200.

Borrego, L. P., J. M. Ferreira, et al. (2001). "Fatigue crack growth and crack closure in an AlMgSi alloy." Fatigue and Fracture of Engineering Materials and Structures **24**(4): 255-266.

Brondyke, K. J. and P. D. Hess (1964). "Intrepretation of vacuum gas test results for aluminum alloys." Transactions of TMS AIME **230**: 1542-1546.

Brownlee, K. A., J. L. Hodges, et al. (1953). "The up-and-down method with small samples." Journal of the American Statistical Association **48**(262): 262-277.

Byczynski, G. E. and D. A. Cusinato (2002). "The effects of strontium and grain refiner additions on the fatigue and tensile properties of industrial Al-Si-Cu-Mg alloy castings produced using the Ford Motor Company - Cosworth precision sand process." International Journal of Cast Metals Research **14**(5): 315-324.

Caceres, C. H. (1995). "On the effect of macroporosity on the tensile properties of the Al-7%Si-0.4%Mg casting alloy." Scripta Metallurgica et Materialia **32**(11): 1851-1856.

Caceres, C. H., M. B. Djurdjevic, et al. (1999). "The Effect of Cu Content on the Level of Microporosity in Al-Si-Cu-Mg Casting Alloys." Scripta Materialia **40**(5): 631-638.

Caceres, C. H. and B. I. Selling (1996). "Casting defects and the tensile properties of an Al-Si-Mg alloy." Materials Science and Engineering **220**(1/2): 109-116.

Campbell, J. (1968). Transactions of the Metallurgical Society of AIME **242**: 264.

Campbell, J. (1981). Production of high-technology aluminium-alloy castings. Engineering Magazine. **March**.

Campbell, J. (1991). Castings. Oxford, Butterworth-Heinemann.

Campbell, J. (1996). The origin of porosity in castings. Asian foundry congress, Upper Mount Gravatt.

Campbell, J. (2001). The entrainment defect: The new metallurgy. ASM International Aluminum Casting Technology Symposium, Ohio.

Caton, M. J. (2001). Predicting fatigue properties of cast Al by characterizing small-crack propagation behavior. Department of Materials Science and Engineering, University of Michigan.

Caton, M. J., J. W. Jones, et al. (1999). "The Effect of Solidification Rate on the Growth of Small Fatigue Cracks in a Cast 319-Type Aluminum Alloy." Metallurgical and Materials Transactions A **30**(12): 3055-3068.

Chien, K. H., T. Z. Kattamis, et al. (1973). "Cast microstructure and fatigue behavior of a high strength aluminum alloy (KO-1)." Metallurgical Transactions **4**(April).

Cibula, A. (1951). Journal of the Institute of Metals **80**: 1-16.

Cochran, C. N., D. L. Belitskus, et al. (1977). "Oxidation of aluminum-magnesium melst in air, oxygen, flue gas and carbon dioxide." Metallurgical Transactions B **8B**(June): 323-332.

Couper, M. J., A. E. Neeson, et al. (1990). "Casting defects and the fatigue behaviour of an aluminium casting alloy." Fatigue and Fracture of Engineering Materials and Structures **13**(3): 213-227.

Crepeau, P. N. (1995a). "Effect of Iron in Al-Si Casting Alloys: A Critical Review." AFS Transactions(103): 361-366.

Crepeau, P. N. (1995b). Molten Aluminum Contamination: Gas, Inclusions and Dross. Molten aluminium processing, Orlando; FL, AFS.

Crossley, F. A. and L. F. Mondolfo (1951). Transactions of AIME, (Journal of Metals) **191**: 1143-1151.

Davidson, C. J., J. R. Griffiths, et al. (2002). "The effect of solution heat-treatment time on the fatigue properties of an Al-Si-Mg casting alloy." Fatigue and Fracture of Engineering Materials and Structures **25**(2): 223-230.

DeJack, M. (2000). Ford Motor Company, Personal Communication. G. E. Byczynski. Dearborn, MI, USA.

Denton, J. R. and J. A. Spittle (1985). "Solidification and susceptibility to hydrogen absorption of Al-Si alloys containing strontium." Materials Science Technology **1**: 305-311.

Dieter, G. E. (1986). Mechanical metallurgy. New York, McGraw-Hill c1986.

Dignam, M. J. (1962). "Oxide films on aluminum." Journal of the Electrochemical Society **109**(3): 184-198.

Dimaguga, F. C. (1988). "The degassing and regassing behavior of Sr modified A356 melts." AFS Transactions **96**: 83-88.

Divandari, M. and J. Campbell (1999). The mechanism of bubble damage in castings. 1st international Conference on Gating, Filling and Feeding of Aluminum Castings., Nashville, Tennessee, AFS.

Divandari, M. and J. Campbell (2000). "A new technique for the study of aluminum oxide films." Aluminium Transactions **2**(2): 233-238.

Divandari, M. and J. Campbell (2001). "Mechanisms of bubble trail formation in castings." AFS Transactions **109**: 203-212.

Dixon, W. J. and A. M. Mood (1948). "A method for obtaining and analyzing sensitivity data." Journal of the American Statistical Association **43**(241): 109-126.

Eady, J. A. and D. M. Smith (1986). "Effect of porosity on the tensile properties of aluminium castings." Materials Forum **9**(4): 217-223.

Edwards, J., R. G. Warwick, et al. (1989). An examination of the CEGB's R6 procedure for the assessment of the integrity of structures containing defects. Report of the ACSNI Study Group on the R6 methodology. London, U.K., Health & Safety Commission.

Elber, W. (1970). "Fatigue crack closure under cyclic tension." Engineering Fracture Mechanics **2**: 37-45.

Emadi, D., J. E. Gruzleski, et al. (1993). "The effect of Na and Sr modification on surface tension and volumetric shrinkage of A356 alloy and their influence on porosity formation." Metallurgical Transactions B **24B**: 1055-1063.

Fang, Q. T. and D. A. Granger (1989). "Porosity formation in modified and unmodified A356 alloy castings." AFS Transactions **97**: 989-1000.

Fisher, J. C. (1948). "The Fracture of Liquids." Journal of Applied Physics **19**: 1062-1067.

Fisher, R. A. and L. H. C. Tippett (1928). "Limiting form of the frequency distribution of the largest and smallest member of a sample." Proceedings of the Cambridge Philosophical Society **24**: 180.

Fox, S. and J. Campbell (2000). "Visualisation of oxide film defects during solidification of aluminium alloys." Scripta Materialia **43**(10): 881-886.

Freudenthal, A. M. (1946). "The statistical aspect of fatigue of materials." Proceedings of the Royal Society of London. Series A, Mathematical and Physical Sciences **187**(1011): 416-429.

Freudenthal, A. M. and E. J. Gumbel (1953). "On the statistical interpretation of fatigue tests." Proceedings of the Royal Society of London. Series A, Mathematical and Physical Sciences **216**(1126): 309-332.

Freudenthal, A. M. and E. J. Gumbel (1954). "Minimum life in fatigue." Journal of the American Statistical Association **49**(267): 575-597.

Fuoco, R., E. R. Correa, et al. (1999). "Characterization of Some Types of Oxide Inclusions in Aluminum Alloy Castings (99-85)." AFS Transactions(107): 287-294.

Gall, K., N. Yang, et al. (1999). "The Debonding and Fracture of Si Particles during the Fatigue of a Cast Al-Si Alloy." Metallurgical and Materials Transactions A **30**(12): 3079-3088.

Garat, M., S. Jacob, et al. (1992). "The state of the art of the use of antimony, sodium and strontium modified aluminum silicon casting alloys." AFS Transactions **100**: 821-832.

Green, N. R. and J. Campbell (1993). "Statistical distributions of fracture strengths of cast Al-7Si-Mg alloy." Materials Science and Engineering **A173**: 261-266.

Green, N. R. and J. Campbell (1995). "Influence of Oxide Film Filling Defects on the Strength of Al-7Si-Mg Alloy Castings." AFS Transactions(102): 341-348.

Griffith, A. A. (1920). Philisophical Transactions **Series A**(221): 163-198.

Gruzleski, J. E. (1984). "The art and science of modification: 25 years of progress." AFS Transactions **92**: 673-683.

Gruzleski, J. E. and B. M. Closset (1990). The treatment of liquid aluminum-silicon alloys. Des Plaines, Ill., American Foundrymen's Society.

Gupta, A. K., B. K. Saxena, et al. (1992). "Review - Pore Formation in Cast Metals and Alloys." Journal of Materials Science **27**: 853-862.

Haginoya, I. and T. Fukusako (1983). "Oxidation of molten Al-Mg alloys." Transactions of the Japan Institute of Metals **24**(9): 613-619.

Herrera, A. and V. Kondic (1977). Proc. Int. Conf. on Solidification and Cast Metals, Sheffield.

Impey, S. A., D. J. Stephenson, et al. (1988). "Mechanism of scale growth on liquid aluminium." Materials Science and Technology **4**(December): 1126-1132.

Impey, S. A., D. J. Stephenson, et al. (1991). A study of the effect of magnesium additions on the oxide growth morphologies on liquid aluminium alloys. First International conference on microscopy of oxidation, Univeristy of Cambridge.

Irwin, G. R. (1948). Fracturing of Metals, ASM: 147-166.

Irwin, G. R. (1956). Sagmore Research Conference Proceedings.

Irwin, G. R. (1957). "Analysis of stresses and strains near the end of a crack traversing a plate." Trans. ASME, J.Appl.Mech. **24**: 361-364.

Jiang, H., P. Bowen, et al. (1999). "Fatigue performance of a cast aluminium alloy AI-7Si-Mg with surface defects." Journal of Materials Science **34**(4): 719-726.

Johnsson, M., L. Backerud, et al. (1993). "Study of the Mechanism of Grain Refinement of Aluminum after Additions of Ti- and B-Containing Master Alloys." Metallurgical Transactions A **24**(2): 481.

Jones, G. P. (1985). Proceedings of the International Seminar on Refining and Alloying of Liquid Aluminum and Ferro-alloys, Trondheim, Norway.

Jones, G. P. (1987). Solidification Processing. London, The Institute of Metals**:** 496-499.

Jorstad, J. L. (1986). An overview of the need for melt cleanliness control. International molten aluminum processing, City of Industry; CA, Des Plaines IL.

Jorstad, J. L., D. L. Zalensas, et al. (1993). Aluminum casting technology. Des Plaines, Ill., American Foundrymen's Society c1993.

Kahl, W. and E. Fromm (1985). Metallurgical Transactions B **16B**: 47-51.

Kahl, W., S. B. Yaneva, et al. (1984). Giesereiforschung **36**(3): 79-84.

Kanicki, D. P. (1994). "Changing Casting Demands Shape Ford's New Foundry." Modern Casting **84**(9): 24.

Knott, J. F. (1984). Models of Fatigue Crack Growth. Fatigue Crack Growth, Cambridge, U.K., Pergamon Press.

Knott, J. F. (1998a). The science and engineering of fracture. Fracture : a topical encyclopedia of current knowledge. G. P. Cherepanov. Malabar, Fla, Krieger Pub. Co 1998**:** 290-315.

Knott, J. F., P. Bowen, et al. (2000). "Plenary - The Structural Integrity of Cast Aluminium Automotive Components Subjected to Fatigue Loads." Materials Science Forum **331/337**(3): 1401-1412.

Knott, J. F. and P. A. Withey (1998b). Fracture mechanics : worked examples. London, Institute of Materials 1998.

Kordes, E. (1935). Z.Kristallogr. **91**: 193.

Kujawski, D. (2001). "Enhanced model of partial crack closure for correlation of R-ratio effects in aluminum alloys." International Journal of Fatigue **23**(2): 95-102.

Laird, C. (1979). Mechanisms and theories of fatigue. Fatigue and Microstructure. Metals Park, Ohio, American Society for Metals**:** 149-203.

Lakshmanan, A. N., S. G. Shabestari, et al. (1995). "Microstructure Control of Iron Intermetallics in Al-Si Casting Alloys." Zeitschrift Fur Metallkunde **86**(7): 457.

Latzko, D. G. H. (1984). Post-yield fracture mechanics. London, Elsevier Applied Science c1984.

Lee, F. T., J. F. Major, et al. (1995a). "Effect of Silicon Particles on the Fatigue Crack Growth Characteristics of Al-12 Wt Pct Si-0.35 Wt Pct Mg-(0 to 0.02) Wt Pct Sr Casting Alloys." Metallurgical and Materials Transactions A **26**(6): 1553.

Lee, F. T., J. F. Major, et al. (1995b). "Fracture Behaviour of Al 12wt.%Si 0.35wt.%Mg(0-0.02)wt.%Sr Casting Alloys Under Fatigue Testing." Fatigue and Fracture of Engineering Materials and Structures **18**(3): 385.

Lee, F. T., J. F. Major, et al. (1996). "Fatigue Crack Growth and Fracture Behavior of Al-12 Wt% Si-0.35 Wt% Mg (0-0.02) Wt% Sr Casting Alloys." AFS Transactions(104): 785-796.

Lessiter, M. (2000). Engineered Cast Components for the Automotive Industry. Engineered Cast Solutions. **Fall:** 37-40.

Lin, S. K., Y. L. Lee, et al. (2001). "Evaluation of the staircase and the accelerated test methods for fatigue limit distributions." International Journal of Fatigue **23**(1): 75-83.

Lu, S. Z. and A. Hellawell (1987). "The mechanism of silicon modification in aluminum-silicon alloys:impurity induced twinning." Metallurgical Transactions A **18A**: 1721-1733.

Lund, J. R. and J. P. Byrne (2000). "Leonardo da Vinci's tensile strength tests: implications for the discovery of engineering mechanics." Civil Eng. and Env. Syst. **00**: 1-8.

Mal'tsev, M. V., I. D. Chistiakov, et al. (1956). Bulletin Academy Sciences USSR **Physics Series**: 747-750.

McLellan, D. L. and M. M. McLellan (1996). "An Approach to Fatigue Design for Aluminum Castings." AFS Transactions(104): 445-450.

Mocarski, S. J., G. V. Scarich, et al. (1991). "Effect of hot isostatic pressure on cast aluminum airframe components." AFS Transactions: 77-81.

Mohanty, P. S. and J. E. Gruzleski (1995). "Mechanism of grain refinement in aluminium." Acta Metallurgica et Materialia **43**(5): 2001.

Muller-Stock, H. (1938). Mitt. Kohle Eisenforsch. GmbH **8**: 83-107.

Narayanan, L. A., F. H. Samuel, et al. (1994). "Crystallization Behavior of Iron-Containing Intermetallic Compounds in 319 Aluminum Alloy." Metallurgical and Materials Transactions A **25**(8): 1761.

Narayanan, L. A., F. H. Samuel, et al. (1995). "Dissolution of Iron Intermetallics in Al-Si Alloys through Nonequilibrium Heat Treatment." Metallurgical and Materials Transactions A **26**(8): 2161.

Nyahumwa, C., N. R. Green, et al. (1998a). "The Concept of the Fatigue Potential of Cast Alloys." Journal of the Mechanical Behavior of Materials **9**(4): 227-236.

Nyahumwa, C., N. R. Green, et al. (1998b). "Effect of Mold-Filling Turbulence on Fatigue Properties of Cast Aluminum Alloys (98-58)." AFS Transactions(106): 215-224.

Nyahumwa, C., N. R. Green, et al. (2001). "Influence of Casting Technique and Hot Isostatic Pressing on the Fatigue of an Al-7Si-Mg Alloy." Metallurgical and Materials Transactions A **32**(2): 349-358.

Otte, M. O., S. D. McDonald, et al. (1999). "Controlling Porosity-Related Casting Rejects: Understanding the Role of Iron in Al-Si Alloys (99-112)." AFS Transactions(107): 471-478.

Ozelton, M. W., S. J. Mocarski, et al. (1991). Durability and damage tolerance of aluminum castings. WL-TR-91-4111, Oct.

Pacz, A. (1921). U.S. Patent #1387900.

Paris, P. and F. Erdogan (1963). "A critical analysis of crack propagation laws." Journal of Basic Engineering, Transactions of the ASME(December): 528-534.

Plummer, M. (1958). "The formation of metastable aluminas at high temperatures." Journal of Applied Chemistry **8**(January): 35-49.

Rading, G. O., J. Li, et al. (1995). "Fatigue Crack Growth in Cast Al-Cu Alloy A206 With Different Levels of Porosity." AFS Transactions(102): 57-62.

Ritchie, R. O. (1979). "Near threshold fatigue crack propagation in steels." International Metals Review **24**(Review # 245): 205-230.

Rooy, E. L. (1993). AFS Transactions **101**: 961-964.

Roy, N., P. R. Louchez, et al. (1996a). "Statistical analysis of porosity in Al-9wt%Si-3wt%Cu-X alloys systems." Journal of Material Science **31**: 4725-4740.

Roy, N., A. M. Samuel, et al. (1996b). "Porosity Formation in Al-9 Wt Pct Si-3 Wt Pct Cu Alloy Systems: Metallographic Observations." Metallurgical and Materials Transactions A **27**(2): 415-430.

Samuel, F. H., A. M. Samuel, et al. (1996). Factors Controlling the Type and Morphology of Cu-Containing Phases in 319 Al Alloy (96-30). Casting, Philadelphia; PA, American Foundrymen's Society.

Schijve, J. (1993). "A normal distribution or a Weibull distribution for fatigue lives." Fatigue and Fracture of Engineering Materials and Structures **16**(8): 851-859.

Shahani, H. and H. Fredriksson (1985). "On the Mechanism of Precipitation of Pores in Melts." Scandinavian Journal of Metallurgy **14**: 316-320.

Shamsuzzoha, M., L. M. Hogan, et al. (1993). "Effects of Modifying Agents on Crystallography and Growth of Silicon Phase in Al-Si Casting Alloys." AFS Transactions(101): 999.

Shigley, J. E. and C. R. Mischke (1986). Standard handbook of machine design. New York, McGraw-Hill c1986**:** Paragraph 13-1.

Sigworth, G. K. (1993). AFS Transactions **101**: 541-548.

Sigworth, G. K. (1996). "Communication on mechanism of grain refinement in aluminum." Scripta Materialia **34**: 919-922.

Silva, M. P. and D. E. J. Talbot (1989). "Oxidation of liquid aluminum - magnesium alloys." Light Metals, edited by P.G. Campbell (The Minerals, Metals & Materials Society): 1035-1040.

Simensen, C. J. and G. Berg (1980). "A survey of inclusions in aluminum." Aluminium **56**: 335-340.

Skallerud, B., T. Iveland, et al. (1993). "Fatigue life assessment of aluminum alloys with casting defects." Engineering Fracture Mechanics **44**(6): 857.

Sleppy, W. C. (1961). "Oxidation of molten high-purity aluminum in dry oxygen." Journal of the Electrochemical Society **108**(12): 1097-1102.

Stanzl-Tschegg, S. E., H. R. Mayer, et al. (1995). "Fatigue and fatigue crack propagation in AlSi7Mg cast alloys under in-service loading conditions." International Journal of Fatigue **17**(2): 149.

Stucky, M. and M. Richard (1998). Degassing or Deoxidizing? American Foundrymen's Society; Molten aluminum processing, Orlando, FL, AFS.

Surappa, M. K., E. Blank, et al. (1986). "Effect of macro-porosity on the strength and ductility of cast Al-7Si-0.3Mg alloy." Scripta Metallurgica **20**: 1281-1286.

Suresh, S. and R. O. Ritchie (1984). "Propagation of short fatigue cracks." International Metals Reviews **29**: 445-476.

Tan, Y. H., S. L. Lee, et al. (1995). "Effects of Be and Fe content on plane strain fracture toughness in A357 alloys." Metallurgical and Materials Transactions A **26A**: 2937-2945.

Taylor, J. A. (1995). "Metal-related castability effects in aluminium foundry alloys." Cast Metals **8**(4): 225-252.

Thiele, W. (1962). Aluminium **38(**11,12): 707-715, 780-786.

Ting, J. C. and F. V. Lawrence (1993). "Modeling the long-life fatigue behavior of a cast aluminum alloy." Fatigue and Fracture of Engineering Materials and Structures **16**(6): 631.

Turner, C. E. (1984). Methods for post-yield fracture safety assessment. Post-Yield Fracture Mechanics. D. G. H. Latzko. London, Elsevier Applied Science c1984**:** 31-33.

Tynelius, K. and J. F. Major (1993). "A Parametric Study of Microporosity in the A356 Casting Alloy System." AFS Transactions(101): 401.

Vader, M. and J. Noordegraaf (1989). "New approach to grain refining." Light Metals, Metallurgical Society of AIME: 937-941.

Wakefield, G. R. and R. M. Sharp (1992). "Fatigue properties of hot isostatically pressed Al-10Mg castings." Materials Science and Technology **8**(12): 1125.

Wang, Q. G., D. Apelian, et al. (2001a). "Fatigue behavior of A356/357 aluminum cast alloys. Part II - Effect of microstructural constituents." Journal of Light Metals **1**(1): 85-97.

Wang, Q. G., D. Apelian, et al. (2001b). "Fatigue behavior of A356-T6 aluminum cast alloys. Part I. Effect of casting defects." Journal of Light Metals **1**(1): 73-84.

Weaver_Engineering (2002). http://www.weavereng.com/Statistics_Detail.htm.

Weibull, W. (1939a). "The phenomenon of rupture in solids." Ing. Vetenskaps Akad. Handl. **153**.

Weibull, W. (1939b). "A statistical theory of the strength of materials." Ing. Vetenskaps Akad. Handl. **151**.

Weibull, W. (1949). K.tekn. Högsk. Handl. **27**.

Weibull, W. (1951). "A statistical distribution of wide applicability." Journal of Applied Mechanics **18**: 293-297.

Whittenberger, E. J. and F. N. Rhines (1952). "Origin of Porosity in Castings of Magnesium-Aluminum and other alloys." Journal of Metals, Transactions of AIME **4**(4): 409-420.

Wickberg, A., G. Gustafsson, et al. (1985). "Microstructural effects on the fatigue properties of a cast Al7SiMg alloy." SAE Transactions(Paper #840121): 1.728-1.735.

Wigant, C. C. and R. I. Stephens (1987). "Fatigue crack growth behaviour of A356-T6 cast aluminum alloy." Fatigue '87 **1**: 165-173.

Wightman, G. and D. J. Fray (1983). "The dynamic oxidation of aluminum and its alloys." Metallurgical Transactions B **14B**(December): 625-631.

Wiltshire and J. F. Knott (1981). The fracture toughness of high strength engineering alloys containing short cracks. 5th International Congress on Fracture, Cannes, Pergamon.

Wirsching, P. H. (1983). Statistical summaries of fatigue data for design purposes, NASA contractor report**:** 3697, N83-29731.

Youdelis, W. V. (1979). "Nucleation entropy and grain refinement of alloys." Metal Science **13**: 540-543.

Youdelis, W. V. and C. S. Yang (1980). "Non-peritectic grain refinement of aluminium by titanium." Aluminium **56**: 411-413.

Zhang, B., D. R. Poirier, et al. (1999). "Microstructural Effects on High-Cycle Fatigue-Crack Initiation in A356.2 Casting Alloy." Metallurgical and Materials Transactions A **30**(10): 2659-2666.

Zhang, J. and D. B. Kececioglu (1998). New Approaches to Determine the Endurance Strength Distribution. Reliability and quality in design, Washington, DC, Issat.

FIGURES

Chapter 2 FIGURES

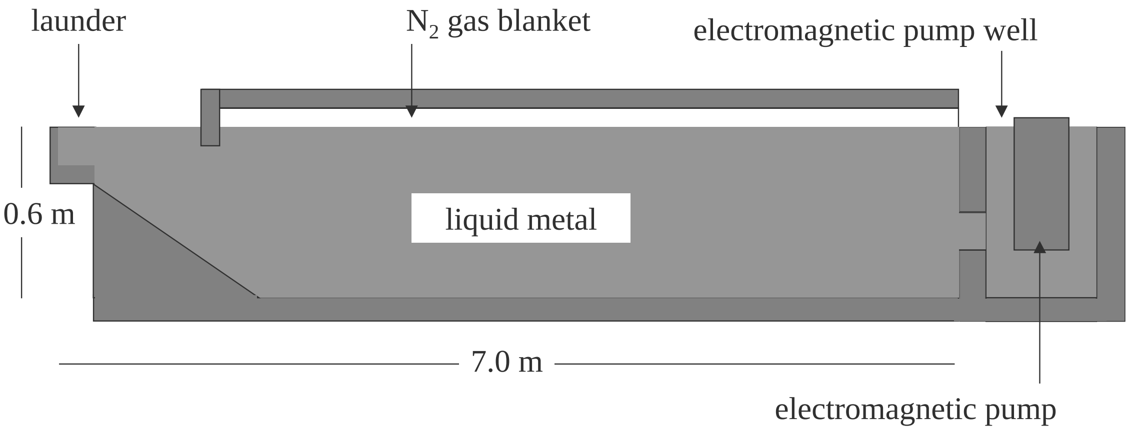

Figure 2.1 Schematic of holding furnace used in the Ford Cosworth Precision Sand Process

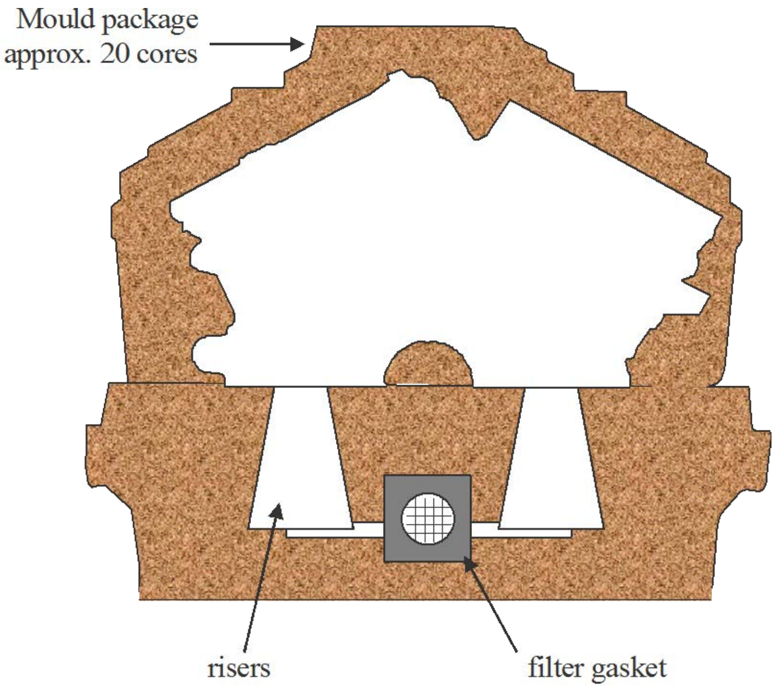

Figure 2.2 Simplified schematic of a V6 mould package (internal cores not shown)

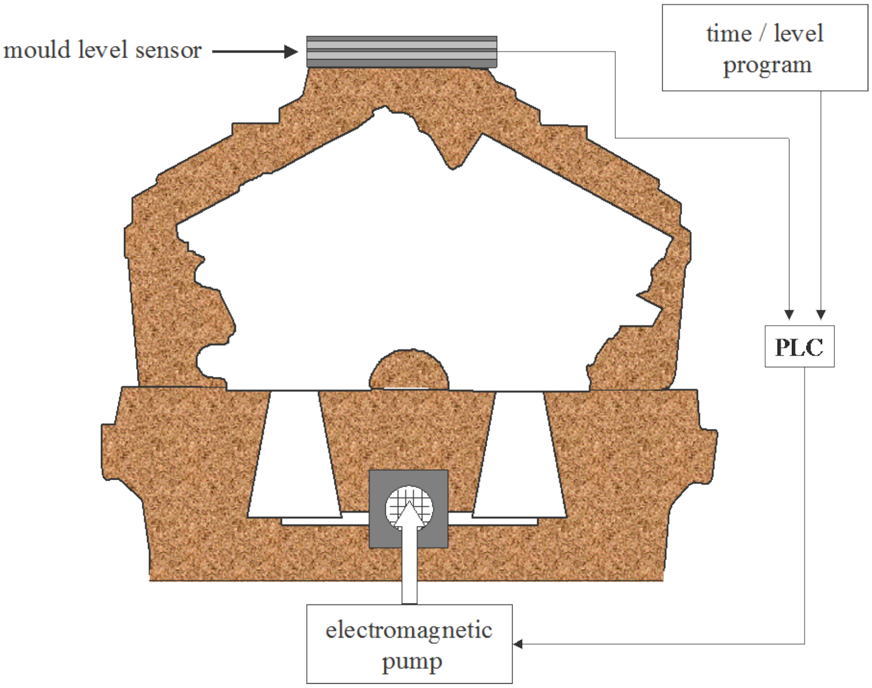

Figure 2.3 As Figure 2.2, showing input and output of mould filling programmable logic controller

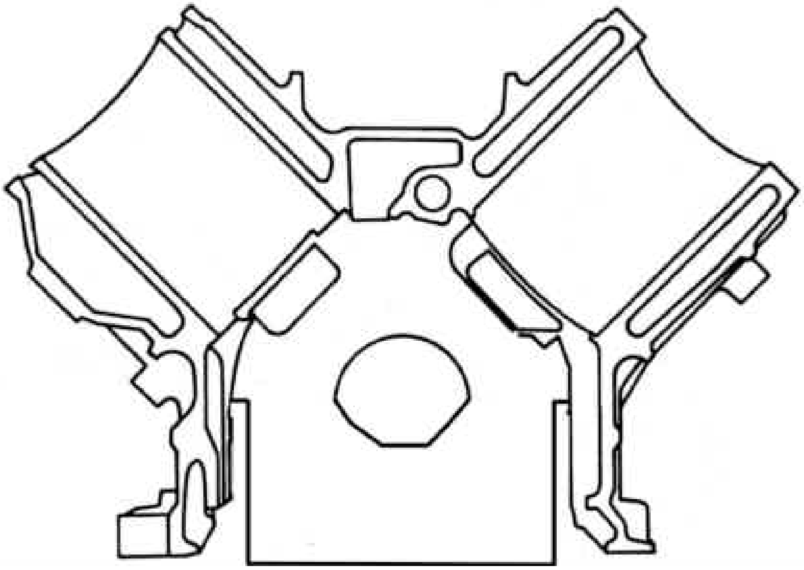

Figure 2.4 Schematic of sectioned V8 cylinder block showing location of feeder (in pre-rollover mould filling orientation)

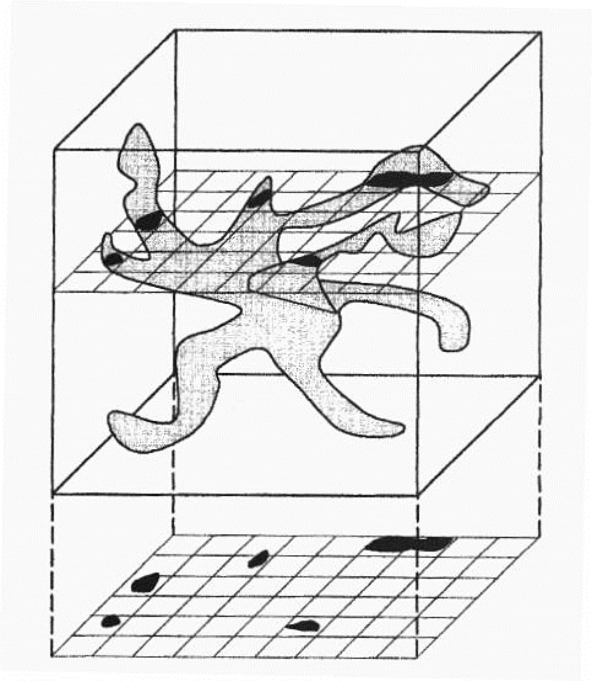

Figure 2.5 Schematic showing the projected pore area of a cross section taken through a shrinkage pore (Anson 1999b)

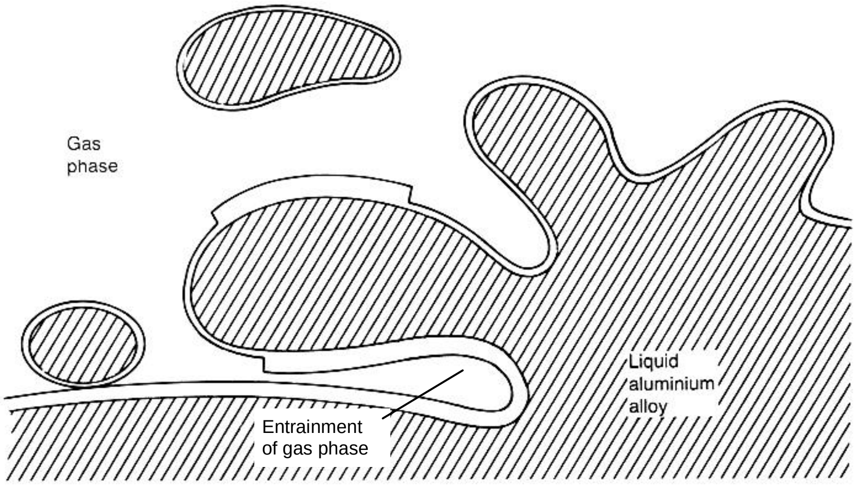

Figure 2.6 Schematic of entrainment mechanism in liquid aluminum note oxide thickness

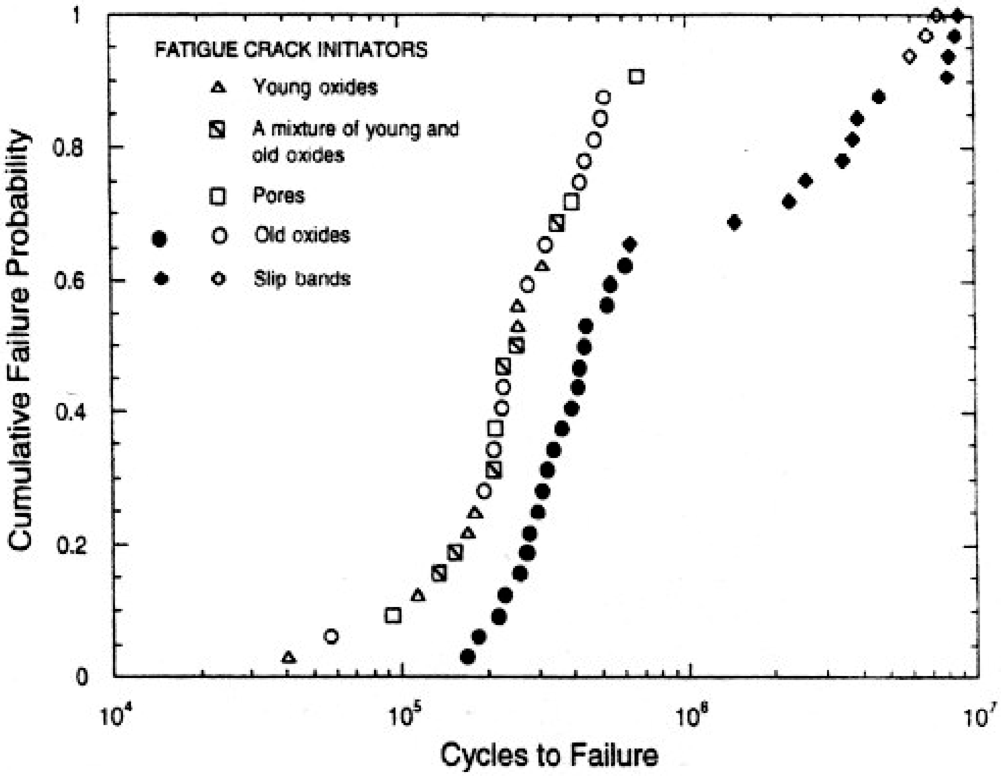

Figure 2.7 Cumulative failure probability of fatigue life for various fatigue crack initiation sites from Nyahumwa (1998a), open symbols are unfiltered castings, solid symbols are filtered castings

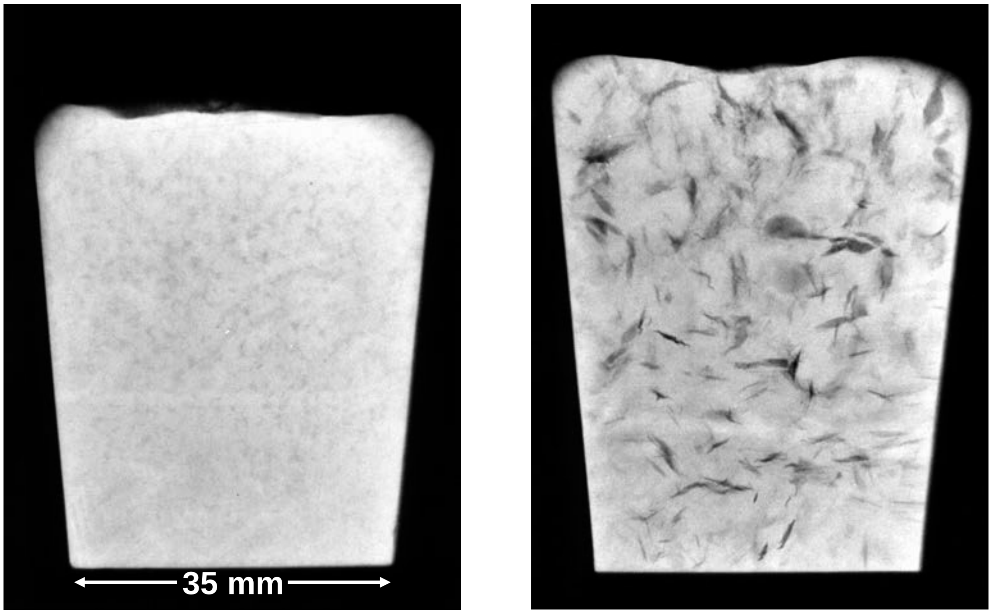

(a) (b)

Figure 2.8 X-ray radiographs of reduced pressure tests in Al-7Si-0.4Mg alloy (a) is solidified at 100,000 Pa (1 bar), (b) is solidified at 1000 Pa (0.01 bar) pressure from (Fox 2000)

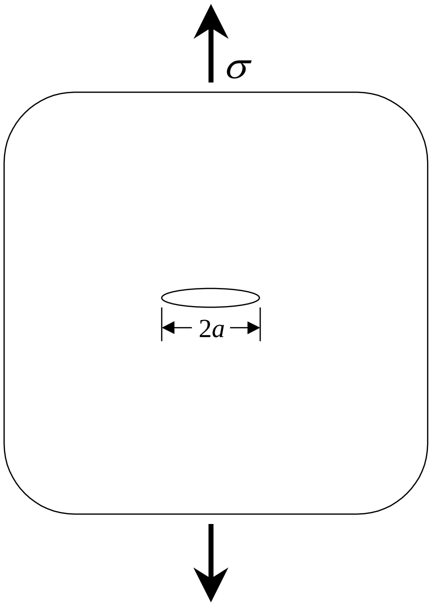

Figure 2.9 Through thickness crack in an infinite plate subject to a remote tensile stress

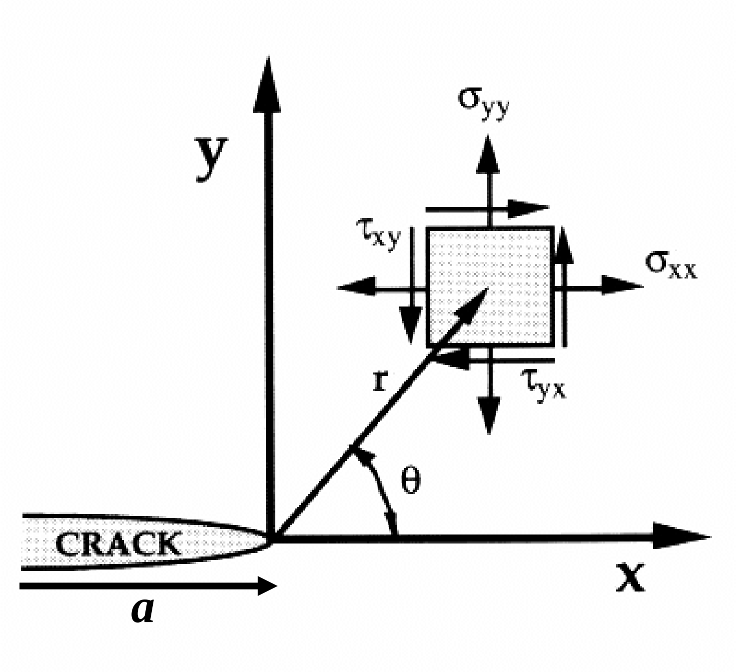

Figure 2.10 Stresses near the tip of a crack in an elastic material, modified from (Anderson 1995)

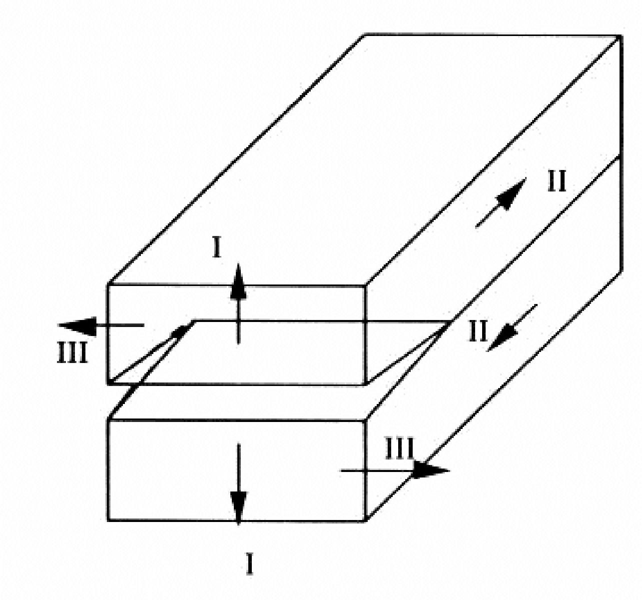

Figure 2.11 Diagram showing the three types of opening modes: I tensile, II plane shear, and III antiplane shear (Knott 1998b)

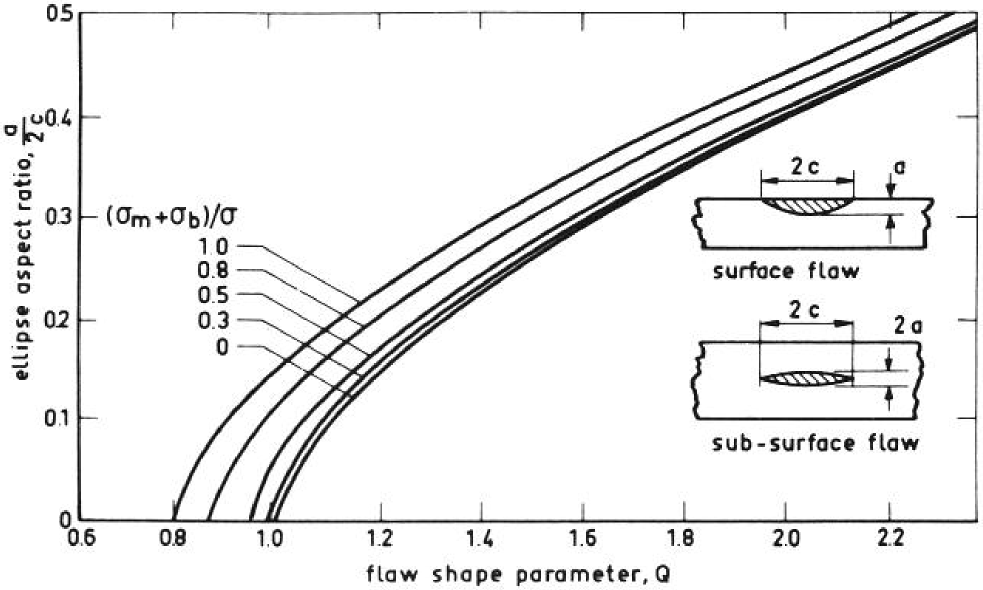

Figure 2.12 Flaw shape parameter curves (ASME 1983)

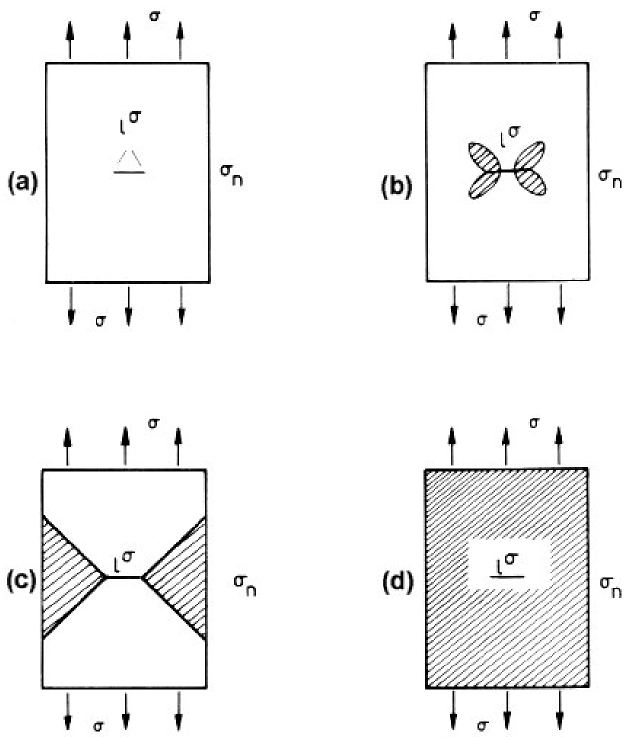

Figure 2.13 Schematic of increasing degrees of yielding: (a) LEFM no yield (b) contained yield (c) gross yield (d) general yield (Turner 1984)

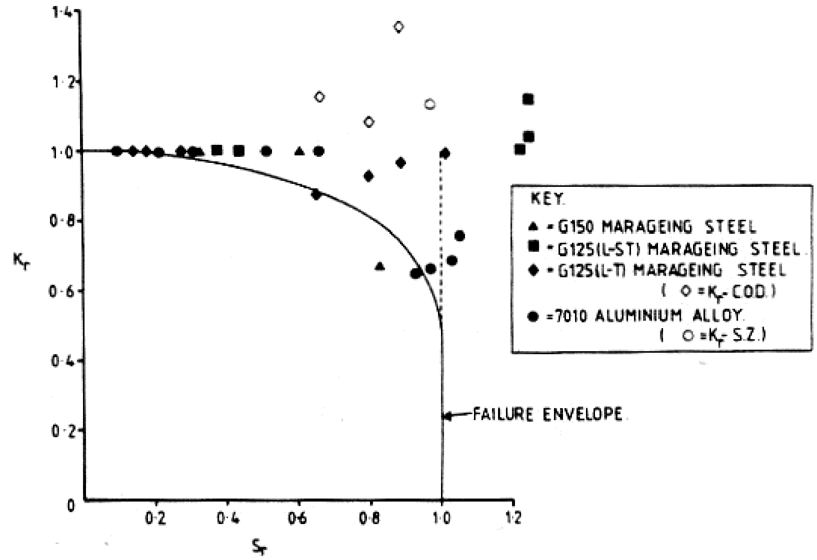

Figure 2.14 Central Electricity Generating Board R6 diagram, showing values for 7010 aluminum alloy (solid circles) (Wiltshire 1981)

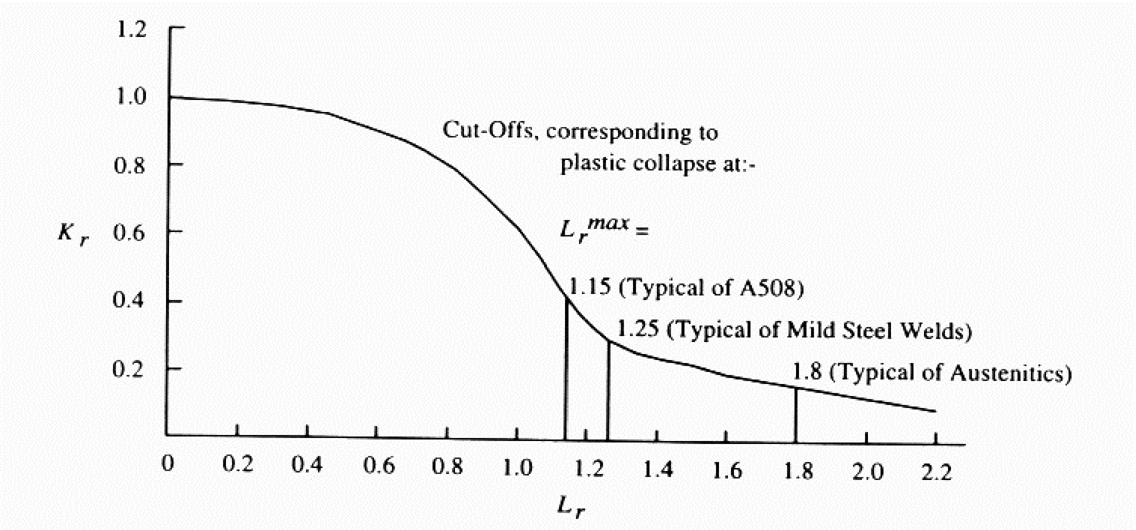

Figure 2.15 Revised R6 diagram showing materials with different strain hardening characteristics (Knott 1998b)

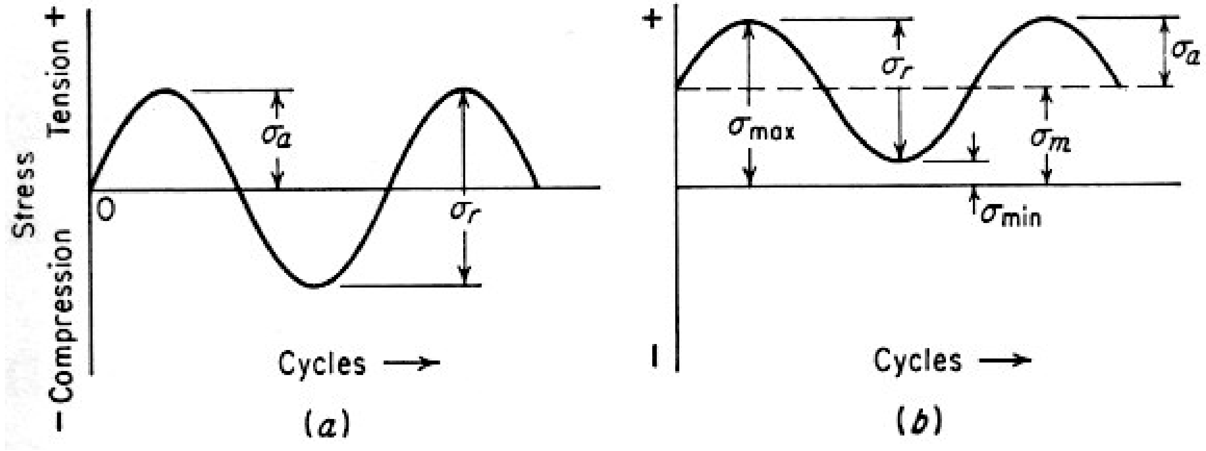

Figure 2.16 Fatigue test schematics showing associated sign convention and nomenclature for (a) tension-compression fatigue test, R = -1 and (b) tension-tension fatigue test R > 0 (Dieter 1986).

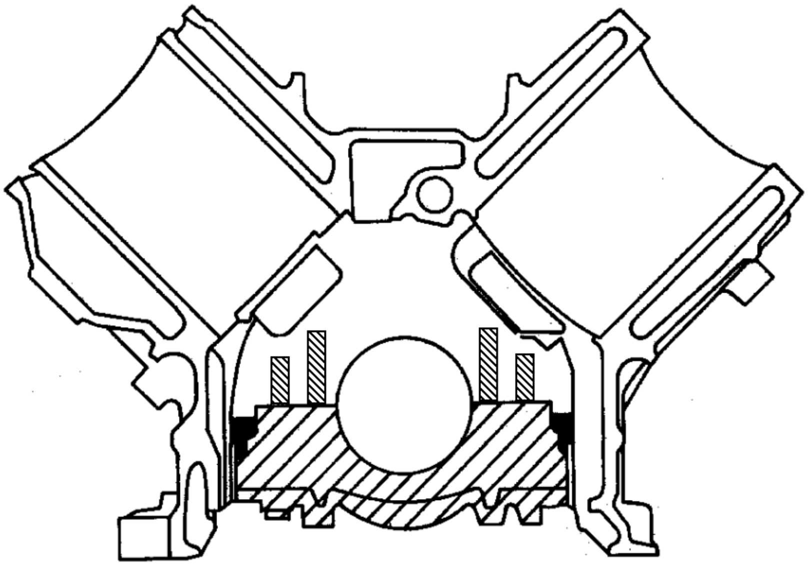

Figure 2.17 Schematic of sectioned V8 cylinder block showing main bearing cap and location of drilled holes

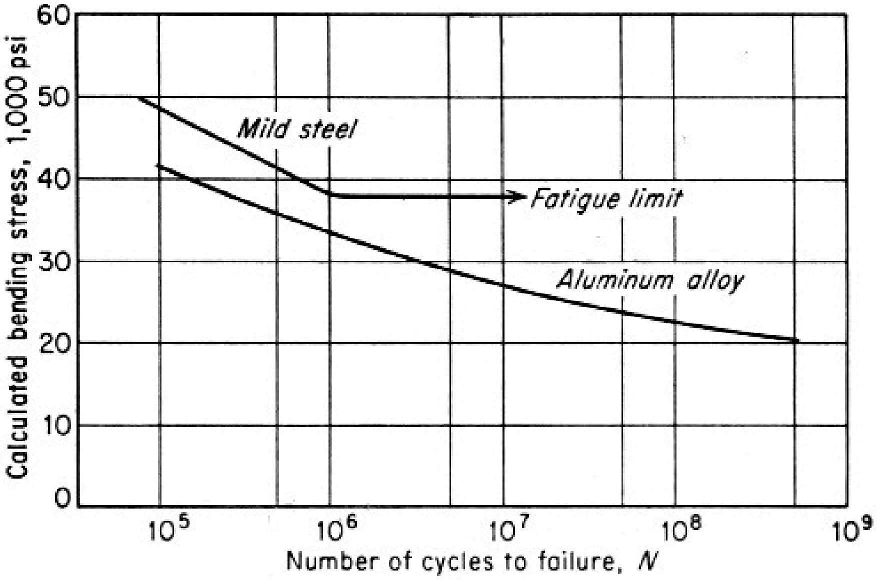

Figure 2.18 Typical S-N fatigue curves for ferrous and nonferrous metals (Dieter 1986)

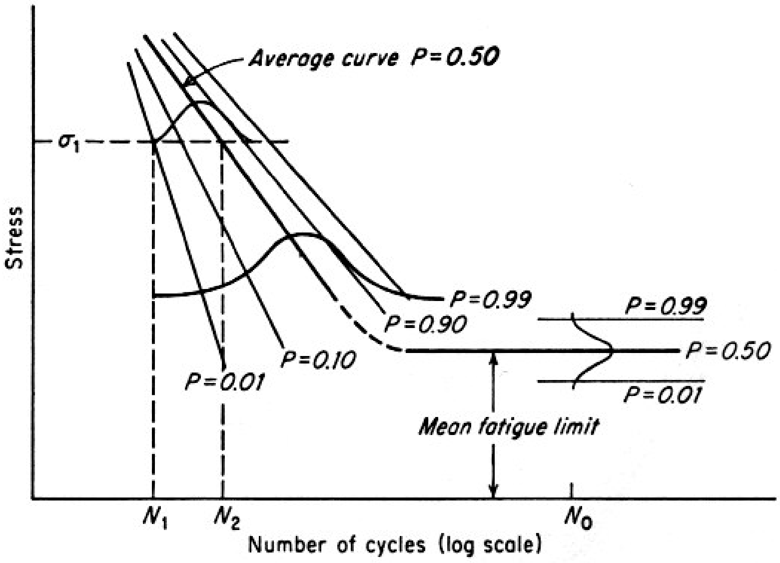

Figure 2.19 Representation of fatigue data on a probability basis (Dieter 1986)

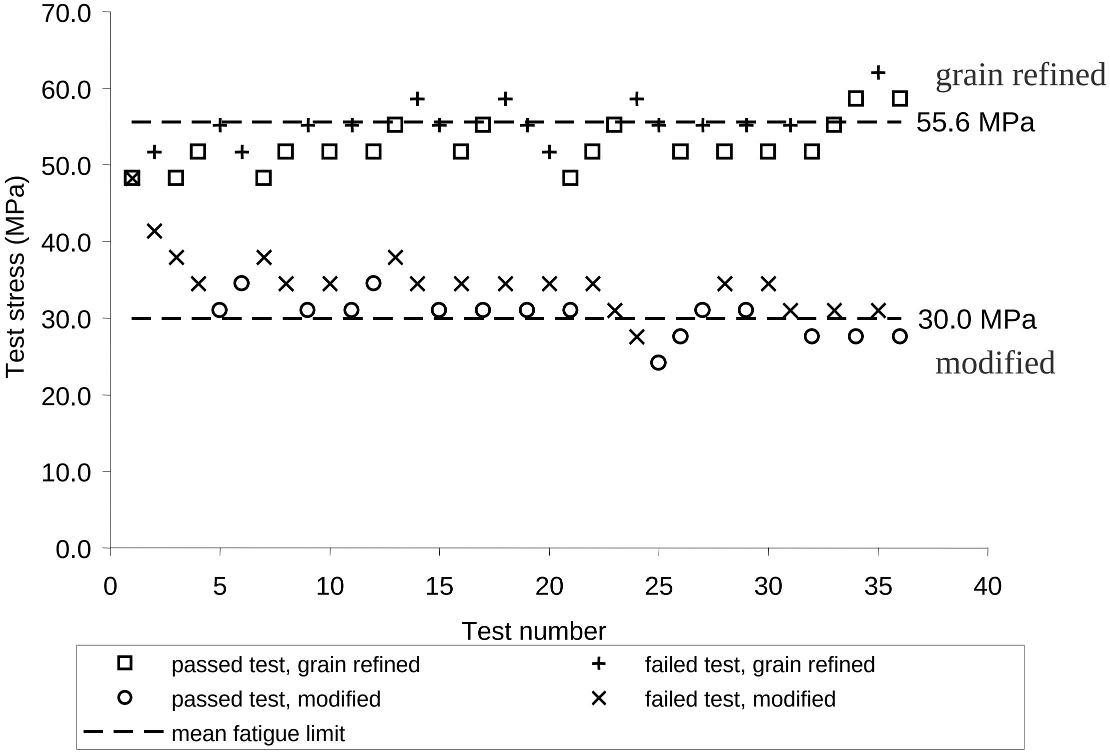

Figure 2.20 Example of staircase fatigue tests for 319 alloy castings produced using different metal treatments (Byczynski 2002)

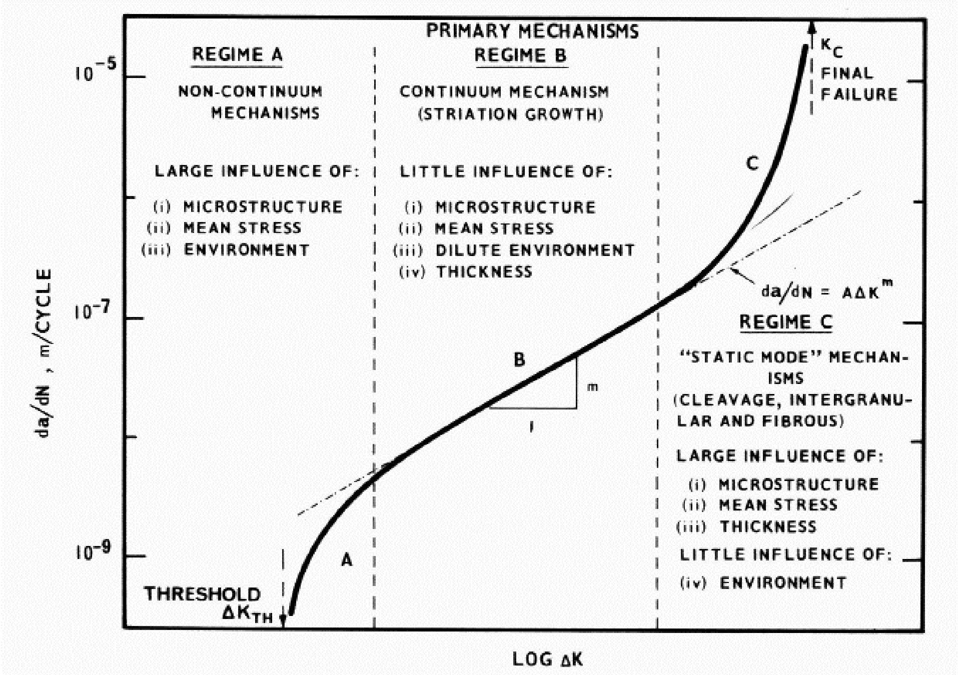

Figure 2.21 Primary fracture mechanisms associated with the variation of the fatigue crack propagation rate *da/dN* with the alternating stress intensity *ΔK*. (Larsson 1984)

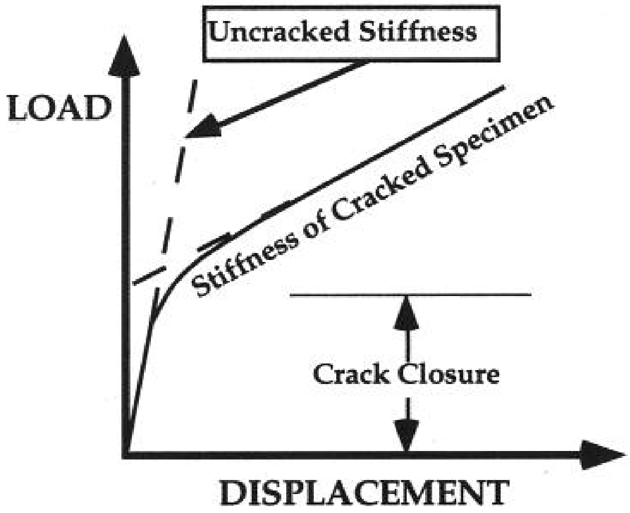

Figure 2.22 Plot of load vs. displacement showing equivalent stiffness of cracked and uncracked specimens at low loads (Anderson 1995).

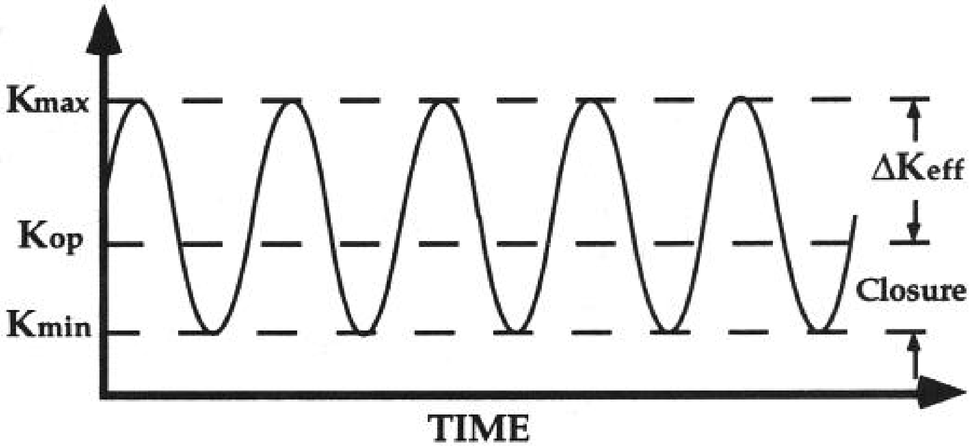

Figure 2.23 Plot of *K* over time for a cyclically loaded specimen, the portion of the curve below K_{op} does not contribute to the propagation of the crack (Anderson 1995).

Chapter 3 FIGURES

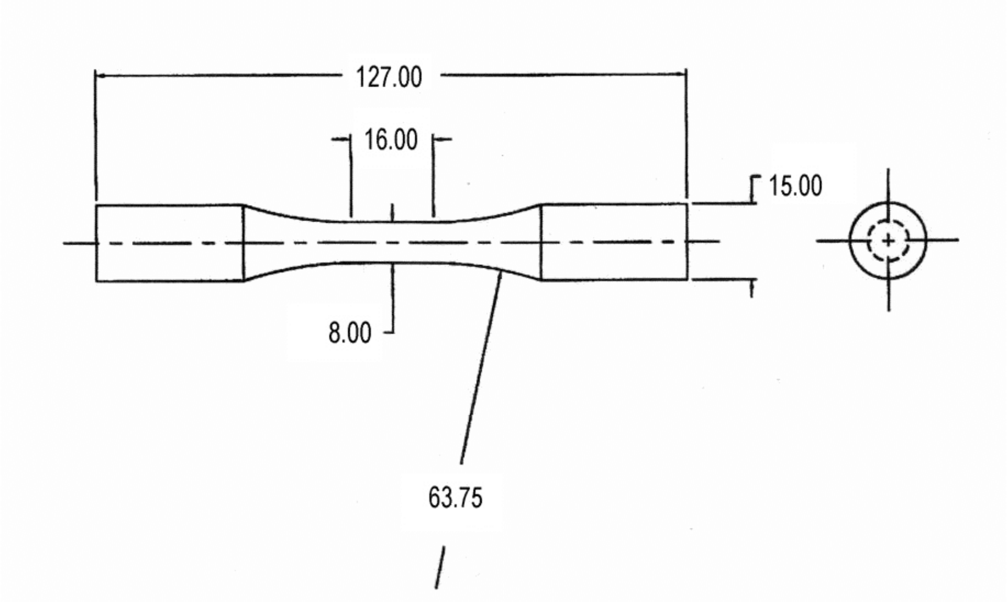

Figure 3.1 Staircase fatigue sample dimensions in millimetres

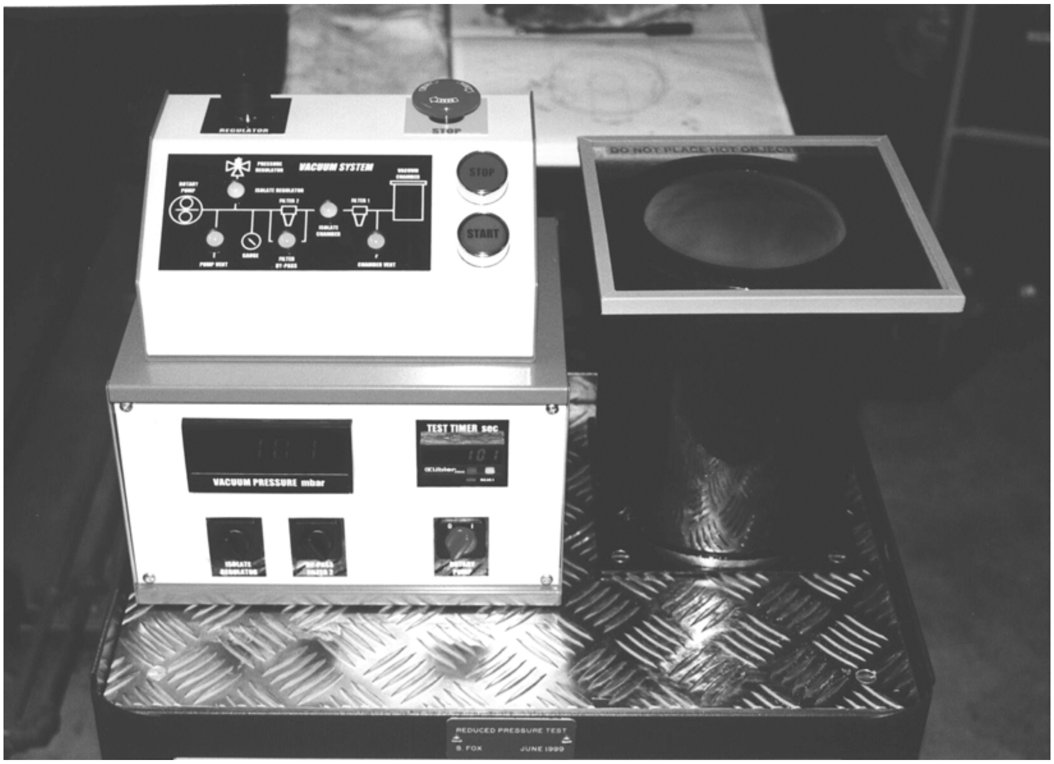

Figure 3.2 The Remelt Reduced Pressure Apparatus (Courtesy of S.Fox)

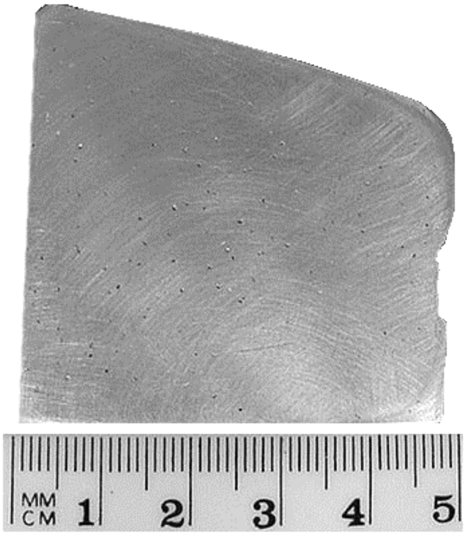

Figure 3.3 Sample of 319 alloy ingot prepared for Remelt reduced pressure test (RRPT), top view

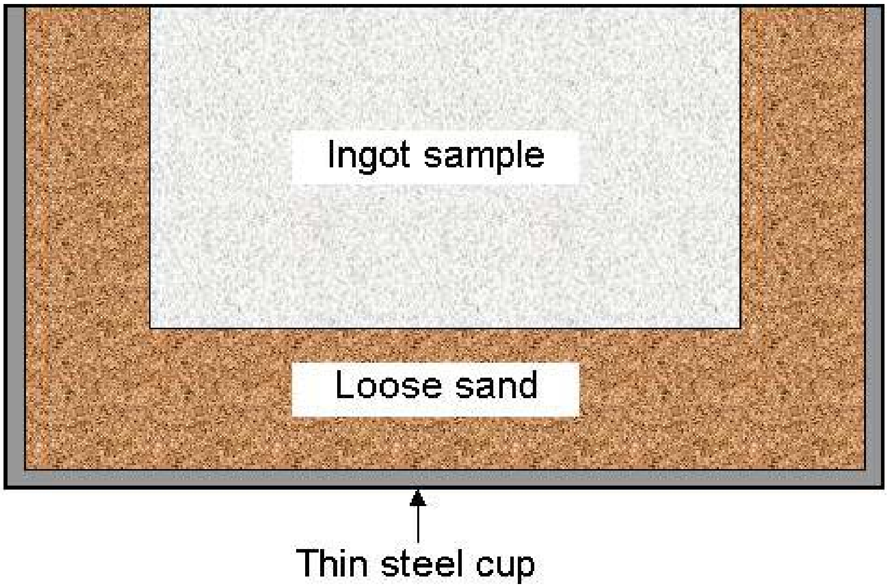

Figure 3.4 Schematic of test configuration in the RRPT, sectioned side view

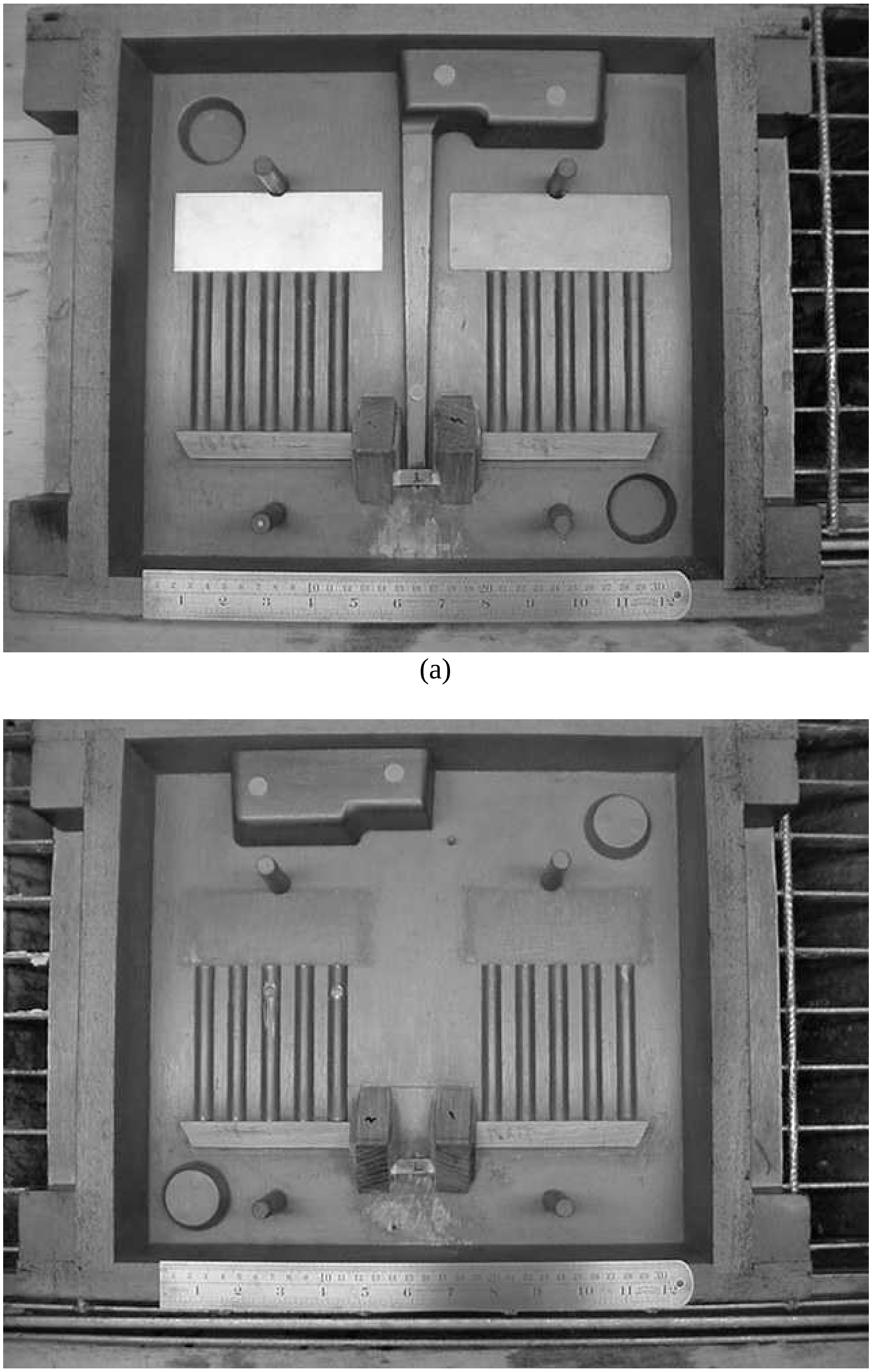

(a)

(b)

Figure 3.5 Pattern used to form the mould used in the production of test bars

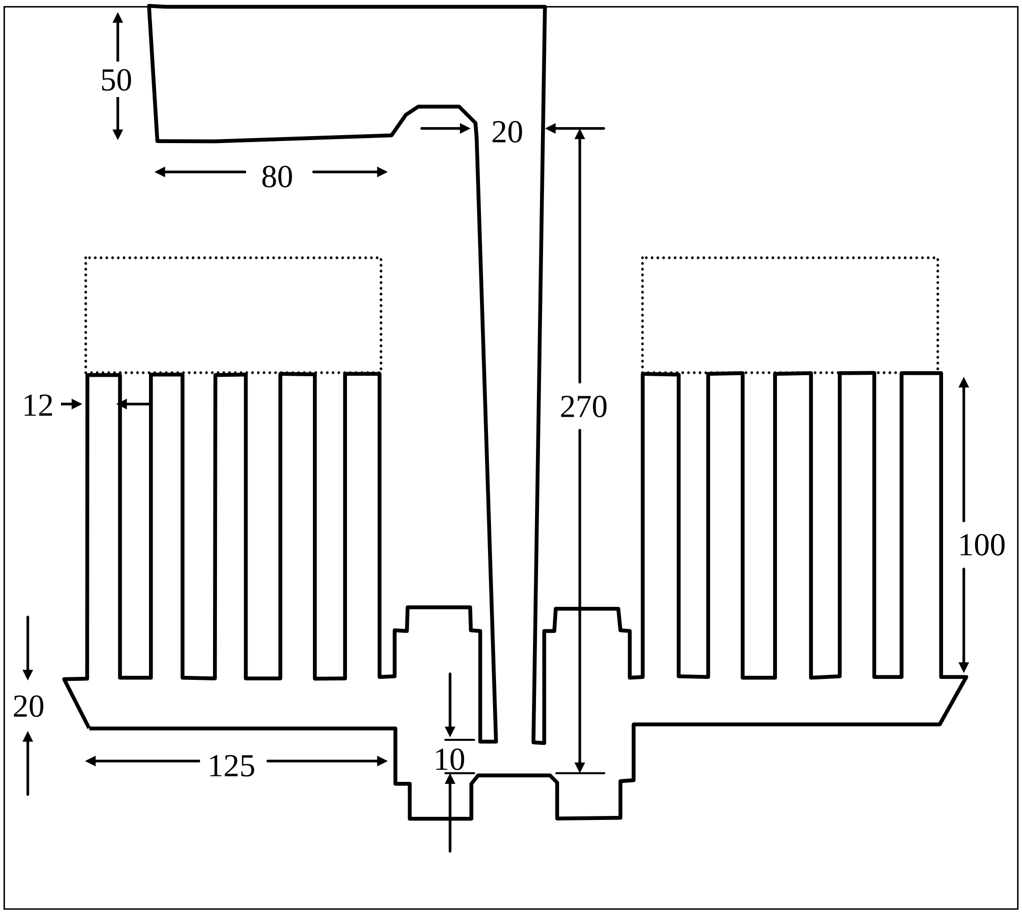

Figure 3.6 Schematic of mould used, principal dimensions in millimeters

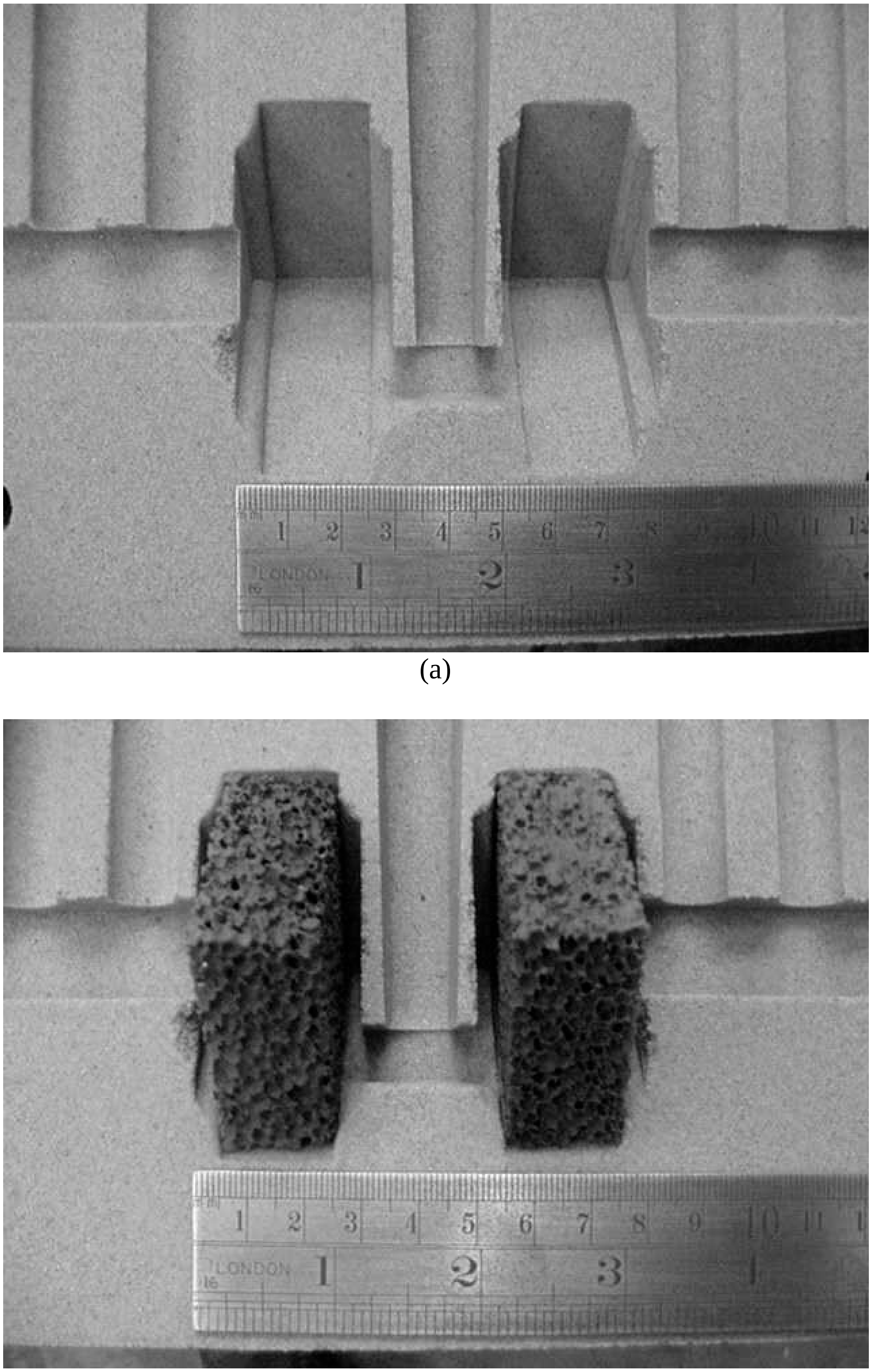

(a)

(b)

Figure 3.7 Filter print area of mould for the (a) unfiltered and (b) filtered cases

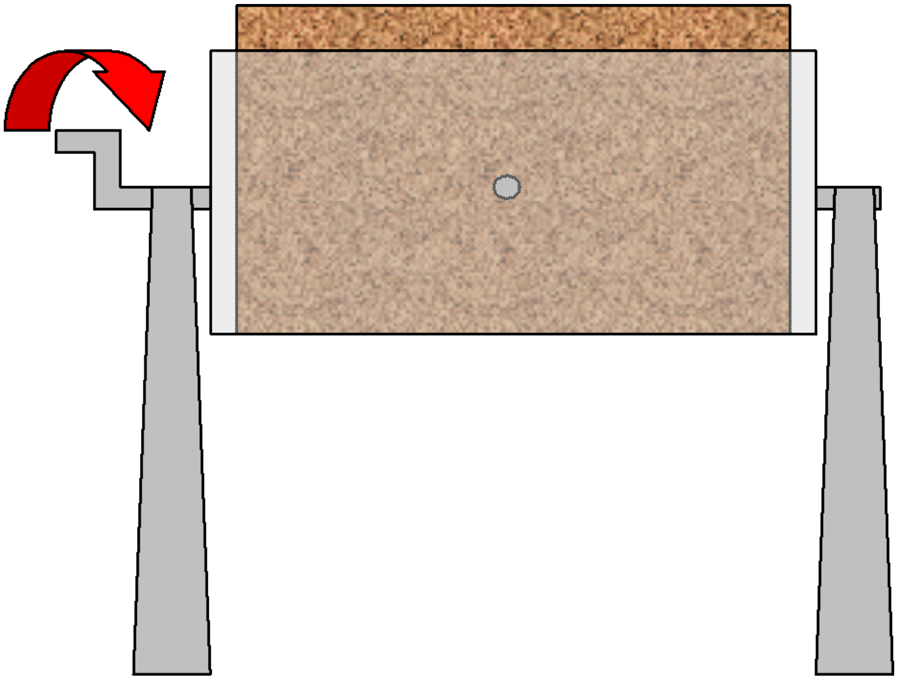

Figure 3.8 Schematic showing mould rotating apparatus

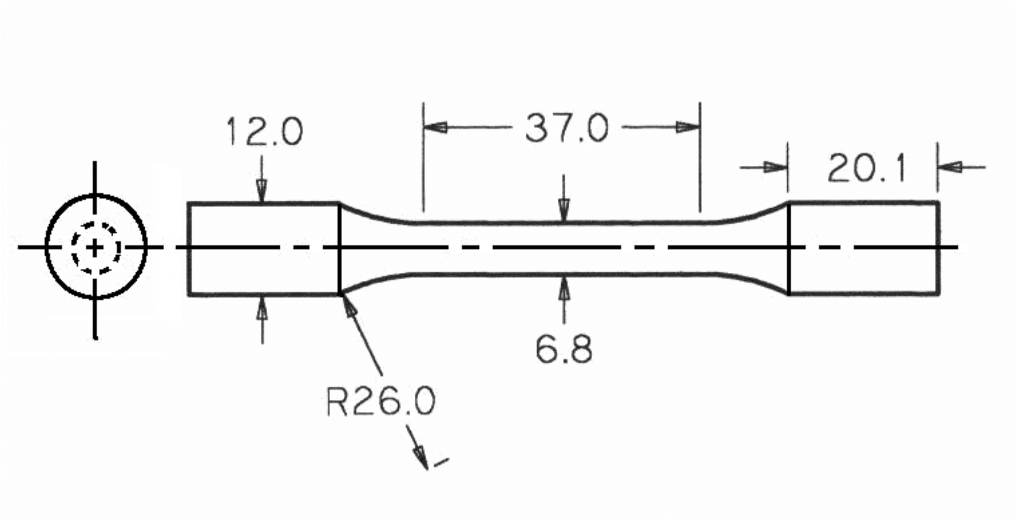

Figure 3.9 Tensile test sample, dimensions in millimeters

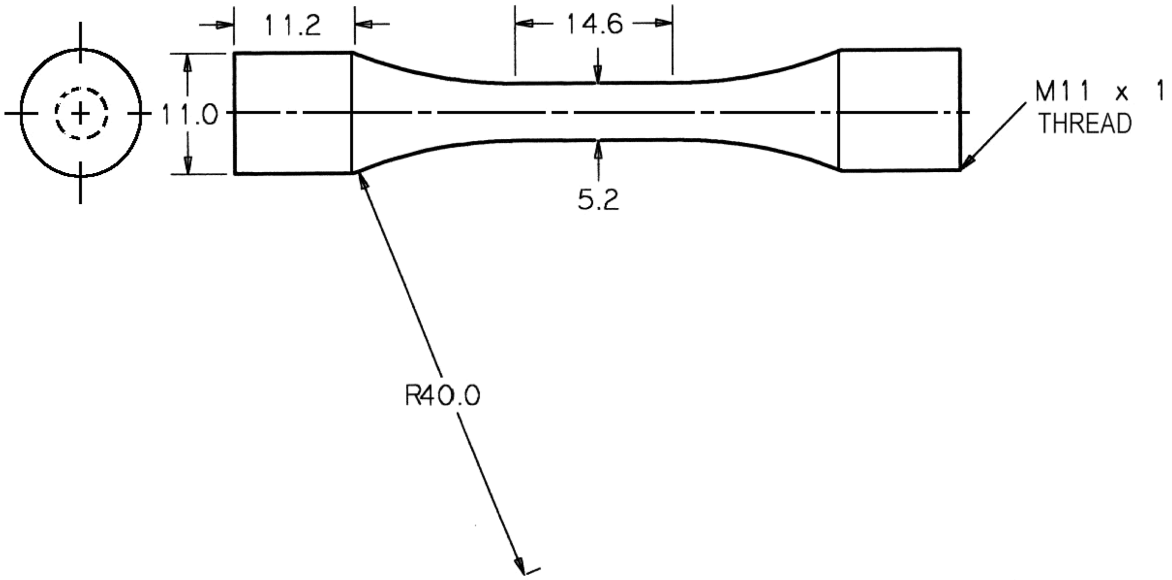

Figure 3.10 Fatigue test sample, dimensions in millimeters

Chapter 4 FIGURES

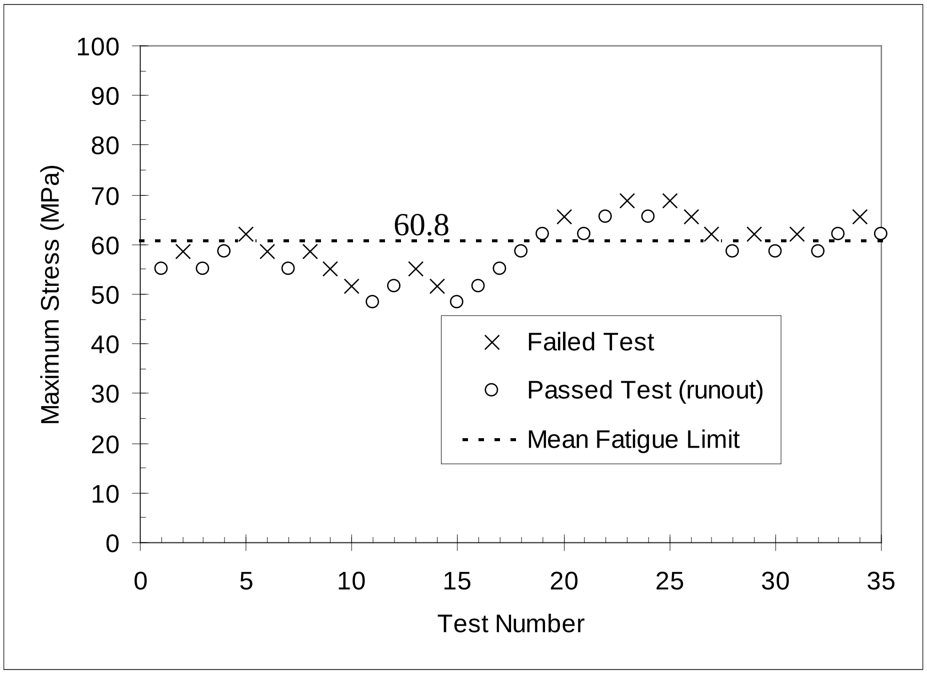

Figure 4.1 Staircase fatigue testing results from production V6 cylinder blocks presented in graphical format

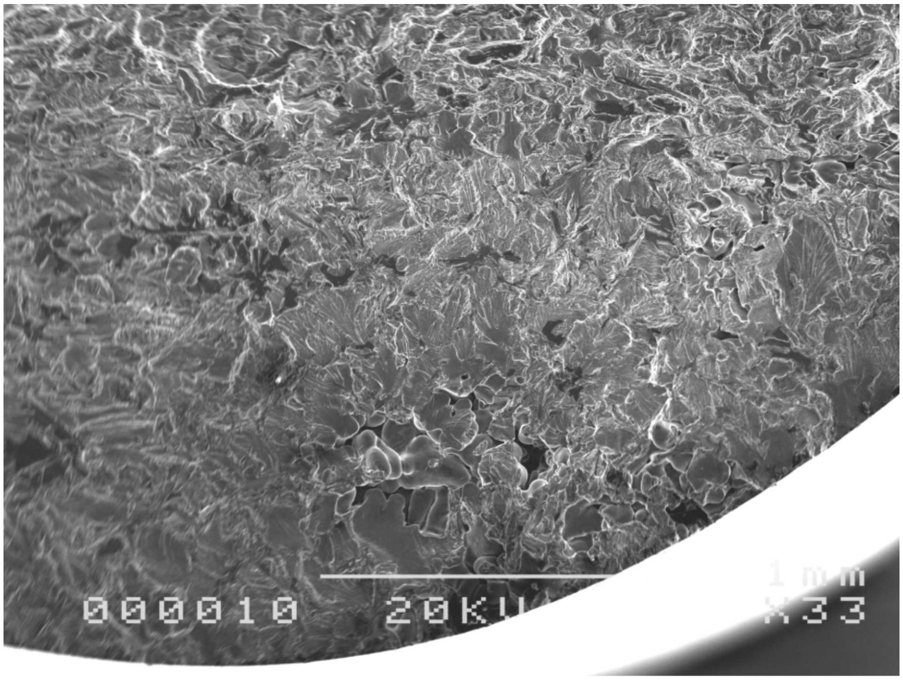

Figure 4.2 SEM micrograph (SEI) showing interconnected shrinkage porosity network acting as fatigue initiation point, staircase sample #1 (58.6 MPa, 601,329 cycles)

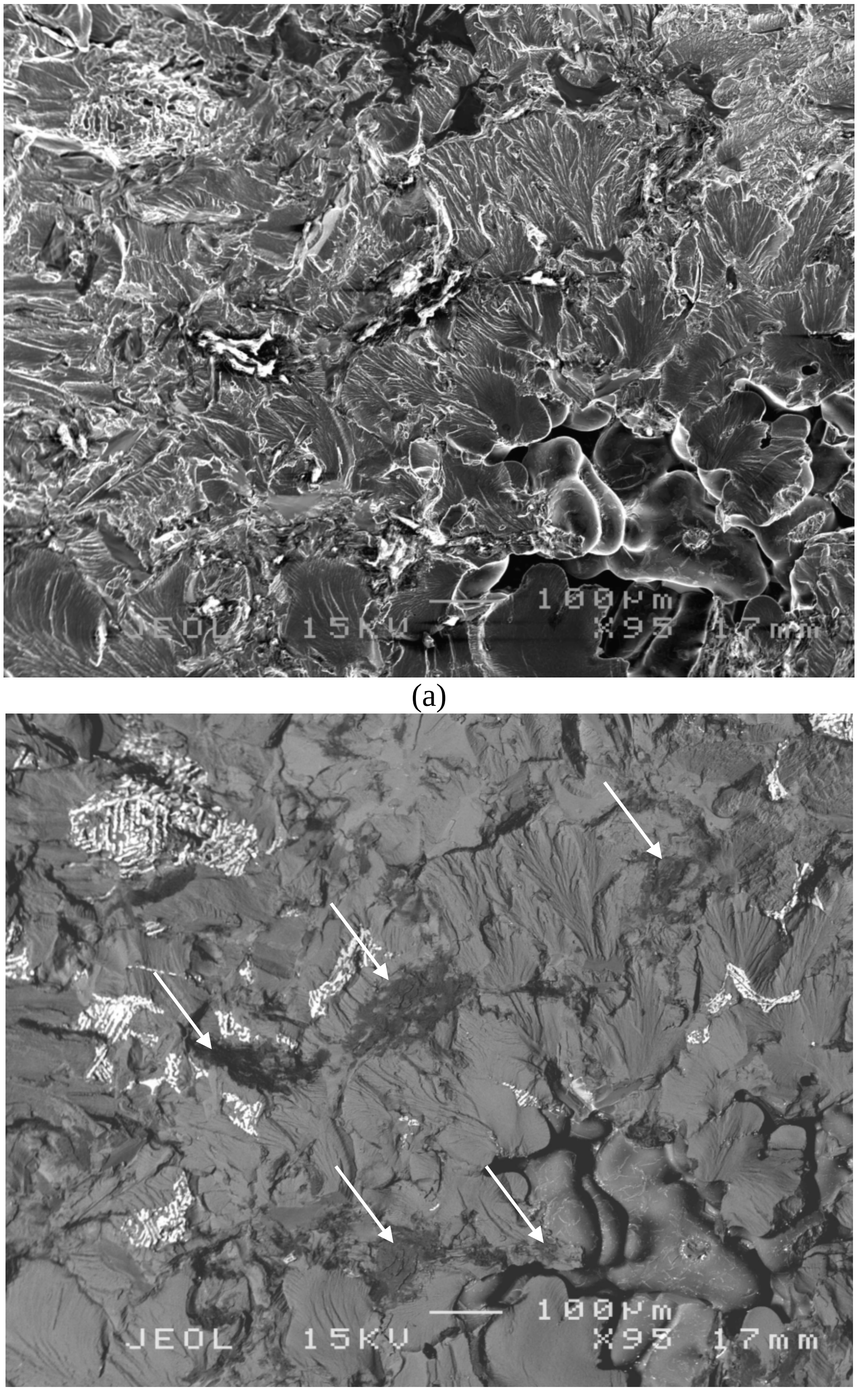

(a)

(b)

Figure 4.3 (a) SEI and (b) BEI SEM micrographs showing oxide films located around shrinkage pore, (arrows) staircase sample #1 (58.6 MPa, 601,329 cycles)

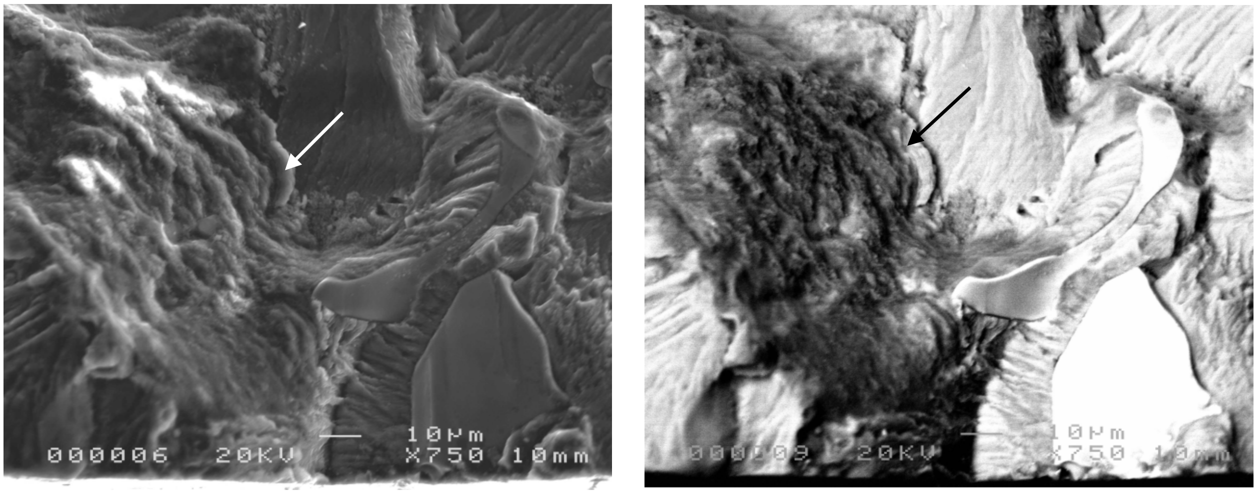

(a) (b)

Figure 4.4 (a) SEI and (b) BEI electron micrographs showing presence of oxide film (arrows) staircase sample #1 (58.6 MPa, 601,329 cycles)

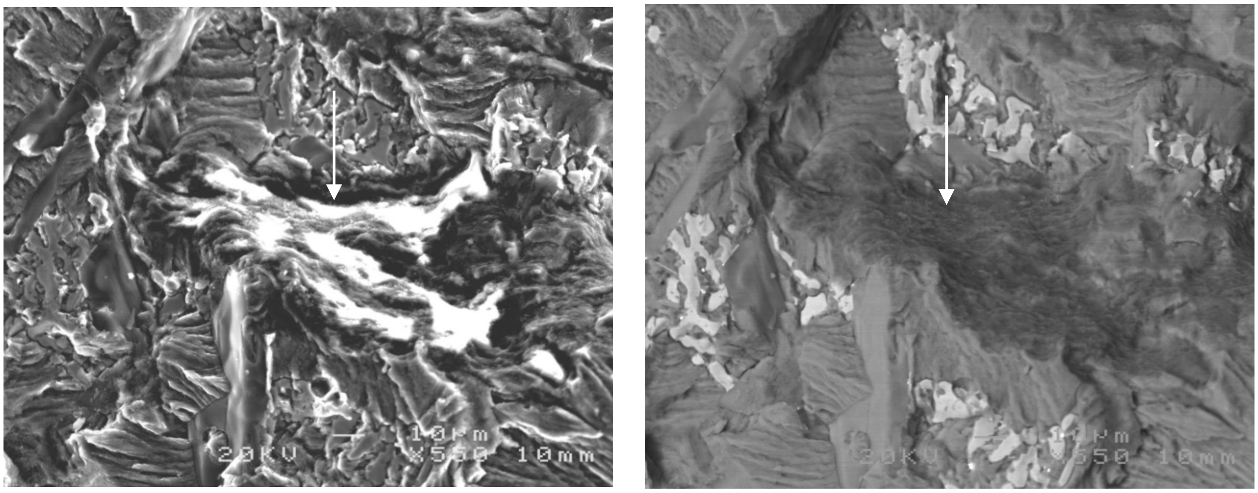

(a) (b)

Figure 4.5 Another example of (a) SEI and (b) BEI SEM micrographs showing presence of oxide film (arrows), staircase sample #1 (58.6 MPa, 601,329 cycles)

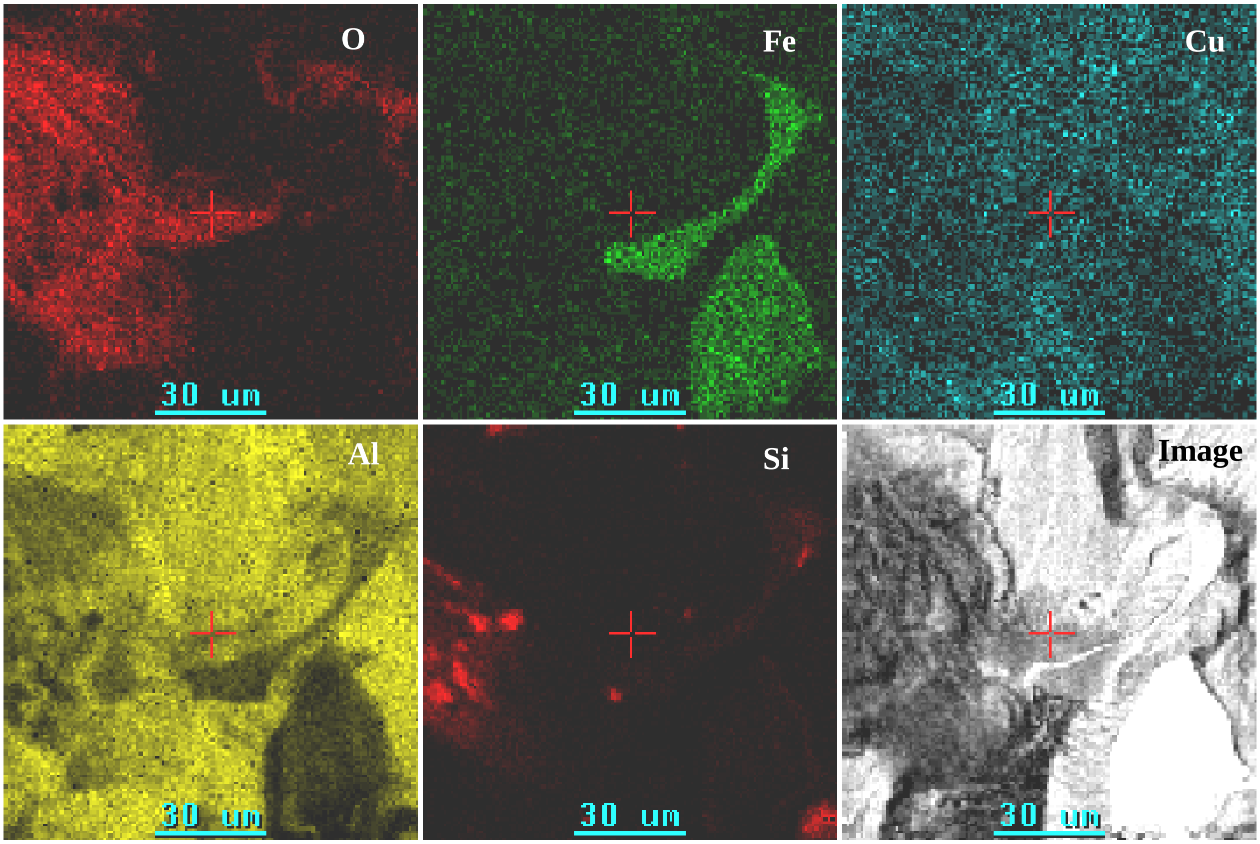

Figure 4.6 EDS X-ray maps showing elements present in BEI image from Figure 4.4. Note elements analyzed are oxygen, iron, copper, aluminum, and silicon.

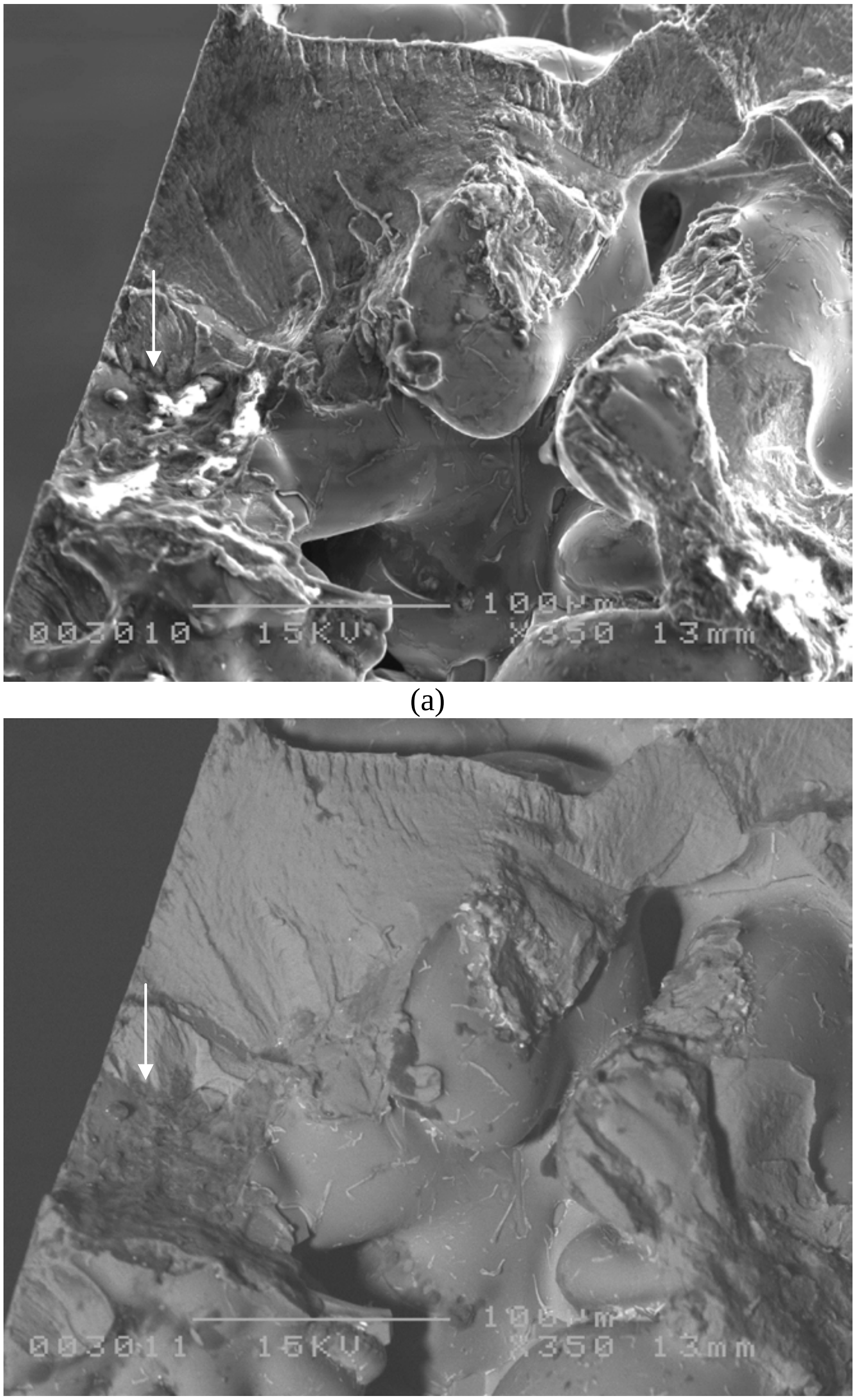

(a)

(b)

Figure 4.7 (a) SEI and (b) BEI SEM micrographs showing oxide film located near shrinkage pore, apparently linking the pore network to the sample surface, staircase sample #2 (55.2 MPa, 1,079,425 cycles)

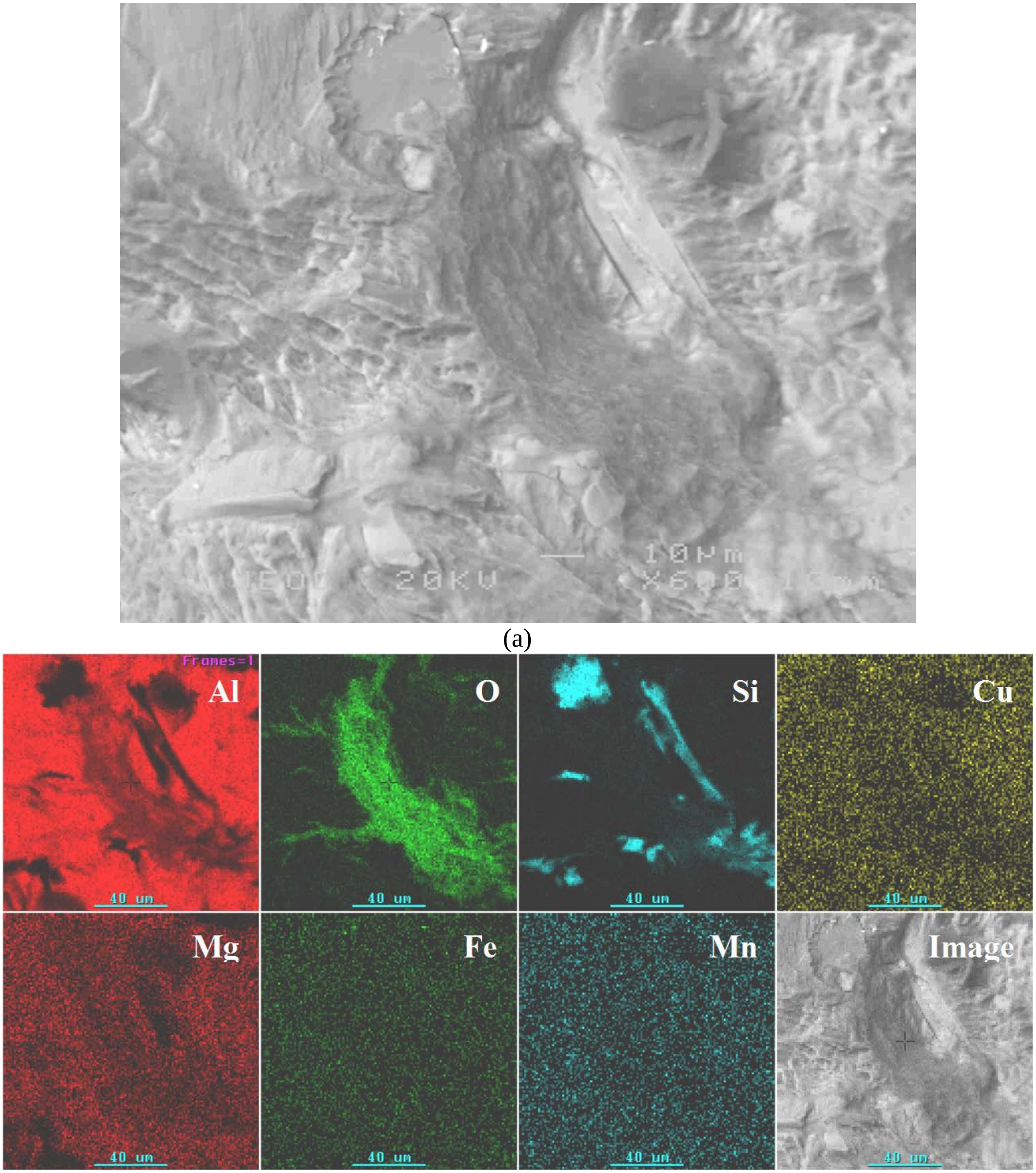

(a)

(b)

Figure 4.8 (a) BEI and (b) x-ray maps showing presence of oxide film on fracture surface, staircase sample #16 (51.7 MPa, 9,649,661 cycles)

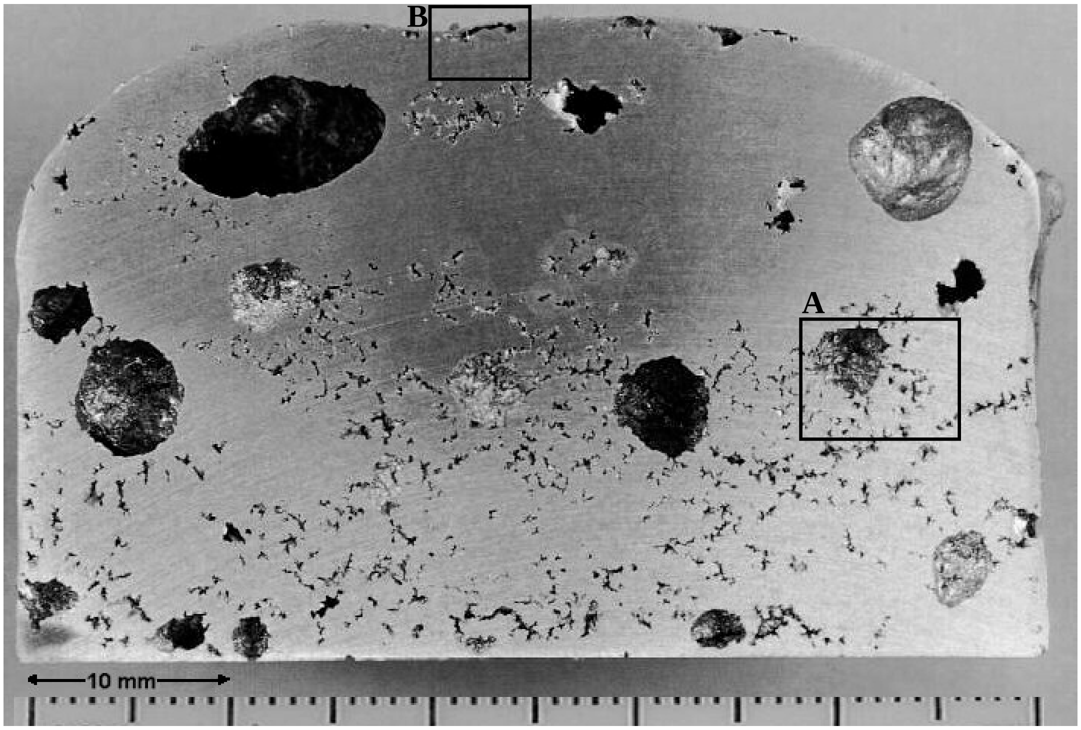

Figure 4.9 Photograph of ingot sample cross section after RRPT tested under 5000 Pa Pressure

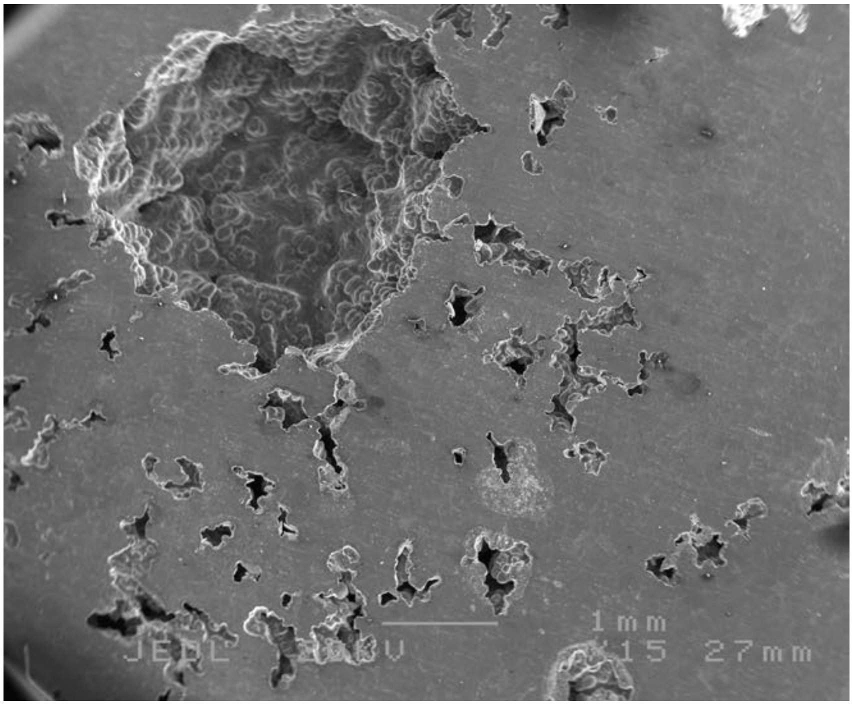

Figure 4.10 SEM micrograph showing pores present on RRPT cross section from Figure 4.9 area A (SEI)

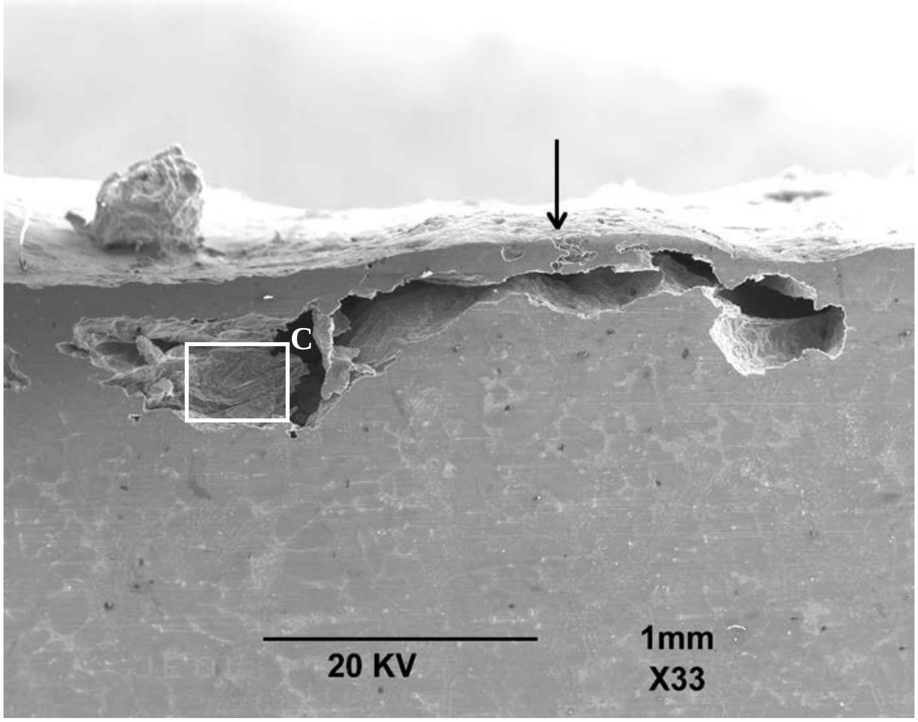

Figure 4.11 SEM micrograph from Figure 4.9 area B showing collapsed bubble; an arrow marks a possible leak path to the free surface (SEI)

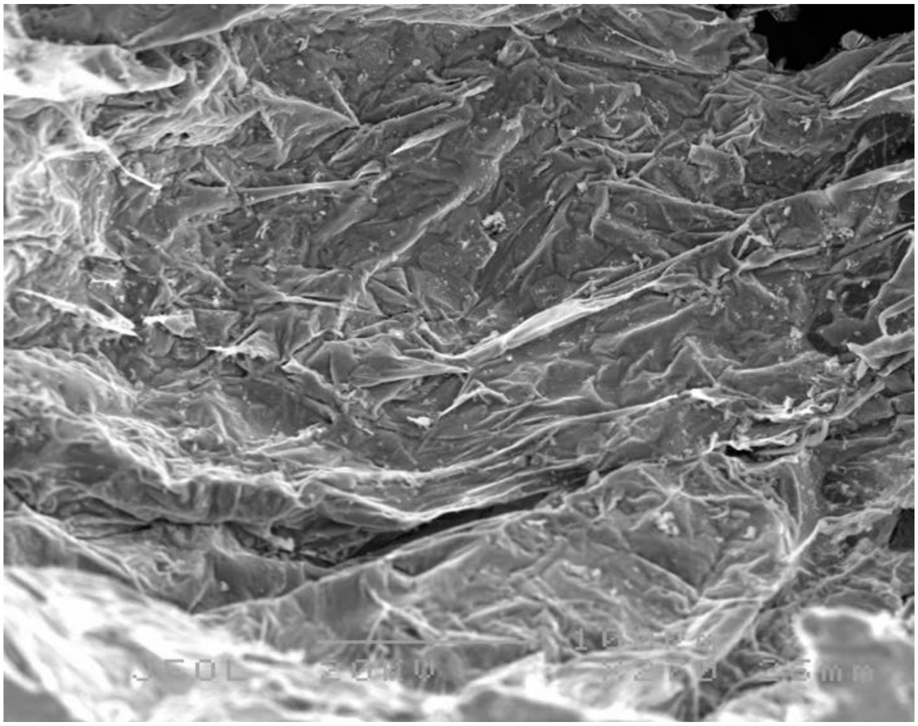

Figure 4.12 SEM micrograph showing fragment of interior surface of collapsed pore seen in Figure 4.11 area C (SEI)

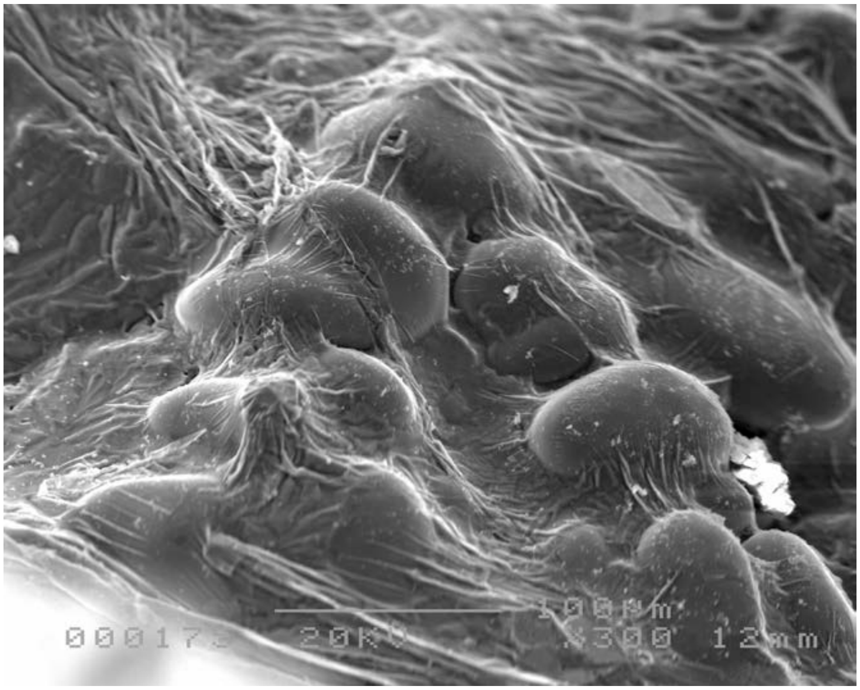

Figure 4.13 SEM micrograph of staircase sample #5, tested at 65.5 MPa lasting 1,544,123 cycles, solidified under a pressure of 5000 Pa, note the presence dendrites under a young oxide film found on the interior surface of a pore

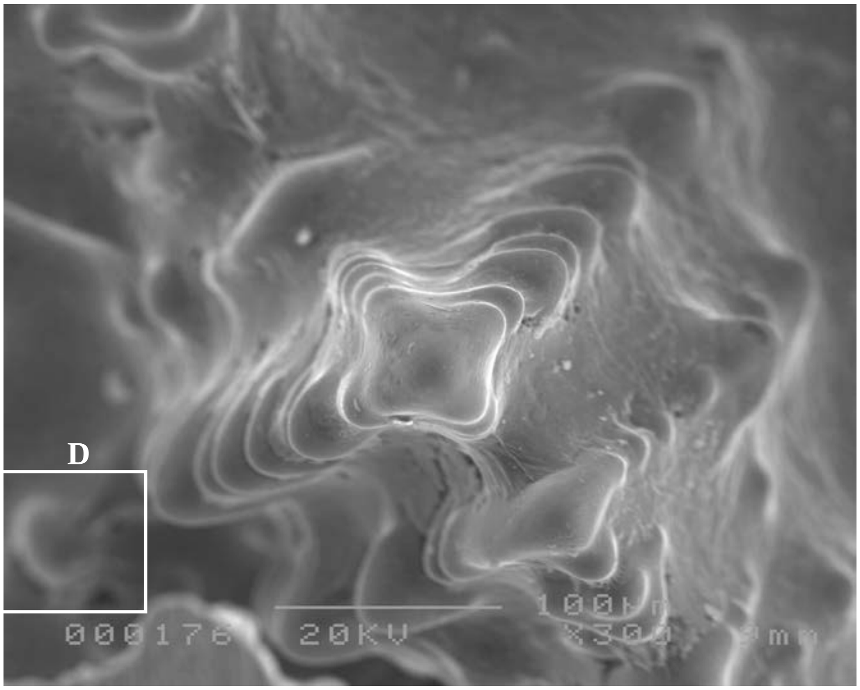

Figure 4.14 SEM micrograph of sample shown in Figure 4.9, interior surface of a pore, note the protruding dendrite stalk, that has broken through the oxide film that forms the pore interior

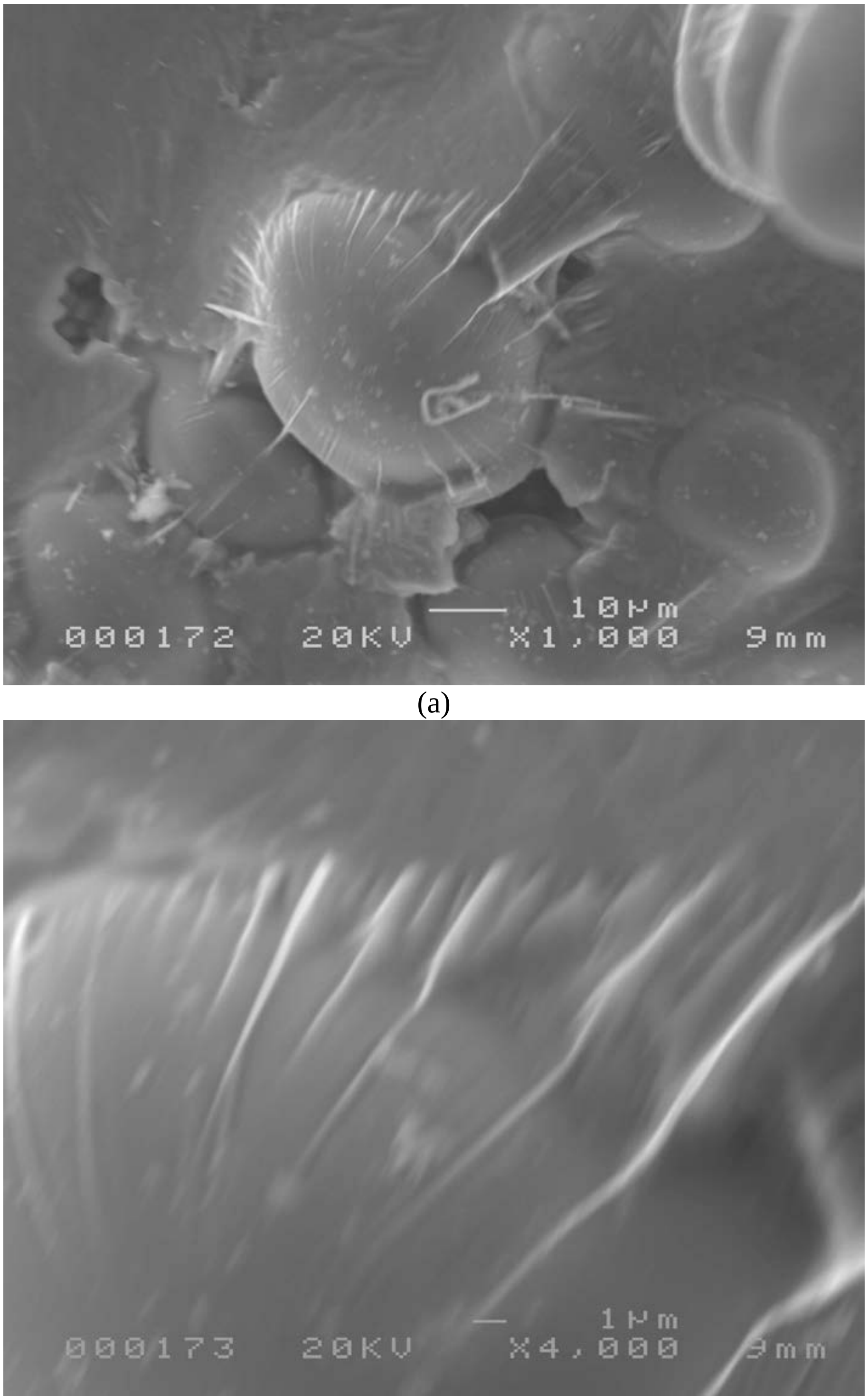

(a)

(b)

Figure 4.15 SEM micrographs of protruding dendrite from Figure 4.14, area D (SEI) (a) showing protruding dendrite causing folds in thin oxide film (b) high magnification showing details of folds, width of a sharp fold can be estimated at approximately 100 nm

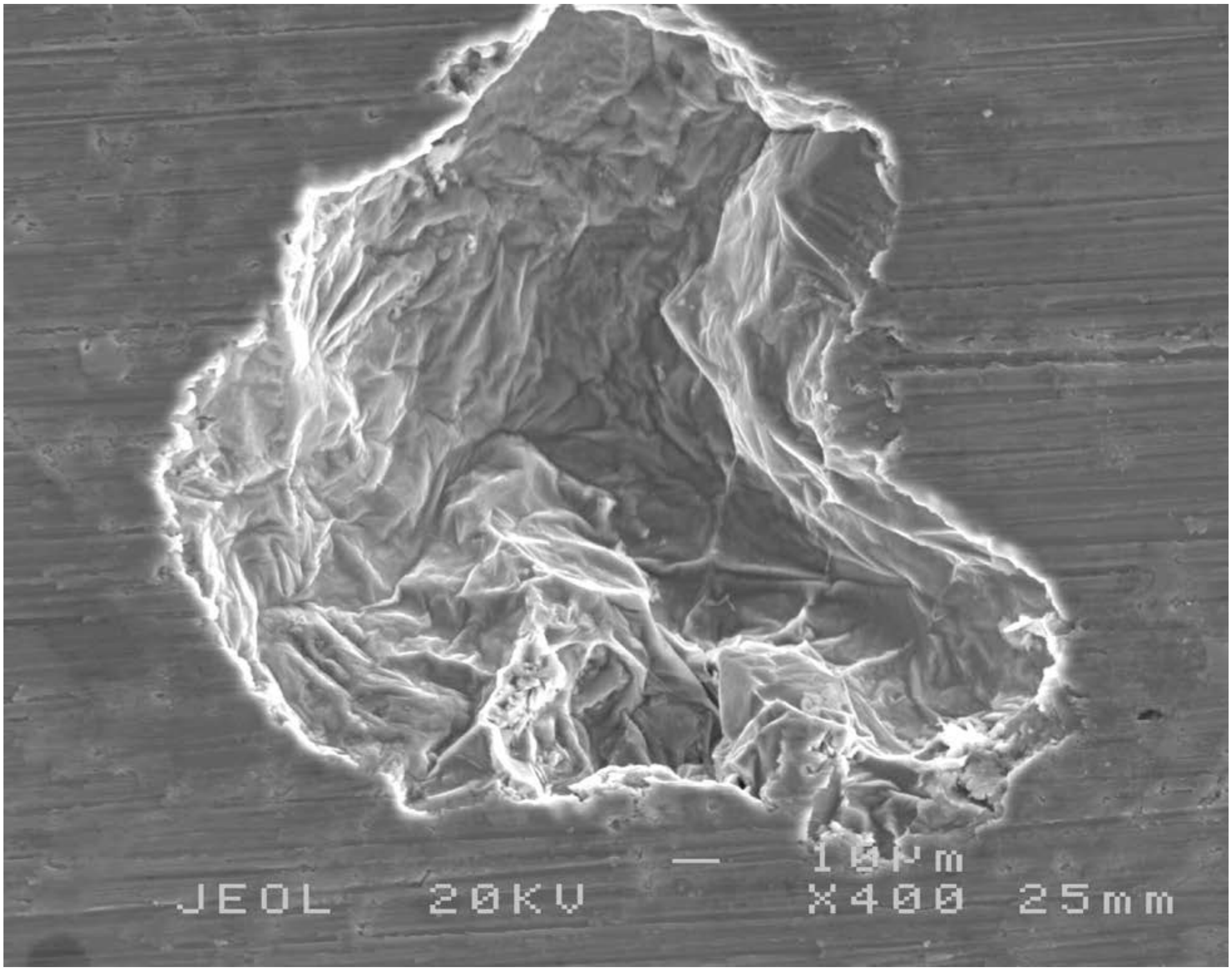

Figure 4.16 SEM micrograph of sample shown in Figure 4.9 showing expanded pore note wrinkled nature of pore interior (SEI)

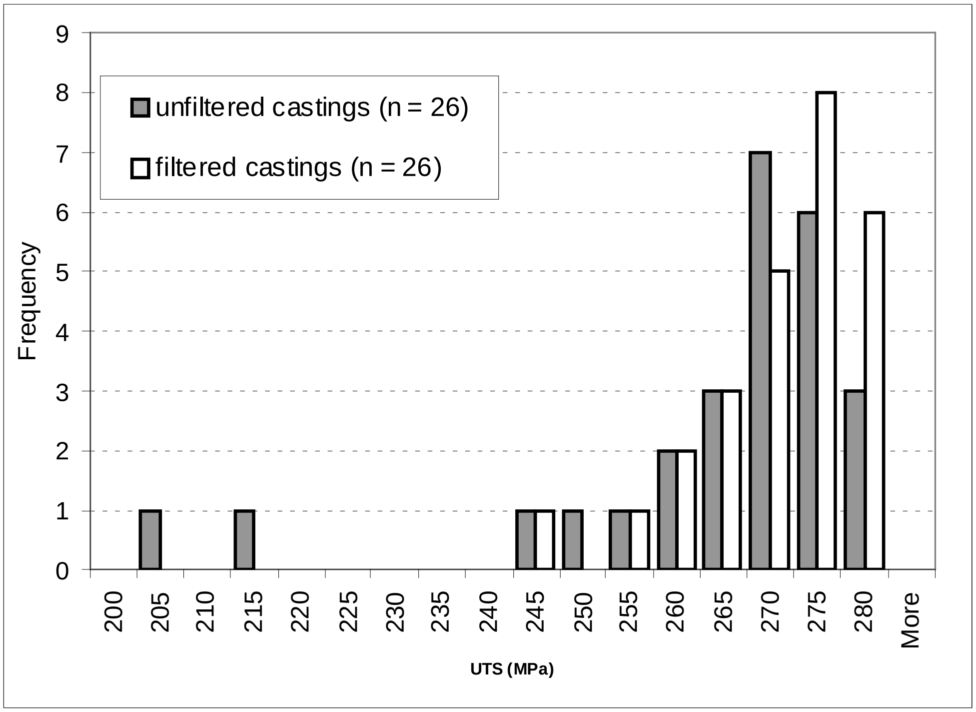

Figure 4.17 Histogram of UTS for unfiltered and filtered samples

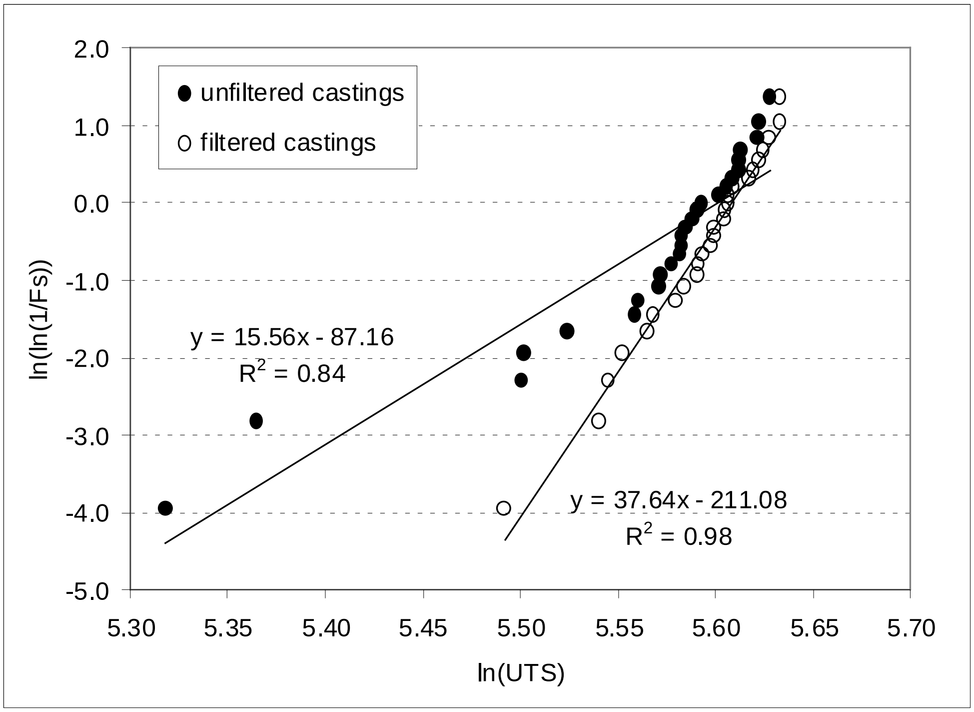

Figure 4.18 Weibull probability plot of UTS for unfiltered and filtered samples

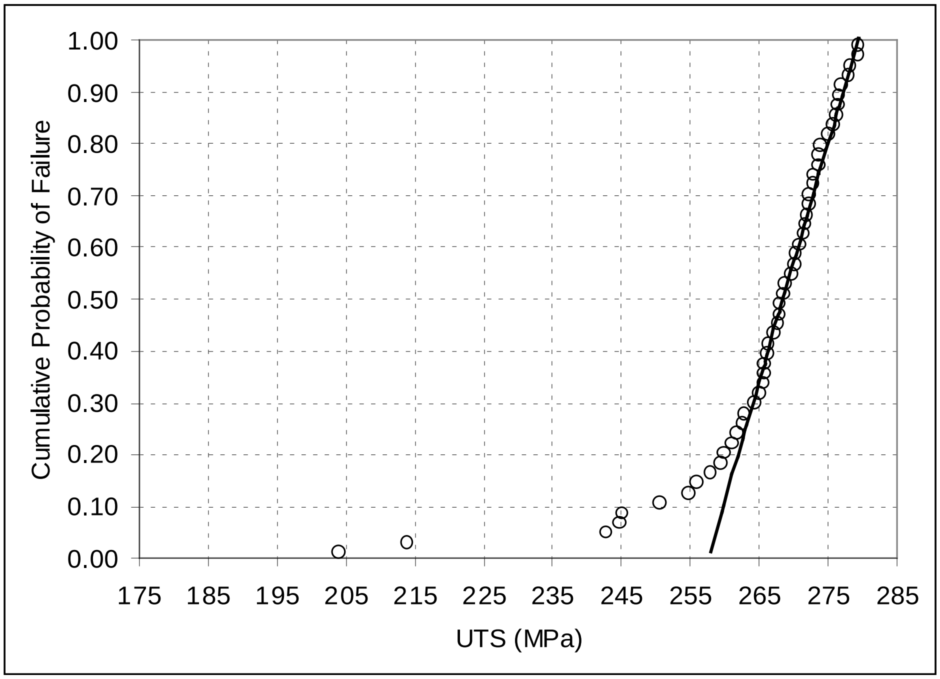

Figure 4.19 Cumulative probability plot of UTS for the combined (unfiltered and filtered) data set.

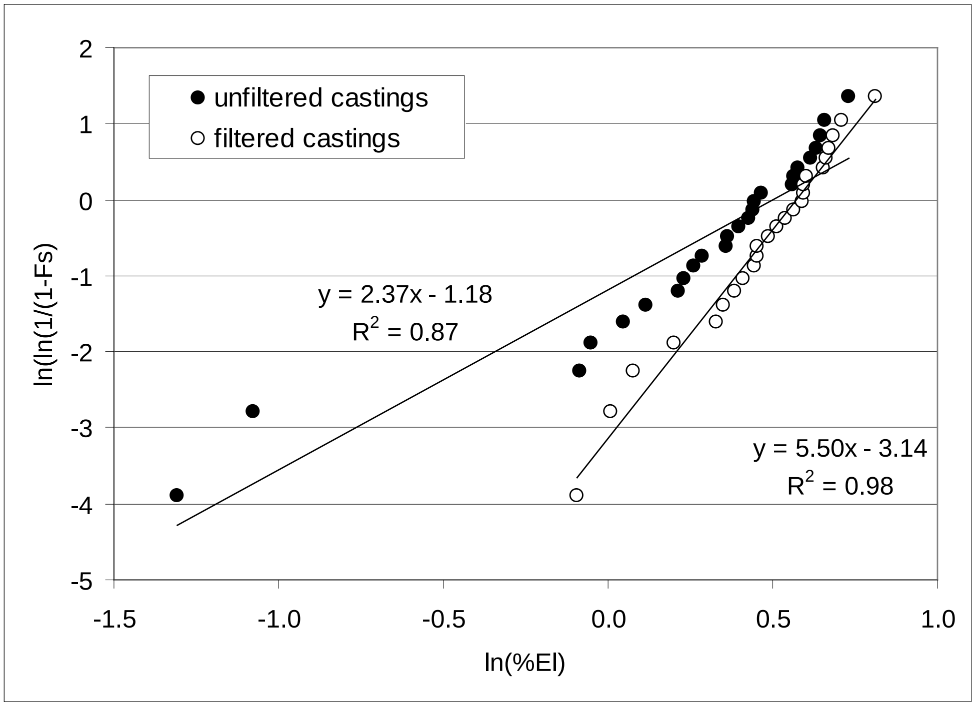

Figure 4.20 Weibull probability plot of percent elongation to fracture for unfiltered and filtered samples

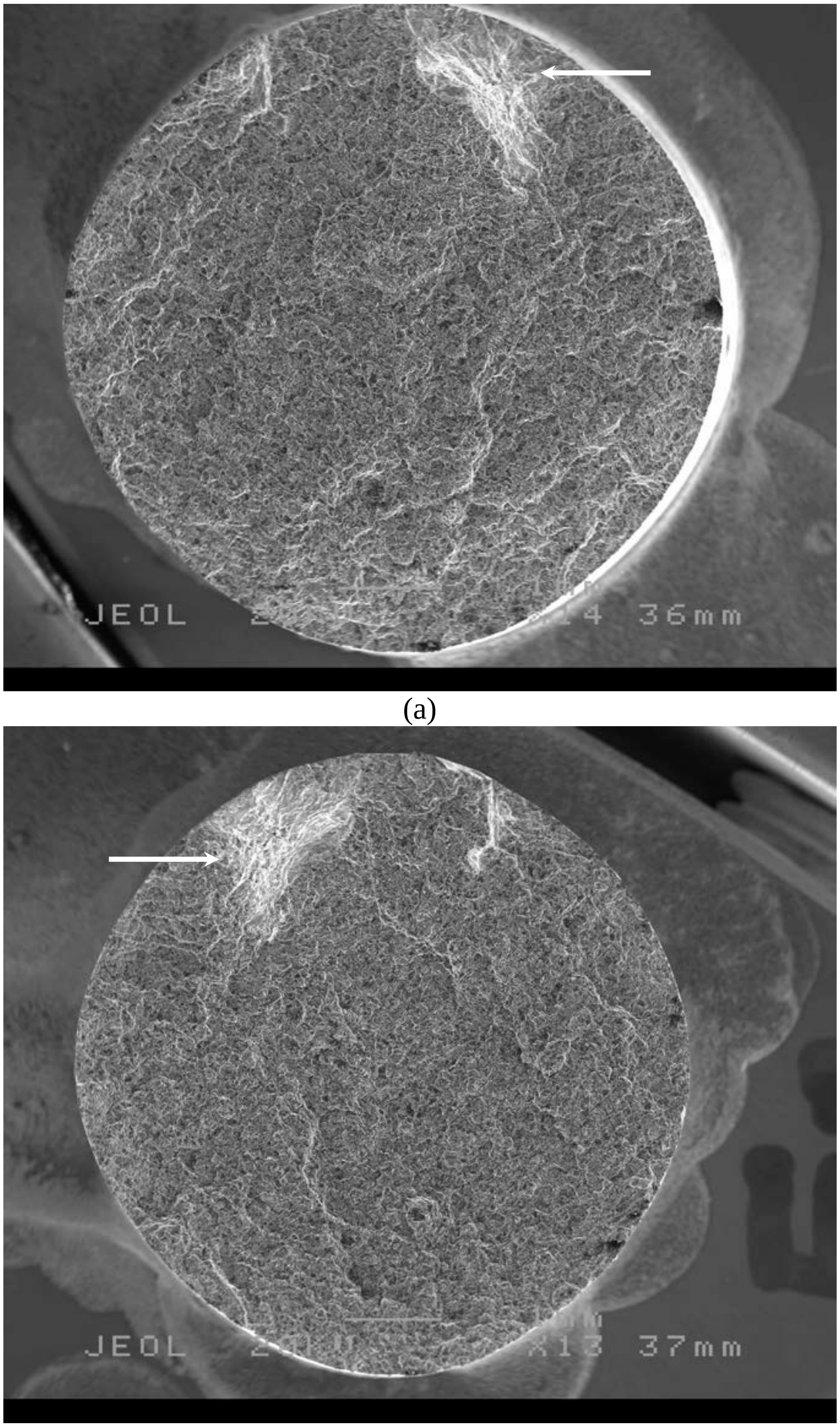

(a)

(b)

Figure 4.21 SEM micrograph of two halves of unfiltered tensile specimen failed at 204.0 MPa (a) side A (b) side B note presence of oxide film on both fracture surfaces (arrows)

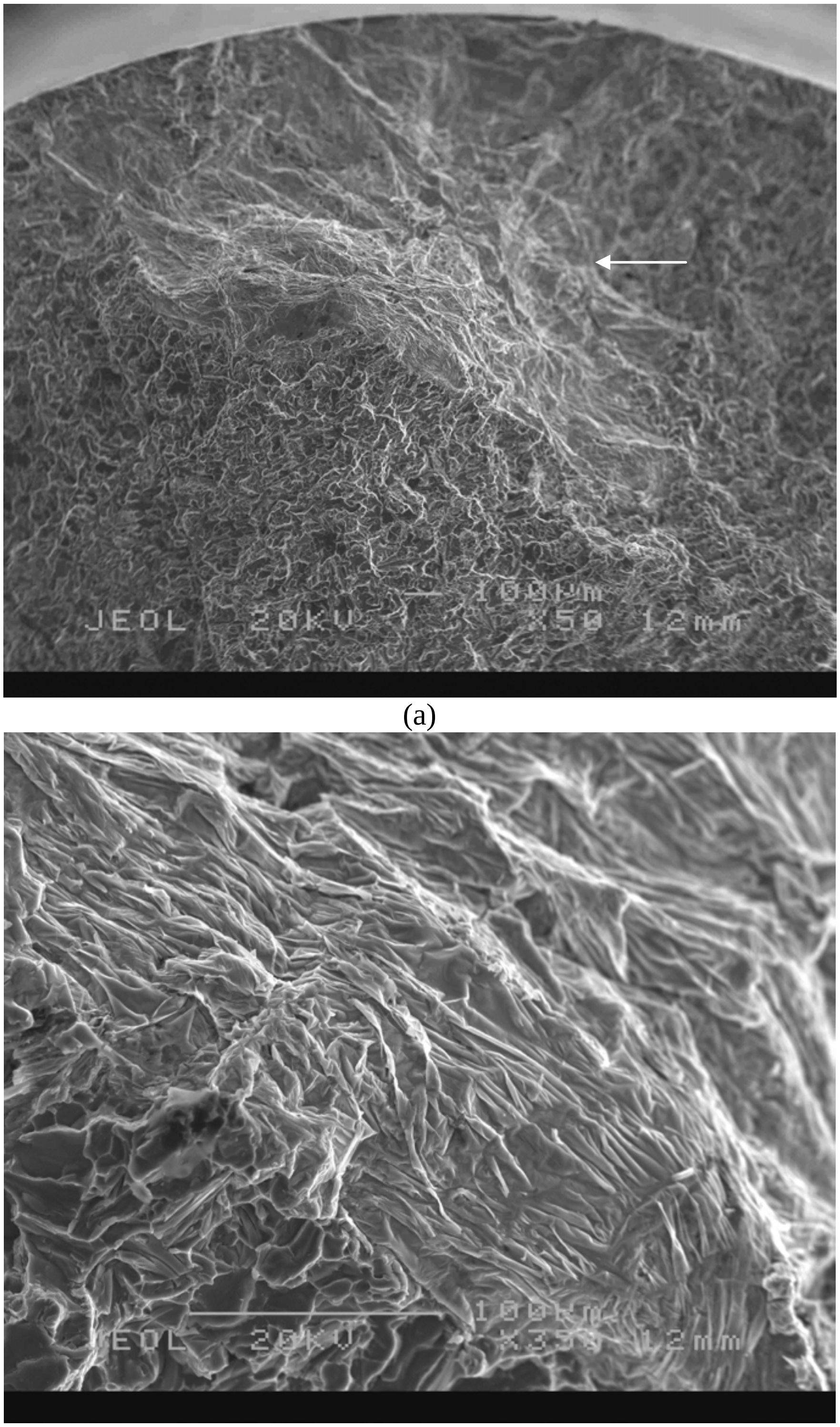

Figure 4.22 Higher magnification SEM micrographs of sample in 4.21, note presence of oxide film (a)X50 (b)X350 note folded structure of oxide film

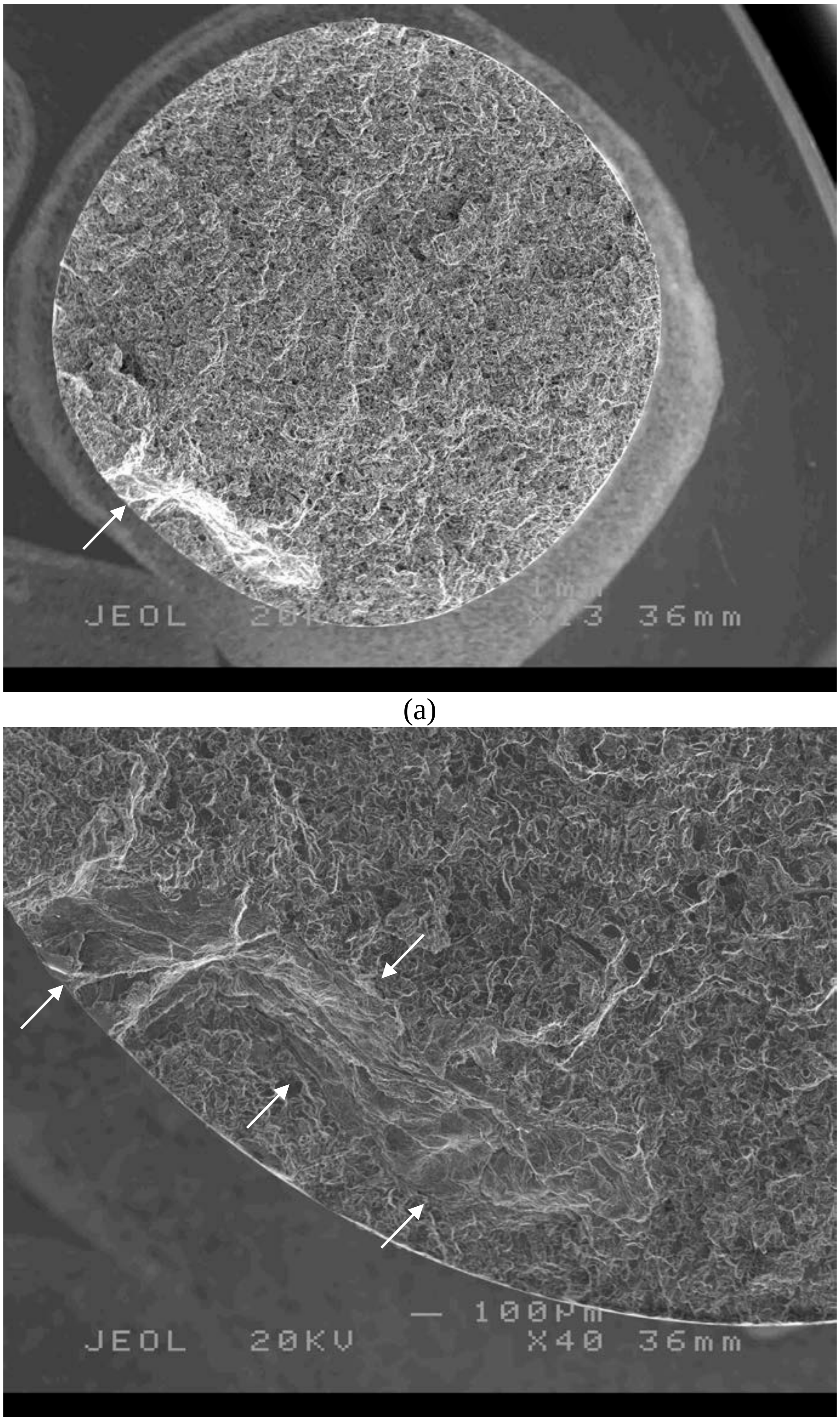

(a)

(b)

Figure 4.23 SEM micrograph of unfiltered tensile specimen failed at 213.8 MPa note presence of oxide film on fracture surface (arrows) (a) X13 (b) X40

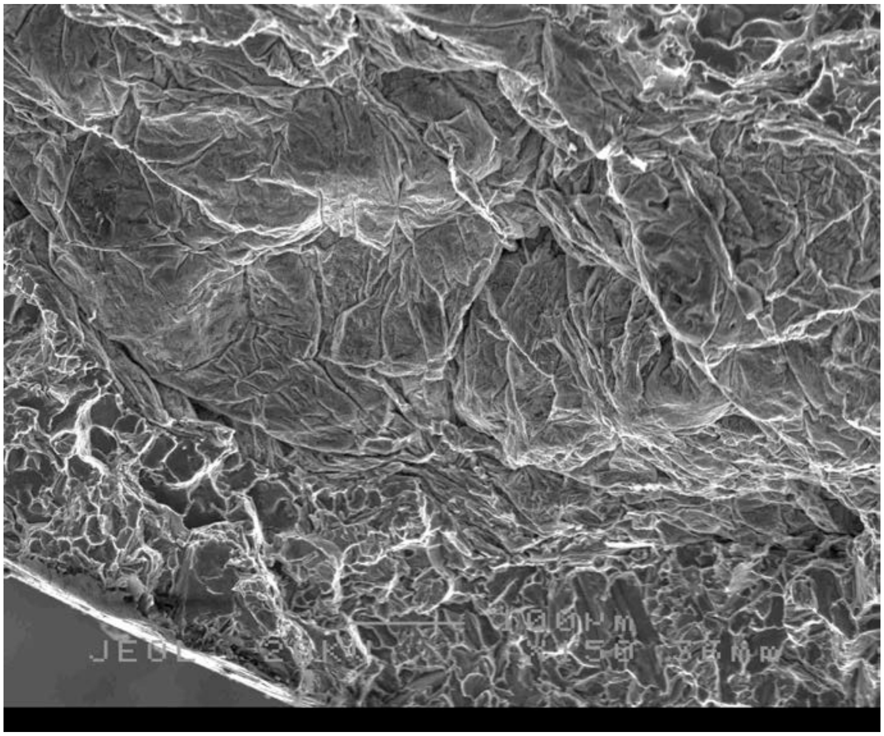

Figure 4.24 Higher magnification (X150) SEM micrograph of sample in 4.22 showing structure of oxide film

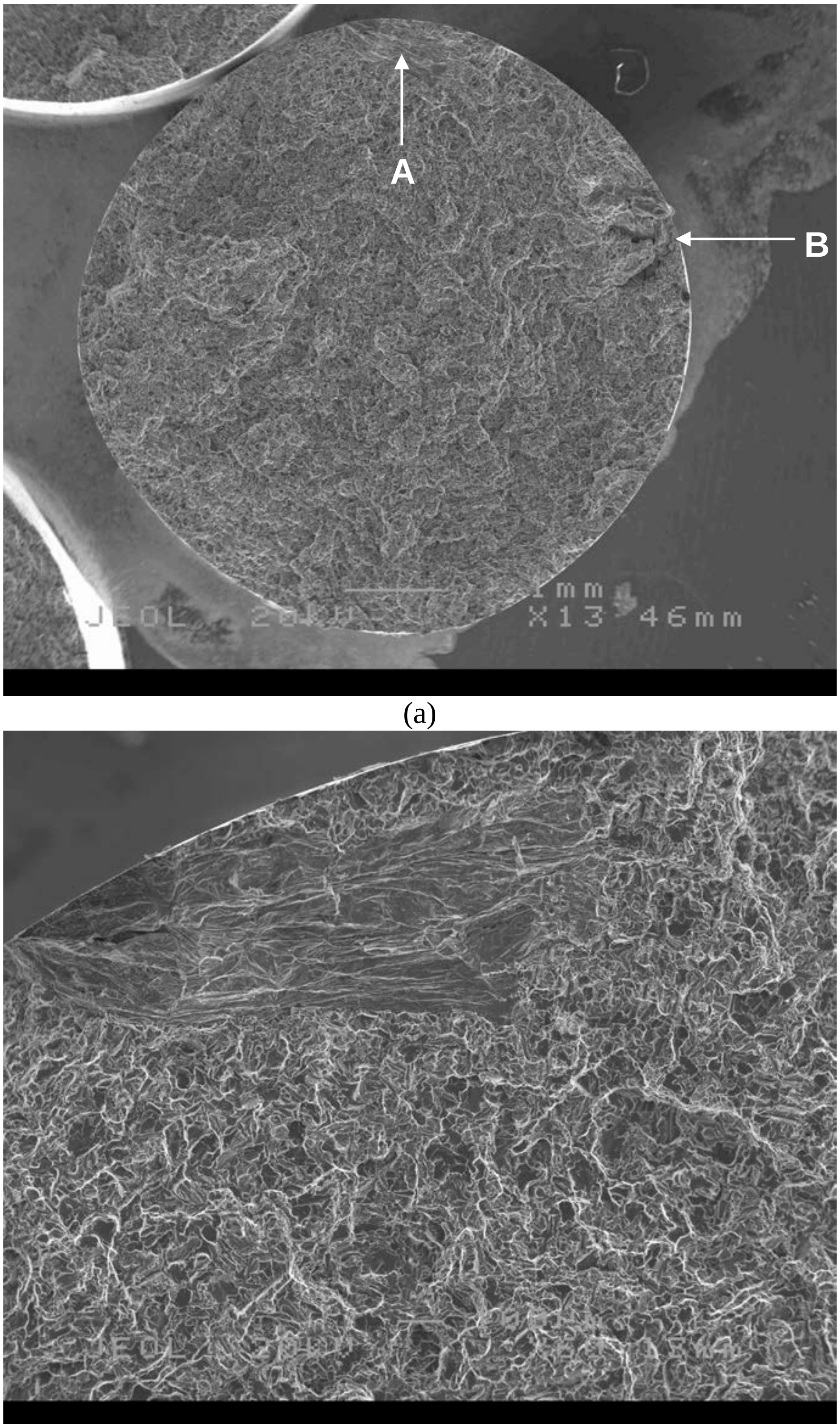

Figure 4.25 SEM micrograph of filtered tensile specimen failed at 242.7 MPa (a)X13 note the presence of two oxide films (b) structure of film A (X60)

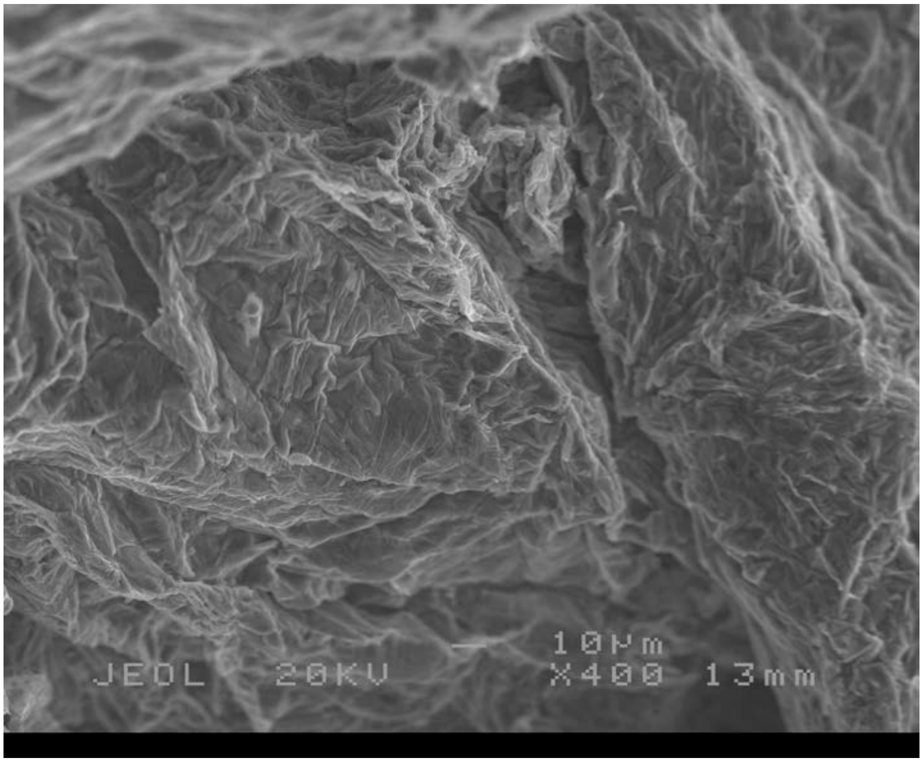

Figure 4.26 Higher magnification SEM micrograph of sample in 4.25, film B, note folded structure of oxide film

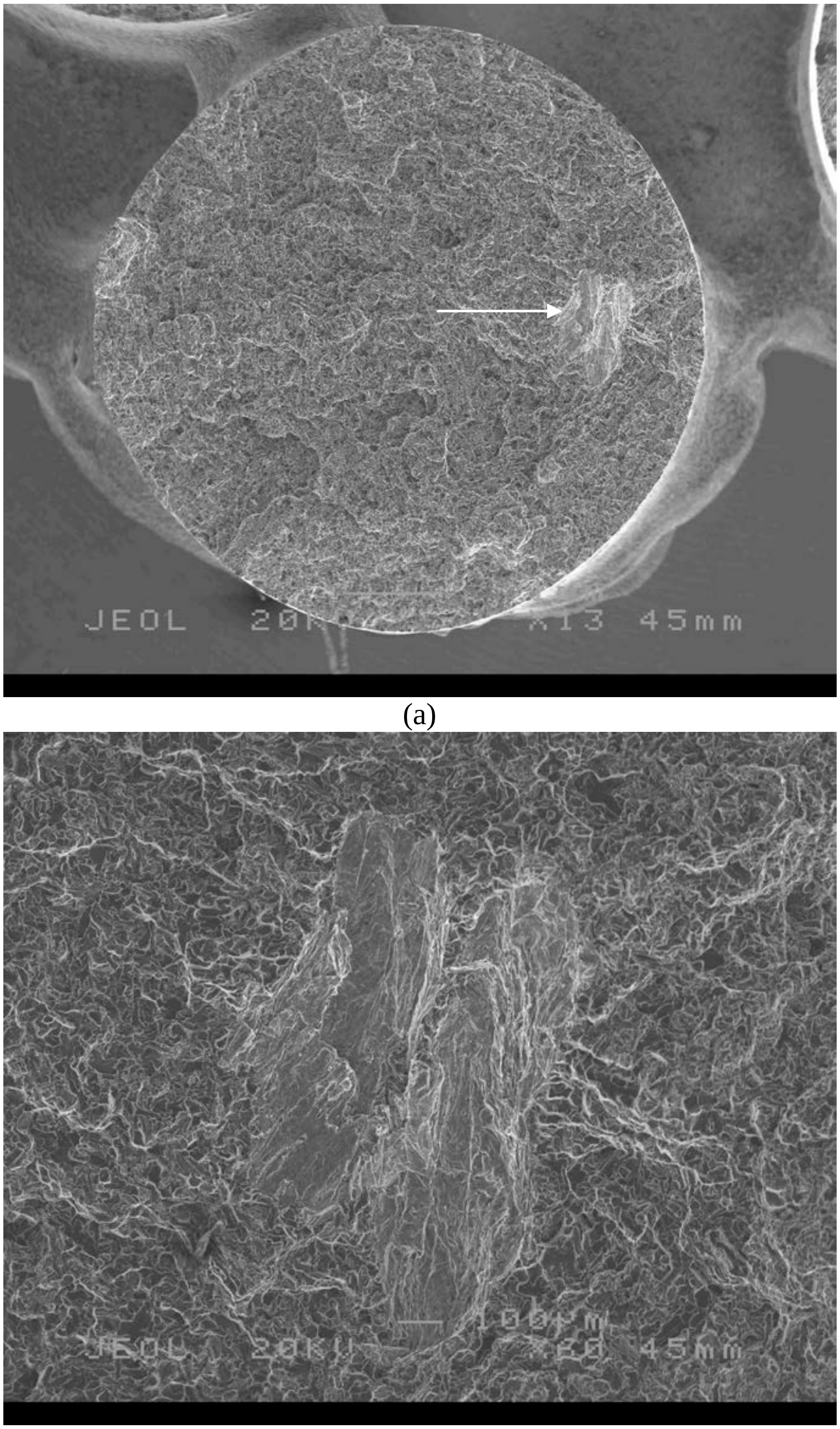

(a)

(b)

Figure 4.27 SEM micrograph unfiltered tensile specimen failed at 244.8 MPa (a) note presence of oxide film on fracture surface (arrow) (b) higher magnification (X60)

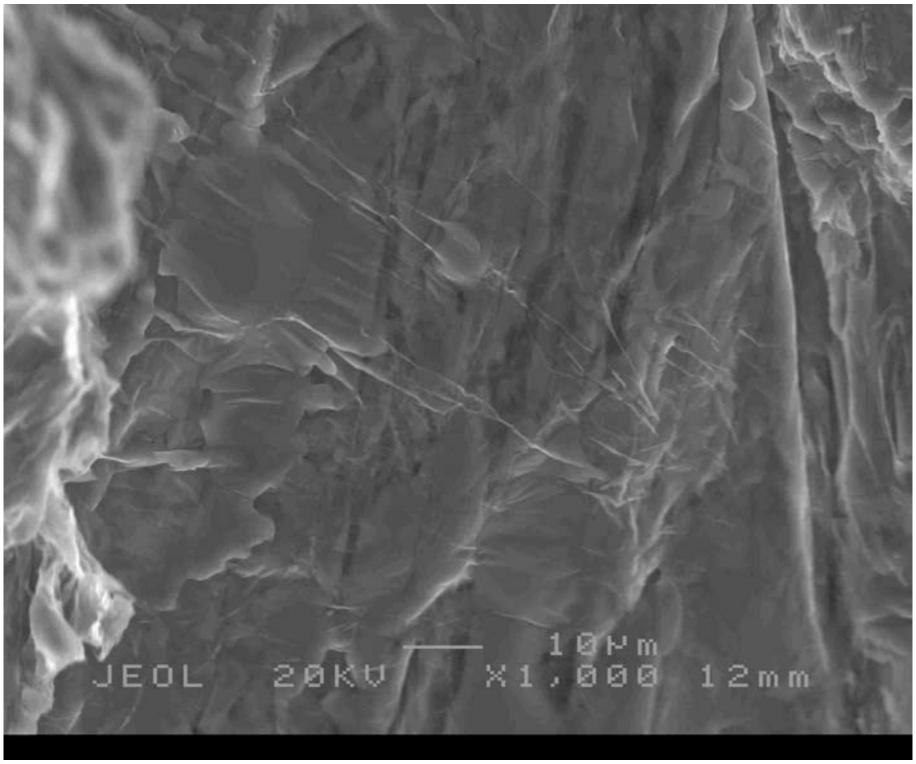

Figure 4.28 Higher magnification SEM micrograph of sample in Figure 4.27 note the presence of a thin transparent oxide film covering thicker oxide film

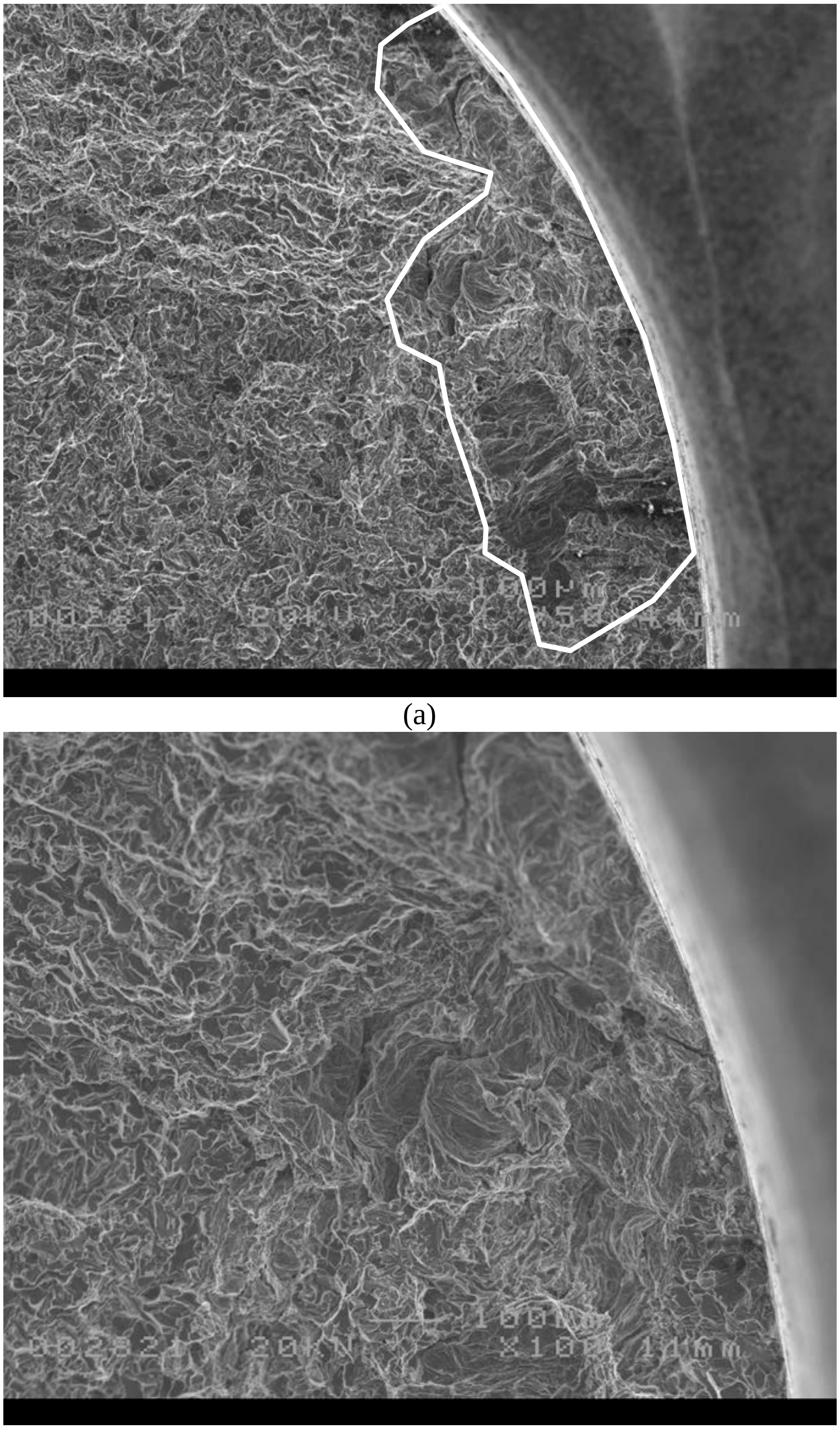

(a)

(b)

Figure 4.29 SEM micrograph of filtered tensile specimen failed at 254.7 MPa (a) note presence of oxide film on fracture surface (enclosed area) (b) X100, note folded structure of oxide film

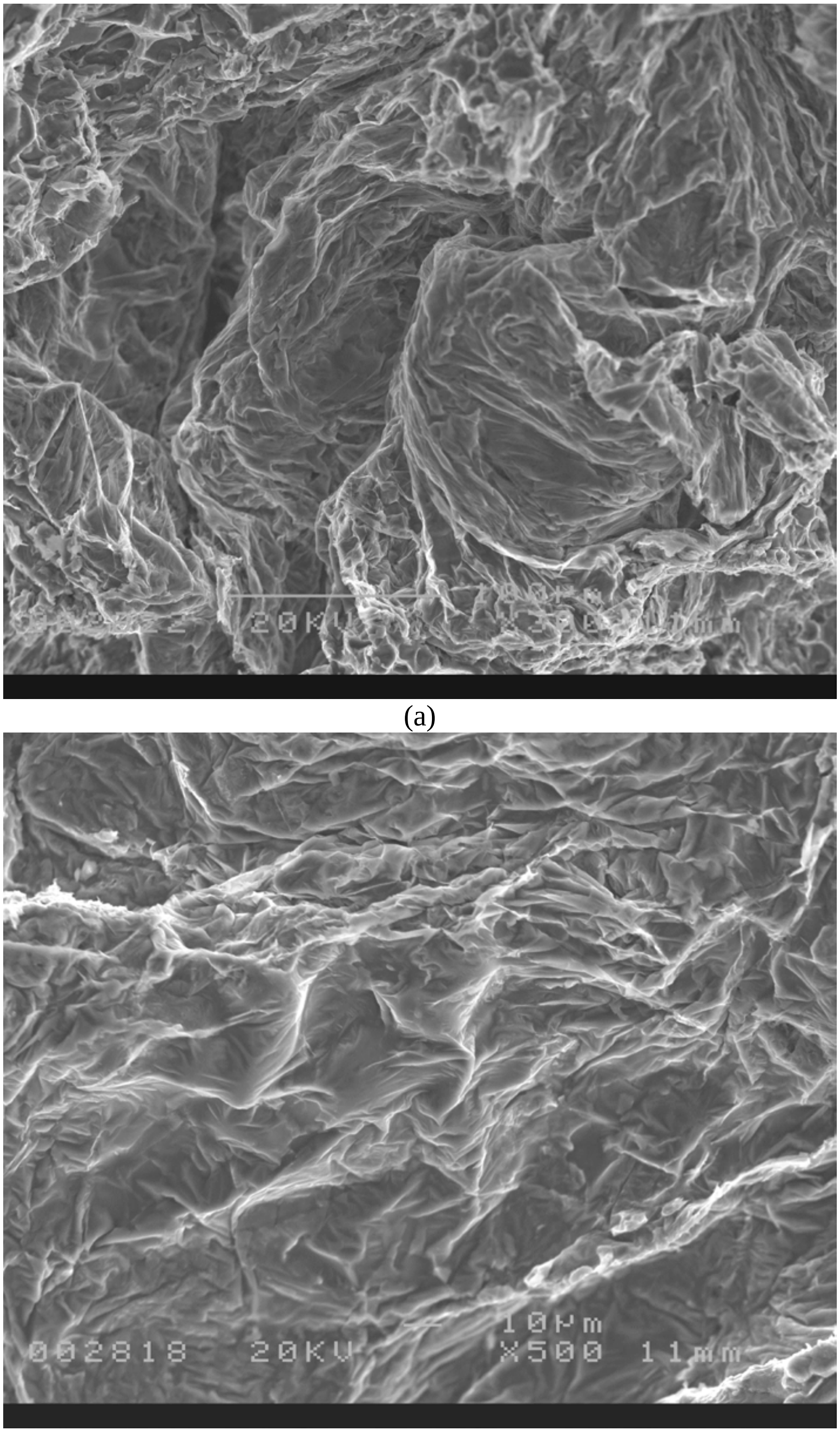

(a)

(b)

Figure 4.30 Higher magnification SEM micrograph of Figure 4.29 (a) X300 (b) X500

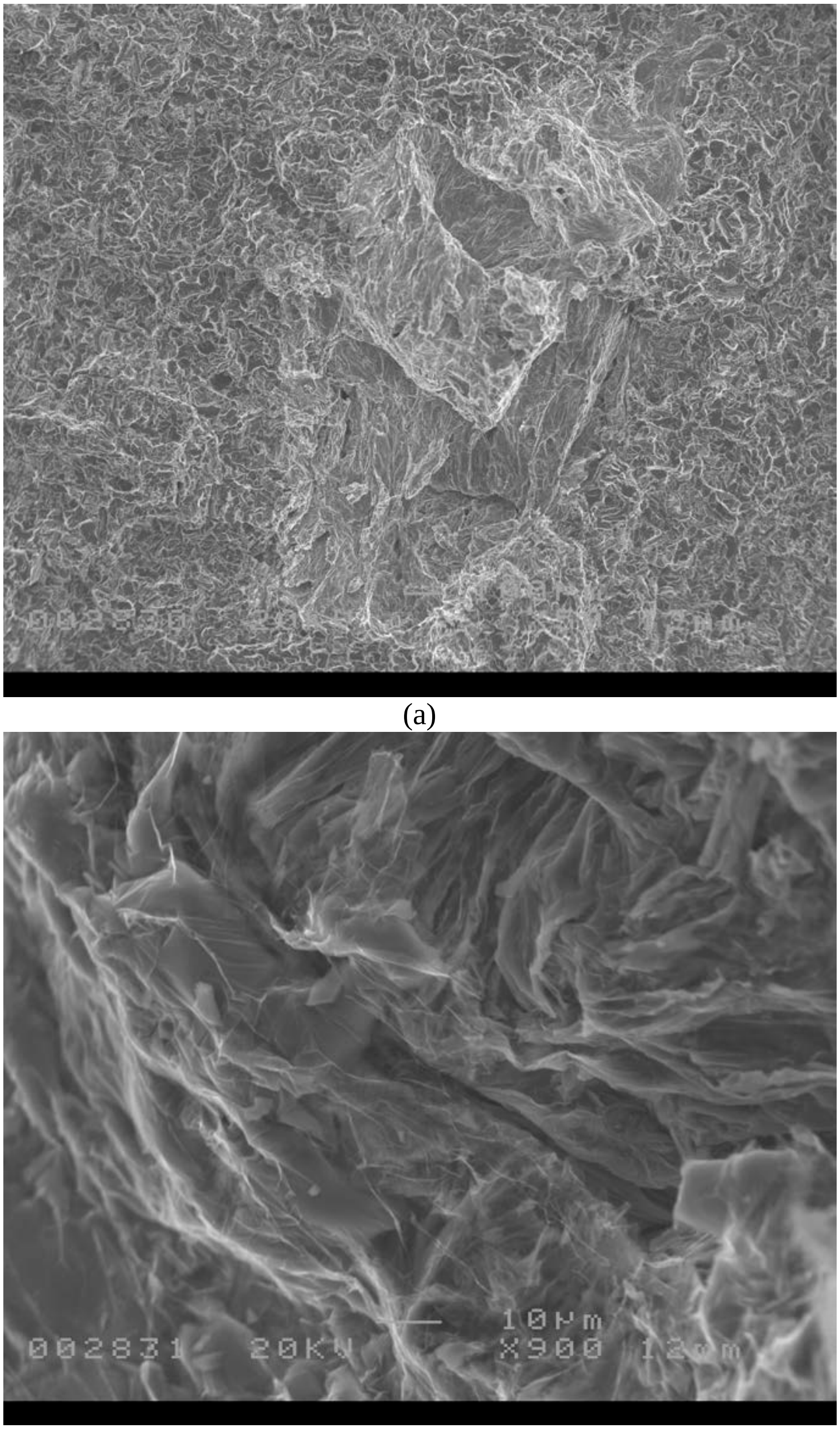

(a)

(b)

Figure 4.31 SEM micrograph of filtered tensile specimen failed at 255.9 MPa note presence of oxide film on fracture surface (a) X50 (b)X900 note the presence of both thin/transparent and thicker oxide films

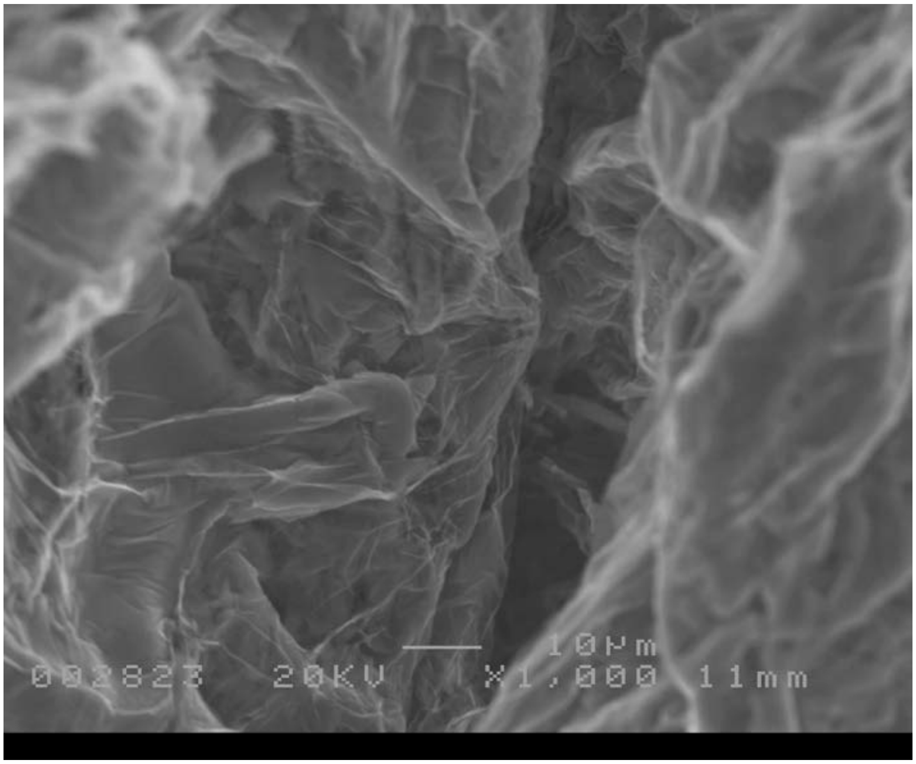

Figure 4.32 Higher magnification SEM micrograph of sample in Figure 4.31 note the thin folded structure of the oxide films present

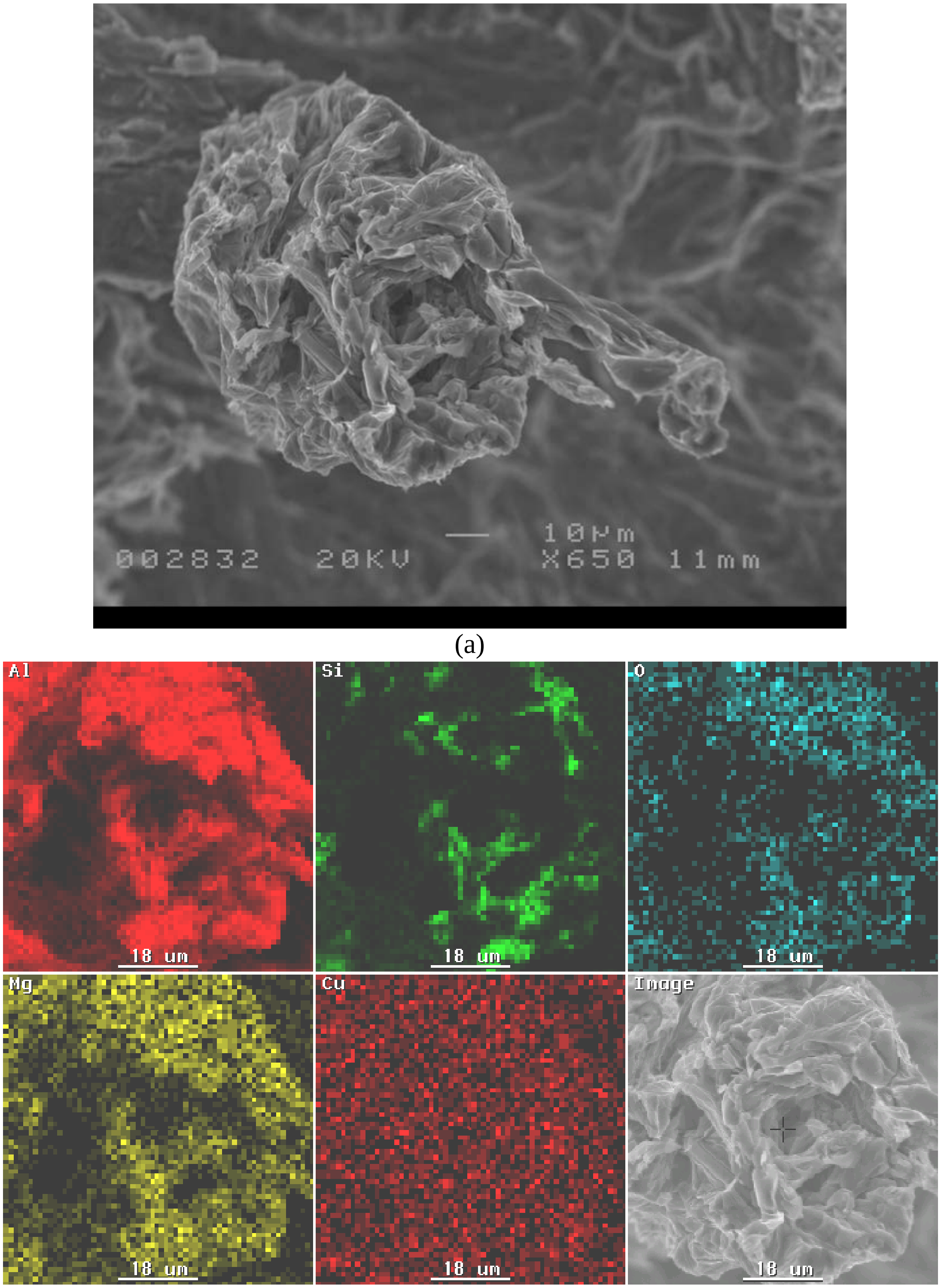

(a)

(b)

Figure 4.33 SEM micrograph of sample shown in Figure 4.31 (a) this spherical entangled film was found rising up from the fracture surface (b) x-ray maps of spherical entangled film, note the relatively high amounts of aluminum, oxygen and magnesium present

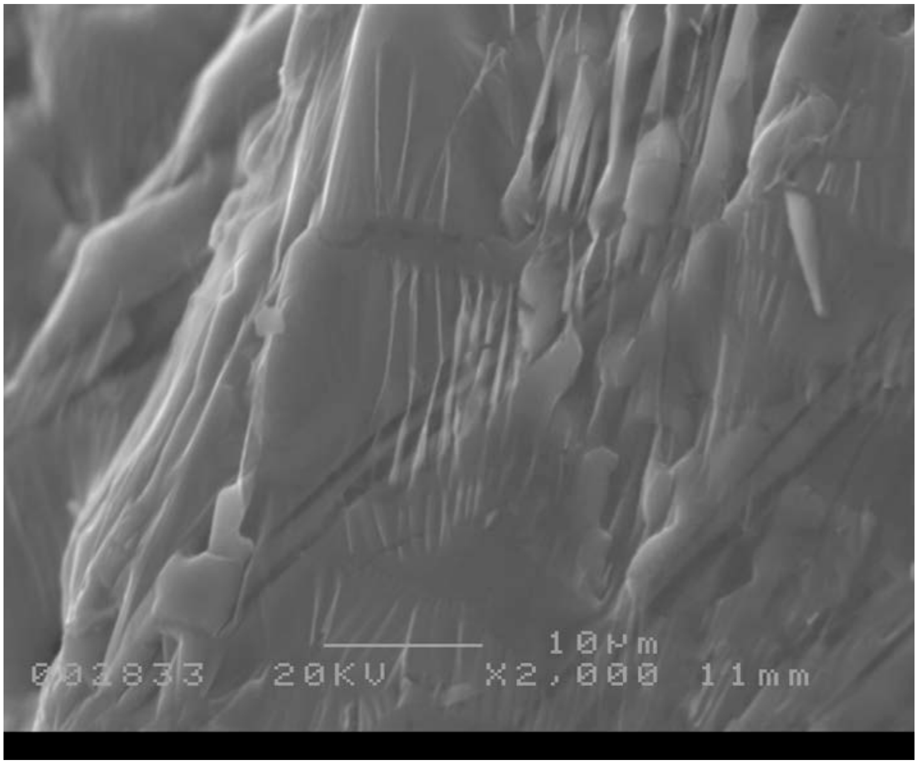

Figure 4.34 Higher magnification SEM micrograph of sample in Figure 4.31 note the presence of thin/transparent oxide films covering thicker oxide films

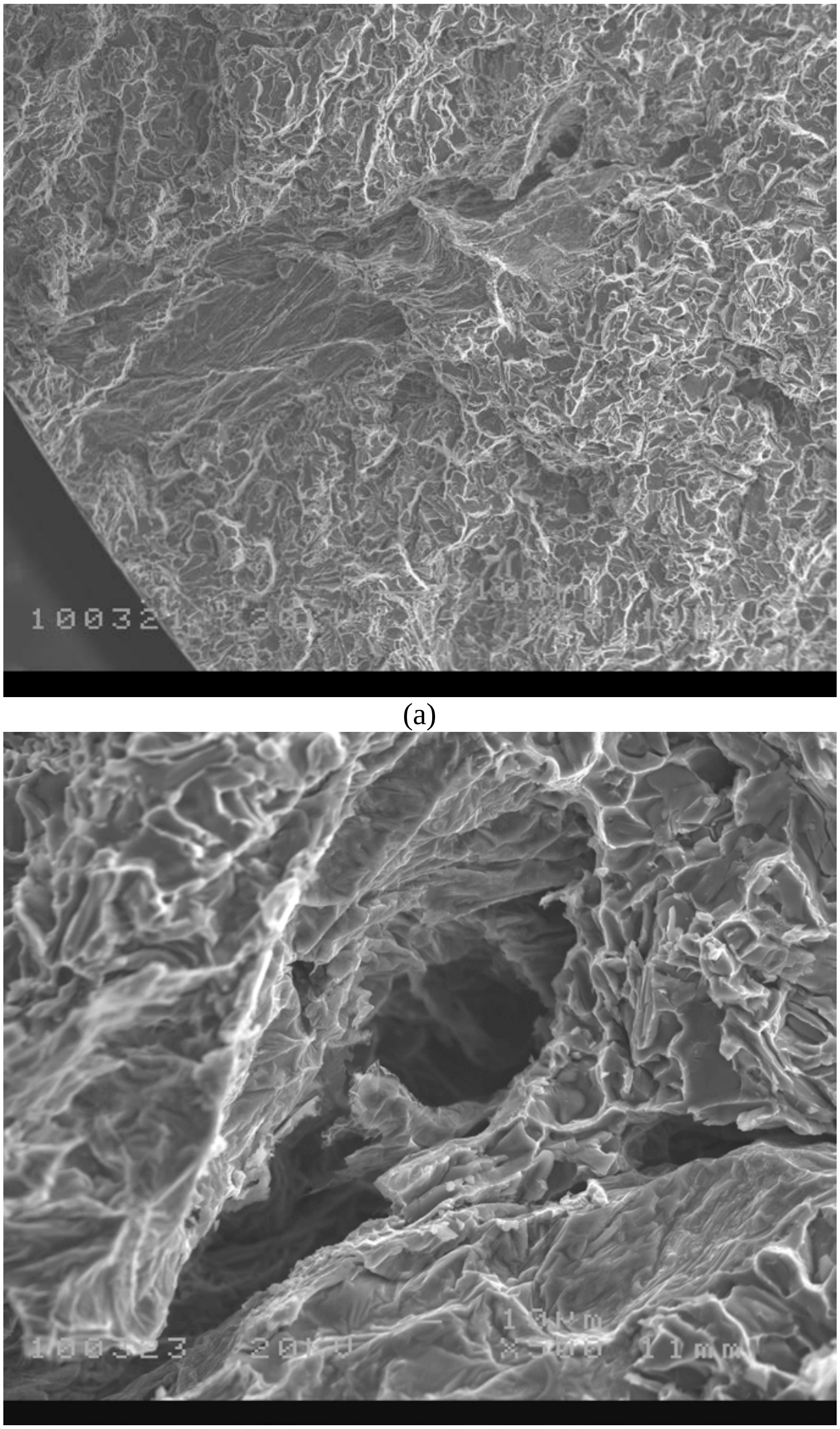

(a)

(b)

Figure 4.35 SEM micrograph of unfiltered tensile specimen failed at 259.5 MPa (a) X85, note the presence of oxide film and pore on fracture surface (b) X500, note the presence of folded oxide films covering inside surface of pore, indicating a bubble trail

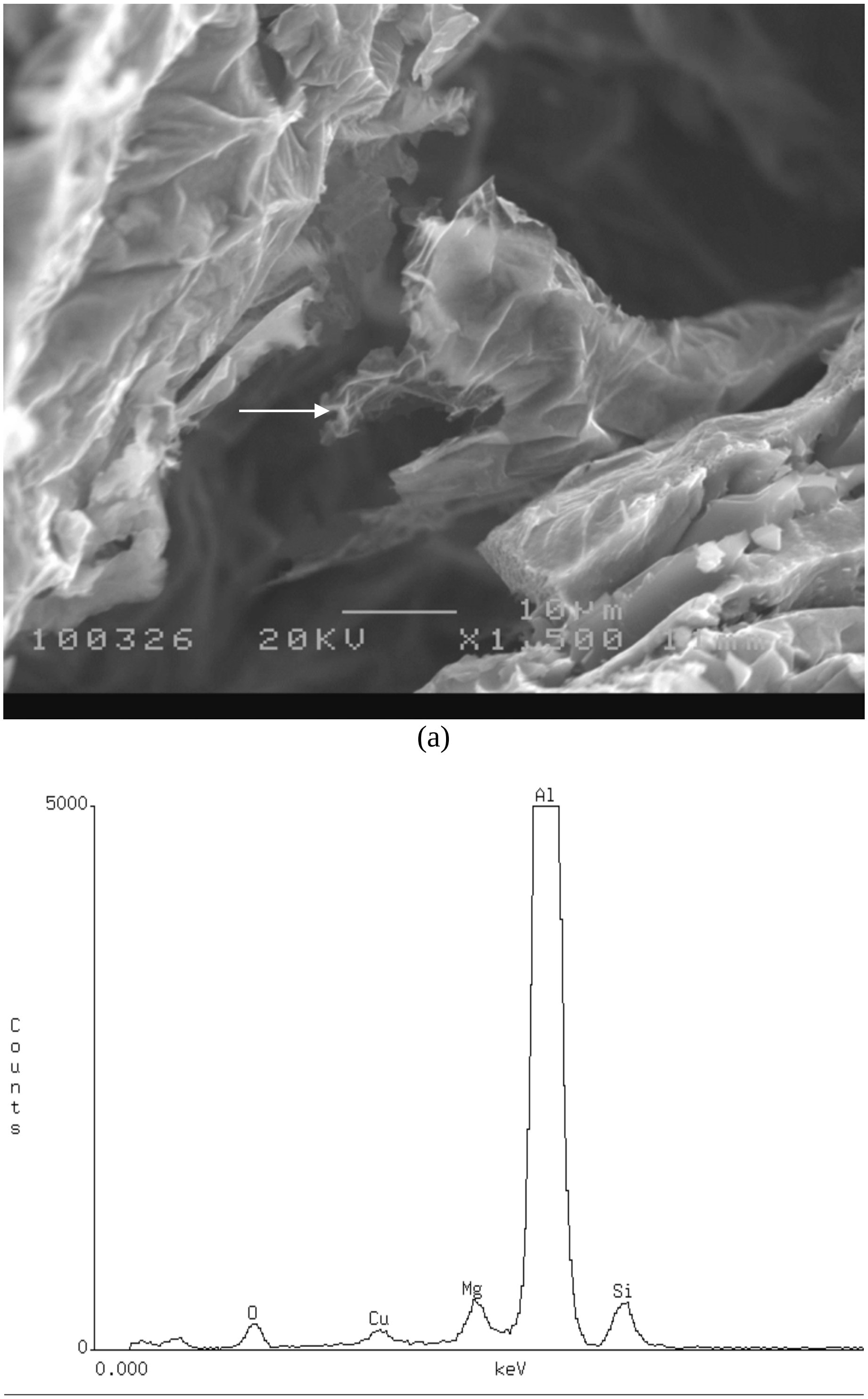

(a)

(b)

Figure 4.36 (a) SEM micrograph of fractured oxide film seen in Figure 4.35 (b) x-ray spectra of the thin film, exact location indicated by the arrow, note the presence of aluminum, magnesium and oxygen

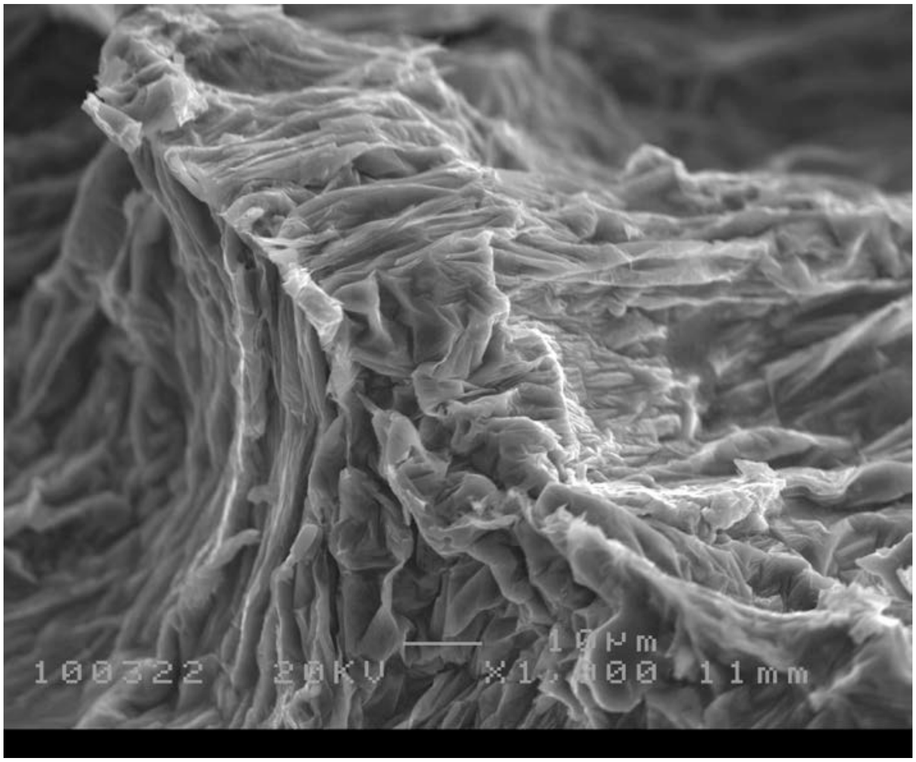

Figure 4.37 Higher magnification SEM micrograph of folded oxide seen near pore in Figure 4.35

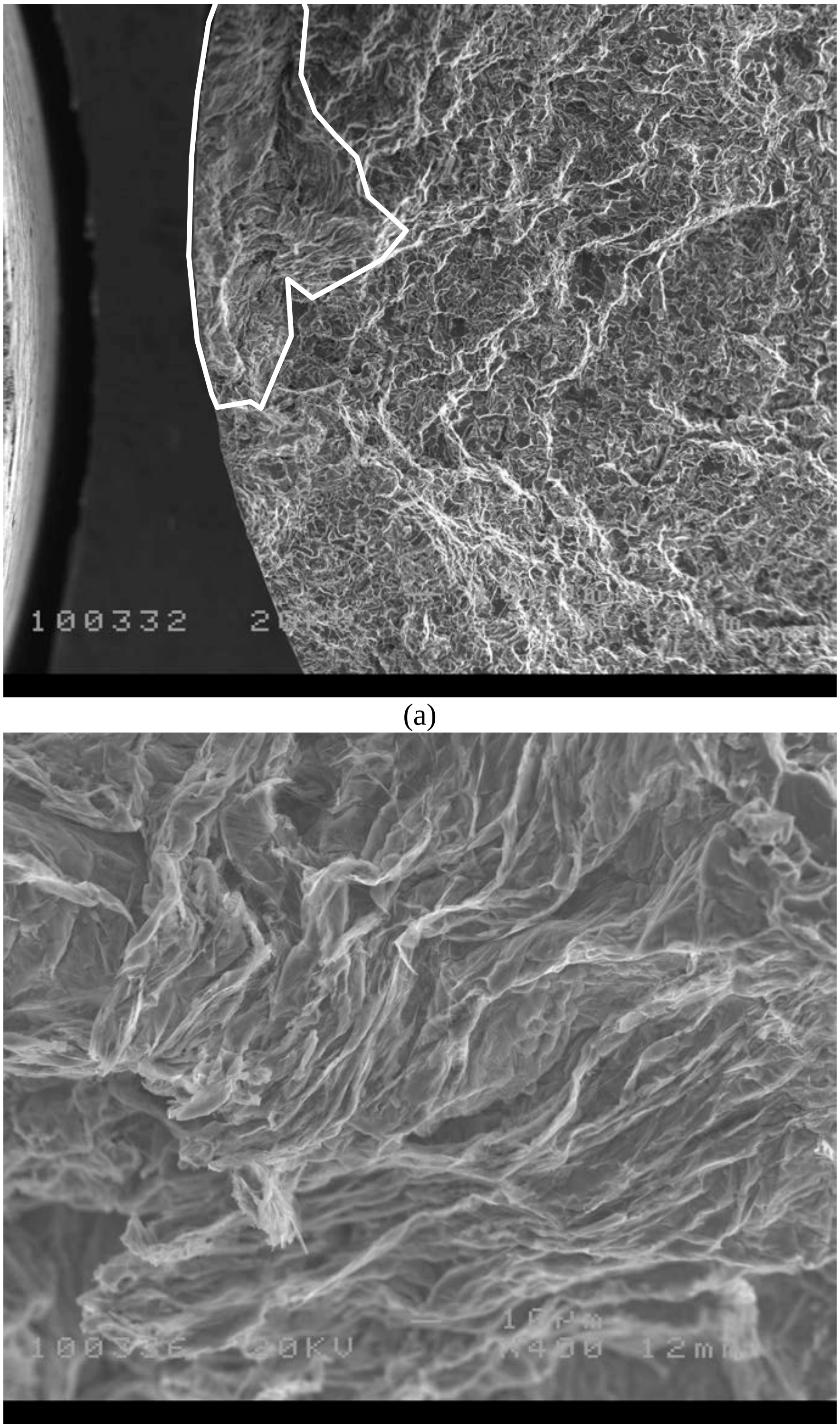

(a)

(b)

Figure 4.38 SEM micrograph of filtered tensile specimen failed at 261.1 MPa (a) X50 note the presence of oxide film on fracture surface (enclosed area) (b) X400, showing folded structure of oxide film

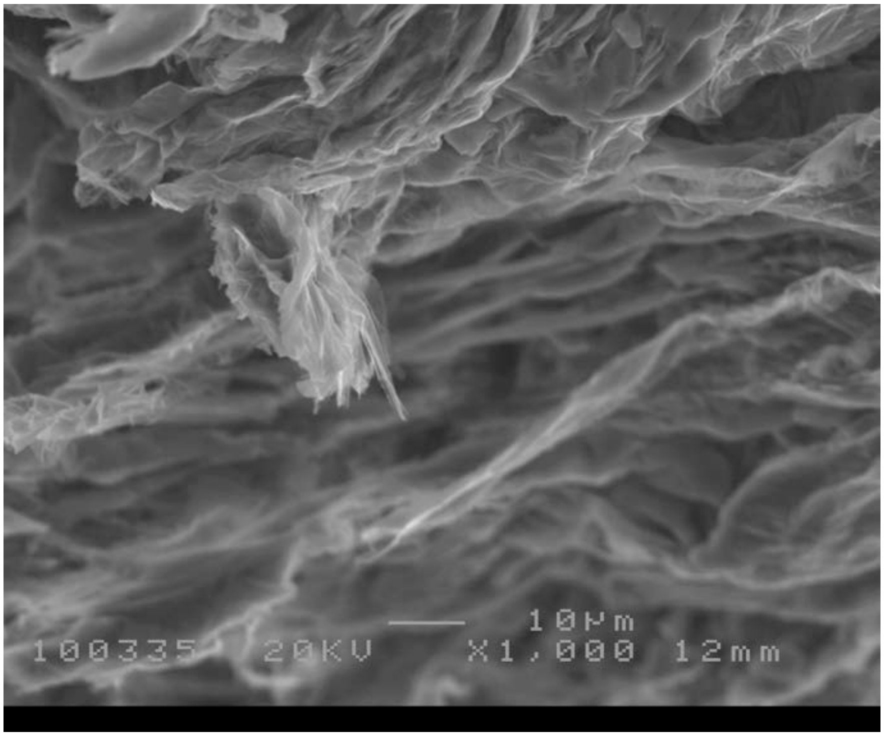

Figure 4.39 Higher magnification SEM micrograph of folded oxide seen in Figure 4.38, showing fractured thin oxide film

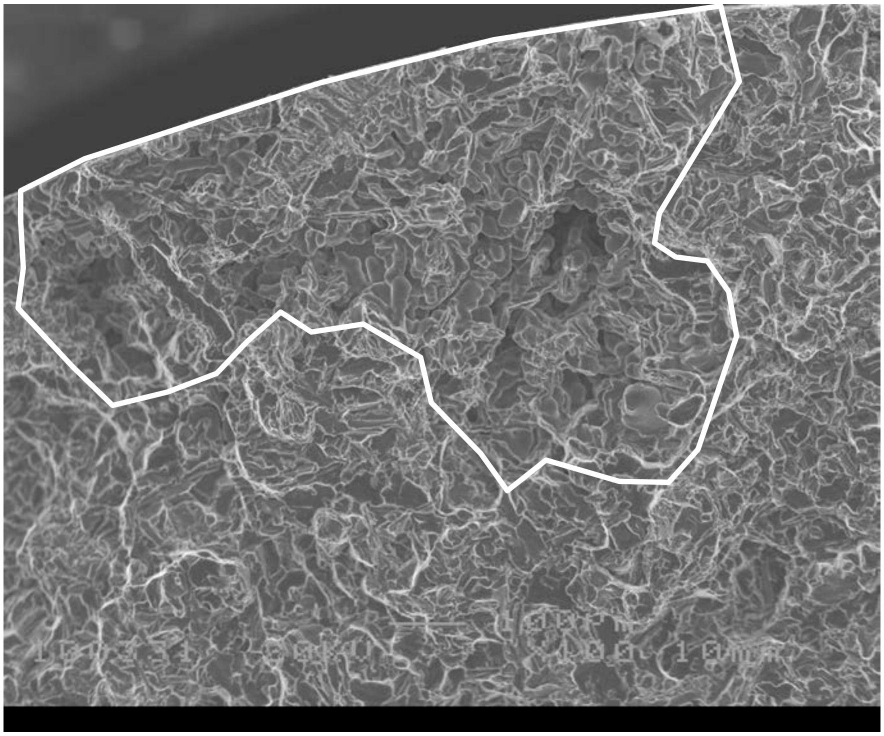

Figure 4.40 SEM micrograph of unfiltered tensile specimen failed at 259.8 MPa note the presence of shrinkage pore network (enclosed area)

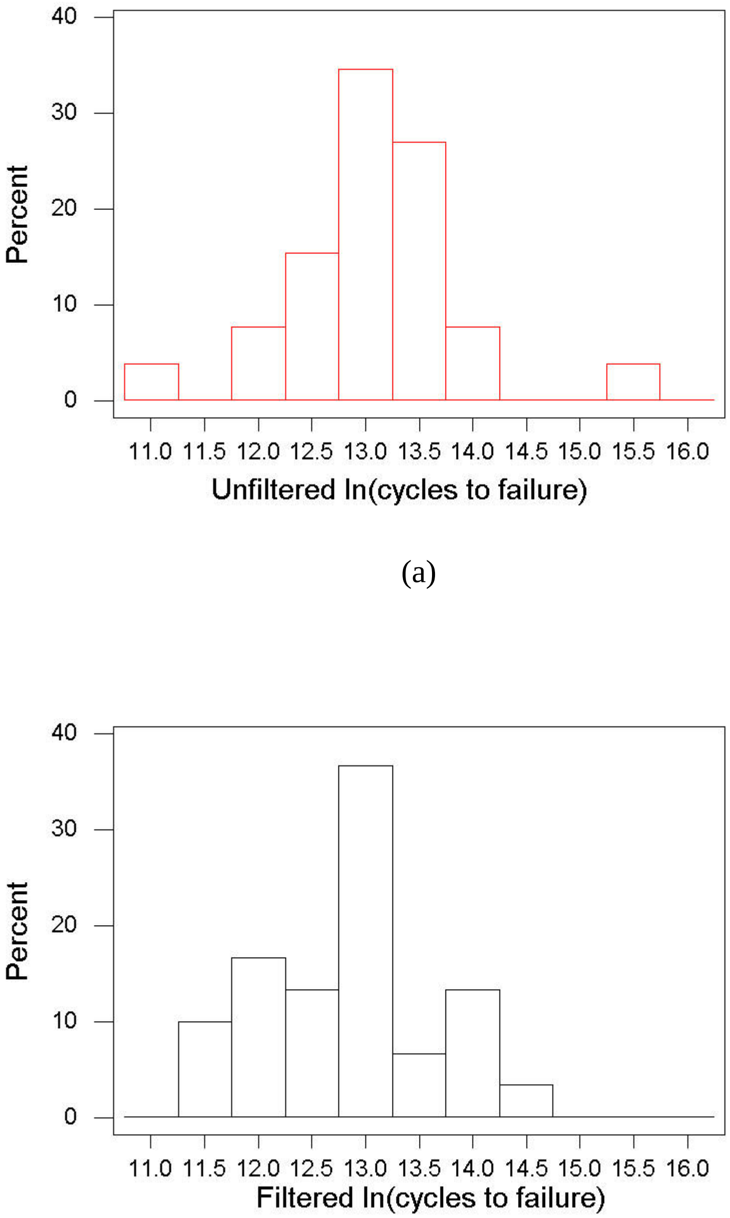

(a)

(b)

Figure 4.41 Histograms of the natural logarithm of fatigue life for (a) unfiltered and (b) filtered samples

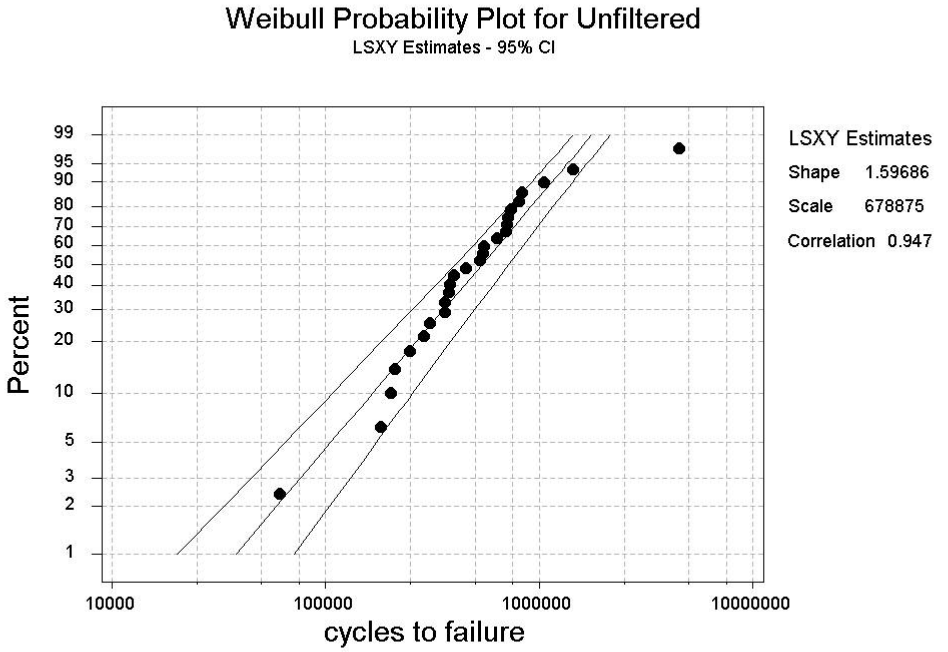

(a)

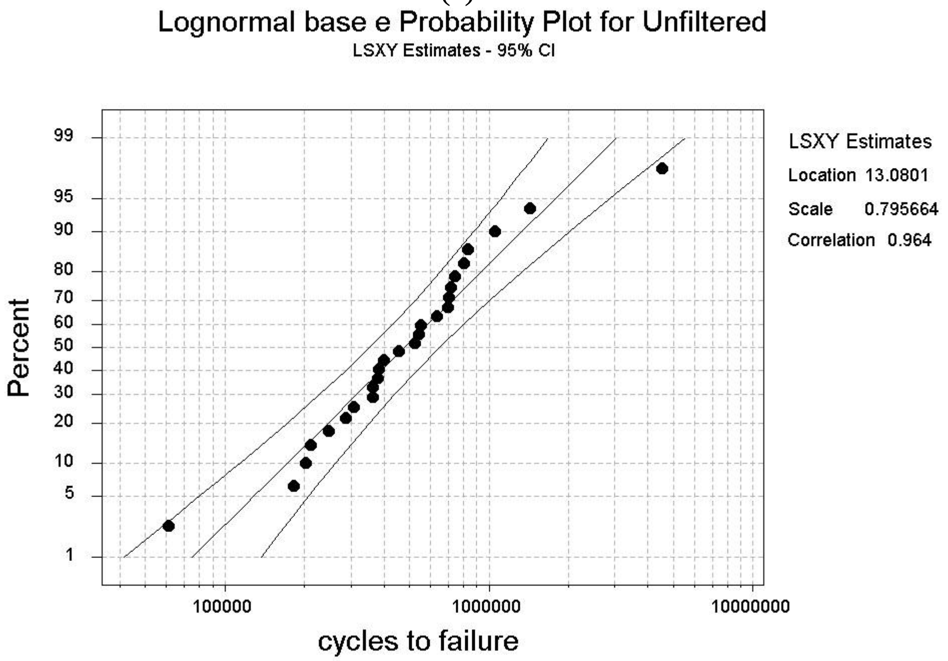

(b)

Figure 4.42 Probability distribution plots for fatigue life of unfiltered samples fitted for (a)Weibull and (b)Lognormal distributions

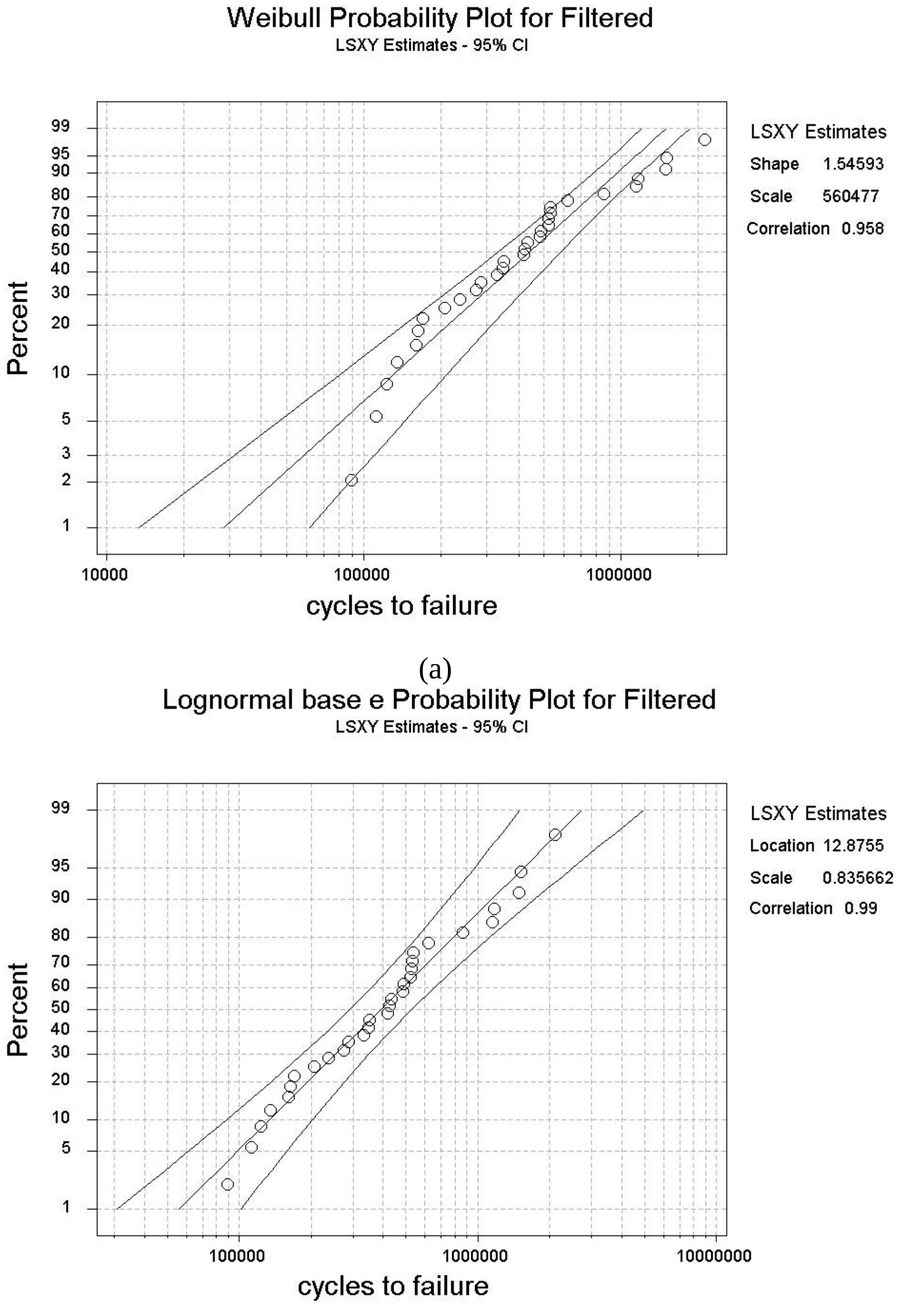

(b)

Figure 4.43 Probability distribution plots for fatigue life of filtered samples fitted for (a)Weibull and (b)Lognormal distributions

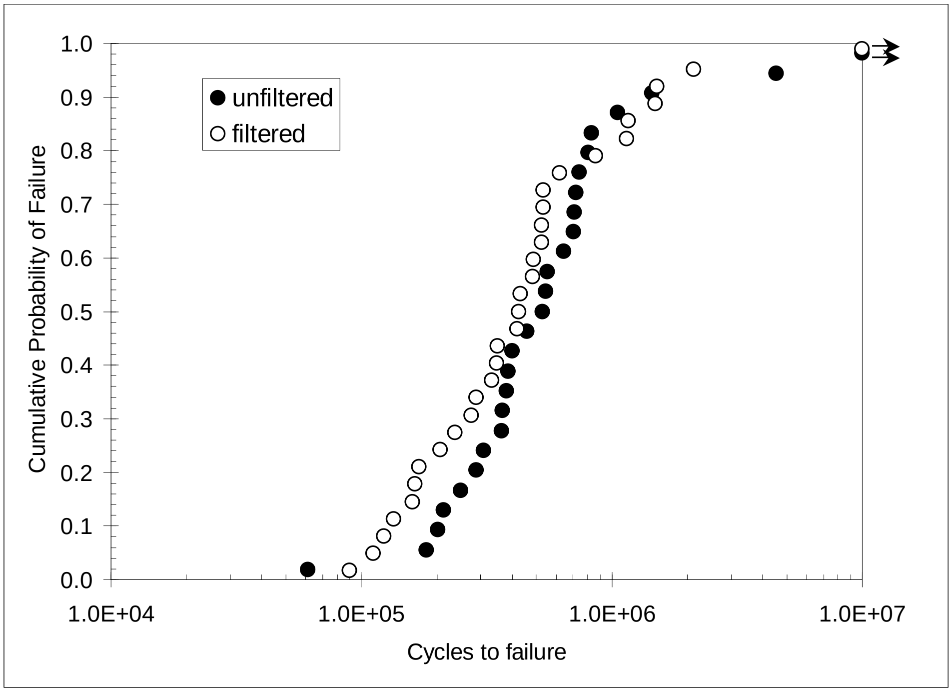

Figure 4.44 Cumulative probability plot of fatigue lives for unfiltered and filtered samples

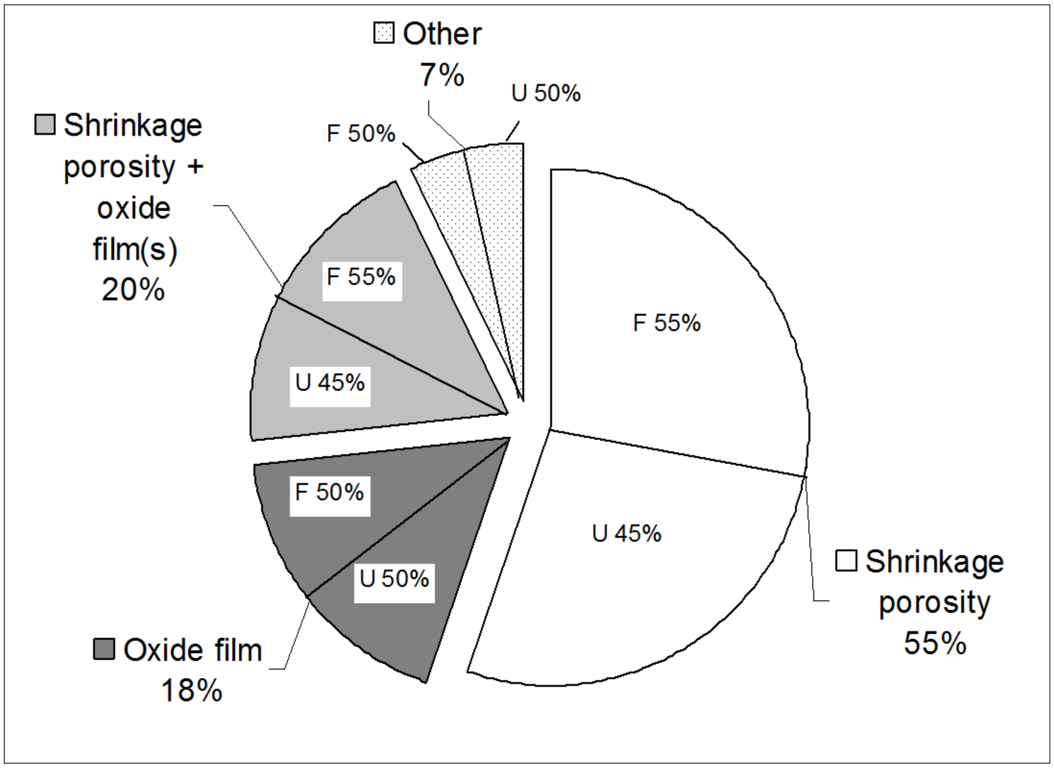

Figure 4.45 Pie chart showing percent frequency of initiation site types (further divided into U, unfiltered and F, filtered)

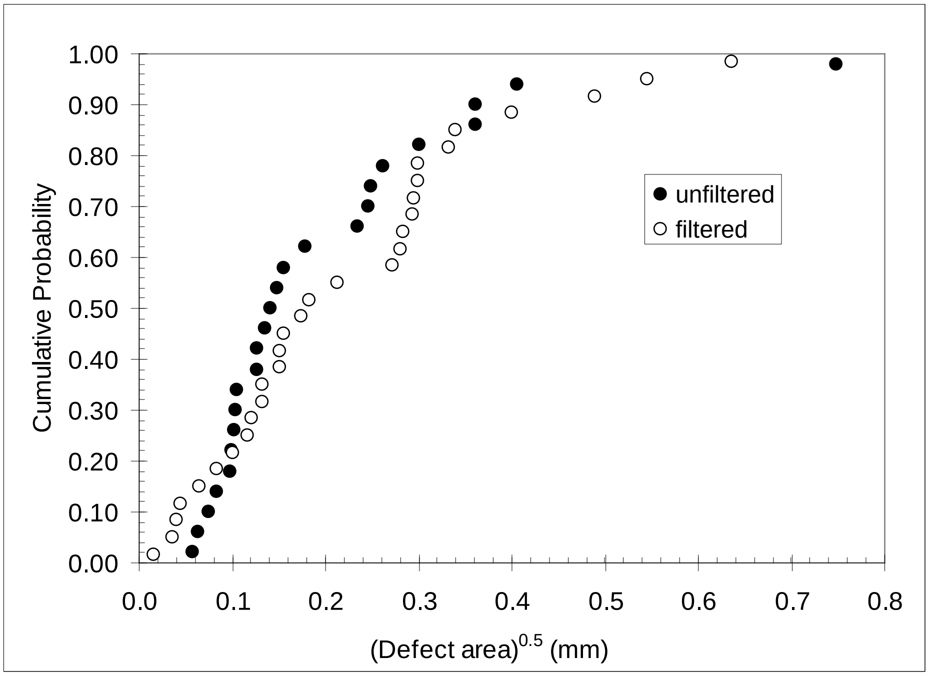

Figure 4.46 Cumulative probability of occurrence of initiation site size (square root of defect area)

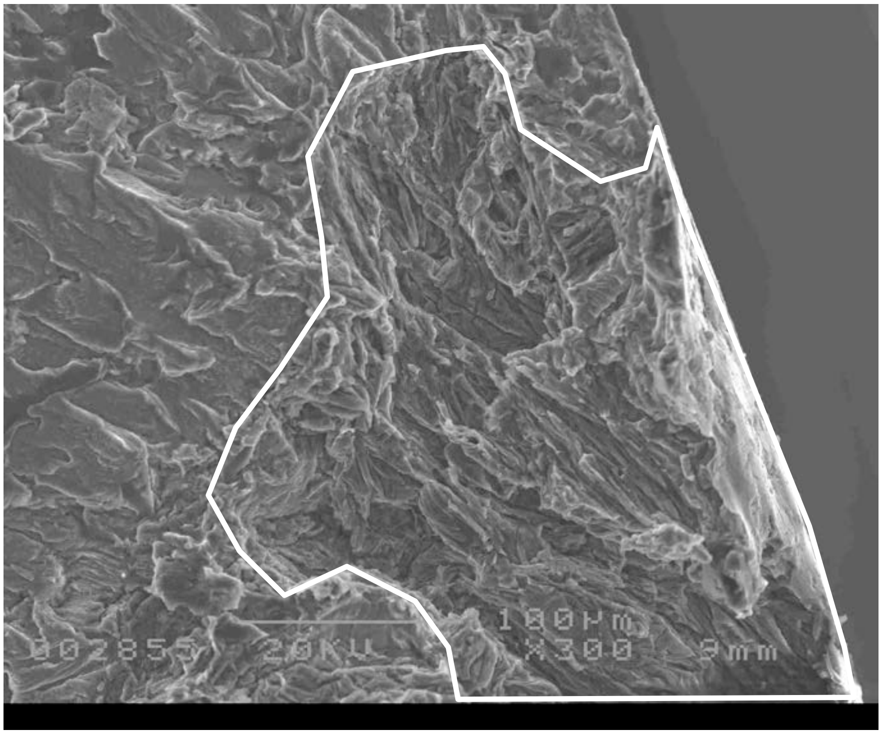

Figure 4.47 SEM micrograph of filtered fatigue sample lasting 123,100 cycles with oxide film acting as initiation site (enclosed area)

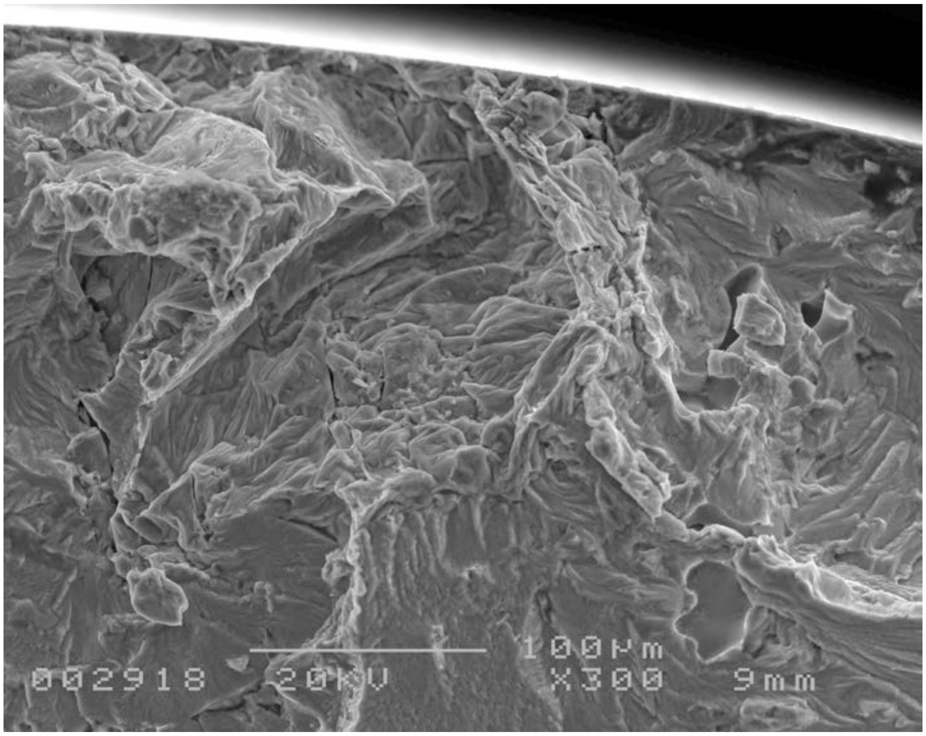

Figure 4.48 SEM micrograph of filtered fatigue sample lasting 286,800 cycles with oxide film acting as initiation site

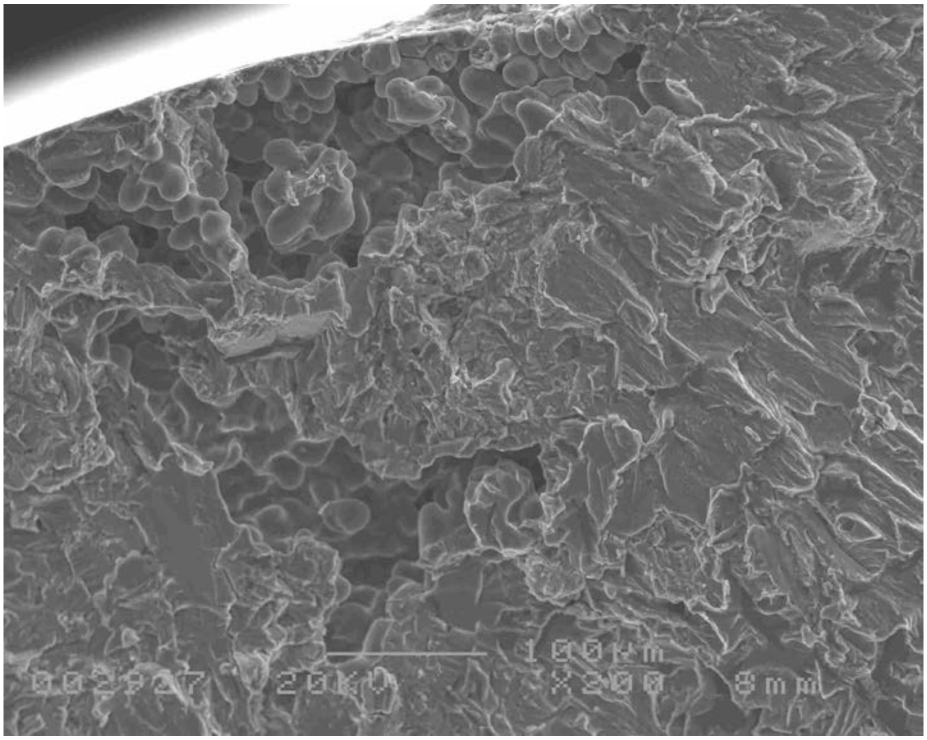

Figure 4.49 SEM micrograph of filtered fatigue sample lasting 163,300 cycles with large shrinkage pore network acting as initiation point

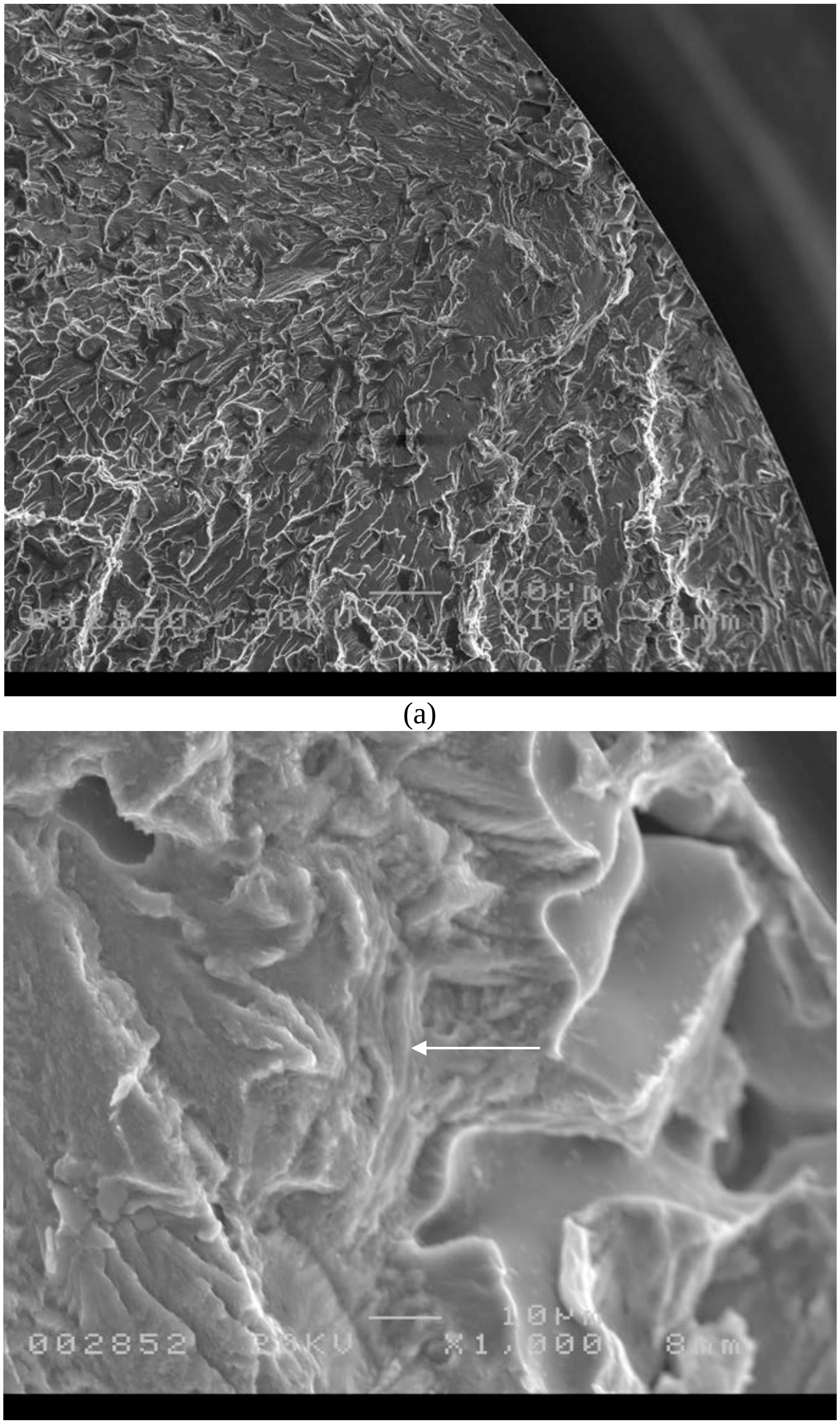

(a)

(b)

Figure 4.50 SEM micrograph of filtered fatigue sample lasting 419,500 cycles with (a) shrinkage pore network acting as initiation site (b) X1000, showing old oxide associated with pore (arrow)

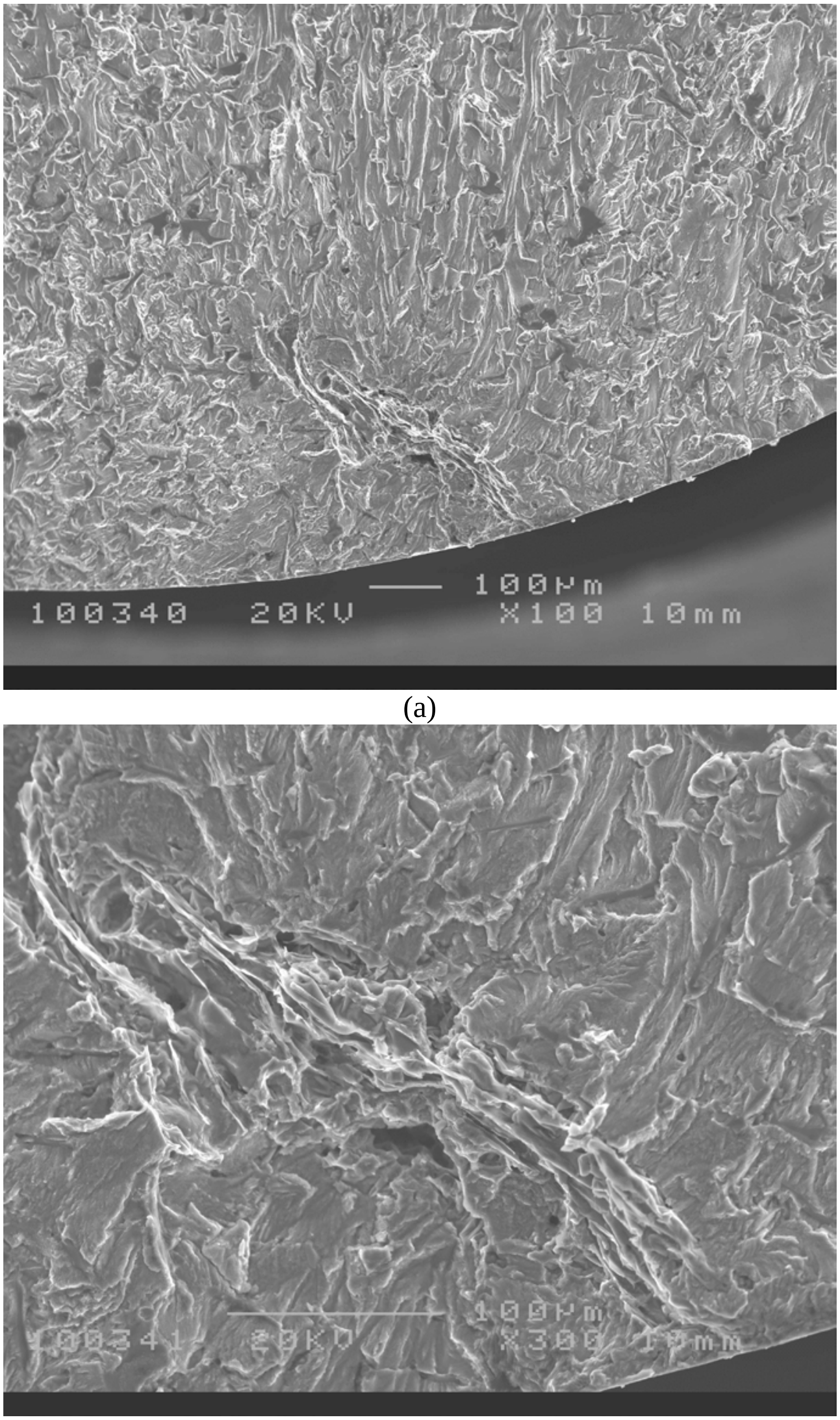

(a)

(b)

Figure 4.51 SEM micrograph of filtered fatigue sample lasting 524,700 cycles with (a) oxide film acting as initiation site (b) higher magnification X300 of oxide film, note folded structure

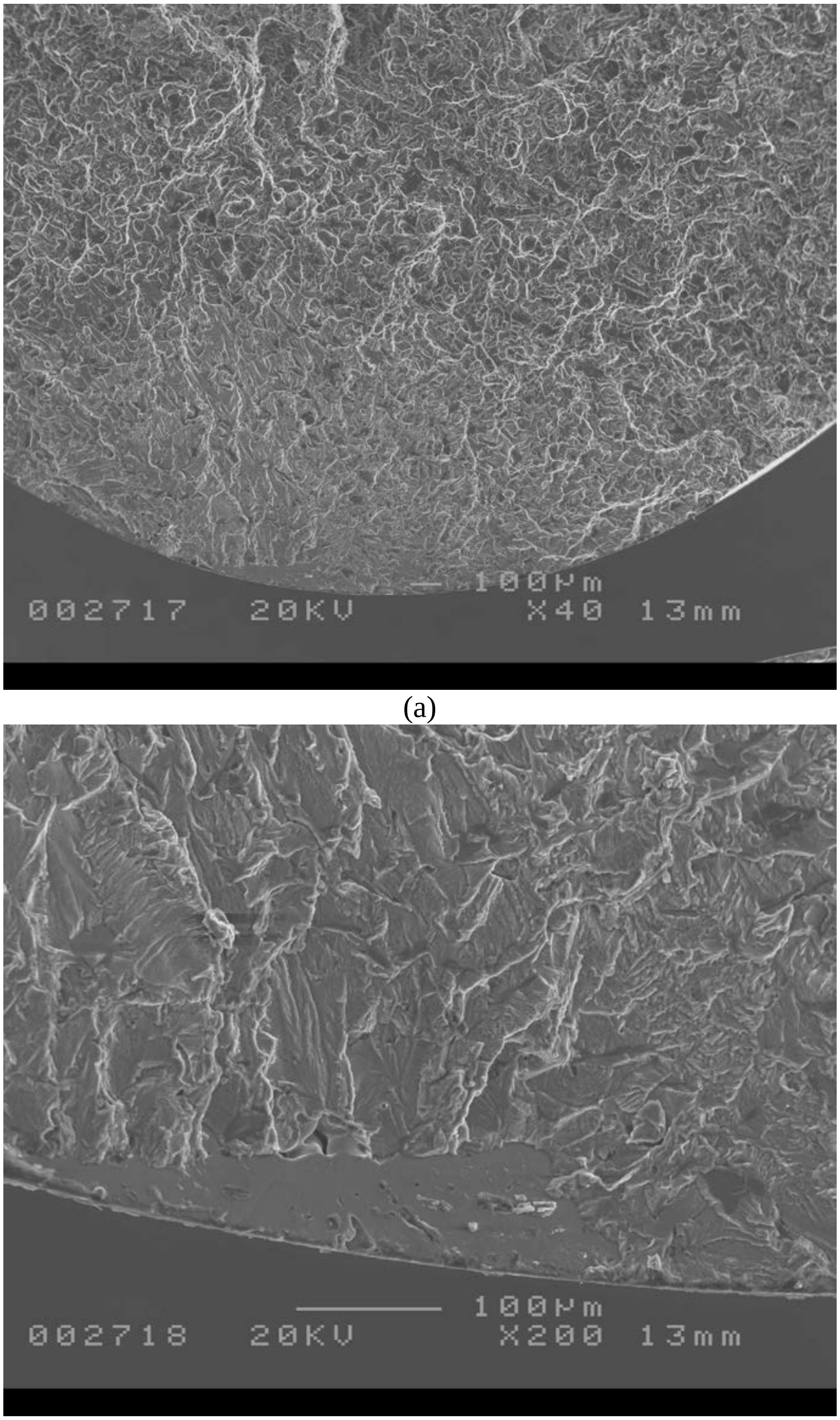

(a)

(b)

Figure 4.52 SEM micrograph of filtered fatigue sample lasting 862,400 cycles (a) showing location of initiation site (b) higher magnification X200, showing small pore and faceted feature containing surface extrusions (slip bands)

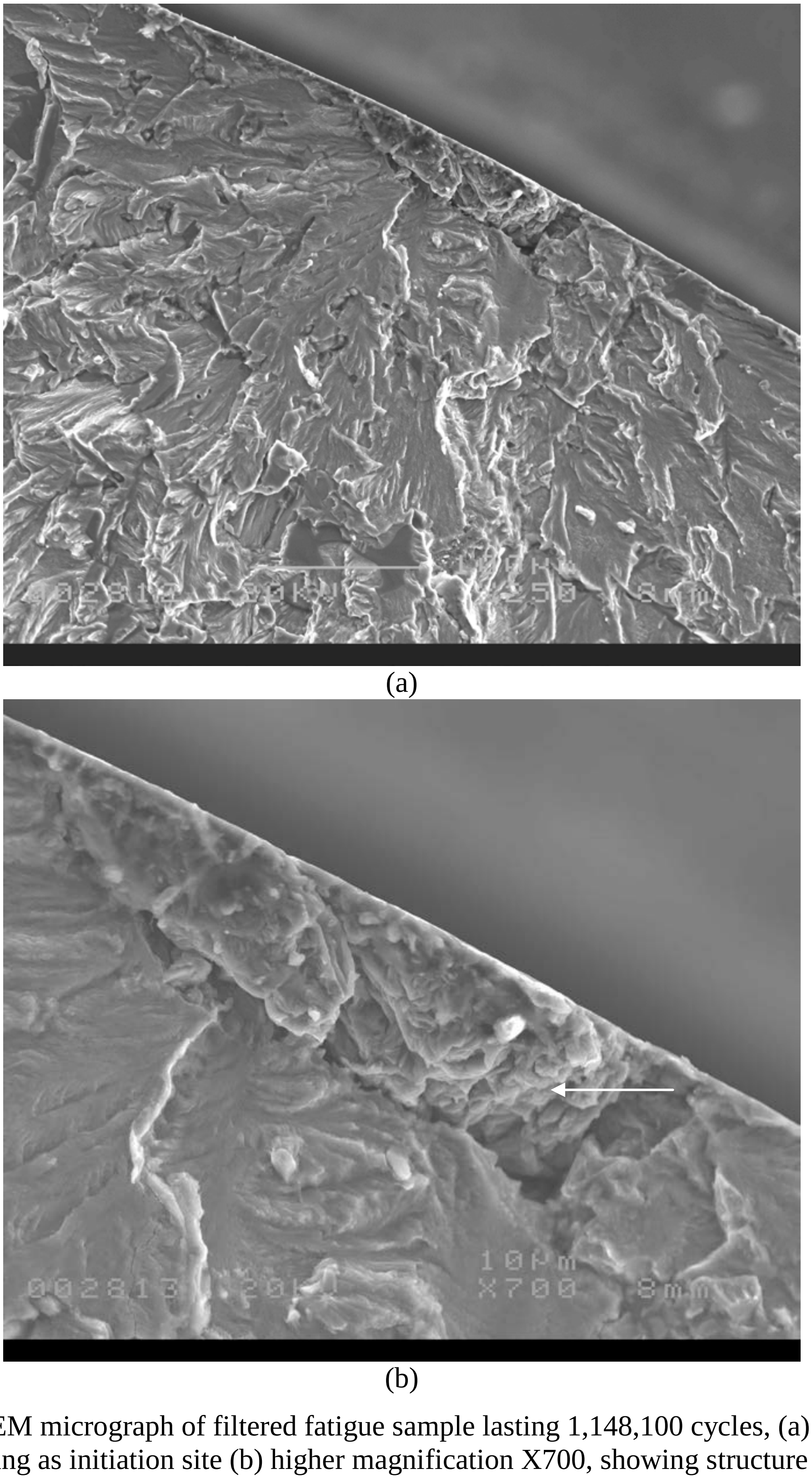

(a)

(b)

Figure 4.53 SEM micrograph of filtered fatigue sample lasting 1,148,100 cycles, (a) showing oxide film acting as initiation site (b) higher magnification X700, showing structure of folded oxide film (arrow)

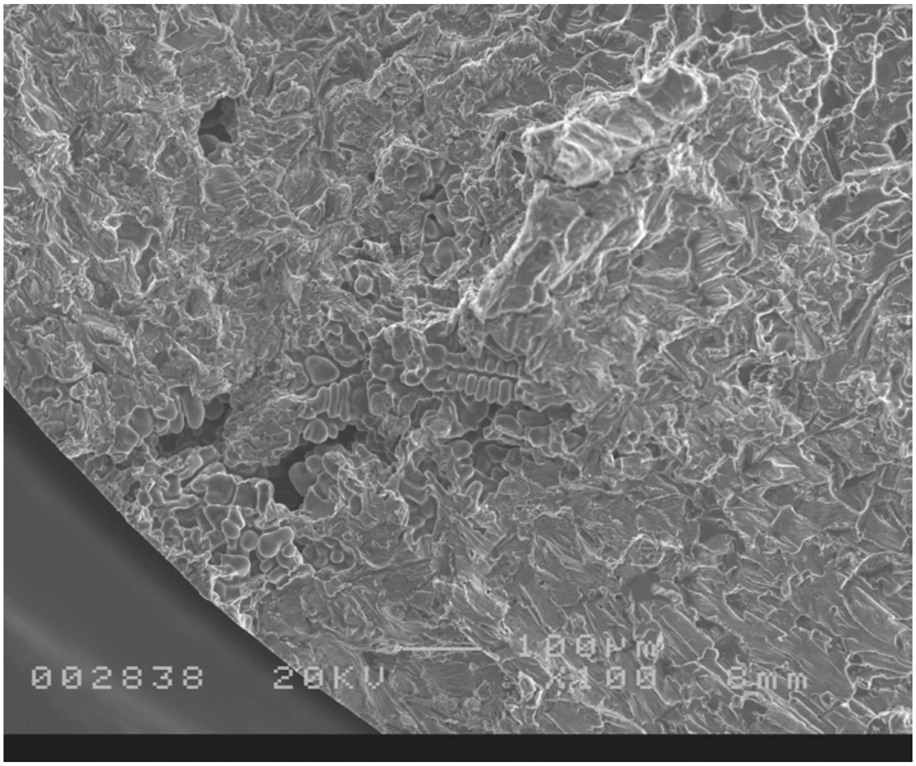

Figure 4.54 SEM micrograph of unfiltered fatigue sample lasting 182,400 cycles with shrinkage pore network acting as initiation site

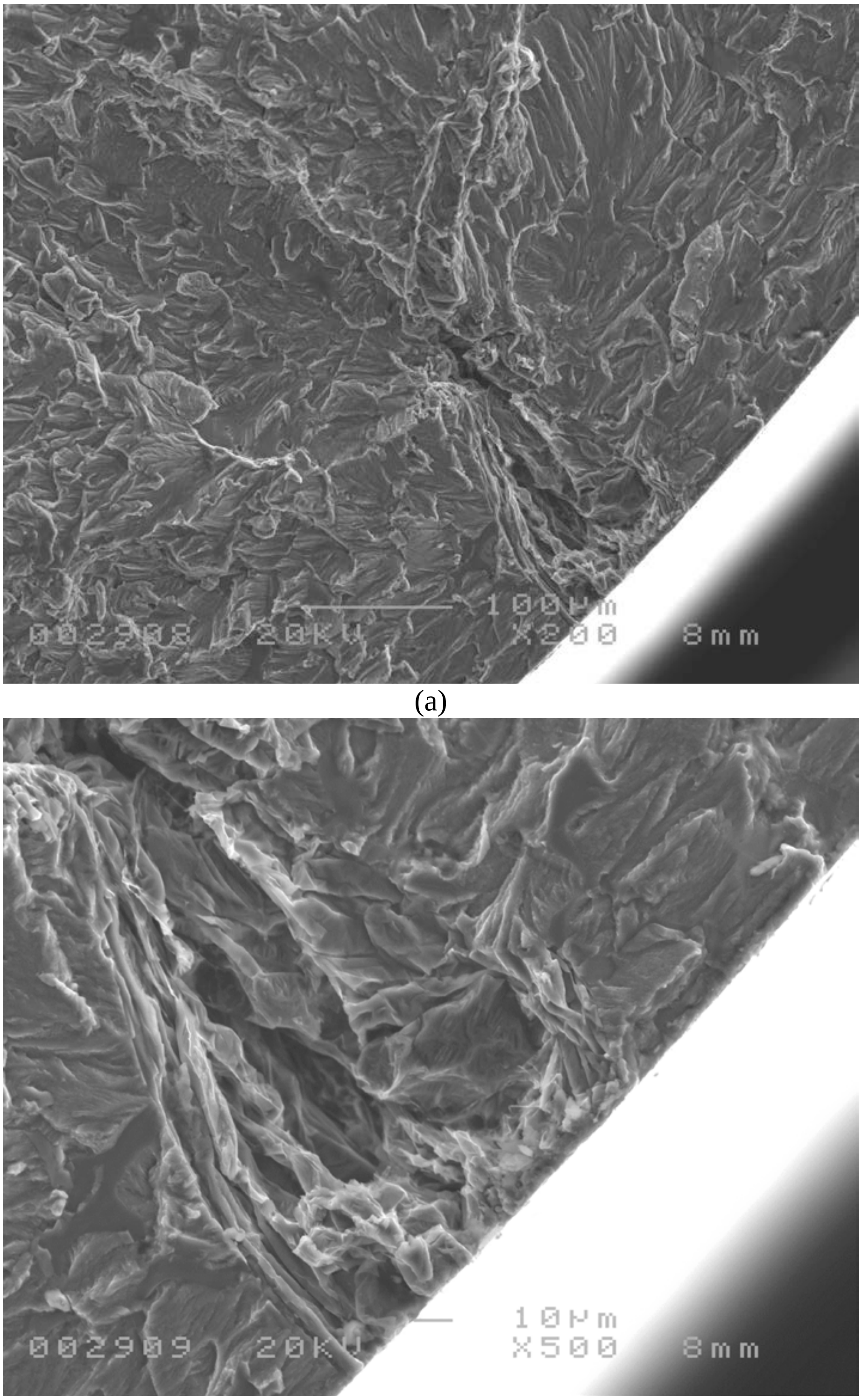

(a)

(b)

Figure 4.55 SEM micrograph of unfiltered fatigue sample lasting 288,900 cycles (a) with oxide film acting as initiation site (b) higher magnification X500, showing structure of folded oxide film

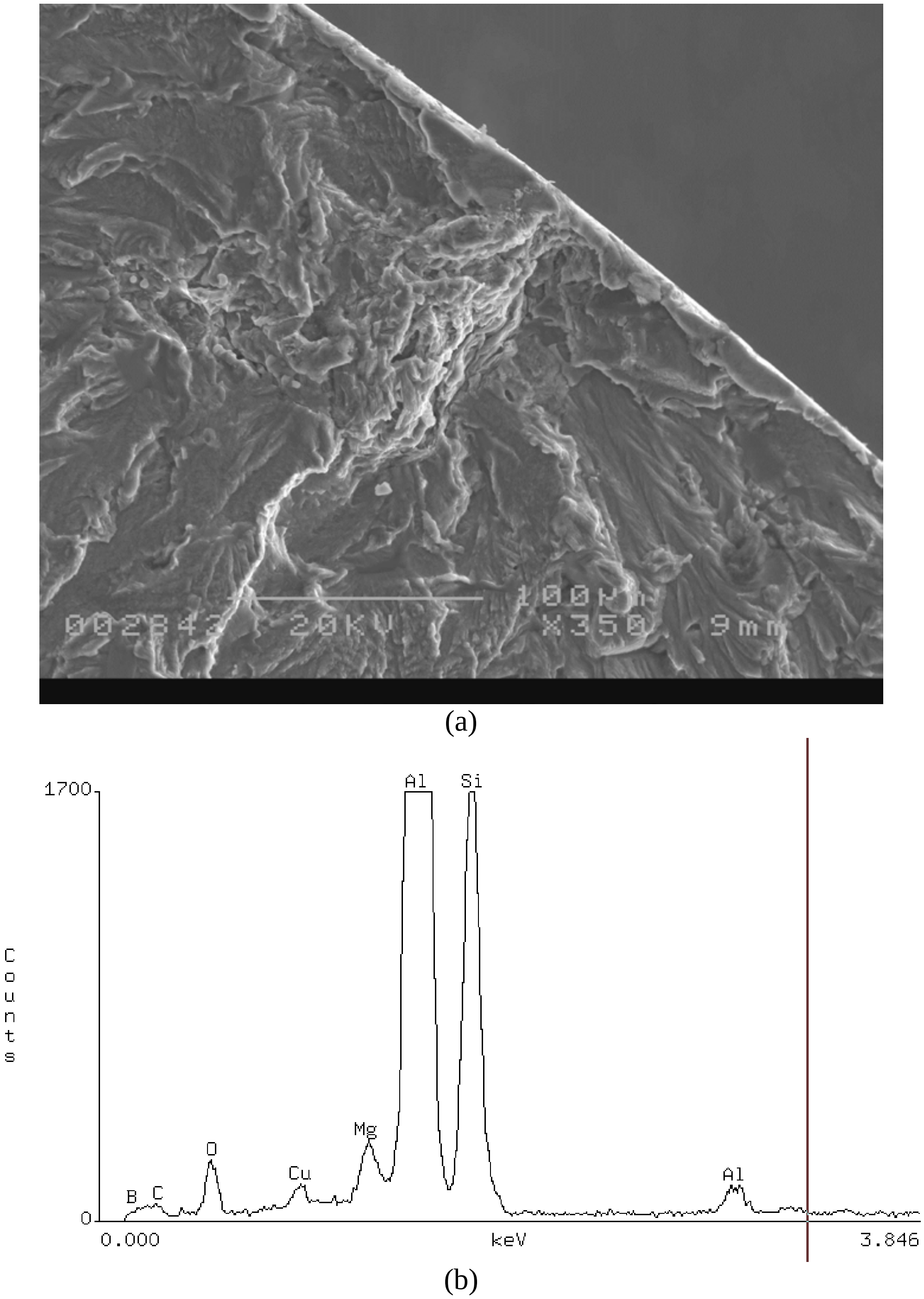

Figure 4.56 SEM micrograph of unfiltered fatigue sample lasting 402,100 cycles (a) with oxide film acting as initiation site (b) x-ray spectra of oxide film acting as initiation note the presence of aluminum, magnesium and oxygen

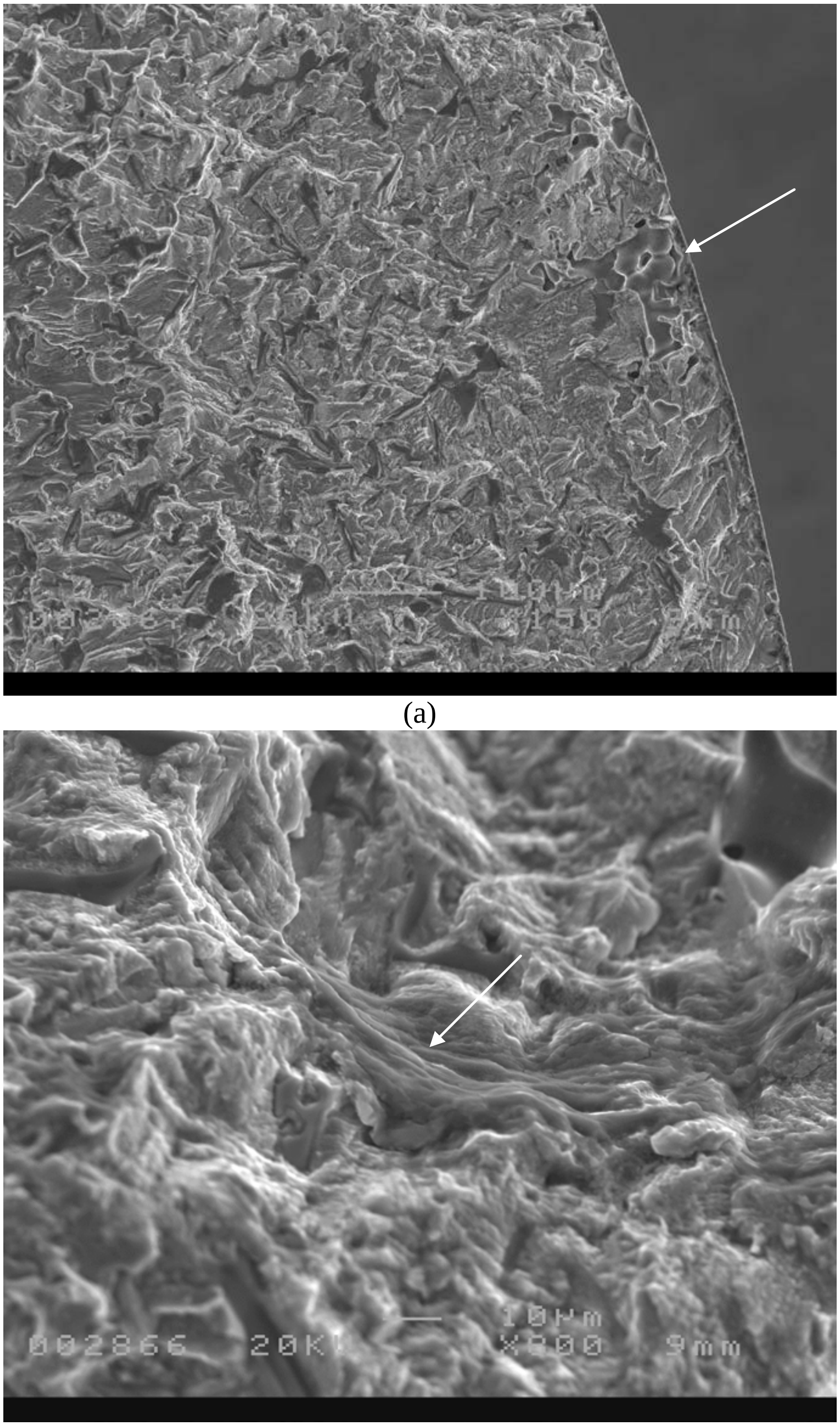

(a)

(b)

Figure 4.57 SEM micrograph of unfiltered fatigue sample lasting 528,800 cycles (a) with shrinkage pore network acting as initiation site (arrow) (b) higher magnification X800, showing old oxide associated with pore (arrow)

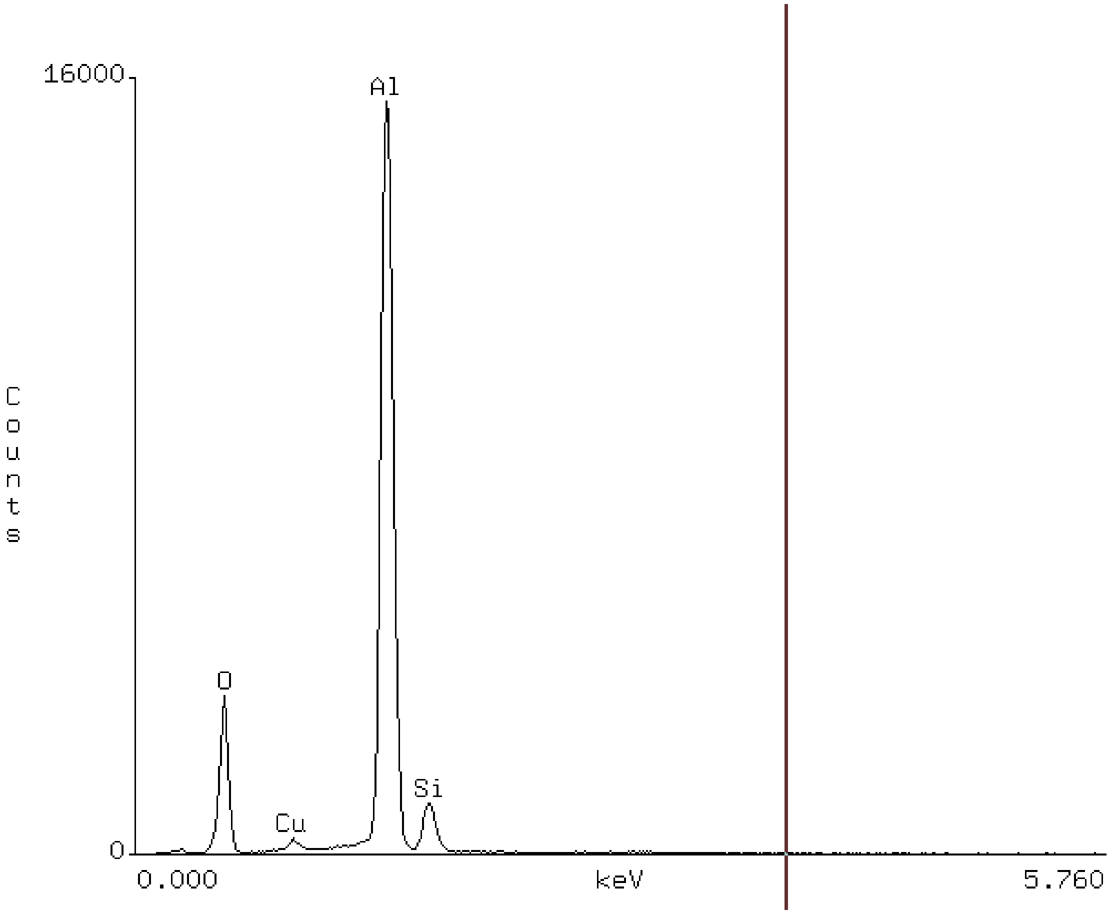

Figure 4.58 X-ray spectra of old oxide film acting as initiation site in, Figure 4.57(b) note the presence of aluminum and oxygen (no magnesium present)

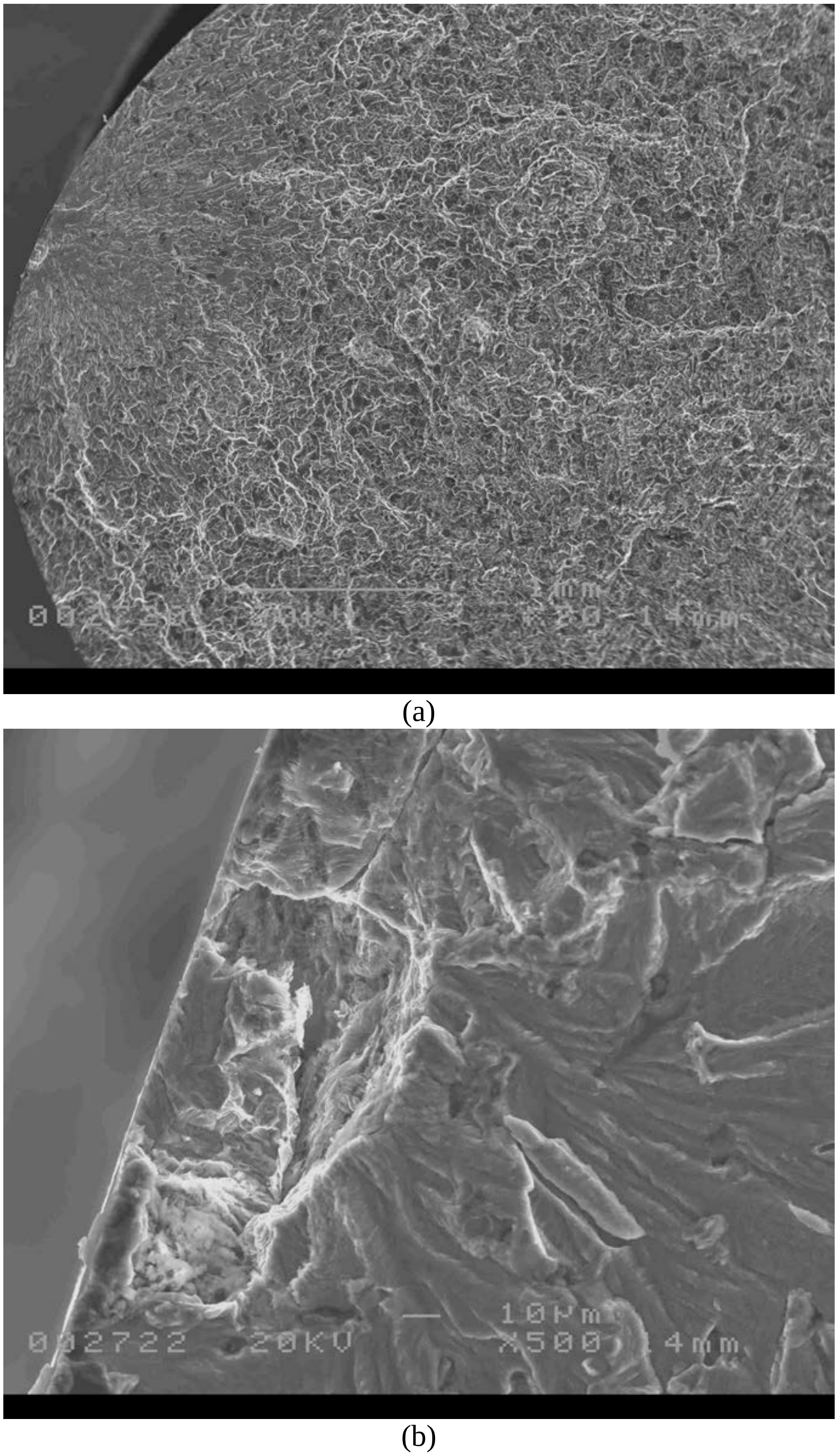

Figure 4.59 SEM micrograph of unfiltered fatigue sample lasting 808,200 cycles (a) with oxide film acting as initiation site (b) higher magnification X500, showing folded oxide

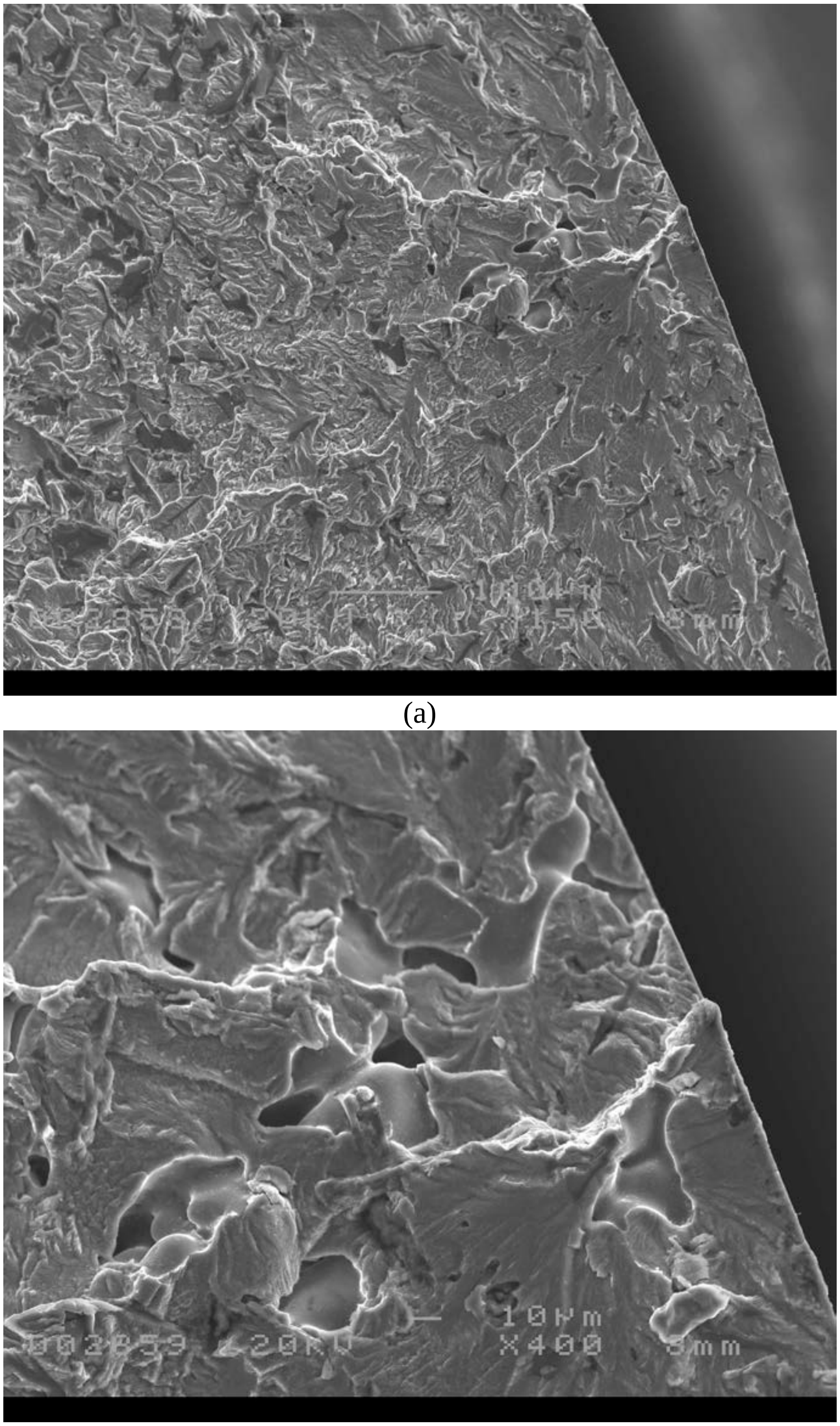

(a)

(b)

Figure 4.60 SEM micrograph of unfiltered fatigue sample lasting 4,557,700 cycles (a) with small shrinkage pore network acting as initiation site (b) higher magnification X400, showing disconnected shrinkage pore network

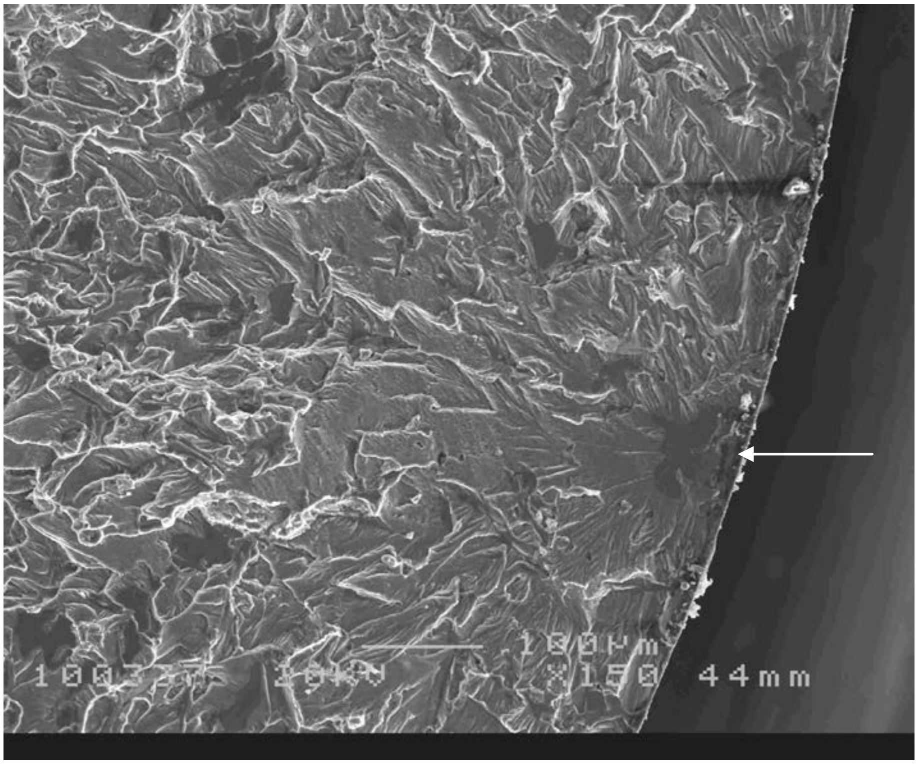

Figure 4.61 SEM micrograph of unfiltered fatigue sample lasting 309,000 cycles showing eutectic silicon particle acting as initiation site

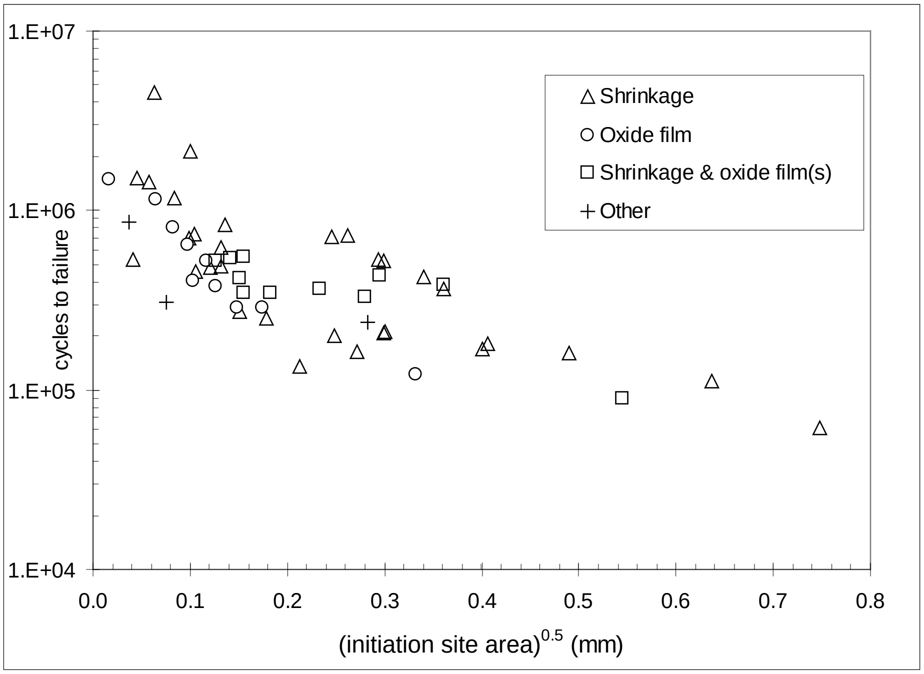

(a)

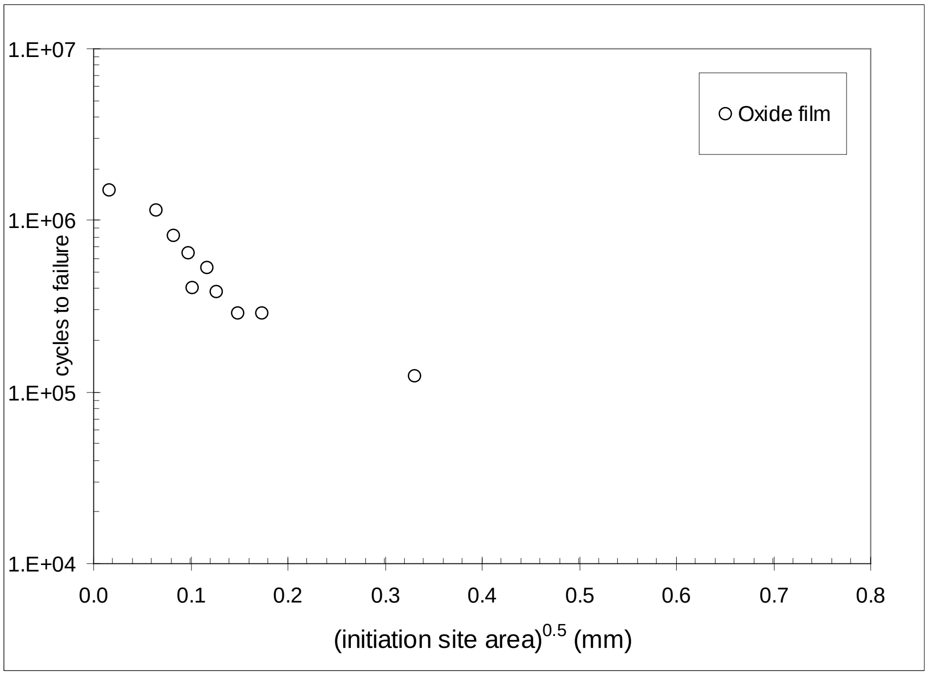

(b)

Figure 4.62 Relationship between fatigue life and initiation site size for (a) different initiation site types (b) oxide films only

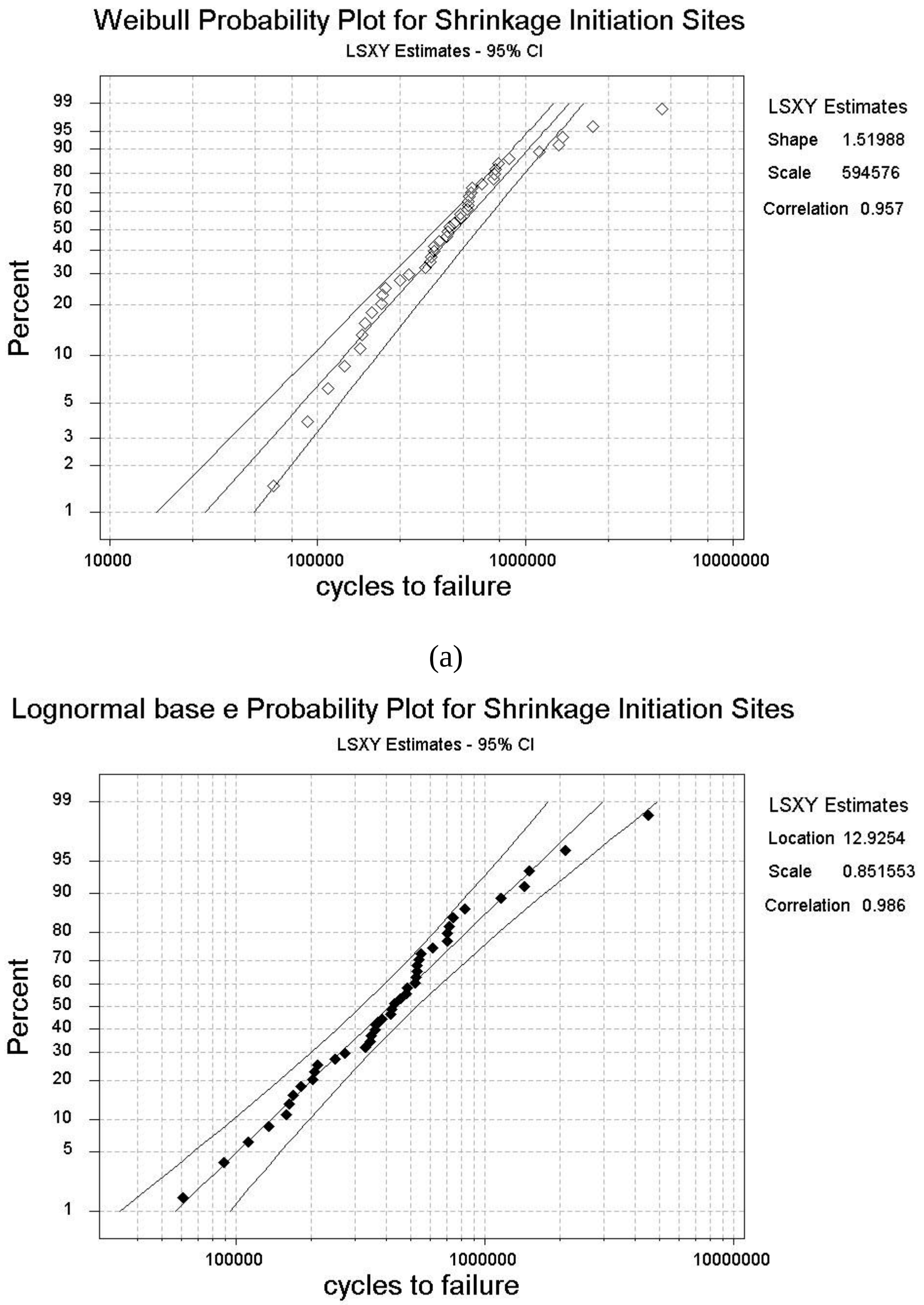

(a)

(b)

Figure 4.63 Fatigue life probability plots for samples initiated from shrinkage pores (a) Weibull (b) lognormal

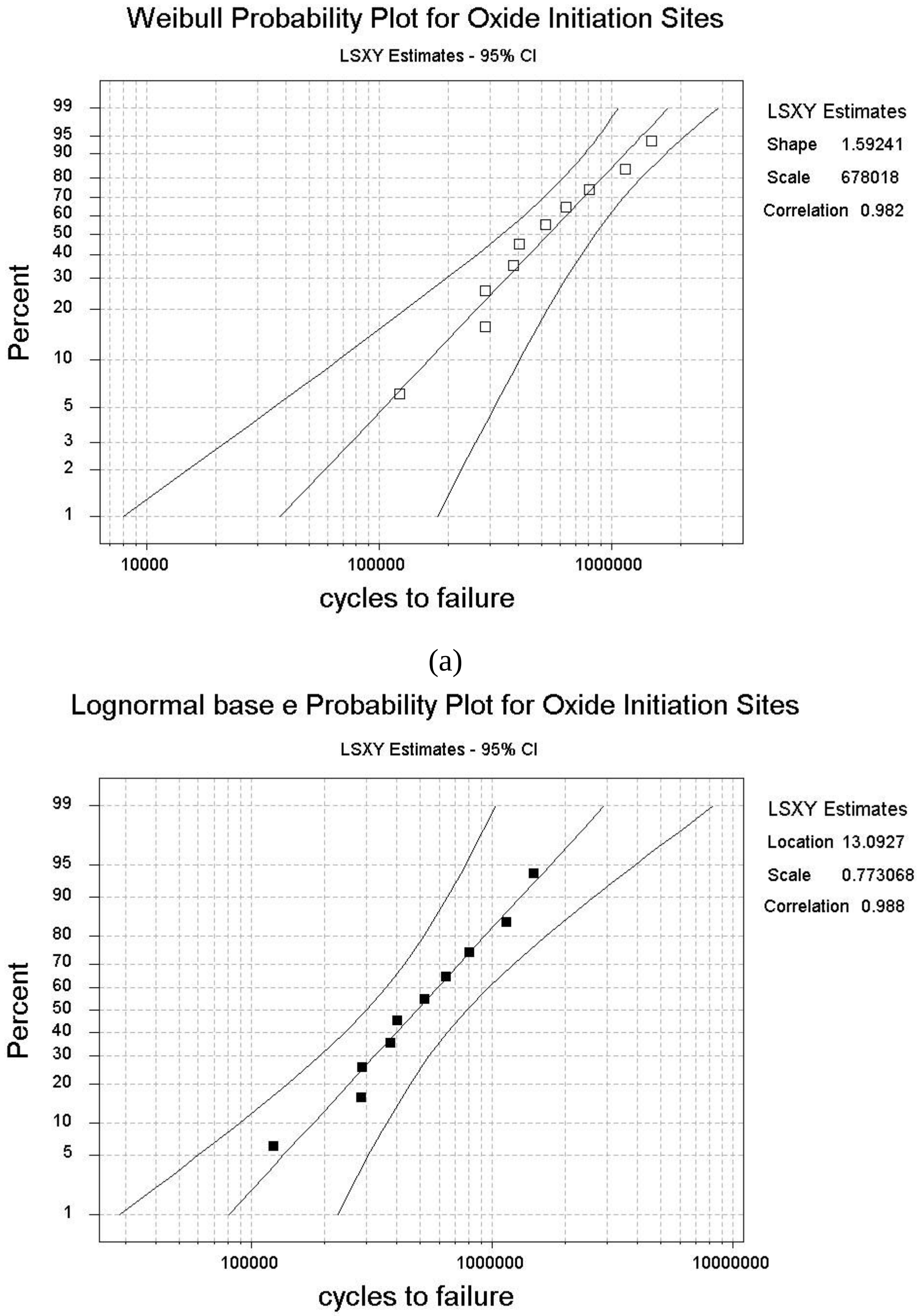

(a)

(b)

Figure 4.64 Fatigue life probability plots for samples initiated from oxide films only (a) Weibull (b) lognormal

Chapter 5 FIGURES

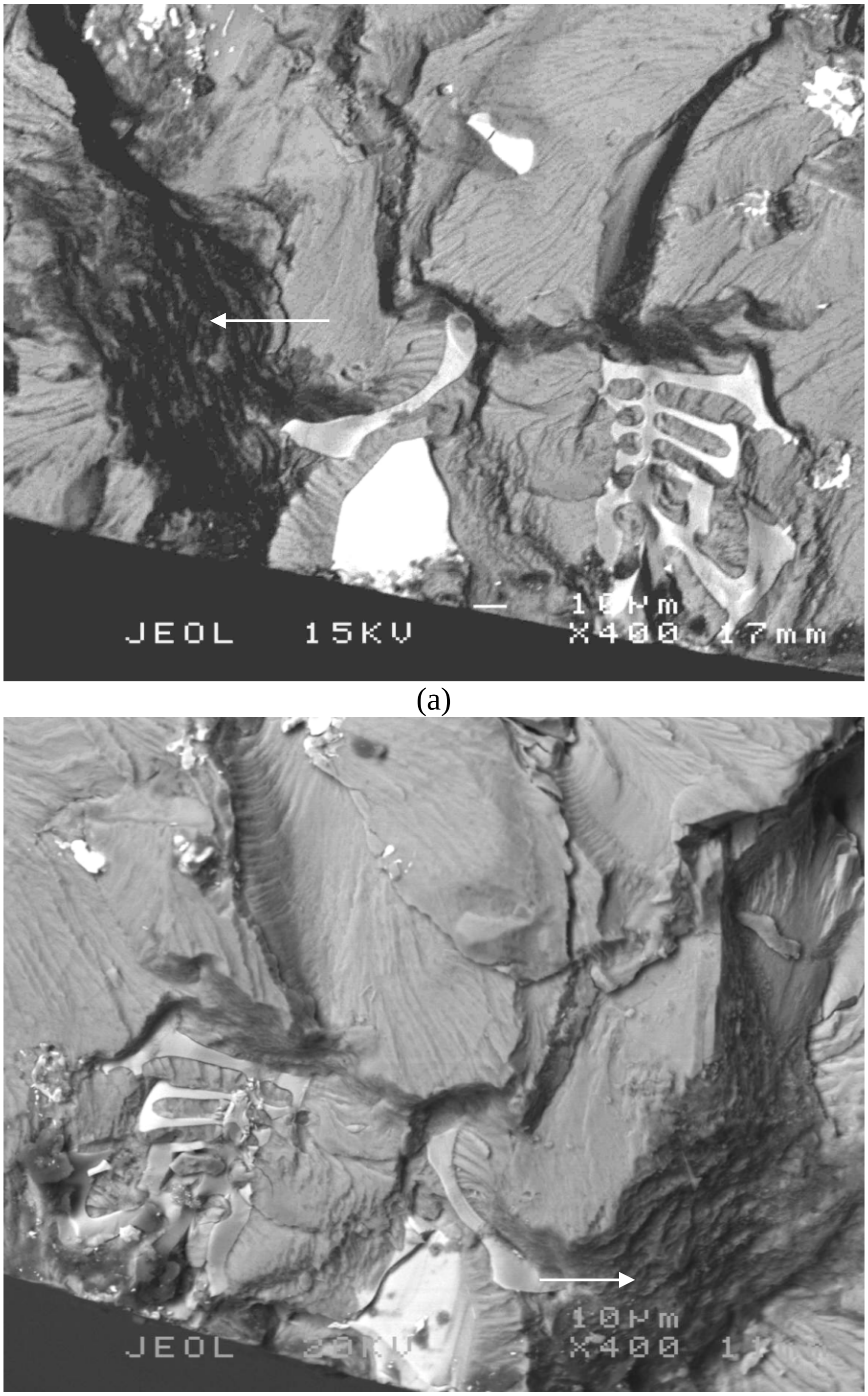

(a)

(b)

Figure 5.1 SEM micrograph showing two opposite sides of a failed staircase test sample # 1, note the presence of the oxide film on both (arrows)

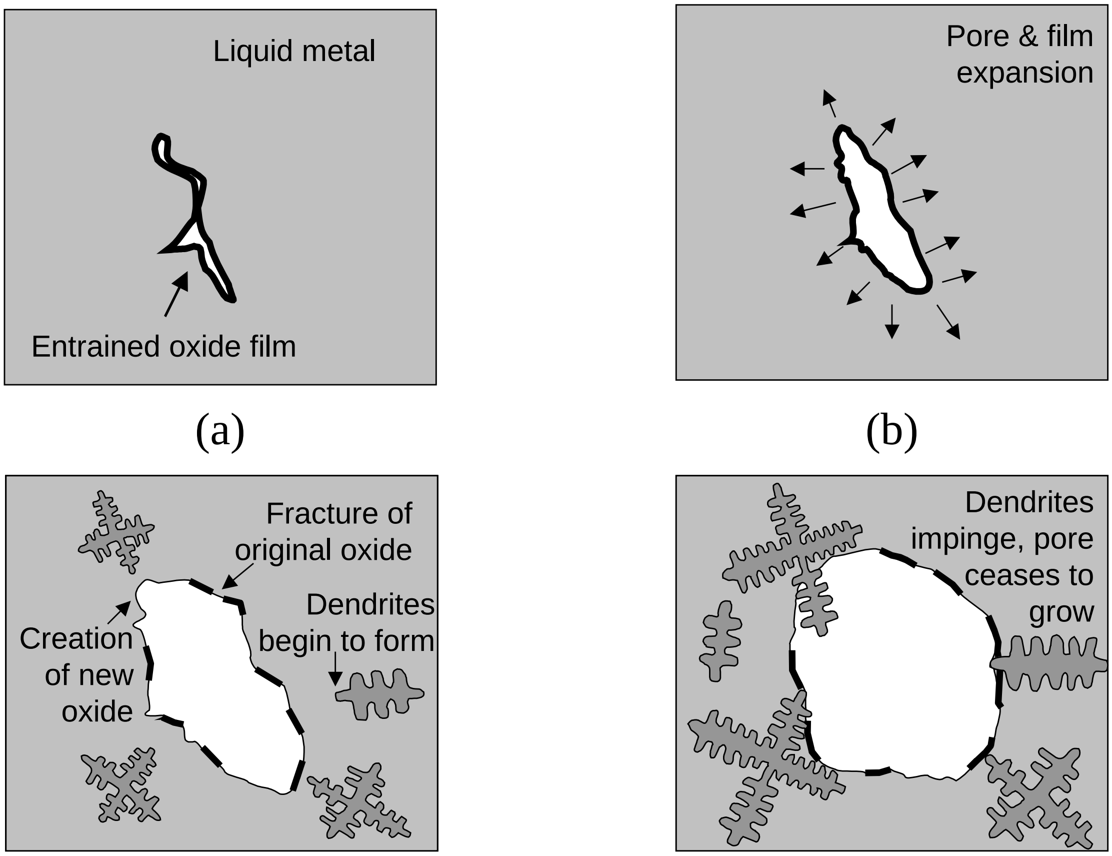

(a) (b)

(c) (d)

Figure 5.2 Schematic illustrating oxide film inflation mechanisms under reduced pressure

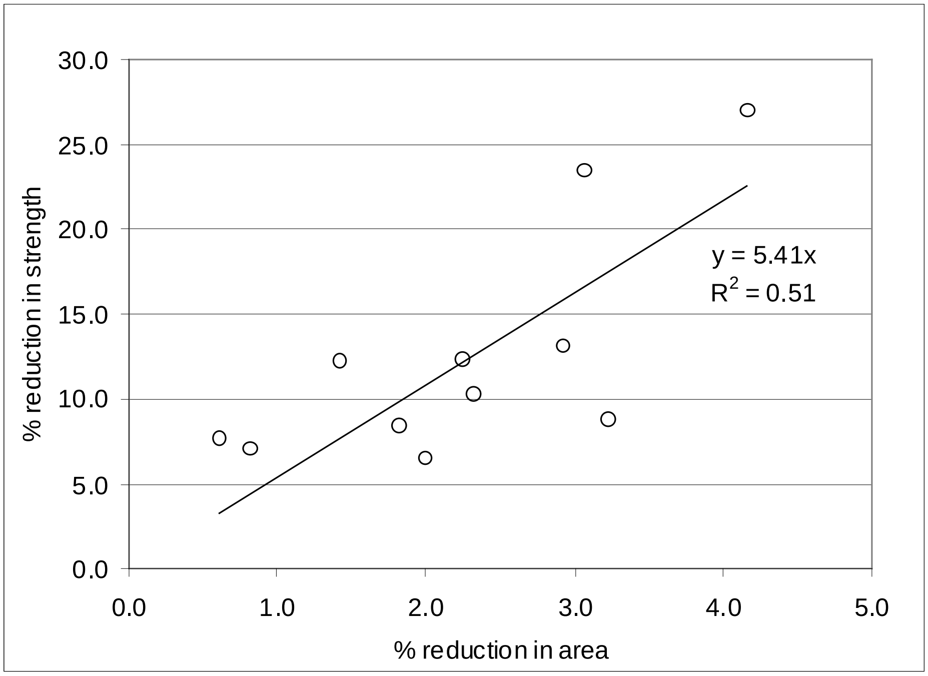

Figure 5.3 Plot of percent reduction in UTS vs percent reduction in area of the fracture surface due to the presence of oxide films

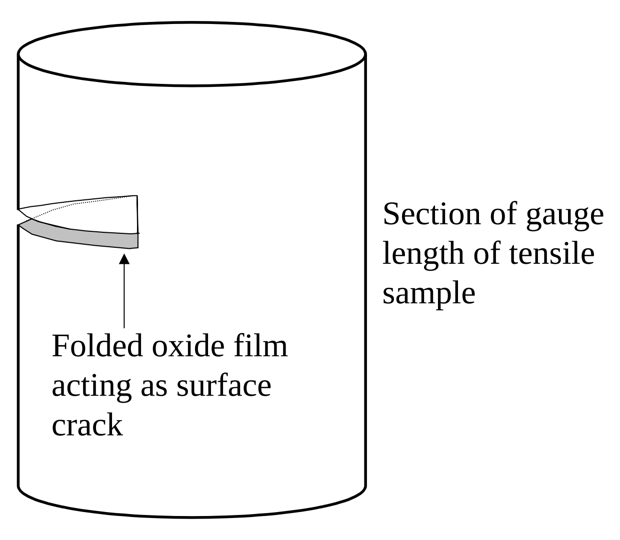

Figure 5.4 Schematic of tensile specimen gauge length showing oxide film acting as a surface crack

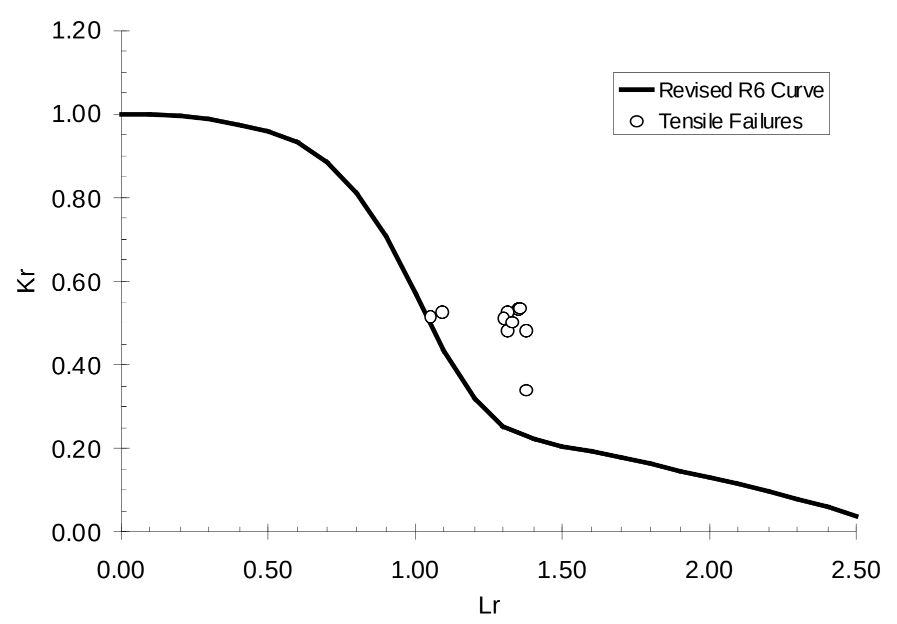

Figure 5.5 R6 (revision 3) failure assessment diagram showing points from the failed tensile bars containing oxide film defects on the fracture surface

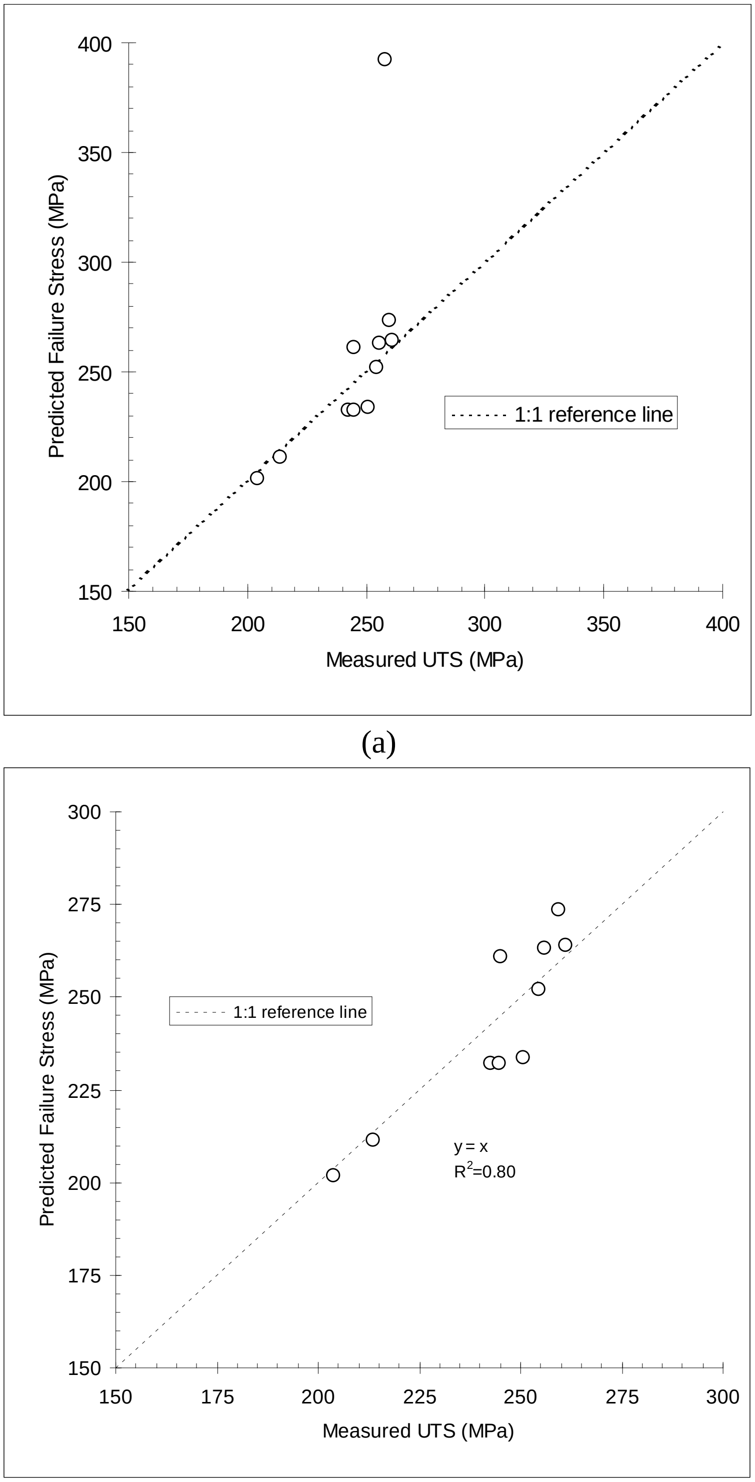

(a)

(b)

Figure 5.6 Fracture mechanics based UTS prediction model (a) using all data (b) after omitting the anomalous point and rescaling the axes

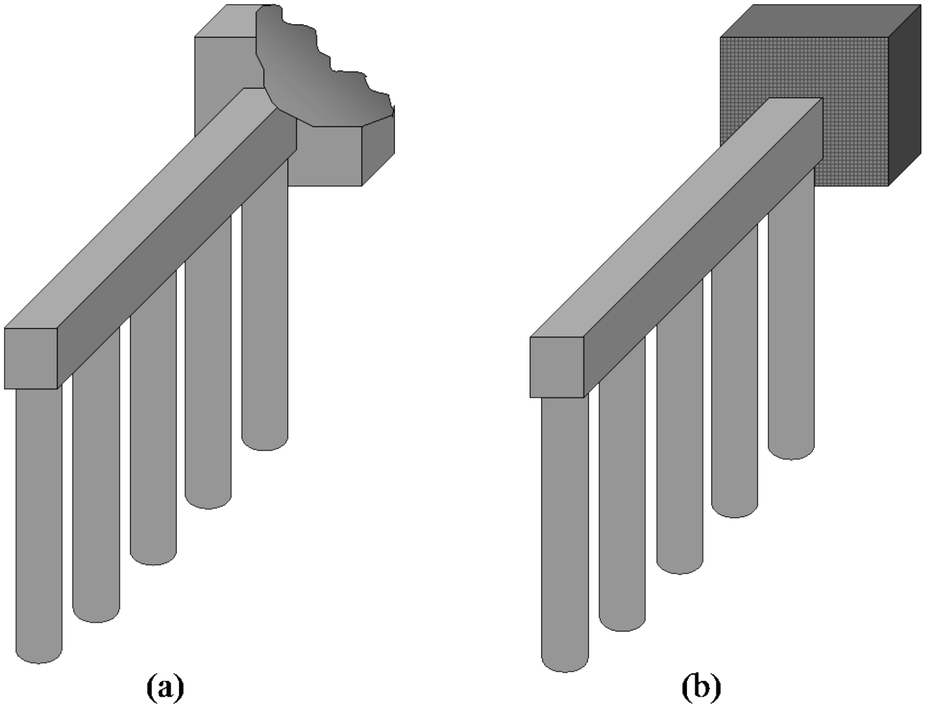

Figure 5.7 Section of running showing the reduction in volume in the filterprint portion of the running system (a) unfiltered (b) filtered cases

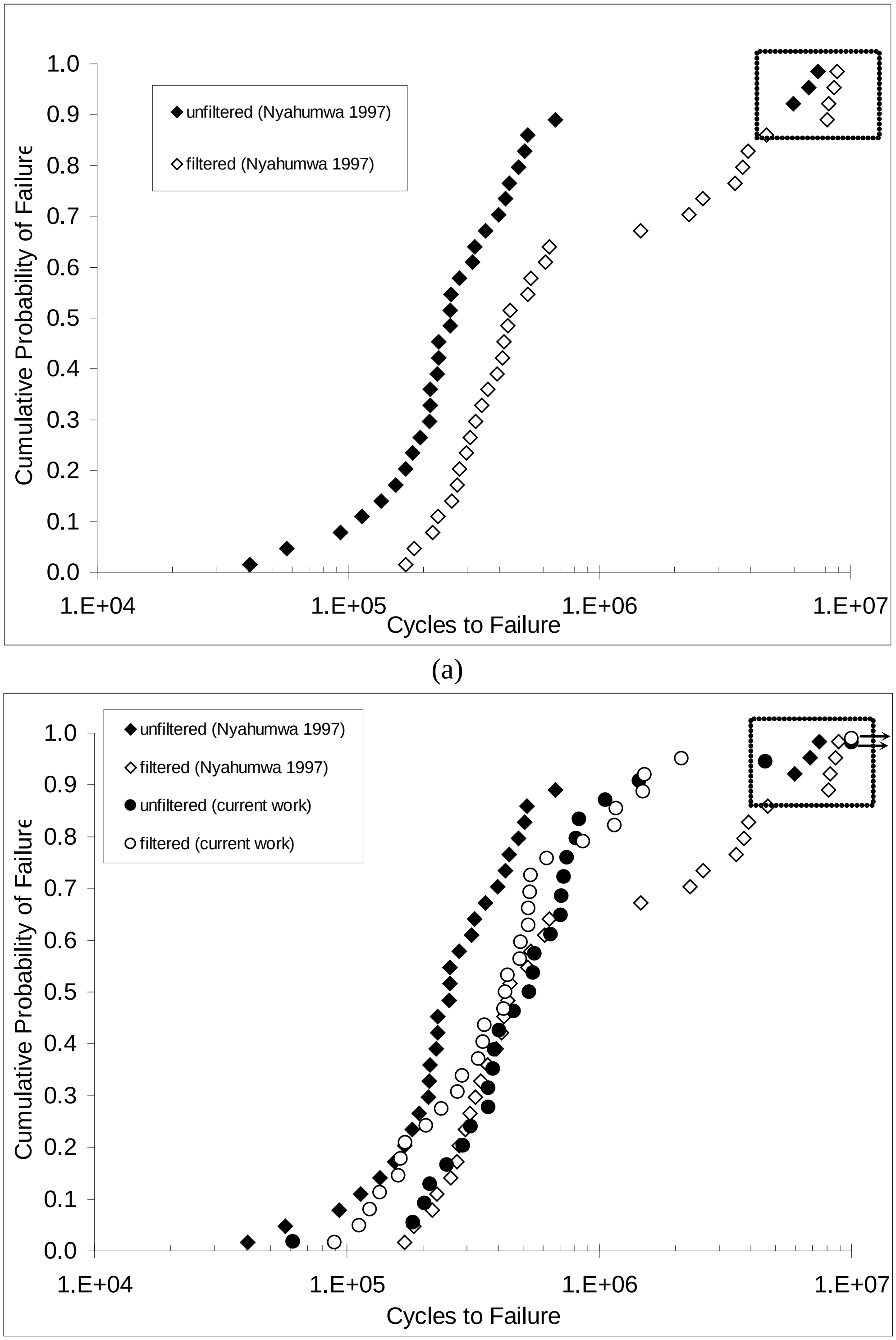

(a)

(b)

Figure 5.8 Cumulative probability plot of fatigue lives for (a) unfiltered and filtered samples from Nyahumwa 1997 (b) current work plotted together with that in (a)

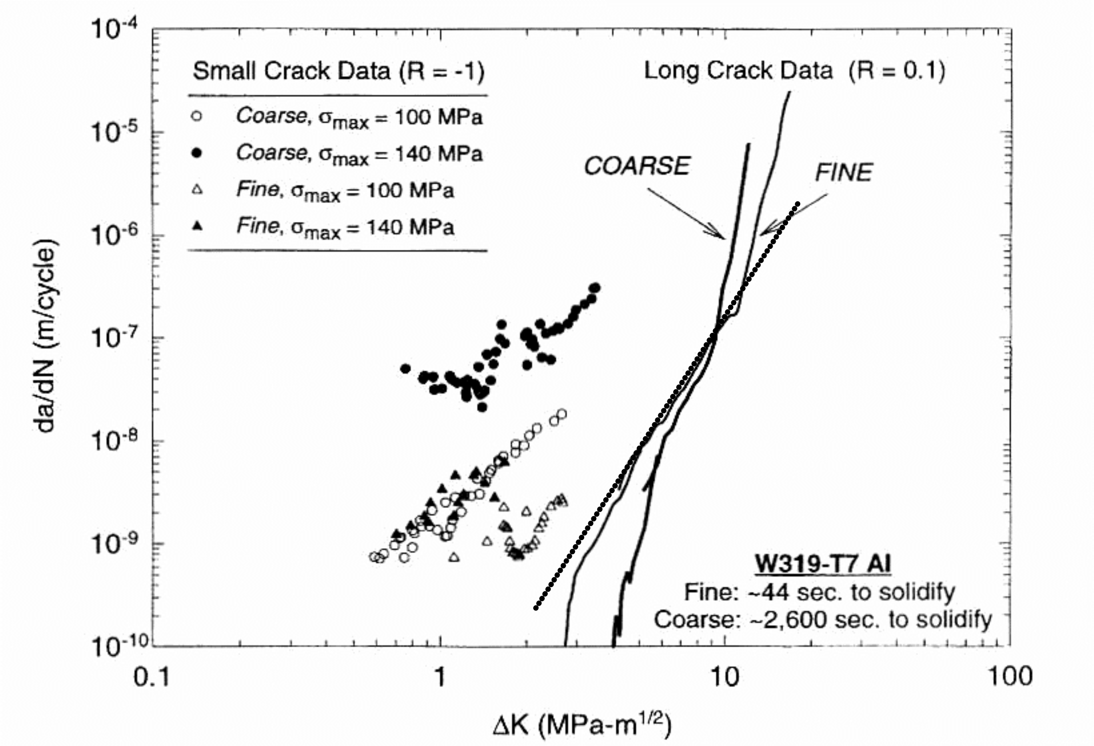

Figure 5.9 Fatigue crack growth rates as a function of stress intensity, for 319 aluminum alloy castings from (Caton, 1999), constants *C* and *m* fatigue were estimated from regime B (recall Figure 2.22) of long crack data (fine microstructure), (dotted line).

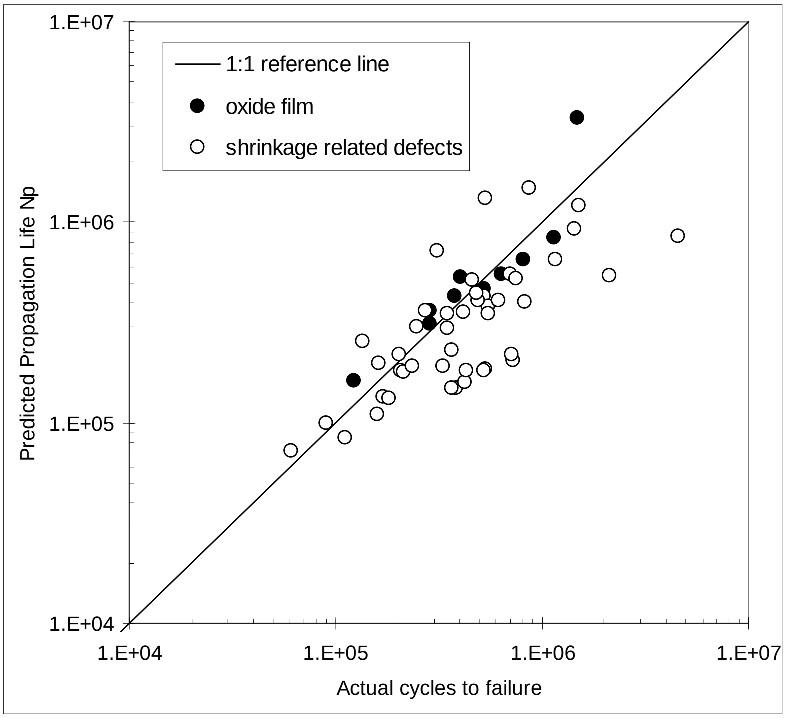

(a)

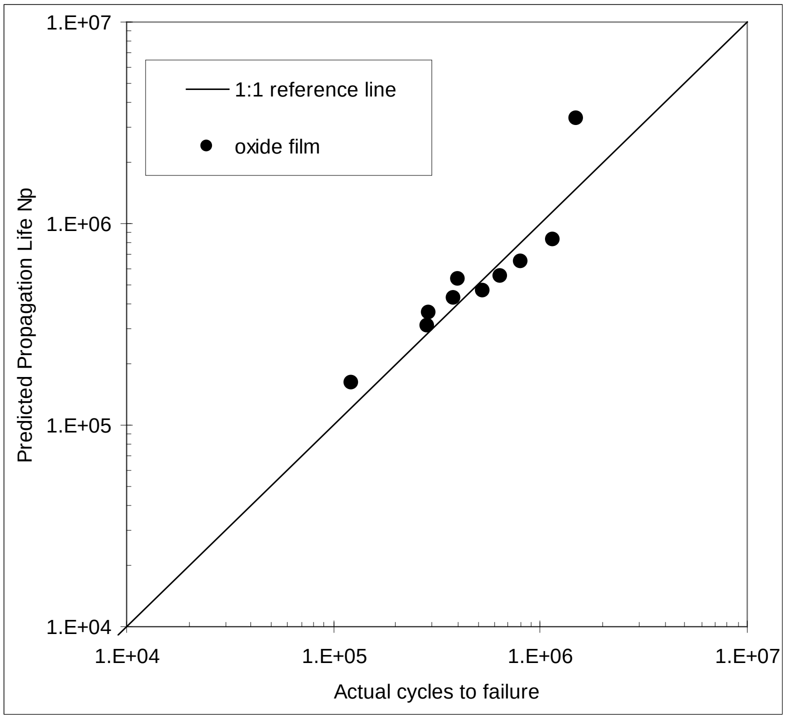

(b)

Figure 5.10 Predicted propagation life vs. actual fatigue life for (a) all samples and (b) sample that initiated on oxide films only

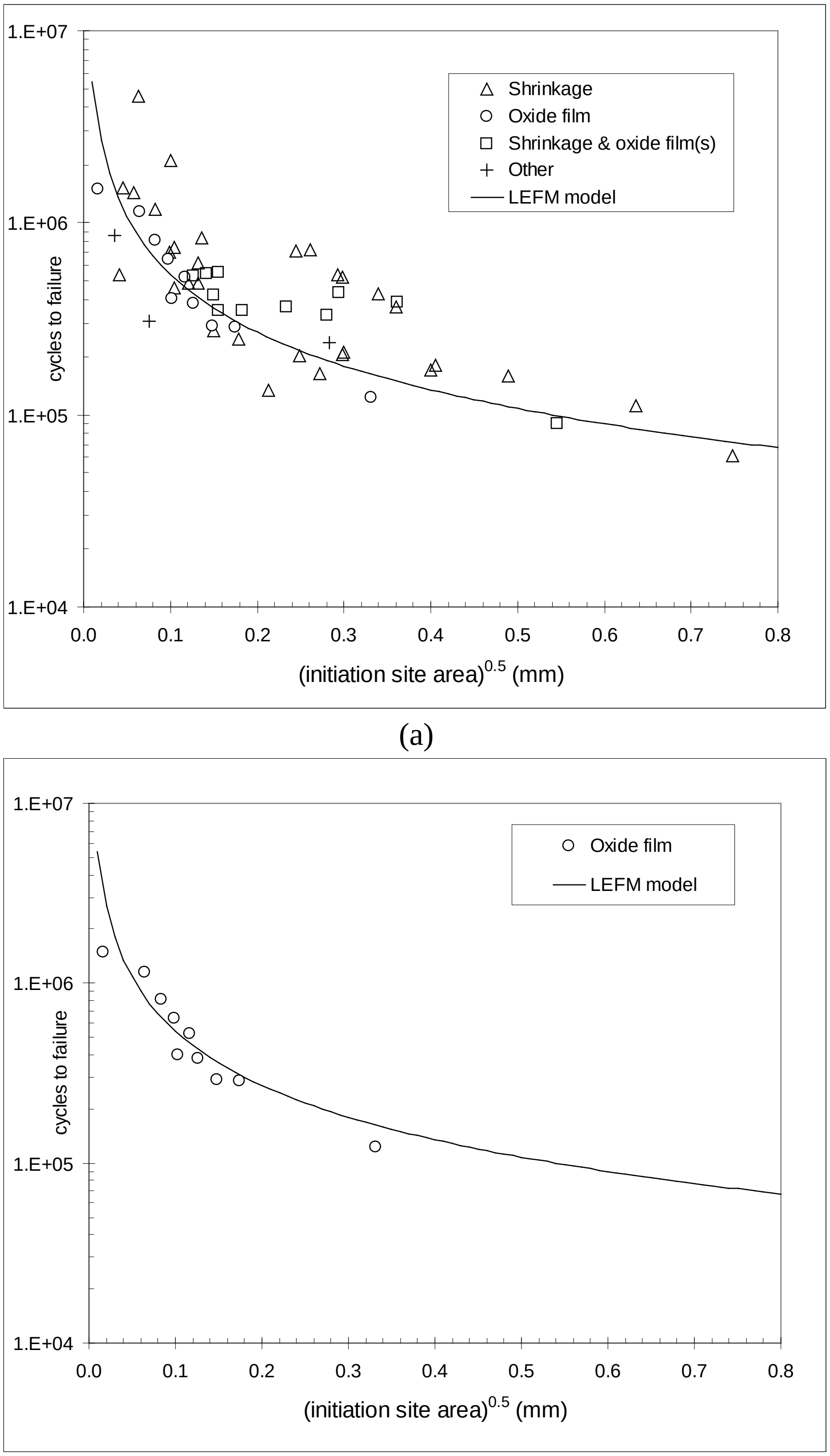

(a)

(b)

Figure 5.11 Plot of cycles to failure against initiation site size (points) compared with LEFM crack propagation model (solid line) for (a) all initiation sites (b) oxide films only